JOURNAL OF APPLIED PHYSICS

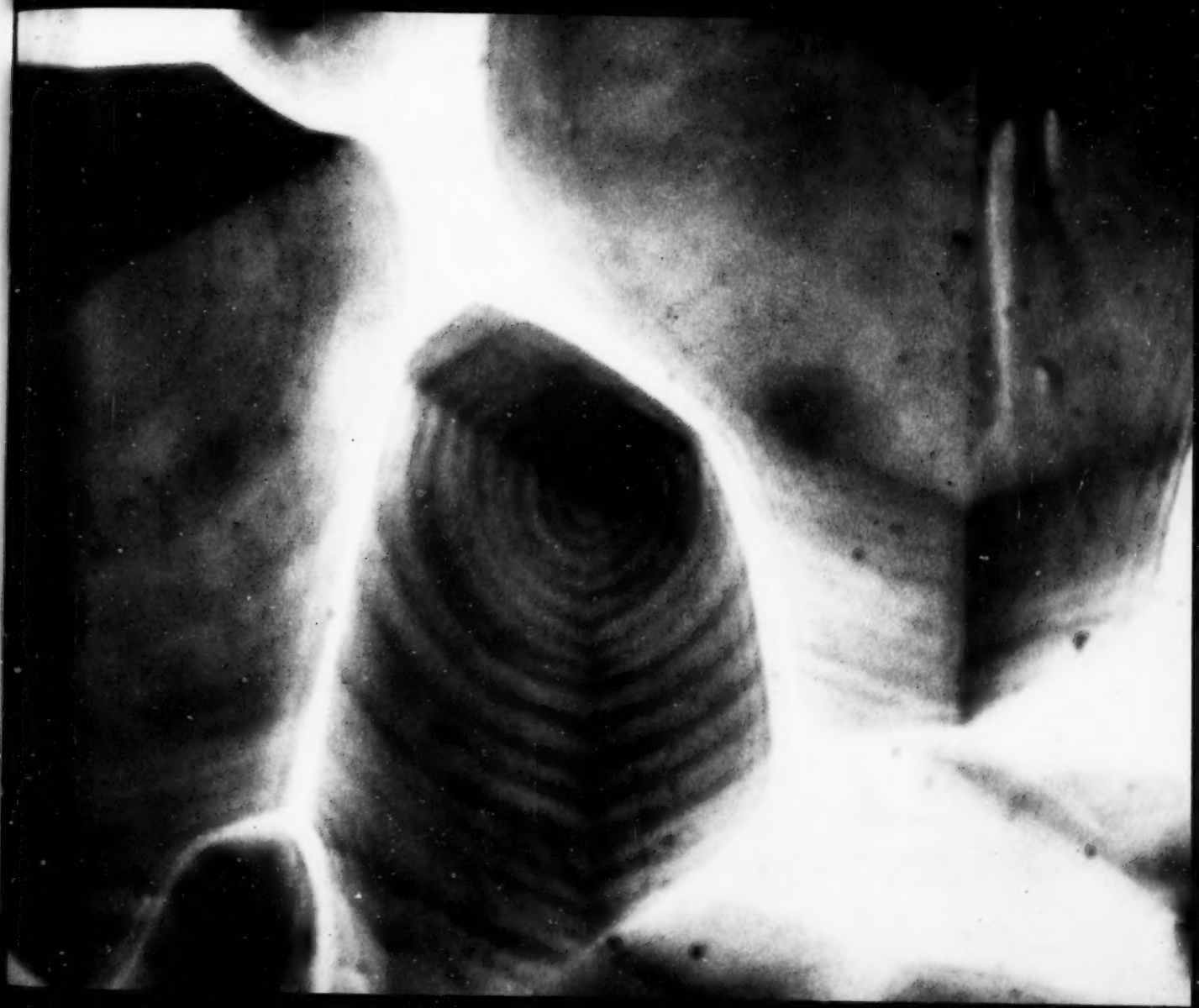

Advances . . . . . in X-ray Spectrographic Instrumentation

NEW SCINTILLATION DETECTORS

The new Norelco Scintillation Detector comprises a thallium activated sodium iodide crystal mounted on a photomultiplier tube in conjunction with a preamplifier and a cathode follower. The unit is designed for use with the Norelco Wide Range Goniometer and mounts directly on the goniometer arm. A separate chassis contains the necessary intermediate electronics permitting coupling to the electronic circuit panel.

This unit features high general efficiency of detection over the entire spectral range; higher usable counting rates *(up to 100,000 c/s)*, and pulses which are directly proportional to the energies of the X-rays which produce them.

NEW PROPORTIONAL DETECTORS

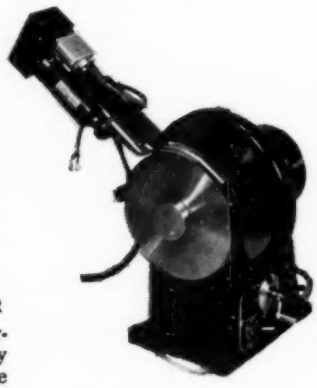

The new Norelco Proportional Detector consists of an assembly which will house either one of two differently filled side window tubes, and a small chassis equipped with a preamplifier, cathode follower and connecting cables. This unit is designed for use with the Norelco Wide Range Goniometer and mounts directly on the goniometer arm. A separate chassis contains the necessary intermediate electronics permitting coupling to the electronic circuit panel.

This unit is suited for use with radiations from elements in the low to middle atomic number range and features linear counting rates *(up to 100,000 c/s)*, excellent energy resolution of pulses, and inherent discrimination against high-energy X-ray scatter and background.

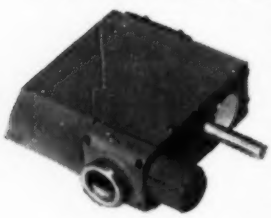

SCINTILLATION/PROPORTIONAL AMPLIFIER-SCALER

The Norelco Scintillation/Proportional Amplifier-Scaler consists of the electronic circuitry necessary for obtaining maximum benefit arising from the performance and high-speed characteristics of both detectors, and may be installed on the Electronic Circuit Panel. It consists of a linear pulse amplifier, an amplitude discriminator and three binary counters, with provision for the optional installation of a pulse height analyzer.

These new detectors are valuable in diffractometric work because they provide high quantum efficiency and greater linearity of counting rate. They are usable with pulse height analyzers effecting energy discrimination against second order radiation, fluorescent radiation from samples, or scattered radiation. In spectrography they permit higher counting rates and provide for the combination of non-dispersive and dispersive techniques, resulting in enhanced resolution and sensitivity.

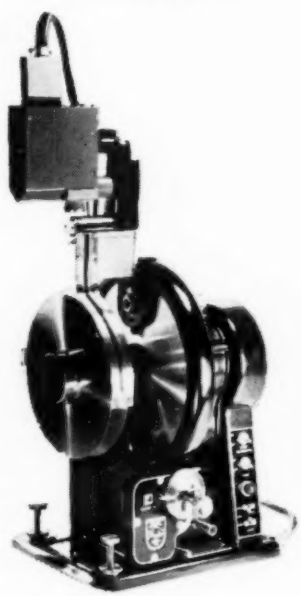

NEW HIGH-VOLTAGE GENERATOR

A new 100 KV power supply is available. Consisting of a constant potential high voltage, positive end-grounded transformer with a maximum output of 50 MA at all voltages up to 100 KV, it contains four high voltage rectifiers which supply full wave rectification to the capacitors — virtually eliminating ripple and yielding superior counting efficiency. The transformer is housed in a welded steel rectangular tank with the entire water cooling system accessible from the top—simplifying water drainage and X-ray tube exchange.

A stepless control provides smooth regulation of tube current and voltage. Values are indicated on precision meters. The control includes a twenty-three hour exposure timer and an operating time totalizer. KV is read directly from a secondary or high voltage meter. The circuit is fully protected.

A **Norelco** PRODUCT NORTH AMERICAN PHILIPS COMPANY, INC.

Serving Science and Industry

750 South Fulton Avenue, Mount Vernon, N. Y.

In Canada: Rogers Majestic Electronics Ltd., 11-19 Brentcliffe Road, Leaside, Toronto 17, Ontario

JOURNAL OF APPLIED PHYSICS

Vol. 26, No. 9 SEPTEMBER, 1955

In This Issue

Special Issue on High Polymer Physics

Retraction of Oriented Polystyrene Monofilaments . . . R. D. Andrews 1061

X-Ray Diffraction Studies of Crystallization in Elastomers . . . Leroy E. Alexander, Stanley Ohlberg, and G. Russell Taylor 1068

Birefringence and Crystallization in Elastomers . . . G. Russell Taylor and Stephen R. Darin 1075

Isothermal Viscosity-Molecular Weight Dependence for Long Polymer Chains . T. G Fox and S. Loshaek 1080

Extension of the Hertz Theory of Impact to the Viscoelastic Case . . . Yoh-Han Pao 1083

Friction of Teflon Sliding on Teflon . . . D. G. Flom and N. T. Porile 1088

Glass Transitions in Polymer-Plasticizer Systems . . . L. Breitman 1092

Proton Magnetic Resonance in Polyamides . . . W. P. Slichter 1099

Unilateral Compression of Rubber . . . Michael J. Forster 1104

Apparatus for Making Simultaneous Stress and Birefringence Measurements on Polymers . . . E. F. Gurnee, L. T. Patterson, and R. D. Andrews 1106

Regular Contributed Original Research

Effects of Attenuating Materials on Detonation Induction Distances in Gases . . . Marjorie W. Evans, Frank I. Given, and William E. Richeson, Jr. 1111

Small Particle X-Ray Scattering by Fibers. II. Radial Distribution of Microcrystallites . A. N. J. Heyn 1113

Semiempirical Expression for the First Townsend Coefficient of Molecular Gases . . . R. W. Crowe, J. K. Bragg, and J. C. Devins 1121

Measurement of Susceptibility Tensor in Ferrites . . . J. O. Artman and P. E. Tannenwald 1124

Tensile Strength of Plastics above the Glass Temperature . . . F. Bueche 1133

Dislocations in Germanium . . . S. G. Ellis 1140

Effect of Nitrides on the Coercive Force of Iron . . . J. Kerr and C. Wert 1147

Application of the Wiedemann Effect to the Magnetostrictive Coupling of Crossed Coils . . U. F. Gianola 1152

Positive-Ion Drainage in Magnetically Focused Electron Beams . . . M. E. Hines, G. W. Hoffman, and J. A. Saloom 1157

Oxide-Impregnated Nickel-Matrix Cathode . . . W. Balas, J. Dempsey, and E. F. Rexer 1163

Internal Friction Peak Associated with Precipitation in an Al-Ag Alloy . A. C. Damask and A. S. Nowick 1165

Shock Waves in Air Produced by Waves in a Plate . . . William A. Allen, Joe M. Mapes, and Earle B. Mayfield 1173

Emission from Hollow Cathodes . . . K. M. Poole 1176

Letters to the Editor:

Sticking Potential of CRT Screens . . . K. H. Jurgen Rottgardt and Wolfgang Berthold 1180

Ferromagnetic Resonance in Magnesium-Manganese Aluminum Ferrite between 160 and 1900 Mc . . . H. Suhl, L. G. Van Uitert, and J. L. Davis 1180

"Spiral Polygon" Tin Whiskers . . . Paul W. Levy and Otto F. Kammerer 1182

Wattage Lost in a Fluorescent Lamp through Elastic Collisions . . . Howard L. Steele, Jr. 1183

Theory of New Ferrite Modes in Rectangular Wave Guide . . . Benjamin Lax and Kenneth J. Button 1184

New Ferrite Mode Configurations and Their Applications . . . Benjamin Lax and Kenneth J. Button 1186

Properties of Pore Conductors . . . Ralph Forman 1187

Errata: Experimental and Theoretical Aspects of Shock-Wave Attenuation . . . Irvine I. Glass and Walter A. Martin 1187

Neutron Irradiation Effects upon Young's Modulus and Internal Friction of Copper . . . D. O. Thompson, D. K. Holmes, and T. H. Blewitt 1188

Rate-Grown Germanium Crystals for High-Frequency Transistors . . . H. E. Bridgers and E. D. Kolb 1188

Books Reviewed . . . 1189

Books Received . . . 1190

Index to Advertisers . . . xxx

JOURNAL OF APPLIED PHYSICS

A journal of applications of physics to other sciences and to industry

Published by the

American Institute of Physics

GOVERNING BOARD

Allen V. Astin
Robert F. Bacher
H. A. Bethe
J. W. Buchta
S. A. Goudsmit
Deane B. Judd
Hugh S. Knowles
W. H. Markwood, Jr.
William F. Meggers
Philip M. Morse
Brian O'Brien
Harry F. Olson
R. F. Paton
Eric Rodgers
Ralph A. Sawyer
Frederick Seitz
William Shockley
H. D. Smyth
J. H. Van Vleck
Mark W. Zemansky

OFFICERS AND STAFF

Frederick Seitz
Chairman, Governing Board

Henry A. Barton
Director

George B. Pegram
Treasurer

Wallace Waterfall
Executive Secretary

Theodore Vorburger
Advertising Manager

Ruth F. Bryans
Publication Manager

Edith I. Neftel
Circulation Manager

Kathryn Setze
Assistant Treasurer

Melvin Loos
Consultant on Printing

Editor
Robert L. Sproull

Editorial Board

Maurice A. Biot
Walker Bleakney
Wallace J. Eckert
Elmer Hutchisson
D. O. North
Louis A. Pipes
W. R. Smythe
Arthur V. Tobolsky
A. M. Weinberg

THE JOURNAL OF APPLIED PHYSICS is devoted to the application of physics to other sciences, to engineering, and to industry. Previous to 1937, this journal was called PHYSICS.

The JOURNAL OF APPLIED PHYSICS welcomes articles of two distinct kinds: (1) Descriptions of new results in experimental or theoretical physics which are of general interest to applied physicists. The author should explain his contribution in such a way that a physicist or engineer in another field of specialization can appreciate its objectives and essential features. (2) Critical reviews of particular areas of applied physics. Authors contemplating writing such reviews should correspond with the Editor before they begin writing.

The JOURNAL OF APPLIED PHYSICS welcomes letters to the editor which describe in a few words the content of laboratory reports and theses and which tell readers how they may obtain copies of such reports.

Manuscripts should be submitted to the Editor, Rockefeller Hall, Cornell University, Ithaca, New York. Authors should read the "Information for Contributors," facing page 1 of the January issue, before writing articles or letters. The *Style Manual* of the American Institute of Physics is also helpful to writers preparing manuscripts for journals published by the American Institute of Physics. It can be obtained for $1.00 from the American Institute of Physics, 57 East 55th Street, New York 22, New York.

Corrected proofs and all correspondence concerning papers in the process of publication should be addressed to the Publication Manager, American Institute of Physics, 57 East 55 Street, New York 22, New York.

Subscriptions, renewals, and orders for back numbers should be addressed to the American Institute of Physics, 57 East 55 Street, New York 22, New York.

Subscription Price	U.S. and Canada	Elsewhere
To members of the American Institute of Physics and Affiliated Societies	$10.00	$11.00
To all others	12.00	14.00

Back Number Prices

Yearly back number rate when complete year is available: $15.00.
Single copies: $1.50 each.

Changes of address should be sent to the American Institute of Physics.

Advertising rates supplied on request. Orders, advertising copy, and cuts should be sent to the American Institute of Physics.

Entered as second class matter January 22, 1937, at the Post Office at Lancaster, Pennsylvania, under the Act of March 3, 1879. Accepted for mailing at the special rate of postage provided for in paragraph (d-2), section 34.40, P. L. & R. of 1948, authorized May 2, 1932.

Journal
of
Applied Physics

Volume 26, Number 9 September, 1955

Special Issue on High Polymer Physics

The following ten papers were presented at the meeting of the Division of High Polymer Physics of the American Physical Society in Baltimore, Maryland, March 17–19, 1955.

Retraction of Oriented Polystyrene Monofilaments

R. D. Andrews
Physical Research Laboratory, The Dow Chemical Company, Midland, Michigan
(Received May 12, 1955)

When oriented polystyrene monofilaments are heated to temperatures in the neighborhood of the transition temperature they retract to an unoriented state at conveniently measurable rates. Curves of length as a function of time have been measured at five different temperatures (75°–95°C, at 5° intervals) for two filaments with different initial amounts of orientation.

When the retraction curves are plotted as length *vs* log time, it is found that the curves at different temperatures are not superposable by lateral shift along the logarithmic time scale, as would be true for simple viscoelastic behavior. Activation energies calculated from these curves are a function of time as well as of temperature; the activation energy at any given temperature tends to level out to a final constant value with increasing time, however. The rate of change of activation energy with time increases with increasing temperature, so that the final value is attained more quickly; the final value also decreases systematically with increasing temperature.

Final activation energy values increase rapidly with decreasing temperature in this region and are very high (300 kcal at 75°). It is postulated that specific volume changes are responsible for the time-dependent activation energies observed in these experiments. It is also of interest that these experiments appear to isolate the viscoelastic mechanism involving molecular configuration change from that involving local molecular distortions.

INTRODUCTION

THE present measurements of the retraction of oriented polystyrene monofilaments in the neighborhood of the transition temperature were carried out as part of a general study of molecular orientation and related optical and mechanical phenomena in polystyrene; two publications[1,2] from this work have already appeared.

The temperature range in which retraction occurs at conveniently measurable rates is fairly narrow: at temperatures much lower than 10° below the transition temperature, retraction takes place extremely slowly, while at temperatures much higher than 10° above the transition temperature, retraction takes place too rapidly to measure without the use of special instrumentation. The temperature range used in the present experiments was 75–95°C, with experimental temperatures spaced at 5° intervals. The transition temperature for polystyrene is roughly 80–85°C.

The retraction of these filaments corresponds to a return of the molecules from a state of one-dimensional orientation to an unoriented state, and also involves a decay of the optical birefringence which is associated with molecular orientation. However, only the changes of length with time will be considered in the present paper.

These retraction experiments are similar to "creep recovery" experiments under zero load. However they are different in that the initial state of the sample does not represent some stage in a simple creep experiment but was arrived at by a more complicated stress-time-temperature path. The retraction curves obtained therefore probably do not have a simple correspondence

[1] R. D. Andrews, J. Appl. Phys. 25, 1223 (1954).
[2] E. F. Gurnee, J. Appl. Phys. 25, 1232 (1954).

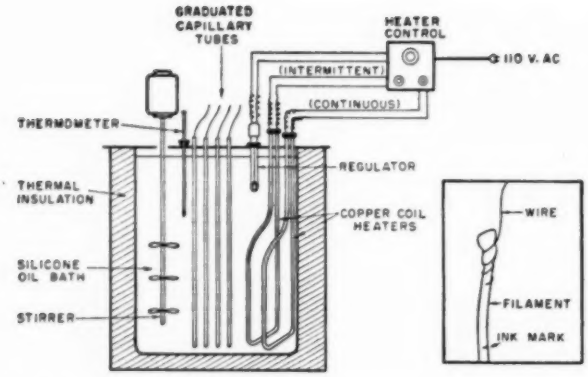

FIG. 1. Sketch of experimental setup for retraction measurements.

with the total distribution of retardation times characterizing the material, even though they can be represented formally by a distribution of retardation times.

EXPERIMENTAL METHOD

The retraction experiments were carried out by inserting pieces of oriented filament into capillary tubes (graduated in millimeters with centimeter divisions numbered) which were immersed in a thermostated oil bath. The bottom ends of the capillary tubes were sealed, so that the oil did not enter the tubes. A schematic sketch of the experimental arrangement is given in Fig. 1. The pieces of filament were held by twisting a piece of wire around the top end and contracting the filament into the twists of the wire by local heating; this is shown in the insert of Fig. 1. The thermostated oil bath was kindly loaned to us by D. R. Stull of the Dow Thermal Laboratory.

The method of fabrication of the oriented filaments has been described previously.[1,3] Retraction measurements were carried out on two filaments with different degrees of orientation. These will be designated as filaments #3 and #7, and data characterizing these filaments are presented in Table I. Definitions of terms can be found in references 1 and 3. Both filaments were made from an ordinary commercial production polystyrene with a light-scattering molecular weight of 310 000. It will be noted that although filament #7 had a higher nominal percent hot stretch than filament #3, the degree of orientation as indicated by average birefringence (retardation at the center divided by the diameter) is actually lower; this is undoubtedly to be explained by the fact that the stretching temperature was higher, and the stretching rate slower, allowing more of the orientation to relax out before the filament was quenched.

An ink mark was placed near the top of the filament by cutting a nick in the filament with a razor blade and filling the nick with India ink. The distance between this ink mark and the lower end was taken as the length of the filament. During the early part of the experiments, when the length was changing rapidly, the positions of the ink mark and lower end were read alternately, and the values of one of these had to be plotted as a function of time, and a curve drawn for interpolation, in order to obtain simultaneous values of the ink mark and lower end which would give length values as a function of time. During the first few minutes of an experiment it was helpful to have two people working together, one taking readings on the filament and the other reading time values and recording data.

The zero-time length of the samples was obtained by measuring the length at room temperature, and applying a correction for the thermal expansion corresponding to the experimental temperature. The linear thermal expansion of filaments #3 and #7 was measured by inserting lengths of filament into calibrated capillary tubes and varying the bath temperature below the transition temperature (10–55°C), and fitting the resulting plot of length *vs* temperature with a straight line by the method of least squares. The values obtained for the expansion coefficient were somewhat different for the two filaments, as seen from Table I, but these values are very approximate, and the difference may not be significant. Initial length values were approximately 26 cm.

Also listed in Table I are values for the elongation at break, and length at total contraction for the two filaments. The unusually high elongation at break of filament #3 (almost 10 times that of filament # 7) is a result of cold-stretching; this phenomenon will be discussed in detail in a future publication. Total contraction was measured by first immersing samples of each filament in boiling water (*ca* 100°C) until contraction was almost complete, and then suspending the samples vertically in test tubes surrounded by hot oil at 120°C. The length was measured at suitable intervals until minimum values were attained; beyond this point the length slowly increased as a result of

TABLE I. Properties of filaments.

	#3	#7
Diameter (mm)	0.51	0.53
Av birefringence (5461 A)	0.0242	0.0080
Temperature of:		
Extruder	191°C	191°C
Stretching baths (B_1, B_2)	104°C	132°C
Quenching bath (B_3)	49°C	49°C
Speed of rolls (rpm):		
R_1	55	20
R_2	120	120
R_3	120	120
Percent hot stretch	118	500
Stretching rate (%/min)	84.5	13.0
Coefficient of linear thermal expansion (fractional length/°C)	4.2×10^{-5}	6.5×10^{-5}
Percent elongation at break (21°C)	42	4.5
Percent of original length when completely contracted	15.2	11.8

[3] Cleereman, Karam, and Williams, Modern Plastics **30**, 119 (May, 1953).

creep of the samples under their own weight. The minimum length values were taken as complete contraction. These values were satisfactorily reproducible and the values listed in Table I represent averages of four duplicate determinations.

Zero time was taken arbitrarily as the moment when the sample was inserted in the capillary tube. One nonideal feature of these experiments is that the filaments do not reach temperature equilibrium instantaneously. The retraction curves may therefore be somewhat in error in the short-time region, and it is desirable to estimate the magnitude of this time lag in order to judge how serious its effects may be. This can be done roughly from consideration of the ideal case of a cylinder with infinite length and finite diameter; the temperature is initially uniform throughout, and the temperature at the surface is then suddenly changed to a new value and maintained constant at that value. This is a classical problem in heat conduction and its solution is discussed, for example, by Carslaw and Jaeger,[4] who give curves for the temperature at the center, the average temperature, and the radial distribution of temperature as a function of time.

The most critical test of how quickly the filament reaches temperature is provided by the temperature at the center of the filament. Numerical values for the variation of center temperature with time, in terms of dimensionless variables, are given in tabular form by Williamson and Adams,[5] and this same universal curve is given in particularly convenient graphical form for use in the present problem (i.e., as a semilogarithmic plot) by Jacob[6] and McAdams.[7] These results all assume negligible surface resistance to heat transmission.

The thermal measurements of Ueberreiter and co-workers[8–10] indicate that the temperature conductivity (or thermal diffusivity) of polystyrene is approximately 0.0008 cm^2/sec, and this value was assumed to apply for the oriented filaments studied here. As an indication of the effects of filament diameter and bath temperature on the time required to reach temperature, the times required for the center of the filament to reach temperatures 1° below, 0.1° below and 0.01°C below the bath temperature were calculated for polystyrene cylinders of diameter 0.5, 1.0, and 1.5 mm and bath temperatures of 75°, 85°, and 95°C, assuming room temperature (initial temperature) to be 23°C.

[4] H. S. Carslaw and J. C. Jaeger, *Conduction of Heat in Solids* (Oxford University Press, London, England, 1947). See in particular Fig. 9 (p. 84) and Fig. 19 (p. 175).

[5] E. D. Williamson and L. H. Adams, Phys. Rev. **14**, 99 (1919).

[6] M. Jacob, *Heat Transfer* (John Wiley and Sons, Inc., New York, 1949), Vol. I. See in particular Fig. 13–2 (p. 266).

[7] W. H. McAdams, *Heat Transmission* (McGraw-Hill Book Company, Inc., New York, 1954), third edition. See in particular Fig. 3–9 (p. 43).

[8] K. Ueberreiter and S. Nens, Kolloid-Z. **123**, 92 (1951).

[9] K. Ueberreiter and E. Otto-Laupenmühlen, Kolloid-Z. **133**, 26 (1953).

[10] K. Ueberreiter and E. Otto-Laupenmühlen, Z. Naturforsch. **8a**, 664 (1953).

TABLE II. Estimated time required for center of filament to reach temperature after insertion in temperature bath.

Filament diameter (mm)	Bath temperature (°C)	Time in seconds required to approach bath temp. within: 1°	0.1°	0.01°
0.5	75	0.6	0.9	1.2
	85	0.6	0.9	1.2
	95	0.6	1.0	1.3
1.0	75	2.4	3.7	4.9
	85	2.5	3.7	5.0
	95	2.6	3.8	5.1
1.5	75	5.4	8.2	11.0
	85	5.6	8.4	11.2
	95	5.8	8.6	11.4

The results are given in Table II. It is obvious that filament diameter has more effect than bath temperature on this time lag. Filaments #3 and #7 both had diameters in the range 0.5–0.6 mm (see Table I), and they should therefore require, in terms of this idealized model, only about one or two seconds to reach temperature (within the accuracy of thermostatic control). An uncertainty of this sort would be negligible except at the shortest times, and if these calculations are reliable even as to order of magnitude, it would appear that this time lag is not too serious. Actually, the time values in Table II should probably be regarded as lower limit values.

Experiments could not be carried out at temperatures above 95° because the filaments tended to stick to the walls of the capillary tubes; attempts to eliminate this difficulty were unsuccessful. Bath temperature fluctuated about ±0.1°C around the mean value at which the bath was set; the fluctuation of filament temperature inside the capillary tubes was probably somewhat less. Measurements with a thermocouple probe indicated that the temperature inside the capillary tubes was accurately at bath temperature at all points more than two inches below the surface of the bath. Accurate temperature control was necessary in these experiments because of the sensitive dependence of retraction rate on temperature. The bath thermometer used for temperature regulation was calibrated with high absolute accuracy against a platinum resistance thermometer.

EXPERIMENTAL RESULTS

The retraction curves obtained, plotted as percentage of original length *vs* logarithmic time, are shown in Figs. 2 and 3. Two duplicate curves are shown at each temperature; in some cases more than two duplicate curves were measured, but only two sets of points are shown here at each temperature to avoid overcrowding. The reproducibility is seen to be good in all cases, illustrating not only the accuracy of temperature control but also the uniformity of duplicate samples of the same filament.

It is evident from Figs. 2 and 3 that retraction rate depends in a very sensitive way on temperature.

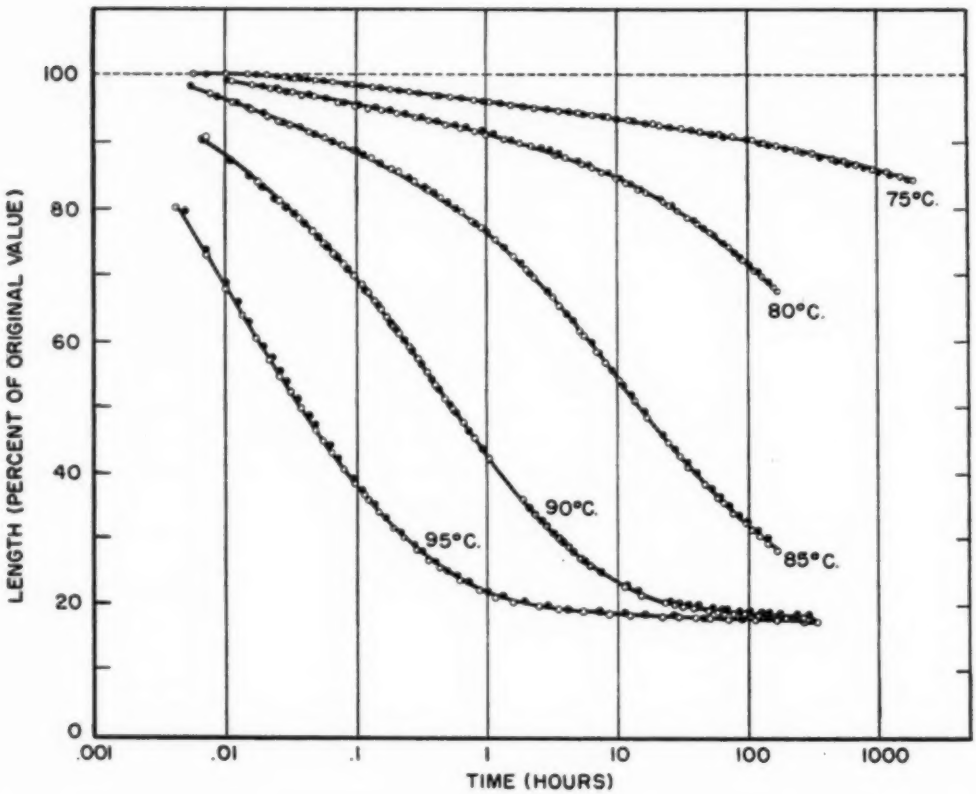

FIG. 2. Retraction curves for filament #3 at different temperatures.

The final length values approached when retraction is complete are similar for the two filaments (see also Table I), but the retraction rates are significantly different; the length decreases more rapidly for filament #3 than for filament #7 at any given temperature.

When the retraction curves for the same filament at different temperatures are compared, it is found that they cannot be superposed by a simple lateral shift along the logarithmic time scale, as is observed to be the case for simple viscoelastic systems.[11] This result is in disagreement with the apparent superposability found for retraction curves of filaments of this same type by Cleereman, Karam, and Williams.[3] However, their curves do not extend over as large an interval of logarithmic time as the curves obtained in the present work, and their experimental points also show much more scatter, so that their data do not really provide a critical test of whether the retraction curves are superposable or not. The present more accurate and complete data indicate clearly that they are not.

Consequently, activation energies for the retraction process cannot be calculated for the different temperatures simply by the amount of shift required for superposition of the curves; a more complicated treatment is required. Perhaps the simplest extension of this basic procedure is to calculate apparent activation energy values for different percent length values from the lateral displacement of the curves (or the time values) corresponding to that length at the different temperatures. These time values are plotted logarithmically against reciprocal absolute temperature, in the usual Arrhenius-type plot and apparent activation energies calculated from the local slopes of these curves at different points corresponding to the experimental temperatures. Arrhenius plots of this sort for different length values, derived from the data in Figs. 2 and 3, are shown in Figs. 4 and 5; the percent length value is indicated beside each curve.

Values of the apparent activation energy, E_{act}, calculated from these curves will then be a function of both length and temperature, rather than just of temperature, as in the more usual case. Or alternatively, since length is a function of time, these activation energy values can be regarded as a function of *time* and temperature.

An extremely interesting result is obtained if these values are plotted as curves of E_{act} *vs* logarithmic time, for each temperature, as illustrated in Figs. 6 and 7. The same general behavior is observed for both filaments. The activation energy increases with time, but tends to level off to a final constant value. The rate of transient drift of activation energy at early times increases with increasing temperature, so that the final constant value is attained more quickly; and this final value also becomes progressively lower with increasing temperature. Although the 75° curves do not reach their final constant value in the time range

[11] Andrews, Hofman-Bang and Tobolsky, J. Polymer Sci. **3**, 669 (1948).

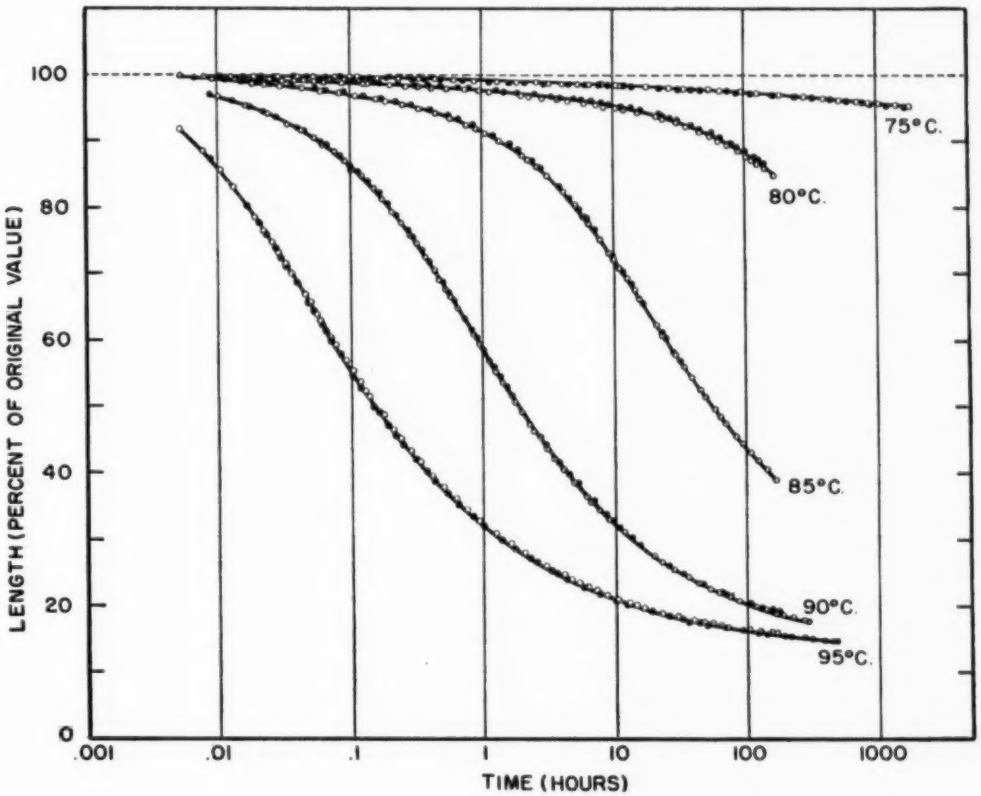

FIG. 3. Retraction curves for filament #7 at different temperatures.

of these experiments, it seems reasonable to assume that they would do so if carried out to longer times; their final values also must be quite high (well above 300 kcal).

Note added in proof.—It should also be mentioned that the apparent activation energies for the two filaments do not give the same pattern when considered as a function of length or degree of orientation (birefringence), but only when considered as a function of time.

DISCUSSION OF RESULTS

The time-dependence of the activation energy in these experiments, as shown in Figs. 6 and 7, is a very striking result which, to the knowledge of the present author, has never before been observed. The over-all pattern of time and temperature dependence is very reminiscent of the behavior of the delayed volume changes observed in the neighborhood of the transition temperature when volume-temperature curves of polystyrene are measured.[12–14] Spencer and Boyer[14] obtain a value of 12 kcal for the activation energy of this delayed volume change process in polystyrene. An interpretation in terms of volume changes is also suggested by some work of McLoughlin and Tobolsky[15,16] in which they found that varying the specific volume (or free volume) of polymethyl methacrylate samples, by quenching heated polymer at different rates, gave samples in which stress relaxation rate

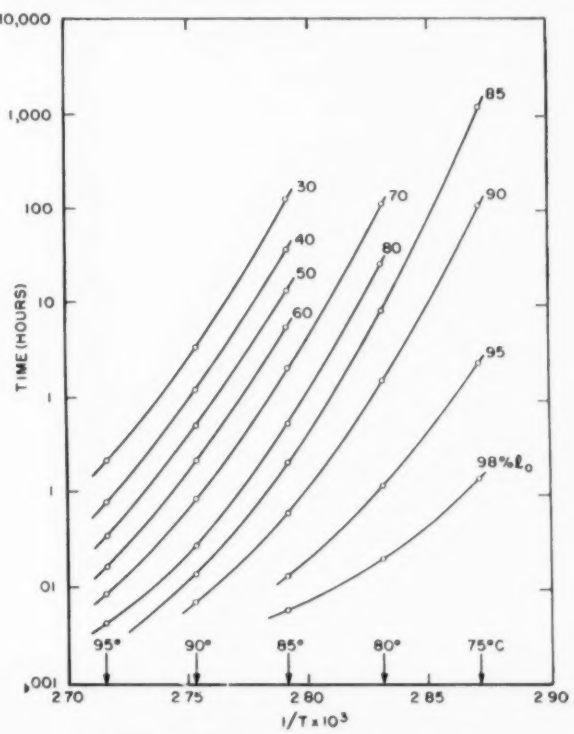

FIG. 4. Arrhenius plots for filament #3.

[12] Alfrey, Goldfinger, and Mark, J. Appl. Phys. **14**, 700 (1943).
[13] R. F. Boyer and R. S. Spencer, J. Appl. Phys. **16**, 594 (1945).
[14] R. S. Spencer and R. F. Boyer, J. Appl. Phys. **17**, 398 (1946).
[15] J. R. McLoughlin and A. V. Tobolsky, J. Polymer Sci. **7**, 658 (1951).
[16] J. R. McLoughlin and A. V. Tobolsky, J. Colloid Sci. **7**, 555 (1952).

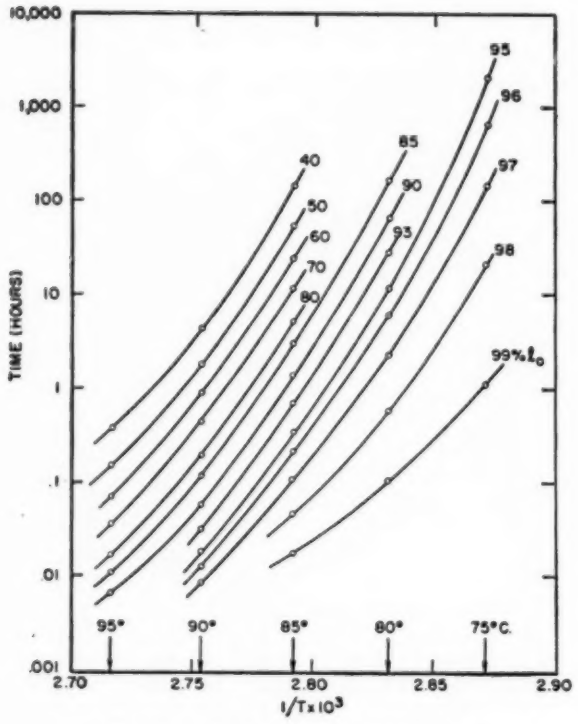

FIG. 5. Arrhenius plots for filament #7.

differed by as much as a factor of 1000. Fox and Flory[17] have emphasized the importance of free volume in connection with the second-order transition temperature, and also with the internal molecular mobility involved in viscoelastic phenomena.

According to this view, then, the leveling off of the activation energies to final constant values would correspond to the samples reaching their final equilibrium volume at the temperature in question, and the transient drift of activation energies at shorter times would be associated with the time-dependent volume changes in the samples required to reach equilibrium volume. The rate of these volume changes would increase with increasing temperature, as observed. Also activation energy should decrease with increasing specific volume, and the fact that the final constant values, $(E_{act})_\infty$, decrease with increasing temperature indicates that the equilibrium specific volume is increasing with increasing temperature, which is again what one would expect (as a result of thermal expansion). It is to be noted that at all temperatures the apparent activation energy *increases* to reach its final value, indicating that in all cases the specific volume is decreasing. This again is reasonable when the method of fabrication of the filaments is considered: they are oriented at a relatively high temperature, and then suddenly quenched to a temperature below the transition temperature by running the strand through a cold bath. This would undoubtedly freeze them in a state of relatively high specific volume—higher than the equilibrium volumes at the temperatures of these contraction experiments (75–95°C). Thus all the facts seem to correlate well in terms of this interpretation.

In experiments such as measurements of melt viscosity,[17] the activation energy appears to be simply a function of temperature because the polymer is always in volume equilibrium in the temperature range where these measurements can be made. However, at least part of this variation with temperature can probably be interpreted as due to the specific volume changes produced by thermal expansion and contraction. The effect of specific volume could be isolated from that of temperature by measuring viscous flow, for example, as a function of both temperature and hydrostatic pressure. Probably the dependence of activation energy on specific volume would be observed as a time-dependent activation energy only in experiments which could be carried out in the transition temperature region, and in which the initial specific volume of the sample was not at its equilibrium value. It is therefore not surprising that this effect has not previously been observed.

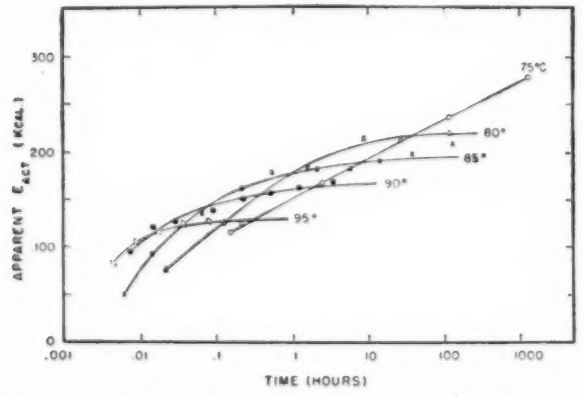

FIG. 6. Apparent activation energy *vs* logarithmic time for filament #3 at different temperatures.

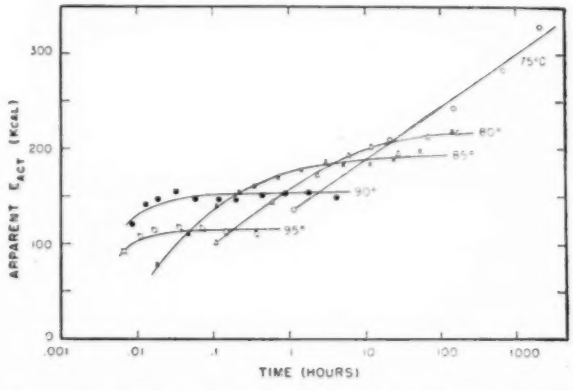

FIG. 7. Apparent activation energy *vs* logarithmic time for filament #7 at different temperatures.

[17] T. G. Fox, Jr., and P. J. Flory, J. Appl. Phys. **21**, 581 (1950).

The final constant values of the activation energy, $(E_{act})_\infty$, are undoubtedly the "equilibrium" values which should be compared with the ordinary "temperature-dependent" activation energies obtained from other viscoelastic experiments. A comparison of this sort is given in Fig. 8, in which $(E_{act})_\infty$ values for filaments #3 and #7 from the present work (Figs. 6 and 7) are compared with activation energy values obtained from melt viscosity experiments by Fox and Flory[17,18] and mechanical vibration experiments by Grandine and Ferry,[19] as a function of temperature. The values of $(E_{act})_\infty$ plotted here are also given in Table III. The melt viscosity and mechanical vibration values agree very well with each other. The activation energy from Fox and Flory's 1950 measurements could be expressed in analytic form, and is therefore shown as a solid curve in the temperature range of the experimental data, and is extrapolated to lower temperatures as a dashed curve. The values from retraction data coincide well with the low-temperature end of the solid curve but show a much sharper rise than the extrapolated dashed curve with decreasing temperature.

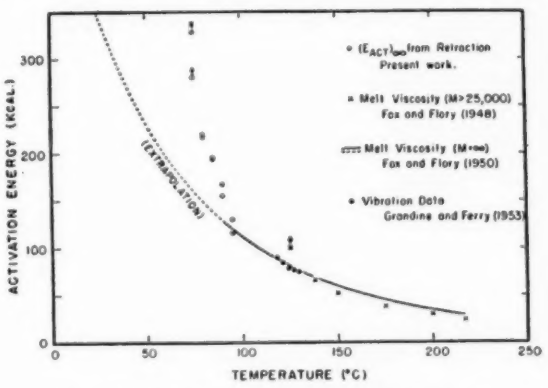

FIG. 8. Activation energy for polystyrene as a function of temperature.

This behavior is in agreement with some recent results of Williams.[20]

Another interesting point is that although the values of $(E_{act})_\infty$ extend through the transition temperature and have reached very large magnitude, they show no indications of going through, or even approaching, a maximum. A sharp maximum has been observed in the activation energy calculated from stress relaxation data on polymethyl methacrylate in the transition region, by McLoughlin and Tobolsky.[16] These results taken together suggest that the peak in the activation energy for stress relaxation is associated with a transition between two viscoelastic mechanisms (probably a molecular configuration-change mechanism above the transition temperature, and a local molecular distortion mechanism below), and that retraction experiments, in which the polymer is under no external stress or constraint, may provide a method of isolating the high-temperature configuration-change mechanism, which seems to have an activation energy which increases indefinitely as the temperature is lowered.

TABLE III. Final activation energy values from retraction experiments.

Temp. (°C)	$(E_{act})_\infty$ in kcal Filament #3	Filament #7
75	>280	>328
80	220	217
85	195	194
90	167	155
95	130	116

Changes of apparent activation energy with time at a fixed temperature, as observed in these experiments, can be taken into account, or corrected for, as follows. If the apparent activation energy at any particular length value is denoted simply as E, the time value at that point can be "corrected" to a time value corresponding to some standard activation energy value E_0 (such as the final "equilibrium" value $(E_{act})_\infty$ at that temperature) by multiplying the original time value by a correction factor q, which has the form

$$q = e^{(E_0 - E)/RT}. \tag{1}$$

Applying this type of correction point-by-point to the whole curve will give a curve with a uniform activation energy E_0 throughout. This will presumably be the retraction curve which would have been obtained if there had been no transient volume changes taking place in the sample. And if this type of correction is applied to curves at different temperatures, the corrected curves will of necessity be superposable by simple lateral shift, even if the values of E_0 used are different at the different temperatures. A composite or "master" retraction curve could then be constructed by superposition of the curves at different temperatures and the time scale of this composite curve would represent not simply some particular standard temperature, but also a particular standard activation energy, which from a formal mathematical standpoint would not have to be the final equilibrium activation energy $(E_{act})_\infty$ for that particular temperature. The distribution of retardation times corresponding to this master curve would then also be a function of activation energy as well as temperature. It may also be noted that the apparent activation energy values derived from plots of the sort illustrated by Figs. 4 and 5 are probably only approximately equal to the exact activation energy values E which should be used in Eq. (1).

Note added in proof.—The interpretation developed in the foregoing to explain the observed characteristics of the retraction curves is obviously a tentative one. It would be very desirable to have some direct experimental confirmation of the specific volume changes which have been assumed to be present here.

[18] T. G. Fox, Jr., and P. J. Flory, J. Am. Chem. Soc. **70**, 2384 (1948).

[19] L. D. Grandine, Jr., and J. D. Ferry, J. Appl. Phys. **24**, 679 (1953).

[20] M. L. Williams, J. Phys. Chem. **59**, 95 (1955).

JOURNAL OF APPLIED PHYSICS VOLUME 26, NUMBER 9 SEPTEMBER, 1955

X-Ray Diffraction Studies of Crystallization in Elastomers*†

LEROY E. ALEXANDER, STANLEY OHLBERG, AND G. RUSSELL TAYLOR
Mellon Institute, Pittsburgh, Pennsylvania

(Received May 2, 1955)

In general, extension of an elastomer results in a degree of preferred orientation of the molecular chains composing the amorphous phase. Therefore the amorphous fraction of a partially crystalline elastomer must be related to the integrated intensity of the amorphous diffraction halo rather than to the intensity at any one azimuth. A noteworthy exception is natural rubber, for which simple meridional measurements suffice.

A Geiger-counter apparatus with beam monitor and temperature-controlling accessories is described for making accurate measurements of the x-ray intensities scattered at any azimuth and at small or moderate Bragg angles. Measurements of crystallinity in natural rubber are in essential agreement with the findings of previous workers. When polybutadiene is extended at room temperature, molecular orientation occurs, but little if any crystallization. Measurements at lowered temperatures show that the crystalline fraction becomes appreciable at about 0°C and that it increases with further reduction in temperature and with increasing extension ratio. Preferred orientation of the crystalline regions in extended polybutadiene has been measured quantitatively with the object of providing jointly with birefringence measurements a value of the birefringence of a single crystal of polybutadiene.

I. GENERAL PRINCIPLES

THE constancy of the total x-ray scattering by a substance, regardless of its degree of crystallinity, has been demonstrated theoretically and experimentally.[1] This principle forms the basis of current x-ray diffraction procedures for measuring the crystalline and amorphous fractions of polymers and other partially crystalline materials. Although the determination of the total crystalline and noncrystalline x-ray intensities is a formidable experimental operation, acceptable simplifications can be devised for most substances. For example, natural and synthetic fibers can be sampled in such a way as to randomize the orientations of the crystalline and amorphous regions, thereby permitting a satisfactory measure of the crystalline and amorphous x-ray scattering to be obtained from a single radial section over a limited angular range.[2] The amorphous fraction f_a of partially crystalline polyethylene can be measured directly by comparing the amorphous intensity of a radial section below $2\theta=60°$ with that of a melted reference specimen. The crystalline fraction is then found by difference, $f_c=1-f_a$.[3] A somewhat similar procedure is applicable to elastomers of technological interest because the completely amorphous reference specimens are available in the form of the unextended elastomers at room temperature. Thus, noteworthy success has been achieved in determining the amorphous fraction of natural rubber specimens by comparing the intensities of radial sections through the amorphous halo for the partially crystalline and totally amorphous specimens.[4–7] As in the case of polyethylene, the crystalline fraction is determined by the difference $f_c=1-f_a$. It should be emphasized that these investigations of natural rubber have made use of the additional assumption, evidently justified, that the properly corrected peak intensity of a radial section through the amorphous halo is proportional to the total amorphous x-ray scattering by the specimen.

Unlike the crystalline phase, the amorphous phase of an elastomer scatters x-rays coherently over the entire range of solid angles, 4π, which is to say, at all radial angles, 2θ, and at all azimuthal angles, β (refer to Fig. 1). Hence, it is apparent that any useful method of measuring the amorphous intensity must confine itself out of practical necessity to some restricted angular range which can be shown to be, or with good reason assumed to be, representative of the whole. The principal amorphous diffraction halo, which is generated mainly by radial vectors between adjacent molecular chains in elastomers, is a suitable subject for measurement because its integrated intensity bulks so large with respect to the total amorphous scatter that the size of possible errors due to any lack of representativeness‡ is very limited, and, furthermore, it can be measured with much better accuracy than other portions of the amorphous pattern. On the other hand, it is important to remember that any preferential orientation of the molecular chains comprising the amorphous regions of an extended elastomer will produce an azimuthal redistribution of intensity in the

* The work discussed herein was performed as part of the research project sponsored by the Federal Facilities Corporation, Office of Synthetic Rubber, in connection with the Government Synthetic Rubber Program.

† Based in part upon material presented before the Division of High-Polymer Physics of the American Physical Society at Baltimore, Maryland, March 18, 1955.

[1] A. W. Coven, Phys. Rev. **41**, 422 (1932); G. E. M. Jauncey and F. Pennell, Phys. Rev. **43**, 505 (1933); **44**, 138 (1933).

[2] P. H. Hermans and A. Weidinger, J. Appl. Phys. **19**, 491 (1948); J. Polymer Sci. **4**, 135 (1949); J. Polymer Sci. **5**, 565 (1950).

[3] S. Krimm and A. V. Tobolsky, Textile Research J. **21**, 805 (1951).

[4] J. E. Field, J. Appl. Phys. **12**, 23 (1941).

[5] J. M. Goppel, Appl. Sci. Research **A1**, 3 (1947); **A1**, 18 (1947).

[6] J. M. Goppel and J. J. Arlman, Appl. Sci. Research **A1**, 462 (1949); Rubber Chem. and Technol. **23**, 310 (1950).

[7] S. C. Nyburg, Brit. J. Appl. Phys. **5**, 321 (1954).

‡ The criterion of representativeness may be defined as constancy in the partition of the total amorphous intensity between the principal halo and the rest of the pattern.

amorphous halo. Such a development would obviously invalidate estimates of the amorphous fraction that are based on a radial section through the halo at only one azimuth. The measurements of crystallinity in natural rubber reported to date have depended tacitly or expressedly upon the immutability of the amorphous intensity distribution when extension and crystallization take place. That this assumption is well founded has been confirmed by at least one precise experimental investigation.[3]

Figure 1 gives the conventions to be employed in describing the sample orientation in relation to the diffraction pattern. With the extension axis vertical as shown, azimuthal angles on the diffraction pattern are measured from the horizontal axis, which will be designated the equator. The azimuth of the meridian, which coincides with the direction of extension, is then 90°. Figure 2 shows the x-ray diffraction patterns produced by a 5°C polybutadiene specimen at elongations of 0 and 535% and at the temperatures 25° and −15°C. At 25° there is unmistakable evidence of molecular orientation in the form of an intensification of the amorphous halo at the equator. Microphotometer sections at various azimuths show the meridional intensity to be less than three fourths that of the equator. The absence of any crystalline diffraction effects confirms that this azimuthal redistribution of intensity is indeed the result of preferential orientation of the molecular chains in the amorphous regions. This intensity redistribution is also present, but less conspicuous, in the pattern prepared at −15° and 535% elongation, which in addition contains the familiar doubled diffraction sickle on the equator produced by the oriented crystalline regions at moderate extensions.[8] At higher extensions the two components of the sickle coalesce on the equator. The unextended specimen at −15°C shows in addition to the amorphous halo a sharper Debye-Scherrer ring, which is produced by randomly oriented crystalline regions.

The photographic technique devised by Goppel[5]

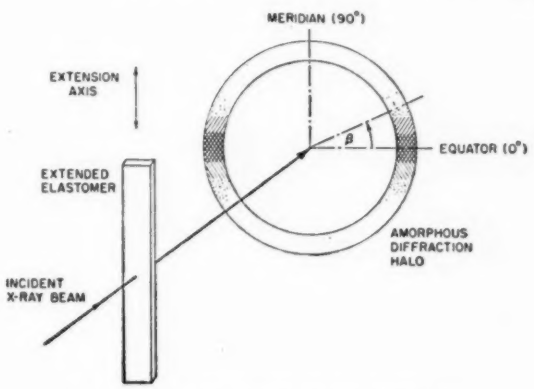

FIG. 1. X-ray scattering by the amorphous phase of an elastomer.

[8] Beu, Reynolds, Fryling, and McMurry, J. Polymer Sci. 3, 465 (1948).

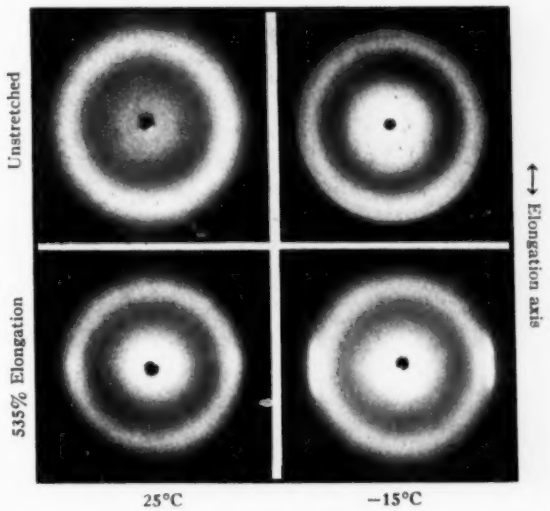

FIG. 2. X-ray pattern of a 5°C polybutadiene specimen.

for measuring the crystalline and amorphous fractions in natural rubber and subsequently improved by Arlman[9] equates the amorphous fraction to six experimental parameters,

$$f_a=\frac{1}{d'}\cdot\frac{I_a'}{I_s'}\Big/\frac{1}{d}\cdot\frac{I_a}{I_s}, \tag{1}$$

wherein primed and unprimed quantities refer respectively to partially and completely amorphous specimens. As this equation was employed by Goppel and Arlman, I_a is the peak intensity of the amorphous halo at a point unaffected by crystalline diffraction effects, and I_s is a measure of the intensity of the direct beam after transmission through the specimen of thickness d. For elastomers consisting principally of light elements ($Z\leq 8$) Eq. (1) is theoretically accurate to within 2% for typical experimental conditions. When applied to elastomers other than natural rubber, the possibility of preferential orientation of the molecules in the amorphous region must be recognized, in which case I_a must be re-defined as the integrated intensity of the amorphous halo. The necessity of employing this definition of I_a in the case of polybutadiene is attested by photographic diffraction evidence, as explained above. The remainder of this paper will deal principally with a study of preferential molecular orientation in polybutadiene and its bearing on the quantitative evaluation of crystallinity from diffraction measurements. Brief accounts will also be given of confirmatory measurements of crystallinity in natural rubber and of crystallite orientation in natural rubber and polybutadiene.

II. EXPERIMENTAL

Figure 3 is a schematic diagram and Fig. 4 a photographic perspective of the Geiger-counter apparatus

[9] J. J. Arlman, Appl. Sci. Research A1, 347 (1949).

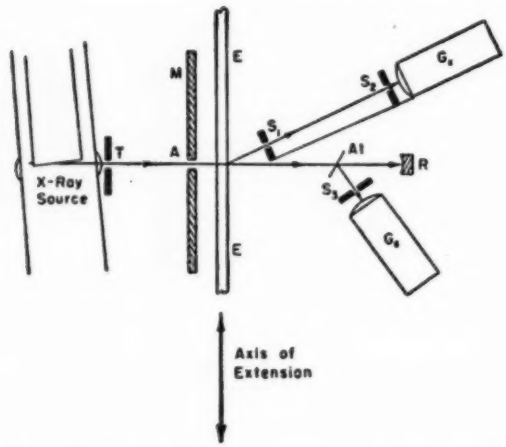

FIG. 3. Schematic diagram of x-ray diffraction apparatus.

developed at Mellon Institute for making precise measurements of the intensities I_a, I_a', I_s, and I_s' of Eq. (1). The necessary geometrical and mechanical features have been obtained by adding accessory devices to a standard Norelco wide-angle goniometer. The direct x-ray beam from a copper-target tube is defined by the $\frac{1}{4}°$ divergence slit T, and its vertical divergence[10] is limited additionally by the aperture A in the brass plate M, which shields the Geiger tubes G_z and G_s from unwanted radiation originating in the neighborhood of the x-ray tube housing. The beam penetrates the elastomer E, and x-rays scattered by the amorphous component are received by G_z. The specimen holder shown in these figures permits extension of the elastomer in a vertical direction only, so that the amorphous intensity can be measured only on the meridian ($\beta=90°$). The slits A and S_1 minimize the air-scattered x-rays that can be received by G_z. The direct beam, weakened by absorption in the elastomer, penetrates the reference sample of 0.002-inch aluminum foil, Al, and is then intercepted by the beam stop R. A diffracted ray from the foil is received by counter G_s, which provides a measure of the direct beam intensity after transmission through the elastomer, I_s or I_s'. Slits S_2 and S_3 are both equipped with nickel filters to remove the Cu$K\beta$ component of the radiation.

The pulses from counter G_z are registered with a Tracerlab Superscaler Model SC–18 and those from G_s with the Norelco scaler. A special interconnecting timing circuit was incorporated to enable both units to register counts simultaneously for the same counting interval. It was found advantageous to set the control switch to shut off the counters when the standard counter G_s had counted a predetermined number of pulses, for example, 25 600. For the measurements at lowered temperatures the entire sample and its supporting mechanism were enclosed in a windowless Styrofoam insulating box of such low density that the absorption of the direct and diffracted x-ray beams is unimportant. Air from the laboratory air line was passed successively through a drying column of silica gel, a flow meter, and a copper cooling coil immersed in a slush of dry ice and 1:1 chloroform-carbon tetrachloride in a Dewar, after which it was introduced into the cooling box through openings in both the top and bottom. By regulating the flow rate, any temperature down to $-40°$C could be maintained for several hours with a mean variation not exceeding $\pm 1°$C. The specimen temperature was measured with either a thermometer or a thermocouple.

Figure 5 is a close-up view of the goniometer with an azimuthal specimen holder in place. This device, which was constructed in the shop by modification of an ordinary machinist's bevel protractor, permits rotation of an extended specimen about the axis of the direct x-ray beam. The specimen is first elongated with the aid of the usual stretching device, after which a small extended section is clamped off in the azimuthal holder. Another insulating box of appropriate dimensions for this specimen holder was constructed for the measurements at lowered temperatures.

Returning to the general Eq. (1) for the amorphous fraction, we see that the net accuracy in f_a will be a function of the accuracies with which four intensities and two thicknesses can be determined experimentally. Experience in this laboratory has shown that the thickness ratio d'/d can with minimum error be equated to α^{-1} (α being the extension ratio) provided only that the specimen is supported so as to permit unconstrained, and therefore proportionate, diminutions in its thickness and width (*affine* extension). The intensities I_a and I_s are derived from the experimental counting rates by (1) correcting them for the dead time loss of the Geiger counter and (2) subtracting the components of intensity due to air scatter and general x-radiation. Correction (1) is made with the standard formula

$$N=N_0/(1-N_0\tau), \qquad (2)$$

in which N is the corrected counting rate in terms of the

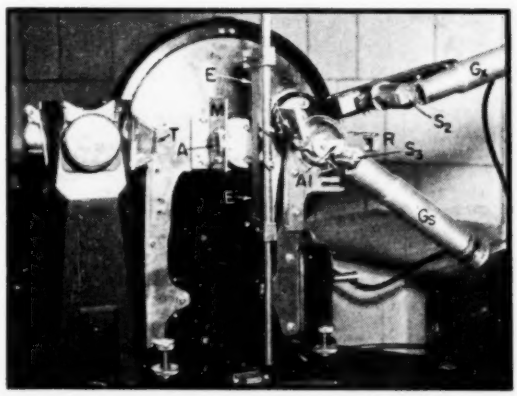

FIG. 4. Perspective of x-ray diffraction apparatus.

[10] H. P. Klug and L. E. Alexander, *X-Ray Diffraction Procedures for Polycrystalline and Amorphous Materials* (John Wiley and Sons, Inc., New York, 1954), p. 239.

observed rate N_0 and the effective dead time of the Geiger tube τ (2.5×10^{-4} sec for the Geiger tube employed, Norelco type 62019, and a full-wave rectifying x-ray generator). The air-scattered component N_A is given by

$$N_A=(N_A)_0\times\frac{N_s}{(N_s)_0}, \qquad (3)$$

$(N_A)_0$ and $(N_s)_0$ being, respectively, the dead-time corrected counting rates of counters G_x and G_s with no elastomer sample and N_s being the G_s counting rate with the sample in place. Because of the low sensitivity of the counter tubes for the general x-radiation, the correction for this component can be made adequately by measuring the diffracted intensity from the specimen after transmission through 0.35 mm of aluminum, which removes more than 99% of the Cu$K\alpha$ radiation but only about 27% of the general radiation.§ The intensities I_a and I_s, when corrected as just described, permit the ratios I_a/I_s and I_a'/I_s' of Eq. (1) to be determined with a probable error as small as 1% when all the experimental conditions are optimum, including that at least 9000 counts be totalized in each measurement in order to keep the statistical errors of counting small. Considering the combined effect of the probable errors in the intensity and thickness ratios, it is possible to realize a net probable error in f_a of about $\pm2\%$. In order to achieve good relative accuracy in small values of the difference, $f_c=1-f_a$, it is evident that the greatest pains must be taken in the experimental measurements.

III. NATURAL RUBBER

A preliminary test of the equipment was made by applying it to the determination of crystallinity in natural rubber at room temperature as a function of extension. The specimen studied was smoked sheet purified and cross linked with 0.6% decamethylene *dis*-methylazodicarboxylate using essentially the method

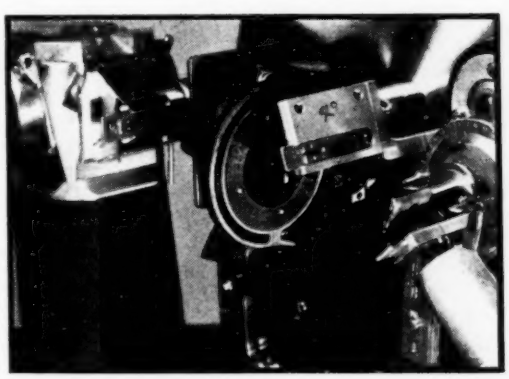

FIG. 5. Close-up view of apparatus showing azimuthal specimen holder.

§ The influence of the general x-radiation can be rendered negligible by employing proportional counters, which were not available for the present investigation.

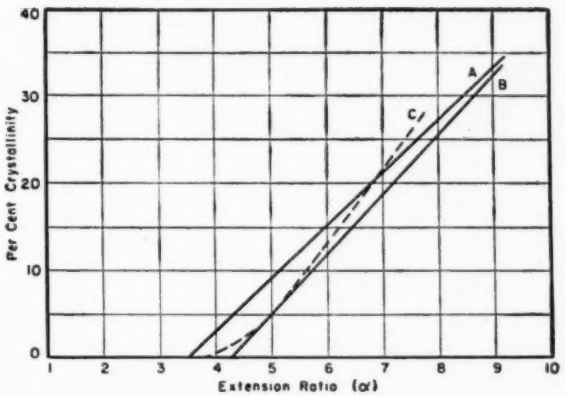

FIG. 6. Crystallinity in natural rubber specimens at room temperature as measured by A, Alexander, Ohlberg, and Taylor; B, Goppel and Arlman;[6] C, Nyburg.[7]

of Flory, Rabjohn, and Shaffer.[11] Following the practice of the earlier investigators, the peak intensity of the amorphous halo at a single azimuth (90°) was accepted as being representative of the over-all amorphous intensity at the several extensions. The results are portrayed in curve A of Fig. 6, which may be compared with the well-known curve of Goppel and Arlman, B,[6] and recently published data of Nyburg, C,[7] for natural rubber specimens of somewhat different types. The three curves agree in failing to reveal appreciable crystallinity at extension ratios much less than 4.0, but they disclose minor differences in the progress of crystallization at the higher extensions.

IV. MOLECULAR ORIENTATION IN POLYBUTADIENE

The samples studied were 2.5×10 cm rectangular strips cut from a sheet of 5°C polybutadiene, 0.15 cm thick, cross linked with 0.6% decamethylene dismethylazodicarboxylate. The extension ratios were determined by measuring the increase in separation of small India ink fiducial marks initially placed 2 mm apart along the center of the specimen strip.

Before any serious efforts could be made to pursue quantitatively the progress of crystallization in polybutadiene with reduction of temperature, it was necessary to evaluate the extent of molecular orientation in the amorphous state and, in particular, to establish that the quantity $(1/d')\times(I_a'/I_s')$ of Eq. (1) does in fact remain invariant when polybutadiene is extended at temperatures above the crystallization point. The demonstration of constancy in this quantity would be significant for two reasons. First, it would confirm that the integrated intensity of the amorphous halo is truly representative of the total amorphous scatter. Second, it would consititute a convincing argument for the applicability of Eq. (1) to polybutadiene in extended states provided I_a and I_a' are defined as the integrated intensities of the halo for totally amorphous and partially crystalline specimens, respectively.

[11] Flory, Rabjohn, and Shaffer, J. Polymer Sci. 4, 225 (1949).

TABLE I. Properties of radial sections through the amorphous halo of polybutadiene for extension ratios of 1.0 and 6.1.

	$\alpha=1.0$	$\alpha=6.1$ $\beta=0°$	$\alpha=6.1$ $\beta=90°$
$2\theta_{max}$(°)	19.75	20.10	19.75
Equivalent R between molecular chains (A)	5.49	5.41	5.49
Integral breadth, W_i, of radial profile (°)	11.1	9.6	11.1
Relative peak intensity, I_{max}	1.00	1.62	0.98

The intensity profile for an extension ratio of 6.1 was mapped out by taking peak intensity measurements at 10° intervals around the halo between azimuths of 0 and 90°, and by making radial sections at several azimuths in order to detect possible variations in the radial profile with azimuth. For the unextended specimen ($\alpha=1$) only a single radial section was prepared, but peak intensities were measured at a number of azimuths to help average out any possible minor inhomogeneities in the sample. It was found for $\alpha=6.1$ that not only the peak intensity, but the breadth of the radial sections and the radial angles of peak intensity as well, showed a dependence upon azimuth. The salient numerical data are given in Table I. In interpreting these figures it must be borne in mind that the heightened equatorial intensity for $\alpha=6.1$ results from an increase in the proportion of molecular chains that are oriented so as to approach parallelism with the extension axis.

The integral breadth of a radial profile is defined by

$$W_i=\frac{\int I_{2\theta}d(2\theta)}{I_{max}}. \tag{4}$$

As might be expected, for $\beta=90°$ and $\alpha=6.1$ the values of $2\theta_{max}$, R, and W_i agree with their values for the unextended elastomer. The highly oriented molecules are more densely packed than the unoriented, as evidenced by an average intermolecular distance of 5.41 A for $\beta=0°$ and 5.49 A for $\beta=90°$. This decrease in R is equivalent to an increased density of 3% for the well-oriented regions of the amorphous phase. The decrease in integral breadth of the radial section through the halo at $\beta=0°$ when extension occurs is indicative of a greater tendency toward discreteness in the distribution of the lengths of the intermolecular vectors about the smaller mean value of 5.41 A.

Two independent measurements of the azimuthal intensity distribution in the amorphous halo at room temperature were made, the extension ratios being 5.55 and 6.1. The resulting curves are shown in Fig. 7, wherein the quantity

$$I_{rel}=\frac{1}{d'}\cdot\frac{I_a'}{I_s'}\Big/\frac{1}{d}\cdot\frac{I_a}{I_s}$$

is plotted as a function of β. This expression has the form of Eq. (1) for f_a in natural rubber, but it can now be equated to f_a only after integration over all azimuths, as explained earlier. At any particular azimuth I_a' is the peak intensity of the halo weighted by its integral breadth W_i. It is seen from the figure that the integrated intensities for the extended specimens agree with that for the unextended state to within 7%, the deviation being positive in one instance and negative in the order. The quality of the agreement is not as good as might be desired, but, in view of the complexity and long duration of the measurements required to arrive at the integrated halo intensity, it was felt that these results tentatively establish the constancy of the integrated intensity with extension. Accordingly attention was next directed to the problem of measuring cyrstallinity in extended specimens at reduced temperatures.

V. CRYSTALLINITY IN POLYBUTADIENE

An important preliminary problem was to ascertain whether or not the intensity of the amorphous halo diminishes uniformly at all azimuths when crystallization occurs. Such proportionate reduction in intensity at all azimuths would be desirable from a practical standpoint because it would permit quantitative evaluation of the amorphous and crystalline fractions by means of measurements at only one azimuth, for example, at the meridian. Such behavior, in addition, would point to a mechanism of crystallization that involves nonpreferential conversion of oriented and unoriented amorphous regions.

The following experimental procedure was followed. Prior to cooling, the specimen was stretched to the desired extension ratio α, mounted in the azimuthal holder, and its azimuth adjusted to some fixed value for the first series of measurements. The intensity ratio $(I_a'/I_s')_{t_0}$ was measured at $t_0=25°$, after which the specimen at the same extension and azimuth was enclosed in the insulating box and its temperature reduced to t_1 (usually about 10°C). An equilibration

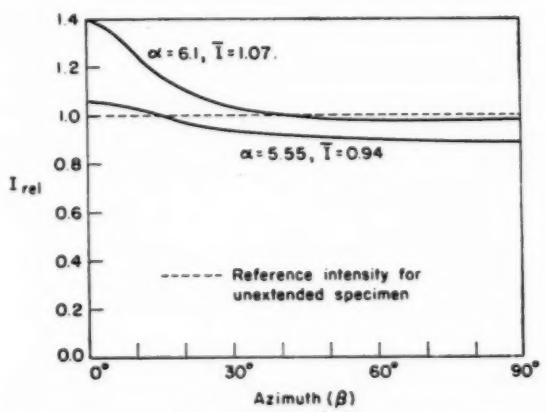

FIG. 7. Azimuthal intensity distributions in the amorphous halo of extended polybutadiene specimens at room temperature.

period of 30 minutes was allowed and then the ratio $(I_a'/I_s')_{t_1}$ was measured until it reached constancy, which occurred within a few minutes except at low extensions. The temperature of the specimen was now reduced to t_2, a second equilibration period was allowed, and the ratio $(I_a'/I_s')_{t_2}$ was measured, an so on. The experimental results for three azimuths, 90°, 60°, and 30°, are plotted in Fig. 8 for temperatures between +25° and −28°C. Confirmatory measurements are still required, especially at $\beta=30°$, where the curve disagrees with the points for 60° and 90°, which are in mutual agreement. At $\beta=0°$ the superposition of the halo by the crystalline reflections is so great (see Fig. 2) that to date no precise measurements have been attempted at this azimuth. The x-ray data for $\beta=60°$ and 90° indicate that crystallization in this specimen at an extension ratio of 5.55 begins somewhat below 0°C and increases rather linearly with further reduction of the temperature.

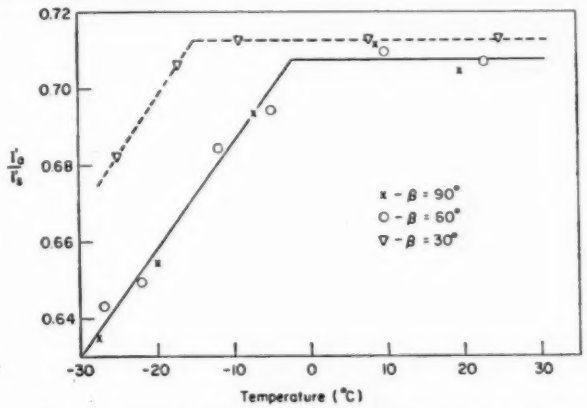

FIG. 8. Amorphous halo intensity of polybutadiene *versus* temperature at three azimuths. Extension ratio 5.55.

The foregoing results do not give a final answer to the question of whether or not the intensity of the amorphous halo diminishes proportionately at all azimuths when crystallization takes place, but the good agreement of the results at azimuths of 60° and 90° make an ultimate affirmative answer seem probable. Further precise studies of the phenomena at $\beta=30°$ and 0° are to be undertaken at an early date. Meanwhile tentative calculations of the crystalline fraction in polybutadiene at reduced temperatures have been made on the basis of simple meridional measurements of the intensity ratio I_a'/I_s'. When applied to the development of crystallinity resulting from reduction of temperature at a constant elongation, Eq. (1) assumes the form:

$$(f_a)_t=\left(\frac{I_a'}{I_s'}\right)_t\Big/\left(\frac{I_a'}{I_s'}\right)_{t_0}. \tag{5}$$

Here t_0 is a temperature at which the extended specimen is presumably completely amorphous, such as 25°C for 5°C polybutadiene. The thickness ratio d_t'/d_{t_0}' is unity for all practical purposes and so may be disregarded. Table II gives the numerical results for two extension ratios, 4.38 and 6.13, and at several temperatures ranging from 25° to −16°C. The amorphous and crystalline fractions were calculated from the x-ray diffraction intensities using Eq. (5) and the relationship $f_c=1-f_a$.

TABLE II. Crystalline and amorphous fractions as a function of temperature for 5°C polybutadiene held at fixed extensions.

Extension ratio, α	Temp. (°C)	Amorphous fraction, f_a	Crystalline fraction, f_c
4.38	25	1.000	0
4.38	9	0.966	0.034
4.38	0	0.952	0.048
4.38	− 5	0.906	0.094
4.38	−16	0.868	0.132
6.13	25	1.000	0
6.13	10	0.934	0.066
6.13	0	0.924	0.076
6.13	−10	0.885	0.115
6.13	−16	0.821	0.179

The crystallinity data of Table II are plotted in Fig. 9, from which it is seen that (1) the crystalline fraction increases as the temperature is lowered and (2) the crystallinity at a given temperature increases with increasing elongation. In consideration of the experimental error limits discussed earlier, it must be recognized that the linear form of the curves indicated in the figure is somewhat tentative, especially at the lower crystallinities. However, the measured crystalline contents of about 13 and 18% at −16°C for extension ratios of 4.38 and 6.13 may be regarded with confidence.

VI. CRYSTALLITE ORIENTATION

The birefringence of the crystalline phase in an elastomer in which the crystalline regions are preferentially oriented with respect to the direction of extension is[12]

$$\Delta n_c=\Delta n_c^0\cdot F, \tag{7}$$

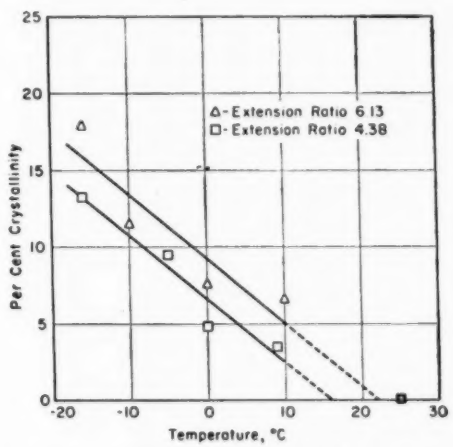

FIG. 9. Percent crystallinity in 5°C polybutadiene as a function of temperature for two extensions.

[12] G. R. Taylor and S. R. Darin, J. Appl. Phys. **25**, 1075 (1955), this issue.

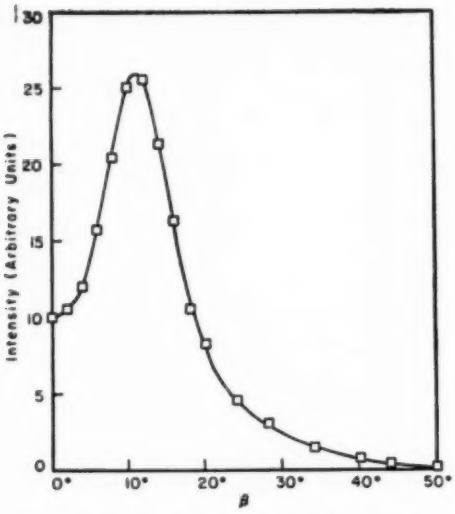

FIG. 10. Azimuthal intensity distribution in the principal paratropic diffraction sickle of polybutadiene ($\alpha=4.25$, $t=-25$°C).

where Δn_c^0 is the birefringence of a single crystal of the crystalline phase and F is the orientation factor, defined by[13]

$$F=1-\tfrac{3}{2}\langle\sin^2\gamma\rangle. \tag{8}$$

The quantity $\langle\sin^2\gamma\rangle$ is the average value of the sine of the angle between the principal axis of a crystallite and the axis of extension. Taylor and Darin[12] have shown how Δn_c^0 can be calculated by combining appropriate x-ray and birefringence data, thus establishing a quantitative relationship between the observed birefringence and the crystalline fraction of an elastomer in extended states. The needful x-ray data are (1) values of f_a at some particular elongation and a series of temperatures and (2) a value of F under the same conditions. The determination of the amorphous fraction f_a has been discussed in the preceding section of this paper.

Reasonable assumptions concerning the distribution of orientations of the paratropic planes about the extension axis of an elastomer lead to the conclusion that Hermans' expression giving $\langle\sin^2\gamma\rangle$ for cellulose crystallites[14] can be applied to the crystalline diffraction sickle of polybutadiene almost unchanged:

$$\langle\sin^2\gamma\rangle=\frac{2\int I(\beta)\cos\beta\sin^2\beta d\beta}{\int I(\beta)\cos\beta d\beta}. \tag{9}$$

[13] P. H. Hermans and P. Platzek, Kolloid Z. 88, 68 (1939).
[14] P. H. Hermans, *Contribution to the Physics of Cellulose Fibers* (Elsevier Publishing Company, Inc., New York, 1946), p. 198.

Here β is the azimuthal coordinate on the diffraction pattern as defined earlier.

The orientation factors of natural rubber and 5°C polybutadiene under different conditions were determined from x-ray diffraction patterns recorded on flat sheets of nonscreen x-ray film with nickel-filtered CuK radiation. A Leeds and Northrup recording microphotometer was used to measure the optical transmission values, which were converted to relative intensities by comparison with microphotometer traces of a graded density scale. The maximum intensities along the diffraction sickle concerned were plotted as a function of β, the background was subtracted, and the net intensities at small increments in β were used to compute $\langle\sin^2\gamma\rangle$ from Eq. (9). The increments chosen were $\Delta\beta=1°$ and 2° respectively for natural rubber and polybutadiene.

Figure 10 is a plot of the azimuthal intensity distribution in the principal paratropic diffraction sickle of polybutadiene at −25°C and an extension ratio of $\alpha=4.25$. It is interesting to note that at this extension ratio the point of maximum intensity does not fall at the equator but at about 10°. This means that the most probable mode of orientation is an inclination of about 10° to the axis of extension. Such an inclination is uncommon in crystallizable elastomers and does not occur in natural rubber.

TABLE III. Experimental orientation factors from x-ray measurements.

Specimen	α	t(°C)	$\langle\sin^2\gamma\rangle$	F
Natural rubber	5.0	25	0.0101	0.985
Natural rubber	7.5	25	0.0176	0.982
Polybutadiene	6.35	−15	0.1158	0.826
Polybutadiene	4.25	−25	0.1307	0.804
Polybutadiene	6.35	−25	0.1020	0.847

Table III gives the results of the x-ray measurements for the specimens studied. The degree of orientation is very high in natural rubber compared with that in polybutadiene and, furthermore, it seems to be practically independent of the degree of extension. On the other hand, the degree of orientation in polybutadiene is less perfect and there appears to be a dependence upon elongation, although the observed values of F do not differ by much more than the limits of experimental error.

ACKNOWLEDGMENTS

The authors are indebted to Dr. Axel Peterson and Mr. John Rickert of the Department of Instrumentation, Mellon Institute, for designing and constructing the interconnecting timing circuit.

Birefringence and Crystallization in Elastomers*

G. Russell Taylor and Stephen R. Darin
Mellon Institute, Pittsburgh, Pennsylvania
(Received May 6, 1955)

The semitheoretical expression,

$$f_c=\frac{\Delta n_0-cs}{F\Delta n_c^0-cs},$$

where f_c = volume fraction crystalline, Δn_0 = observed birefringence, c = the stress-optical coefficient, s = the stress on actual cross section, F = a known function of crystallite orientation, and Δn_c^0 = the birefringence of a single polymer crystal, is proposed for relating birefringence, stress, and degree of crystallinity in polycrystalline elastomers under tensile stress. This expression is shown to yield results in substantial agreement with x-ray results for the degree of crystallinity of 5°C polybutadiene when $\Delta n_c^0=0.157$. Birefringence-density data on natural rubber (due to L. R. G. Treloar) are shown to be a special case of the foregoing expression, yielding a value $\Delta n_c^0=0.218$ for natural rubber which is in good agreement with the theoretical value for this quantity.

I. INTRODUCTION

It has been shown both experimentally and theoretically[1,2] that the stress-optical coefficient (the ratio of birefringence to tensile stress) in linear amorphous elastomers is a constitutive constant at small stresses. In partially crystallized elastomers, however, and in elastomers in which crystallization can be induced by stress, the birefringence is due not only to the stress-optical properties of the amorphous phase, but is also due, and indeed significantly, to the birefringence of the oriented crystallites. This qualitative relation between excess birefringence and crystallinity in elastomers has been known since at least 1935,[3] however, to the author's knowledge, no quantitative statement of a relation between the birefringence, the degree of crystallinity, and the stress is available in the literature. It is the purpose of this paper to present a semitheoretical relation of this sort and to show its applicability by comparing x-ray and birefringence determinations of the degree of crystallinity of stretched 5°C polybutadiene.

II. THEORY

In general, the optical properties of a medium are completely specified when the indexes of refraction along the mutually perpendicular principal axes, (x, y, z) are specified. To relate the optical properties of the medium to its constitution, it is assumed that the principal refractive indexes $n_i(i=x, y, z)$ are related to the principal components of the polarizability tensor, $A_{ii}(i=x, y, z)$, by the Lorentz-Lorenz relations,

$$(n_i^2-1)/(n_i^2+2)=4\pi A_{ii}/3. \quad (1)$$

Then, using the approximation,

$$(n_z^2-1)/(n_z^2+2)-(n_x^2-1)/(n_x^2+2)=\frac{6\bar{n}\Delta n}{(\bar{n}^2+2)^2}, \quad (2)$$

the difference in any two refractive indexes, which is called the birefringence, can be calculated from,

$$\Delta n=\frac{2\pi}{9}\frac{(\bar{n}^2+2)^2}{\bar{n}}(A_{zz}-A_{xx}), \quad (3)$$

where $\bar{n}=(n_z+n_x)/2$ and $\Delta n=n_z-n_x$. If the medium is optically uniaxial, with its optic axis along the z axes, $A_{xx}=A_{yy}$ and it has one nonzero value for the birefringence. Stretched elastomers are uniaxial with the optic axis along the axis of extension.

To evaluate the polarizability tensor for a medium, it is generally assumed to be composed of n noninteracting elements per unit volume, small with respect to the wavelength of light, for which the principal polarizabilities and orientations are known or postulated. If the elements are uniaxial and are oriented with cylindrical symmetry about the z axis, the medium is uniaxial and the optical anisotropy can be shown to be,

$$A_{zz}-A_{xx}=n\int_0^{\pi}(1-\tfrac{3}{2}\sin^2\gamma)(\alpha_{\parallel}-\alpha_{\perp})\rho(\gamma)d\gamma, \quad (4)$$

where $\alpha_{\parallel}$ is the polarizability of the element along its optic axis, $\alpha_{\perp}$ is the polarizability of the element perpendicular to its optic axis, and $\rho(\gamma)d\gamma$ is the fraction of the elements in the medium oriented with their optic axis at an angle γ to $\gamma+d\gamma$ with the optic axis of the medium. In the special case where $\alpha_{\parallel}-\alpha_{\perp}$ is independent of the orientation of the elements, this reduces to,

$$A_{zz}-A_{xx}=(A_{zz}-A_{xx})_0F, \qquad F=(1-\tfrac{3}{2}\langle\sin^2\gamma\rangle_{Av}), \quad (4a)$$

where $(A_{zz}-A_{xx})_0$ is the optical anisotropy which

* The work discussed herein was performed as part of the research project sponsored by the Federal Facilities Corporation, Office of Synthetic Rubber, in connection with the Government Synthetic Rubber Program.

[1] L. R. G. Treloar, *The Physics of Rubber Elasticity* (Oxford University Press, Oxford, England, 1949), first edition, Chap. 8.
[2] W. Kuhn and F. Grun, J. Polymer Sci. **1**, 183 (1946).
[3] P. A. Thiessen and W. Wittshadt, Z. physik. Chem. **B29**, 359 (1935).

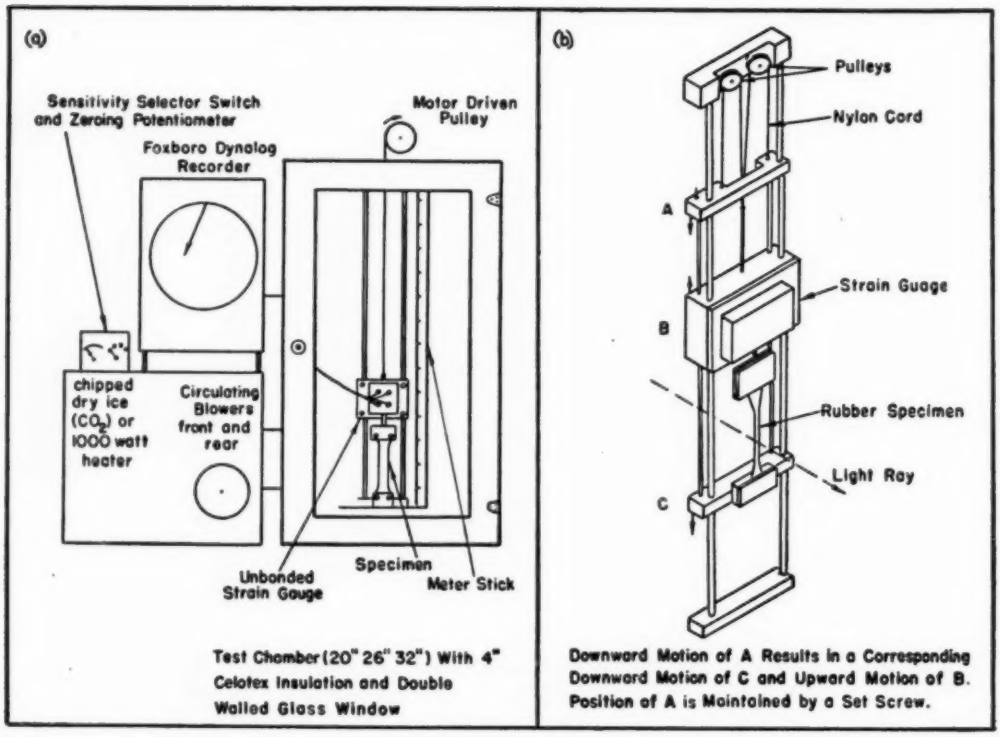
(a)
Sensitivity Selector Switch and Zeroing Potentiometer
Motor Driven Pulley
Foxboro Dynalog Recorder
chipped dry ice (CO_2) or 1000 watt heater
Circulating Blowers front and rear
Specimen
Unbonded Strain Gauge
Meter Stick
Test Chamber (20" 26" 32") With 4" Celotex Insulation and Double Walled Glass Window
(b)
Pulleys
Nylon Cord
A
Strain Guage
B
Rubber Specimen
Light Ray
C
Downward Motion of A Results in a Corresponding Downward Motion of C and Upward Motion of B. Position of A is Maintained by a Set Screw.

FIG. 1. Stress-birefringence apparatus.

would be obtained if the elements were perfectly oriented, and $\langle \sin^2\gamma \rangle_{Av}$ is the average of the square of the sine of the angle between the optic axes of the element and the medium. F is called the orientation factor.[4] If the medium is composed of more than one type of element, the optical anisotropy can be written, under the above assumptions, as,

$$A_{zz}-A_{xx}=\sum_i (A_{zz}-A_{xx})_i f_i, \qquad \sum_i f_i=1, \tag{5}$$

where f_i is the volume fraction of i-type elements and $(A_{zz}-A_{xx})_i$ is the optical anisotropy pure i would have with the same angular distribution of elements as that (of i-type elements) existing in the composite medium. In rewriting Eq. (5) in terms of the birefringence, if it is assumed that the function involving the mean refractive index in Eq. (3) is the same in the separate phases, we obtain,

$$\Delta n_0=\sum_i f_i \Delta n_i, \tag{6}$$

where Δn_0 is the observed birefringence of the composite material, and Δn_i is the birefringence pure i would have in the same state of orientation.

To apply Eq. (6) to polycrystalline elastomers, they are assumed to be composed of two types of elements; namely, very small crystallites, and amorphous chains. In this case, Eq. (6) can be written in the form,

$$f_c=(\Delta n_0-\Delta n_a)/(\Delta n_c-\Delta n_a), \tag{7}$$

[4] P. H. Hermans, *Contribution to the Physics of Cellulose Fibers* (Elsevier Publishing Company, Inc., New York, 1946), p. 198.

where the subscripts c and a refer to the crystalline and amorphous phases, respectively. The birefringence of the crystalline phase can be written from Eqs. (3) and (4a), as

$$\Delta n_c=\Delta n_c^0 F, \tag{8}$$

where Δn_c^0 is the birefringence of a pure crystal and F is the orientation factor, both of which can, in principle, be experimentally determined. To evaluate the birefringence of the amorphous phase, we must know something about the state of orientation of the amorphous chains. We adopt as a working approximation, the assumption that insofar as they affect the stress-optical properties of the amorphous phase, crystallites act only as additional cross links. This assumption permits us to evaluate Δn_a from[1,2]

$$\Delta n_a=cs, \tag{9}$$

where c is the stress-optical coefficient of the amorphous material, and s is the tensile stress on actual cross section. The critical point here is that the stress-optical coefficient is independent of the degree of cross linking at low stresses and thus independent of the degree of crystallization.

III. GENERAL EXPERIMENTAL APPROACH

The general experimental procedure used for testing the relation between birefringence, stress, and crystallinity as given in Eqs. (7)–(9) was to measure the birefringence and stress on a lightly cross-linked specimen of 5°C polybutadiene held at constant length as the

temperature was lowered from +30°C to −30°C The degree of crystallinity and orientation factor were obtained under the same conditions using x-ray diffraction techniques[5] and it was then determined whether the degree of crystallinity calculated from the birefringence stress data could be made to agree with the x-ray results using a single reasonable value for Δn_c^0, the birefringence of a single crystal of polybutadiene.

IV. PREPARATION OF VULCANIZATES

The crude polymer (5°C polybutadiene prepared at the Government Laboratories, Akron, Ohio) was cleaned by alcohol precipitation of its filtered benzene solution after which it was dried in a vacuum at room temperature. The polymer was then redissolved in toluene with 1% (based on polymer weight) of PBNA added as antioxidant and the concentration (~5%) was accurately determined by evaporating to dryness a weighed portion of the solution. The desired weight of cross-linking reagent, decamethylene dismethyl azodicarboxylate,[6] dissolved in a little toluene was then added to the remaining weighed solution. The resulting solution was then transferred to 4-in.×5-in. ×1-in. flat-bottomed glass trays, and bubbles and dissolved air were removed by placing the tray in a vacuum desiccator for 15 minutes. The solvent was then allowed to evaporate at room temperature and atmospheric pressure for 24 hours, after which the dry polymer sheet was heated to 60°C in a ventilated oven for 2 hours to complete the cross-linking reaction. The finished sheets were then stripped from the trays and stored under dry ice refrigeration until used.

V. MEASUREMENT OF BIREFRINGENCE AND STRESS

The specimens used for the measurement of birefringence and stress were small dumbbells 5.88 cm in over-all length, 1.2 cm long, and 0.25 cm wide in the uniform central section, died from the sheets. The specimen thickness (0.005 to 0.015 inch) was measured to ±0.0002 inch with a dial micrometer, the length between India ink fiducial marks placed about 1 cm apart in the uniform central section was measured to 0.01 cm with a cathetometer, and the specimen was clamped in place in the apparatus illustrated in Fig. 1. The stretching device, illustrated in some detail in Fig. 1(b), elongated the specimen without appreciably moving its center, through which passed the polarized light beam used in the measurement of the birefringence. The polarized light beam came through a small double-walled window in the rear of the working chamber. The birefringence of the specimen was measured with a Babinet compensator mounted in front of the working chamber, and the stress was measured by an unbonded strain gauge [Fig. 1(b)], the output of which was continuously recorded on a millivolt recorder. In calculating the birefringence and the stress, the thickness and cross-sectional area of the specimen were assumed to be $d_0/\alpha^{\frac{1}{2}}$ and A_0/α, respectively, where d_0 = initial thickness, A_0 = initial cross section, and α = extension ratio; i.e., the deformation was assumed to be a constant volume affine extension.

Temperature control to ±1°C was maintained by varying the speed of the blowers which cycled the working chamber air over chipped dry ice. In an attempt to approximate equilibrium conditions, each stretched specimen was relaxed for at least two hours at room temperature before cooling, and each fixed temperature was maintained until the birefringence and stress were approximately constant.

VI. RESULTS

The birefringence and stress on actual cross section as a function of temperature and extension ratio for 5°C polybutadiene cross linked with 0.6% decamethylene *dis*-methylazodicarboxylate are given in Table I. The fourth column in Table I, Δn_a, the contribution of the amorphous fraction of the specimen to the birefringence, was calculated from

$$\Delta n_a = (0.566 - 0.00356t)s \times 10^{-3},$$

t = temperature (°C),

s = stress on actual cross section (kg/cm²).

The value $0.566 - 0.00356t$ for the stress-optical coeffi-

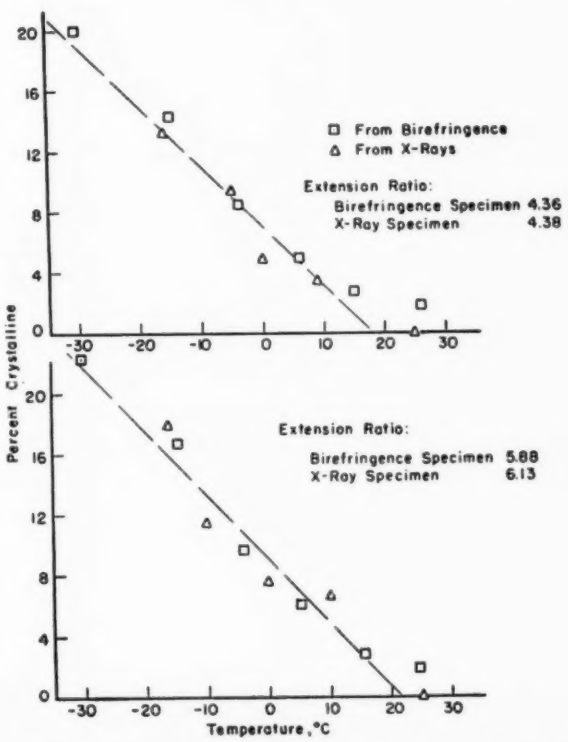

FIG. 2. Percent crystallinity *vs* temperature for 5°C polybutadiene from x-ray and birefringence measurements.

[5] Alexander, Ohlberg, and Taylor, J. Appl. Phys. **26**, 1068 (1955).

[6] Flory, Rabjohn, and Shaffer, J. Polymer Sci. **4**, 225 (1949).

TABLE I. Birefringence, stress, and percent crystallinity at fixed elongation as a function of temperature for 5°C polybutadiene, cross linked with 0.6% decamethylene *dis*-methylazodicarboxylate.

Extension ratio	Birefringence ($\Delta n_0 \times 10^3$)	Stress on actual cross section (kg/cm²)	$\Delta n_a \times 10^3$ [a]	Percent[b] crystallinity	Temp. °C
2.18	2.734	5.79	2.78	−.04	23.9
	2.975	5.79	3.04	−.05	11.6
	3.122	5.58	3.15	−.02	0.2
	9.109	4.59	2.74	5.00	− 9.2
3.472	6.957	13.90	6.63	0.27	25.0
	7.809	12.70	6.52	1.04	15.0
	9.359	11.98	6.55	2.28	5.3
	14.703	9.82	5.73	7.21	5.1
	19.558	6.23	3.86	12.44	−15
	25.532	1.20	0.81	19.12	30.1
	26.976	0.48	0.33	20.53	34.9
4.36	9.827	16.27	7.71	1.73	25.7
	10.997	15.06	7.73	2.67	15.0
	13.572	13.92	7.56	4.91	6.3
	17.271	12.09	6.99	8.35	− 3.5
	22.611	7.91	4.90	14.15	−14.9
	28.115	3.57	2.40	20.14	−30.0
	30.058	2.51	1.73	22.06	−35.3
5.88	13.364	23.05	11.02	1.96	24.6
	14.193	21.24	10.85	2.80	15.5
	17.702	19.08	10.44	6.07	5.3
	21.450	16.81	9.73	9.73	− 3.9
	28.268	12.83	7.92	16.65	−14.5
	33.048	7.61	5.12	22.34	−30.0
	34.911	6.47	4.48	24.23	−35.8
6.86	16.484	27.18	13.05	2.93	24.1
	17.331	24.93	12.74	3.91	15.3
	20.528	22.69	12.37	6.93	5.8
	26.273	19.82	11.63	12.35	− 6.0
	30.358	15.83	9.83	17.07	−15.8
	35.946	10.22	6.88	23.60	−30.1
	38.777	8.85	6.12	26.34	−35.1
7.77	18.785	33.78	15.37	2.98	31.1
	19.971	29.11	14.82	4.47	15.9
	23.720	27.19	14.74	7.78	6.7
	27.292	23.90	13.91	11.51	− 4.6
	31.845	20.82	12.80	16.24	−14.0

[a] The birefringence of the amorphous fraction.
[b] Calculated from $f_c = (\Delta n_0 - \Delta n_a)/(0.130 - \Delta n_a)$.

cient for amorphous 5°C polybutadiene was obtained from unpublished experimental data and is accurate from 0 to 50°C.

The degree of crystallinity can now be calculated from the data of columns two and four of Table I, using Eq. (7), provided Δn_c^0 and the orientation factor are known. The orientation factor has been measured[5] at extension ratios of 4.25 and 6.35 and it was found to be a constant, within experimental error, with a mean value of 0.826 $\pm$0.020. Since, furthermore, the orientation factor is insensitive to small changes in the state of orientation, the quantity Δn_c can be treated as a constant (except possibly at very small extensions) which can be evaluated from a single known value of the degree of crystallinity. To this end we use the x-ray result[5] $f_c = 0.132$ at −16°C at an extension ratio (α) of 4.38 in conjunction with the birefringence observations at −14.9°C and $\alpha = 4.36$ to obtain the approximate value $\Delta n_c = 0.139$. Since this calculation puts too much emphasis on a single x-ray result which may be in error by 0.02, it would obviously be more satisfactory to adjust Δn_c to obtain the best over-all fit with all of the x-ray data available.[5] When this is done, it is found that, with $\Delta n_c = 0.130$, the birefringence measurements agree with the x-ray measurements to the extent shown in Fig. 2. This general agreement can hardly be considered a spurious result of a combination of x-ray and birefringence errors.

Making use of the value 0.130 for Δn_c, the degree of crystallinity as a function of extension and temperature has been calculated from the birefringence measurements. The results of these calculations are given in column 5 of Table I and in Fig. 3. It is to be noted once again (see Sec. V) that these results are not purported to be true equilibrium values although apparent steady states (on the time scale of the measurements) were attained.

VII. DISCUSSION

In a test of the applicability of the proposed expression relating degree of crystallinity with birefringence, the principal points to be considered are the constancy and magnitude of Δn_c^0, the need of a correction for the contribution of the amorphous material to the birefringence, and the possibility of calculating this correction by the use of the stress-optical coefficient for the amorphous material. From the foregoing results, Δn_c^0 is satisfactorily constant, and its magnitude (0.157) is quite reasonable since the theoretical value of Δn_c^0 for the closely related material, *trans*-polyisoprene, is 0.171 (see below). The need for an amorphous correction is evidenced by the magnitude of the corrections (see Δn_a in Table I) that were applied; and the fact that these corrections, calcuated by use of the experimental stress-optical coefficient and the stress, yield satisfactory results, at least indirectly validates the procedure.

An interesting special case occurs when the birefringence measurements are taken under conditions of no stress. In this case, Eq. (7) becomes

$$f_c = \Delta n_0 / F \Delta n_c^0. \tag{10}$$

Measurements of this type could be taken, for example, by stretching a specimen, freezing it and observing the birefringence of the unclamped specimen at reduced temperatures. While we have made no measurements of this type, Treloar[7] has published density and birefringence data on natural rubber at 0°C under conditions such that Eq. (10) should apply. He records values of the ratio birefringence to the increase in density (relative to the amorphous material) and finds thats this quantity increases to a limiting value as the specimen extension is increased. This is exactly what Eq. (10) predicts, for the crystallite orientation improves with extension and F approaches unity. Using his limiting value for the ratio, and assuming the density of crystalline natural rubber at 0°C to be 1.006 g/cm³, the value of Δn_c^0 is found to be 0.218. It is possible to compare this figure directly with theory by calculating the birefringence of a natural rubber crystal (as a uniaxial crystal) using the crystal structure data of Bunn[8] and the bond polarizabilities of Denbigh[9] in conjunction with Eqs. (3) and (4a). The result, 0.215, is in remarkable agreement with Treloar's value. The figure 0.171 given previously for the birefringence of crystalline polyisoprene was similarly calculated using Bunn's[8] structure data on gutta percha.

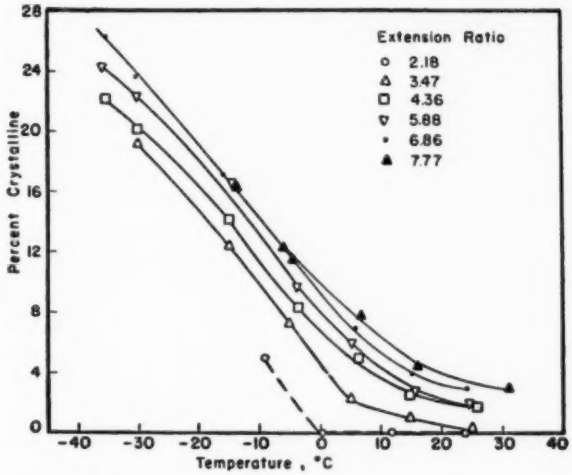

FIG. 3. Percent crystallinity *vs* temperature for 5°C polybutadiene cross linked with 0.6% decamethylene *dis*-methylazodicarboxylate.

It is interesting to note that attempts have been made to measure directly the birefringence of pure crystals of natural rubber and gutta percha using a polarizing microscope. The reported results are Δn_c^0 (natural rubber)=0.050,[10] Δn_c^0 (gutta)=0.036.[11] The discrepancy between these values and the calculated values is rather large, however there can be little doubt but that the crystals studied experimentally were a more or less imperfectly oriented aggregate of submicroscopic crystallites and hence that a significant correction by way of the orientation factor is to be expected. Further serious doubt is cast on the experimental value 0.050 for natural rubber by the fact that Treloar records birefringence values for stretched partially crystalline natural rubber as high as 0.090 and we have observed values greater than 0.070.

ACKNOWLEDGMENTS

The authors wish to acknowledge their indebtedness to Dr. T. W. DeWitt for numerous helpful discussions during the course of this work.

[7] L. R. G. Treloar, Trans. Faraday Soc. **37**, 84 (1941).
[8] C. W. Bunn, Proc. Roy. Soc. (London) **A180**, 40 (1942).
[9] K. G. Denbigh, Trans. Faraday Soc. **36**, 936 (1940).
[10] L. A. Wood, J. Research Natl. Bur. Standards **15**, 580 (1940).
[11] W. Schlesinger and H. M. Leeper, J. Polymer Sci. **11**, 203 (1953).

Isothermal Viscosity-Molecular Weight Dependence for Long Polymer Chains

T. G Fox and S. Loshaek
Rohm & Haas Company, Philadelphia, Pennsylvania
(Received May 12, 1955)

Evidence is given showing that the equation, $\log\eta = 3.4\log Z + K$, represents an empirical law of flow which holds generally for sufficiently long flexible chain molecules in bulk or in solution. Here η is the viscosity, Z is the number of atoms in the chain, and K is a constant which is dependent on the polymer type and on the temperature. All of the available data which cover wide molecular weight ranges for linear (and branched) molecules in bulk or in solution, including results on polyesters, polyamides, polystyrene, polyisobutylene, polydimethyl siloxane, and polymethyl methacrylate, support this conclusion. For chains having fewer than a critical number, Z_c, of chain atoms (Z_c being characteristic of the polymer species) the dependence of η on Z is less severe but more complex. These results are in semiquantitative agreement with the recent theory of F. Bueche. On the basis of this theory, values for the concentration of chain entanglements in various polymers are obtained from the observed values of Z_c.

ACCORDING to currently accepted concepts of flow,[1-4] the viscosity η of a liquid composed of long polymer chains in bulk or in a solution sufficiently concentrated that interchain entanglements occur, is determined by the frequency J at which a chain segment jumps from one equilibrium position to another and a statistical factor F which expresses the requirement that the jumps of the various segments in a given chain (or in a series of entangled chains) cannot be completely independent but must be coordinated. Thus

$$\eta = F/J. \tag{1}$$

The segmental jump frequency J is dependent on the temperature and on the local configuration arrangement (radial distribution function) of nearest neighbor segments in the liquid. The statistical factor F is independent of these variables but may be expected to vary with chain length in a manner which is the same for all linear flexible chain molecules. By examining the available data on the dependence of viscosity on chain length at constant J, i.e., at constant temperature and density, we shall establish here an empirical expression for F which is generally applicable to flexible chain molecules. We shall demonstrate further that the result is in semiquantitative agreement with the theory of F. Bueche.[4]

In 1940 Flory[2] reported the results of accurate viscosity determinations on molten linear polyesters (e.g., decamethylene adipate, of known molecular weight and molecular weight distribution). He found that over the unusually broad ranges in molecular weight (200 to 10 000) and temperatures (0 to 200°C) investigated, the data were represented accurately by the equation

$$\log\eta = CZ_w^{\frac{1}{2}} + A. \tag{2}$$

Here C is a constant, A is temperature dependent, and Z_w is the weight average chain length defined as

$$Z_w = \sum w_x Z_x,$$

where w_x is the weight fraction of species x having a chain length (number of chain atoms) of Z_x. By measuring viscosities of mixtures of polyesters of widely differing molecular weights, Flory was able to show that Eq. (2) was applicable to any molecular weight distribution provided the weight average chain length was used therein.

Evidence that Eq. (2) does not apply universally to other polymers was provided by viscosity data[3] on fractionated polymers of polyisobutylene and of polystyrene. Plots of $\log\eta$ *vs* $Z^{\frac{1}{2}}$ covering a wide molecular weight range in each case are not linear for either of these polymers even in the low molecular weight range for which the data on the polyesters were obtained. Instead, except for the lower molecular weight fractions, the data in both cases[3,5,6] when plotted on log-log plots of η *vs* Z are represented by straight lines of identical slope, corresponding to the relation

$$\log\eta = 3.4\log Z_w + K \qquad (Z \geq Z_c), \tag{3}$$

where K is a function of temperature. By measuring viscosities of mixtures of fractions[3] it was shown that the weight average chain length was the pertinent average applicable in this case.

More recently, viscosity measurements on concentrated solutions of polystyrene,[7] polyisobutylene,[8] and of polymethyl methacrylate[9] over a wide range in temperature and concentration show that, at fixed concentration of diluent and fixed temperature, the viscosity is proportional to $Z_w^{3.4}$ just as in Eq. (3), except below a certain critical chain length Z_c, where approximate proportionality to a lower power of Z is

[1] W. Kauzmann and H. Eyring, J. Am. Chem. Soc. **62**, 3113 (1940); W. Kauzmann, Chem. Rev. **43**, 219 (1948).
[2] P. J. Flory, J. Am. Chem. Soc. **62**, 1057 (1940).
[3] T. G Fox and P. J. Flory, J. Am. Chem. Soc. **70**, 2384 (1948); J. Appl. Phys. **21**, 581 (1950); J. Phys. Chem. **55**, 221 (1951); J. Polymer Sci. **14**, 315 (1954).
[4] F. Bueche, J. Chem. Phys. **20**, 1959 (1952).
[5] R. D. Andrews and A. V. Tobolsky, J. Polymer Sci. **7**, 221 (1951).
[6] Leaderman, Smith, and Jones, J. Polymer Sci. **14**, 47 (1954).
[7] F. Bueche, J. Appl. Phys. **24**, 423 (1953).
[8] Johnson, Evans, Jordan, and Ferry, J. Colloid Sci. **7**, 498 (1952).
[9] F. Bueche, J. Appl. Phys. **26**, 738 (1955).

observed. The value of Z_c for a given polymer series varies inversely as the concentration of polymer in solution, i.e., for a given type of polymer the product $v_2 Z_c$ is constant,[7,9] where v_2 is the volume fraction of polymer in solution.

It is noteworthy that Eq. (3) applies to at least three dissimilar polymers both in bulk and in concentrated solution, over extremely wide ranges in Z_w, i.e., at least 87-fold for polyisobutylene and 10-fold for polystyrene. Furthermore, failure of this equation was not observed even for the highest molecular weight investigated but instead occurred only *below* some relatively low critical chain length Z_c, where Z_c is <1000 for bulk polymers. This failure at low chain length, whose value for a polymer series depends inversely on the polymer concentration, suggests some abrupt change in the mechanism of flow when the domains of the chains fail to overlap to some critical extent.

We have, therefore, re-examined on isothermal plots of $\log\eta$ *vs* $\log Z_w$ all of the available viscosity data which cover wide molecular weight ranges for well-characterized polymers.[2,3,5–12] As illustrated by typical examples in Fig. 1, the data in each case can be represented by two lines which intersect at a value of the chain length which we shall call Z_c. For chains longer than this critical length, the data covering a wide range of temperature and polymer concentrations in most cases may be represented within the experimental uncertainties in Z and η by a straight line of slope 3.4. Thus the data on polyesters which have heretofore been represented by Eq. (2) are also represented adequately by Eq. (3).

We have summarized in Table I the systems for which data are available which conform to Eq. (3). It is evident that we must regard this equation as an empirical law of flow which may be expected to hold generally for long flexible chain molecules in bulk or in solution.

It has been demonstrated[3] that for polymers of heterogeneous molecular weight distribution the viscosity in Eq. (3) is dependent on the weight average chain length Z_w, while the viscosity temperature coefficient is constant for long chains but varies for short chains with the number average chain length Z_n. Thus Eq. (3) applies to such heterogeneous mixtures provided that $Z_w > Z_c$ and that Z_n is above some critical value as well. Since for a given polymer species the density is also constant above this same critical value of Z_n,[3] it follows that Eq. (3) applies at conditions of constant temperature and volume, i.e., at constant J. We therefore deduce from Eqs. (1) and (3) that for $Z > Z_c$ the statistical factor F is proportional to $Z_w^{3.4}$. Below Z_c

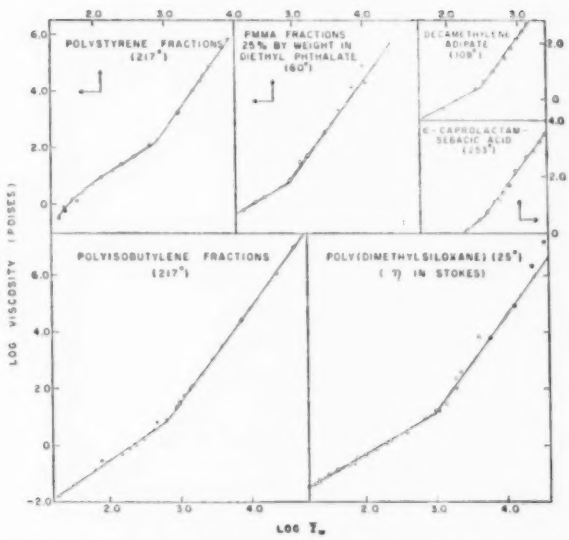
POLYSTYRENE FRACTIONS (217°)
PMMA FRACTIONS 25% BY WEIGHT IN DIETHYL PHTHALATE (60°)
DECAMETHYLENE ADIPATE (108°)
ϵ-CAPROLACTAM-SEBACIC ACID (253°)
POLYISOBUTYLENE FRACTIONS (217°)
POLY(DIMETHYL SILOXANE) (25°) (η IN STOKES)
LOG VISCOSITY (POISES)
LOG Z_w

FIG. 1. Plots of $\log\eta$ *versus* $\log Z_w$ for polymers of different types including: polystyrene,[3] poly(methyl methacrylate),[9] decamethylene adipate,[2] ϵ-caprolactam-sebacic acid,[12] polyisobutylene,[3] poly(dimethyl siloxane).[10] The dark circles for poly(dimethyl siloxane) represent viscosity values in poises for a slightly different temperature (43°C).[10]

there is an abrupt change to a less sensitive dependence of F on Z_n.

A molecular theory for the isothermal viscosity-molecular weight dependence for flexible polymer chains in bulk or concentrated solution has been advanced by F. Bueche.[4] According to this theory, for polymer chains short enough to have an average of less than one entanglement per molecule with neighboring chains, the resistance to flow arises predominately from the ordinary friction of one chain segment moving past another or past a solvent molecule. Hence, in this range the resistance to flow is proportional to the chain length, i.e., $\eta \propto Z$. With increasing chain length, the average number of entanglements per chain increases, and when it equals one the conditions for an infinite network formation through chain entanglements are suddenly met.[13] Here with further increase in Z the viscosity would suddenly become infinite, except for the fact that the chain entanglements are not permanent but allow a certain amount of slippage between entangled chains. In this region Bueche has shown that the resistance to flow of a particular chain arises primarily from the viscous drag of the train of entangled chains which must be pulled along with the motion of the chain in question. He showed that in the limit of very long slipping entangled chains $\eta \propto Z^{2.5}$. At intermediate chain lengths, representing an abrupt transition from one limiting flow law to another, the viscosity may increase even faster than the 2.5 power of the chain length.

The isothermal viscosity-molecular weight dependence illustrated in Fig. 1 and Eq. (3) is in semiquantitative agreement with the above prediction. Thus the

[10] A. J. Barry, J. Appl. Phys. **17**, 1020 (1946); Hunter, Warrick, Hyde, and Currie, J. Am. Chem. Soc. **68**, 2284 (1946); Warrick, Piccoli, and Stark (unpublished results).

[11] Baker, Fuller, and Heiss, J. Am. Chem. Soc. **63**, 2142 (1941).

[12] J. R. Schaefgen and P. J. Flory, J. Am. Chem. Soc. **70**, 2709 (1948).

[13] P. J. Flory, J. Am. Chem. Soc. **63**, 3083 (1941).

TABLE I. Applicability of the empirical law $\log\eta = 3.4 \log Z_w + K$ to long polymer chains.

Polymer-solvent pair	Wt. fraction of polymer	$v_2 Z_e$ at break[a]	Range of applicability: Highest Z studied	Range of applicability: Temp. range studied, °C	Polymers & mol. wt. deter.[b]
Linear nonpolar polymers					
Polyisobutylene[3]	1.0	610	53 000	−9 to 217	f:(η)
Polyisobutylene-xylene[8]	0.05–0.20	~1400	140 000	25	W&f:(η)
Polyisobutylene-decalin[8]	0.05–0.20	——	140 000	25	W&f:(η)
Polystyrene[3]	1.0	730	7300	130 to 217	f:(η)
Polystyrene-diethyl benzene[7]	0.14–0.44	~1000	22 500	30 to 100	f:(η)
Poly(dimethyl siloxane)[10]	1.0	~ 950	34 000	25	W:π, *L.S.*
Linear polar polymers					
Poly(methyl methacrylate)-diethyl phthalate[9]	0.25	208	24 000	60	f:(η)
Decamethylene sebacate[2]	1.0	290	960	80 to 200	W:E
Decamethylene adipate[2]	1.0	280	1320	80 to 200	W:E
Decamethylene succinate[2]	1.0	290	990	80 to 200	W:E
Diethylene adipate[3]	1.0	290	1190	0 to 200	W:E
ω-hydroxy undecanoate[11]	1.0	< 326	1443	90	W:E
Effect of branching					
Poly(ε-caprolactam):[12]					
linear	1.0	324	2300	253	W:E
tetrachain	1.0	390	1560	253	W:E
octachain	1.0	550	2000	253	W:E

[a] Z_e is the lowest chain length for which Eq. (3) is valid for the solution wherein v_2 is the volume fraction of polymer.
[b] f=fraction, W=whole polymer. Chain lengths determined from: (η)=intrinsic viscosity, π=osmotic pressure, *L.S.*=light scattering data, E=end group analysis.

abrupt change in slope observed at $Z=Z_e$ may be identified as the point at which network formation through chain entanglement becomes possible. The predicted dependence of η on $Z^{2.5}$ is in semiquantitative agreement with the empirical dependence of η on $Z^{3.4}$ observed for long chains. It is not clear whether the discrepancy in the exponent arises from the approximate nature of the theory, or from the possibility that the experimental data happen to be in the transition region where a higher dependence of η on Z is theoretically possible. In the low molecular weight region ($Z<Z_e$) where the theory requires $\eta \propto Z$, an abrupt lessening of the dependence of η on Z is observed, but it is found that $\eta \propto Z^a$, where a is usually greater than 1, and varies with Z. This complicated behavior is reasonable if we consider that in this range the viscosity changes because of the dependence of J on Z (at low Z only) as well as on the dependence of the cooperative factor F on Z.

One of the most important parameters affecting the viscoelastic behavior of a polymer is the concentration of chain entanglements, or its equivalent, the number of chain atoms between entanglement points. According to the foregoing theory, the value of Z_e in Table I furnishes a direct evaluation of this parameter. In confirmation of this, the values of Z_e obtained here for polymethyl methacrylate and polyisobutylene are in good agreement with the corresponding values determined from the height of the plateau region in viscoelastic creep, stress relaxation, or dynamic mechanical response investigations on these polymers.[9,14]

Inspection of Table I shows the value of Z_e to be about 1000 chain atoms for the nonpolar polymers, and about 200 to 400 for the polar molecules. This increase in the number of chain entanglements with increasing polarity is reasonable since the more polar polymers will have higher interchain forces. Introducing branches into the molecule, on the other hand, causes a decrease in the viscosity (for a given total number of chain atoms in the molecule) and increases Z_e. Both of these effects no doubt reflect the fact that a branched molecule is necessarily more compact than a linear one of the same molecular weight, consequently, it has less opportunity to form *interchain* entanglements. In short, for a given molecular weight such that $Z>Z_e$, the concentration of chain entanglements and the viscosity can be increased by increasing the polarity of the chain and decreased by increasing the degree of branching of the molecule.

[14] F. Bueche and H. Leaderman (private communications). See Ferry, Landel, and Williams, J. Appl. Phys. **26**, 359 (1955).

JOURNAL OF APPLIED PHYSICS VOLUME 26, NUMBER 9 SEPTEMBER, 1955

Extension of the Hertz Theory of Impact to the Viscoelastic Case

YOH-HAN PAO
Polychemicals Department, E. I. du Pont de Nemours and Company, Inc., Experimental Station, Wilmington, Delaware
(Received May 6, 1955)

The problem considered is that of two bodies coming into normal contact over smooth curved surfaces. The initial relative velocity and the total kinetic energy involved is low. Contact is, however, confined to such small volumes of the objects involved that very high concentrations of energies are obtained at those places. The rates of application of stress are correspondingly high. The Hertz solution to this type of problem provides a useful approximation in the case of elastic objects.

In the present treatment one of the impinging bodies is of viscoelastic material. Two viscoelastic bodies may also be treated if they are of the same material. The Laplace transform method is used to obtain the viscoelastic expression for the force developed between the two surfaces. This expression is then applied to the impact case. The expression can also be applied to other truly static cases; e.g., contact between gear tooth surfaces.

The results are of technological interest, since it is not possible to say if a plastic is suitable for a certain category of impact applications, unless the rates of straining or stressing obtained in those applications can be estimated.

HIGH concentrations of energy accompanied by high rates of application of load can be obtained in materials in one of two ways. In the one case the controlling factor is time. Part of the material is caused to move so rapidly that in essence there is not sufficient time for the energy to be propagated to the surrounding parts. A specific example of this would be the case of long rods impinging longitudinally. This problem is sometimes also known as the St. Venant problem, and one of the assumptions involved in the solution of the problem is that the ends of the rods are planes, so that during contact the pressure is uniform over the whole of the two end faces. The problem of propagation of plane waves in semi-infinite viscoelastic bars has been studied by several persons. A general treatment of the problem has been given by Sips.[1] Cases involving two-parameter and four-parameter models have been studied in greater detail by Lee and Kanter[2] and Glauz and Lee,[3] respectively.

In the other case the controlling factor is geometry. For example, if a sphere is dropped on a plane, the relative velocity preceding contact may be quite low and the total amount of kinetic energy involved may be quite low. Contact is, however, confined to such small volumes of the materials involved that very high concentrations of energies are obtained at those places. The rates of application of load are correspondingly high. The Hertz solution to this type of problem provides a useful approximation in the case of elastic bodies, but is valid only if the duration of impact is long in comparison with the time taken for wave propagation or in comparison with the periods of the gravest modes of vibration which can be excited in the bodies. If this latter condition is not satisfied, both wave propagation and local contact will have to be considered.[4]

This paper is concerned with the Hertz type of impact. In the present treatment one of the impinging bodies is of viscoelastic material. Two viscoelastic bodies can also be considered if they are of the same material.

A general method of solution is indicated. The method of solution consists essentially of obtaining the Laplace transform of the elastic solution, replacing the shear modulus of the elastic case in the transformed expression with a viscoelastic function and obtaining the inverse transform of the altered expression. If the resulting expression satisfies the boundary and initial conditions of the physical situation, it is the unique viscoelastic solution to the problem considered. The justification for this procedure is shown in the following section.

Sips[5] was probably the first to consider the possibility of this specific method of solution of viscoelastic problems although somewhat equivalent forms of operational methods had been considered before. Since then Brull[6] and Didonato *et al.*[7] have also presented less general derivations incorporating simplifications and minor modifications of this method.

The present problem is one in which the solution for the elastic case is nonlinear although the material is considered to be linear. Technologically, the problem is of considerable interest. It is widely recognized that the deformation and fracture aspects of plastics are strongly time dependent. It is, therefore, not possible to say if a plastic is suitable for a certain category of impact applications, unless the rates of straining or stressing obtained in those applications can be estimated.

[1] R. Sips, J. Polymer Sci. **6**, 3, 285–293 (1951).
[2] E. H. Lee and J. Kanter, J. Appl. Phys. **24**, 9, 1115–1122 (1953).
[3] R. D. Glauz and E. H. Lee, J. Appl. Phys. **25**, 8, 947–953 (1954).
[4] J. E. Sears, Trans. Cambridge Phil. Soc. **21**, 49–105 (1908).
[5] R. Sips, J. Polymer Sci. **7**, 2, 3, 191–206 (1951).
[6] M. Brull, Proc. First Midwestern Conf. on Solid Mech. (1953).
[7] Didonato, McLeod, and Webber, paper presented at annual meeting of the American Physical Society (1954) (to be published).

The results of this analysis show that the viscoelasticity of the impinging bodies interacts strongly with the geometry of the bodies to determine the final pattern of impact.

Numerical results have been obtained to illustrate how all other things being the same, very much higher loads and rates of loading are obtained in the case of the more rigid materials. It is also shown how two bodies of the same geometrical shape and apparently of the same "static modulus" may behave in significantly different manner in impact depending on how their viscoelastic spectra are distributed.

METHOD OF SOLUTION

Using the bulk modulus and shear rigidity, the stress-strain relation of classical elasticity can be written as[7a]

$$\tau_{ij}=k\delta_{ij}e_{ii}+2\mu(e_{ij}-\tfrac{1}{3}\delta_{ij}e_{ii}) \tag{1}$$

or

$$\tau_{ij}=k\delta_{ij}e_{ii}+2\mu\epsilon_{ij}, \tag{2}$$

when $\epsilon_{ij}=e_{ij}-\frac{1}{3}\delta_{ij}e_{ii}$ and is the strain that is associated with change of shape or distortion.

Making use of Eq. (2) and the definition of strain in terms of displacements, the usual equilibrium equations can be written in terms of displacements as

$$k\mu_{j,ji}+2\mu[\tfrac{1}{2}(u_{i,jj}+u_{j,ji})-\tfrac{1}{3}u_{j,ji}]+F_i=0, \tag{3}$$

where F_i are the body forces.

The Laplace transform of this equation is

$$kL(\mu_{j,ji})+\mu[L(u_{i,jj})+\tfrac{1}{3}L(u_{j,ji})]+L(F_i)=0. \tag{4}$$

It is clear that any problem of elasticity is solved if Eq. (4), either in the original or transformed form, is solved in conjunction with boundary conditions. In Eq. (4) the inertia forces are neglected. This form is used because the Hertz solution is a static solution. The same procedure would hold for cases where the inertia forces cannot be neglected.

It will now be assumed that in viscoelasticity, the dilatation e_{ii} is independent of rate effects, whereas the distortional strains are related to the respective stress components by the relations

$$\sigma_{ij}(t)=2\mu\left[\epsilon_{ij}-\int_0^t\bar{\psi}(t-x)d\epsilon_{ij}(x)\right]. \tag{5}$$

Equation (5) is based on the Boltzmann superposition principle. The quantity $\bar{\psi}(t-x)$ is commonly called the relaxation function and $\bar{\psi}(0)=0$, $\bar{\psi}(\infty)=1$.

The general stress-strain relations in viscoelasticity are, therefore,

$$\tau_{ij}=k\delta_{ij}e_{ii}+2\mu\left[\epsilon_{ij}-\int_0^t\bar{\psi}(t-x)d\epsilon_{ij}(x)\right] \tag{6}$$

[7a] See Appendix I for notation.

or

$$\tau_{ij}=k\delta_{ij}e_{ii}+2\mu[e_{ij}-\tfrac{1}{3}\delta_{ij}e_{ii}]-2\mu\int_0^t\bar{\psi}(t-x)d[e_{ij}-\tfrac{1}{3}\delta_{ij}e_{ii}]. \tag{7}$$

Integrating by parts we have

$$\tau_{ij}=k\delta_{ij}e_{ii}+2\mu[e_{ij}-\tfrac{1}{3}\delta_{ij}e_{ii}]-2\mu[\{e_{ij}(x)-\tfrac{1}{3}\delta_{ij}e_{ii}(x)\}\bar{\psi}(t-x)]-2\mu\int_0^t(e_{ij}-\tfrac{1}{3}\delta_{ij}e_{ii})\langle\dot{\psi}\rangle(t-x)dx, \quad \begin{matrix}x=t\\x=0\end{matrix} \tag{8}$$

where $\langle\dot{\psi}\rangle$ denotes differentiation of $\bar{\psi}$ with respect to time.

Since $\bar{\psi}(0)=0$ and $e_{ij}(0)-\frac{1}{3}\delta_{ij}e_{ii}(0)=0$, Eq. (8) can be simplified to be

$$\tau_{ij}=k\delta_{ij}e_{ii}+2\mu[e_{ij}-\tfrac{1}{3}\delta_{ij}e_{ii}]-2\mu\int_0^t(e_{ij}-\tfrac{1}{3}\delta_{ij}e_{ii})\langle\dot{\psi}\rangle(t-x)dx. \tag{9}$$

Differentiating Eq. (9) with respect to coordinate j and substituting the displacements in place of the strains, one obtains

$$\tau_{ij,j}=k\mu_{j,ji}+2\mu[\tfrac{1}{2}(u_{i,jj}+u_{j,ji})-\tfrac{1}{3}u_{j,ji}]-2\mu\int_0^t[\tfrac{1}{2}(u_{i,jj}+u_{j,ji})-\tfrac{1}{3}u_{j,ji}]\langle\dot{\psi}\rangle(t-x)dx. \tag{10}$$

Substitution of this into the equation of equilibrium gives

$$k\mu_{j,ji}+2\mu[\tfrac{1}{2}(u_{i,jj}+u_{j,ji})-\tfrac{1}{3}u_{j,ji}]-2\mu\int_0^t[\tfrac{1}{2}(u_{i,jj}+u_{j,ji})-\tfrac{1}{3}u_{j,ji}]\times\langle\dot{\psi}\rangle(t-x)dx+F_i=0. \tag{11}$$

The Laplace transform of this equation is

$$kL(\mu_{j,ji})+\mu[L(\mu_{i,jj})+\tfrac{1}{3}L(\mu_{j,ji})]\times[1-L\langle\dot{\psi}\rangle]+L(F_i)=0. \tag{12}$$

If Eq. (12) is compared to Eq. (4), it is seen that both equations have the same form. In fact, we could consider the two equations to represent the same problem for two different materials, with the shear modulus being μ in the first case and $\mu[1-L(\langle\dot{\psi}\rangle)]$ in the second case.

Therefore, to obtain the solution to the viscoelastic case, simply obtain the solution to the elastic case, obtain the Laplace transform of this solution, and then in the transformed solution replace by $(1-L\langle\dot{\psi}\rangle)$. The

viscoelastic solution is obtained by taking the inverse transform of the modified elastic solution.

The viscoelastic solution so obtained is a solution to the actual physical problem because it satisfies the stress-strain relations of the viscoelastic material, the equation of continuity, and the equation of equilibrium. It satisfies the boundary conditions so long as the area of contact for a given load does not increase appreciably due to viscoelastic effects during the duration of loading, and its initial condition is the elastic solution. It is also a unique solution because the elastic solution is unique. The viscoelastic solution is the inverse transform of an expression involving only the elastic solution and a viscoelastic function. Such an inverse transform when it exists is unique.[8] This method is applied in the following to the impact problem.

SOLUTION OF IMPACT PROBLEM

In the elastic case the relation between the force developed between two bodies in contact over curved surfaces and the "approach" is given by the relation

$$\alpha^{\frac{3}{2}}=C(\theta_1+\theta_2)P. \tag{13}$$

In Eq. (13) the approach α is defined to be the amount by which the centers of mass of the two colliding bodies approach each other after contact has been made. The quantity C is a parameter incorporating the geometry of the two curved surfaces; it is a function of the principal radii of curvature of those surfaces. It is not necessary at this point to be more specific than this. The θ_1 and θ_2 involve the material constants and can be written as

$$\theta_1=\frac{k_1+4/3\mu_1}{4\mu_1\pi(k_1+1/3\mu_1)}, \tag{14}$$

$$\theta_2=\frac{k_2+4/3\mu_2}{4\mu_2\pi(k_2+1/3\mu_2)}. \tag{15}$$

The analysis leading up to expression (13) can be found in Hertz's work[9] and in Love's.[10]

In the following we take $\theta_1\gg\theta_2$ so that θ_2 can be neglected. We also take body 2 to be stationary. This corresponds then to the case of a moving viscoelastic body coming into contact with a much more rigid (e.g., steel) and stationary surface. Equation (13) can then be written as

$$(k+\tfrac{1}{3}\mu)\alpha^{\frac{3}{2}}=C\left(\frac{k}{4\mu\pi}+\frac{1}{3\pi}\right)P. \tag{16}$$

In Eq. (16) the subscript 1 has been dropped from μ and k. The Laplace transform of this equation is

$$[k+\tfrac{1}{3}\mu]L(\alpha^{\frac{3}{2}})=C\left[\frac{k}{4\pi\mu}+\frac{1}{3\pi}\right]L(P). \tag{17}$$

Replacing μ by $\mu(1-L\langle\psi\rangle)$ in Eq. (17), we obtain

$$[k+\tfrac{1}{3}\mu(1-L\langle\psi\rangle)]L(\alpha^{\frac{3}{2}})=C\left[\frac{k_1}{4\pi\mu(1-L\langle\psi\rangle)}+\frac{1}{3\pi}\right]L(P), \tag{18}$$

$$L(\alpha^{\frac{3}{2}})=C\left[\frac{1}{4\pi\mu(1-L\langle\psi\rangle)}+\frac{3}{4\pi[3K+\mu(1-L\langle\psi\rangle)]}\right]L(P). \tag{19}$$

For all known plastics $3k\gg\mu(1-L\langle\psi\rangle)$ such that $\mu(1-L\langle\psi\rangle)$ can be neglected in comparison with $3k$ in the denominator of the second term on the right-hand side of Eq. (21). For plastics, other than the comparatively rigid laminates, the entire term $3/\{4\pi[3k+\mu(1-L\langle\psi\rangle)]\}$ may be neglected with respect to $1/\{4\pi\mu(1-L\langle\psi\rangle)\}$.

Therefore, Eq. (19) can be written either as

$$L(\alpha^{\frac{3}{2}})=C\left[\frac{1}{4\pi\mu(1-L\langle\psi\rangle)}+\frac{1}{4\pi k}\right]L(P) \tag{20}$$

or as

$$L(\alpha^{\frac{3}{2}})=C\left[\frac{1}{4\pi\mu(1-L\langle\psi\rangle)}\right]L(P). \tag{21}$$

It can be shown[11] that the relationship between the Laplace transforms of the creep and relaxation functions is

$$L\bar{\psi}=\frac{\beta L(\psi)}{1+\beta pL(\psi)}, \tag{22}$$

where ψ is the creep function and β is a normalizing factor. In terms of $d\bar{\psi}/dt$ and $d\psi/dt$, Eq. (22) can be rewritten

$$\frac{1}{1-L\langle\dot{\psi}\rangle}=1+\beta L\dot{\psi}. \tag{23}$$

Substituting expression (23) into Eq. (21), we have

$$L(\alpha^{\frac{3}{2}})=\frac{C}{4\pi}\left[\frac{1+\beta L\dot{\psi}}{\mu}+\frac{1}{k}\right]L(P) \tag{24}$$

or

$$L(\alpha^{\frac{3}{2}})=\frac{C}{4\pi}\left[\frac{1}{\mu}+\frac{1}{k}\right]L(P)+\frac{C}{4\pi}\frac{\beta}{\mu}L(\dot{\psi})L(P). \tag{25}$$

Taking the inverse of this equation we have

$$\alpha^{\frac{3}{2}}=\frac{C}{4\pi}\left[\frac{1}{\mu}+\frac{1}{k}\right]P+\frac{C\beta}{4\pi\mu}\int_0^t\dot{\psi}(t-x)P\,dx, \tag{26}$$

[8] H. S. Carslaw and J. C. Jaeger, *Operational Methods in Applied Mathematics* (Oxford University Press, New York, 1941).

[9] H. Hertz, *Gesammelte Werke* (Johann Ambrosius Barth, Leipzig, 1895), Vol. I, p. 155. English translation.

[10] A. E. H. Love, *Theory of Elasticity* (Dover Publications, New York), fourth edition, pp. 183–201.

[11] B. Gross, J. Appl. Phys. **18**, 2, 212–221 (1947).

TABLE I. Assumed relaxation times of four plastics.

Case 1: Object of rigidity similar to glass laminate.	
$\mu=1\times10^6$ psi/in./in.	$\tau=\infty$
$k=2.6\times10^6$ psi/in./in.	
$\dot{\alpha}_0=192$ in./sec (corresponding to a free fall of 4 ft)	
$m=4.5\times10^{-3}$ 16 sec^2/ft	
$C=2.1$	
Case 2: Object of rigidity similar to polyethylene.	
$\mu_1=1.5\times10^4$ psi/in./in.	$\tau_1\leq10^{-6}$ sec
$\mu_2=8\times10^4$	$\tau_2=10^{-5}$
$\mu_3=1.6\times10^4$	$\tau_3=10^{-4}$
$\mu_4=0.6\times10^4$	$\tau_4\geq1$
$m=3.3\times10^{-3}$ 16 sec^2/ft	
$\dot{\alpha}_0=192$ in./sec	$C=2.1$
Case 3: Object of rigidity similar to nylon.	
$\mu_1=8.3\times10^4$ psi/in./in.	$\tau_1\leq10^{-7}$ sec
$\mu_2=4.2\times10^4$	$\tau_2=5\times10^{-6}$
$\mu_3=6.6\times10^4$	$\tau_3=10^{-5}$
$\mu_4=1\times10^5$	$\tau_4\geq1$
$m=3.3\times10^{-3}$ 16 sec^2/ft	
$\dot{\alpha}_0=192$ in./sec	$C=2.1$
Case 4: Object of same "static" rigidity as the nylon described in case 3.	
$\mu_1=8.3\times10^4$	$\tau_1=10^{-7}$
$\mu_2=4.2\times10^4$	$\tau_2=10^{-3}$
$\mu_3=6.6\times10^4$	$\tau_3=10$
$\mu_4=1\times10^5$	$\tau_4=1$
$m=3.3\times10^{-3}$ 16 sec^2/ft	
$\dot{\alpha}_0=192$ in./sec	$C=2.1$

which expresses the relation between the load P and the approach. Strictly speaking, it is a static relation and may be used for all cases where the inertia forces can be neglected with respect to the static applied forces and where the area of contact for a given load does not increase appreciably due to viscoelastic effects during the duration of loading. Thus, Eq. (26) can be applied to cases of contact between gear teeth. In the Hertz theory of impact, Eq. (26) in any one of its equivalent forms is solved simultaneously with the differential equation of motion of the moving body,

$$m\alpha''=-P. \tag{27}$$

In the following, Eq. (21) is used instead of Eq. (20).

The equations to be solved simultaneously are then

$$P=\frac{4\pi}{C}\mu\alpha^{\frac{3}{2}}-\frac{4\pi}{C}\mu\int\langle\psi\rangle(t-x)\alpha^{\frac{3}{2}}(x)dx \tag{28}$$

and

$$m\alpha''=-P. \tag{29}$$

The initial conditions are

$$\alpha'=\alpha_0' \quad \text{at} \quad t=0, \tag{30}$$

$$\alpha=0 \quad \text{at} \quad t=0. \tag{31}$$

In theoretical derivations, it is preferable to take the viscoelastic functions as continuous functions of τ, but in applying the resulting formulas it is more convenient to use line spectra instead. In general, it is easier to represent actual spectra obtained experimentally with line spectra. This means that viscoelastic behavior is represented by a finite number of relaxation or retardation times.

If we take

$$=\mu\bar{\psi}=\sum_i\mu_i(1-e^{-t/\tau_i}), \tag{32}$$

then

$$\mu\langle\dot{\psi}\rangle=\sum\mu_i/\tau_i e^{-t/\tau_i}. \tag{33}$$

Combination of Eqs. (28), (29), and (33) gives

$$m\alpha''=-4\pi\mu/C\alpha^{\frac{3}{2}}+\frac{4\pi}{C}\int_0^t\sum_i\mu_i/\tau_i e^{-t-x/\tau_i}\alpha^{\frac{3}{2}}(x)dx. \tag{34}$$

This equation can now be solved by numerical integration. Numerical calculations[12] were carried out for the four cases described in the following. The cases correspond to the impact of a plastic object on a steel surface after a free fall of four feet. The first three plastics considered are of the rigidities of glass laminate, polyethylene, and nylon, respectively. The fourth case is also for nylon, but the distribution of relaxation times is different from that of the material considered in the third case (see Table I). The relaxation times used in the four cases are used for illustration and are not meant to describe specific materials. The factor C is taken to be 2.1 for all cases and this corresponds roughly to the surface of contact of the plastic object having principal radii of curvature of 0.7 in. and 0.9 in. In the first case, that is for glass laminate, since there is no viscoelastic effect, the elastic solution involving both μ and k was used.

The results for the four cases are shown plotted in Figs. 1 and 2. It is seen that all other things being the same, smaller loads and stresses are developed in materials with lower values of E. The stress plotted is the maximum tensile stress which occurs on the surface

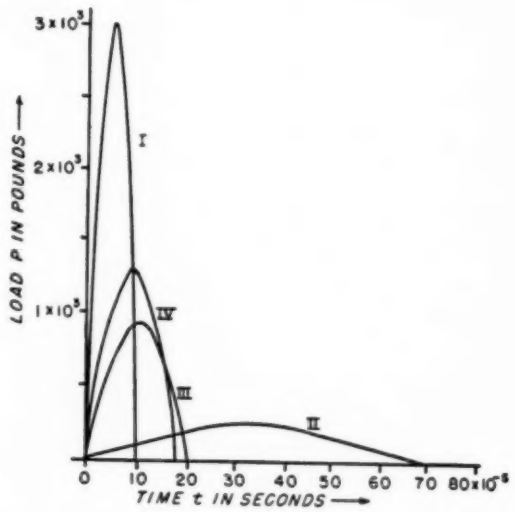

FIG. 1. Load-time curves for impact of plastic object on steel surface.

[12] W. E. Milne, *Numerical Calculus* (Princeton University Press, Princeton, 1949), p. 140.

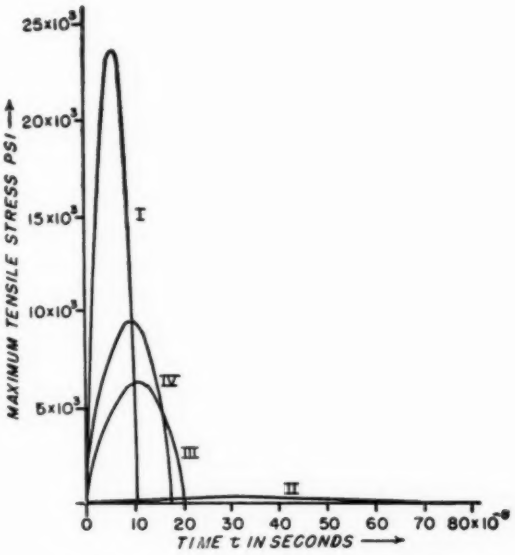

FIG. 2. Stress-time curves for impact of plastic object on steel surface.

of the plastic object. The duration of impact is longer in the case of a less rigid material.

Comparison of the cases 3 and 4 shows that, even though two materials may have the same static modulus, the forces and stresses developed in impact may be different depending on the distribution of their relaxation times.

SUMMARY OF RESULTS

(1) The Hertz theory for contact stresses and deformations has been extended to apply to the viscoelastic case.

(2) The extended theory has been applied to the forces and stresses developed in plastic objects in impact.

(3) Numerical calculations were carried out for the case of plastic objects dropped onto a plane steel surface from a height of 4 ft.

(4) The results show that very high stresses can be obtained in impacts even when the impact velocity is quite low. The rates of loading can also be very high. The total duration of impact is of the order of 10^{-5} to 10^{-3} sec.

(5) Materials which are similar when judged by their static moduli may behave differently in impact if their viscoelastic functions are not the same.

(6) Relations derived in this paper can be applied to static cases e.g., contact between gear teeth as well as to impact conditions.

APPENDIX I. NOMENCLATURE

x_i $i=1, 2, 3$	rectangular coordinates
ii or jj	repeated subscript indicates summation as i or j takes on the values of 1, 2, 3
$,i$ or $,j$	comma indicates differentiation with respect to x_i or x_j, respectively
$\delta_{ij}=1,\ i=j$ $=0,\ i\neq j$	Kronecker delta
τ_{ij}	stresses
e_{ij}	strains
e_{ii}	dilatational strains
$e_{ij}-\frac{1}{3}\delta_{ij}e_{ii}$	deviational strains
σ_{ij}	deviational stresses
u_i	displacements
F_i	body forces
λ, μ	Lames's constants (μ also referred to as rigidity)
$k=\lambda+\frac{2}{3}\mu$	modulus of compression or bulk modulus
τ_i (with single subscript or no subscript)	relaxation or retardation time of viscoelasticity
$\bar{\psi}$	relaxation function of viscoelasticity
$\langle\dot{\psi}\rangle$	rate of relaxation; dot denotes differentiation with respect to time
$\beta\psi$	creep function of viscoelasticity; β is normalizing factor
$\beta\dot{\psi}$	rate of creep
m	mass of the moving body involved in the impact
α	"approach" or the distance by which the centers of mass of the two colliding bodies approach each other after contact has been made
$\dot{\alpha}_0$	initial relative velocity of the two bodies force developed between the two colliding bodies while in contact
C	parameter incorporating the geometry of the two surfaces which come into contact

APPENDIX II

This problem has also been solved by the direct method. The displacement in the z-direction of a point $(x,y,0)$ within the compressed area is given by the elastic solution as

$$w=\alpha-Ax^2-By^2=\tfrac{3}{4}\theta P\int_0^\infty \times\{1-x^2/(a^2+\zeta)-y^2/(b^2+\zeta)\}d\zeta/\{(a^2+\zeta)(b^2+\zeta)\zeta\}^{\frac{1}{2}}, \quad \text{(A-1)}$$

where the total force P is distributed in such a manner that the unit pressure is given by

$$P'=\frac{3P}{2\pi ab}\{1-x^2/a^2-y^2/b^2\}^{\frac{1}{2}}. \quad \text{(A-2)}$$

In Eq. (A-1), A and B are constants. For the visco-

elastic case, at any time ξ the force is of value $P(\xi)$, and the dimensions of the semiaxes are a and b. The displacement is therefore given as

$$w=\alpha-Ax^2-By^2=\tfrac{3}{4}\theta P\int_0^\infty \times\{1-x^2/(a^2+\zeta)-y^2/(b^2+\zeta)\}d\zeta/\{(a^2+\zeta)(b^2+\zeta)\zeta\}^{\frac{1}{2}} +\tfrac{3}{4}\theta\int_0^t \psi(t-\xi)P(\xi)d\xi\int_0^\infty \times\{1-x^2/(a^2+\zeta)-y^2/(b^2+\zeta)\}d\zeta/\{(a^2+\zeta)(b^2+\zeta)\zeta\}^{\frac{1}{2}}. \quad \text{(A-3)}$$

Expression (A-3) is equivalent to three equations from which Eq. (26) can be obtained. Expressions for the semiaxes may also be obtained.

The solution so obtained would be exact except for the fact that in the time-dependent part of the solution, all points are treated as interior points. The effect of this is to make the dimensions a and b somewhat larger than they should be.

Actually this problem has three aspects which might have led one to believe that the Laplace transform method would not be strictly applicable. These are the following:

(1) Although the differential equations are linear, the boundary conditions make the relation between the total force P and the approach α nonlinear.

(2) Both the magnitude and area of distribution of P change with time.

(3) The solution for the displacement at a point $(x,y,0)$ is different depending on whether the point is an exterior or interior point.

It turns out that only item (3) prevents the Laplace transform method from being exactly applicable. The nature of the approximation is to make the dimensions of the compressed area somewhat larger than they should be. The upper limits for the magnitude of these dimensions are those values for which the points $(x,y,0)$ in question would be interior points.

JOURNAL OF APPLIED PHYSICS VOLUME 26, NUMBER 9 SEPTEMBER, 1955

Friction of Teflon Sliding on Teflon

D. G. Flom and N. T. Porile*
General Electric Company, Schenectady, New York
(Received March 2, 1955)

The low coefficient of friction for Teflon sliding on Teflon, as observed previously by others, has been found in this study to hold only if low sliding speeds and newly prepared surfaces are used. At high sliding speed, the nature of the surface is irreversibly changed such that subsequent sliding at low speed reveals a two- to threefold increase in the friction coefficient.

In addition to the effect of high speed sliding, there are reversible changes in the friction of Teflon on Teflon dependent in part on temperature. As the temperature of Teflon is increased from below room temperature, a sharp and pronounced increase in the coefficient of friction is observed in the vicinity of 20°C. The existence of a phase transition in Teflon at this temperature indicates a close correlation between the frictional and the structural properties of this material.

I. INTRODUCTION

THE importance of surface conditions in solid friction is strikingly illustrated by the case of Teflon (polytetrafluoroethylene) sliding on Teflon where we have found rather unexpected effects dependent upon the previous sliding history of the material. In previous investigations in other laboratories, the coefficient of friction for this system has been found to be low, ranging from 0.04 to 0.1.[1–4] In those studies, measurements were made either of the static coefficient of friction μ_s or the kinetic coefficient μ_k at sliding speeds of the order of 0.01 cm/sec.† New or "freshly prepared" surfaces (not subjected to previous sliding) were used. In this laboratory we have found, in addition, that the low coefficient of friction for Teflon on Teflon holds only at low sliding speeds and then only if the surfaces have not undergone previous sliding at high speeds. These results, of which we have already given a preliminary description,[5] demonstrate frictional limitations of Teflon which had not been previously described. The results also demonstrate the advantage of including, in frictional studies, measurements on surfaces which have been modified by sliding.

* Department of Chemistry, University of Chicago, Chicago, Illinois.

[1] K. V. Shooter and P. H. Thomas, Research **2**, 533 (1949).

[2] K. V. Shooter and D. Tabor, Proc. Phys. Soc. (London) **B65**, 661 (1952).

[3] Bowers, Clinton, and Zisman, NRL Report 4167 (1953).

[4] R. F. King and D. Tabor, Proc. Phys. Soc. (London) **B66**, 728 (1953).

† Shooter and Thomas found no appreciable effect on the friction when the speed was increased to 1.0 cm/sec.[1]

[5] D. G. Flom and N. T. Porile, Nature **175**, 682 (1955).

Although the effect of repetitive sliding on the coefficient of friction for Teflon on Teflon seems not to have been reported before, a related observation by Bowers, Clinton, and Zisman should be noted.[3] In their work it was found that for steel rubbing on Teflon, both μ_s and μ_k increased slightly after 30 passes, the steel rider being cleaned after each pass. After 100 passes μ_s and μ_k, both initially equal to 0.04, had increased to 0.13 and 0.08, respectively. These results, further substantiated by our own, indicate that an irreversible change takes place.

In addition to the foregoing *irreversible* change in the coefficient of friction for Teflon on Teflon produced by high-speed sliding, we have found other *reversible* changes dependent in part on temperature. The temperature effect shows up as a twofold increase in the coefficient of friction and takes place in the vicinity of 20°C where a phase transition in Teflon is known to occur.

II. PHASE TRANSITION AND TEMPERATURE EFFECTS

One might expect the friction of Teflon to parallel in some way its structural properties. For example, the existence of a phase transition in Teflon would lead one to expect a change in frictional properties accompanying the transition.

That a phase transition in Teflon *does* exist was first reported by Rigby and Bunn in 1949.[6] This transition, appearing at room temperature, is one in which the polymer changes from a relatively "crystalline" phase to a "waxy" phase as the temperature is raised.‡ The existence of the transition has been further substantiated by Quinn, Roberts, and Work, who measured the change in volume of a rod of Teflon as a function of temperature.[7] Furukawa, McCoskey, and King investigated the heat capacity of Teflon and their work confirmed the existence of two first order transitions, the more pronounced one occurring at 293°K.[8]

The most complete work on the room temperature phase transition of Teflon was carried out by Weir who measured the compression $(-\Delta V/V_0)$ of Teflon as a function of pressure at a series of temperatures.[9] He reported the transition at 20°C as being a "reversible first-order transition producing reversible changes in the x-ray diffraction pattern."

More recently, the transition in Teflon and its accompanying change in the x-ray diffraction pattern have been studied by Bunn and Howells.[10]

The possibility of a correlation between a change in phase and a change in frictional properties for Teflon has not been pointed out by other workers although in several studies the effect of temperature on the friction of Teflon has been determined, usually above room temperature. Shooter and Thomas found the coefficient of friction for Teflon on Teflon to be 0.04 at temperatures ranging from 20° to 200°C.[1] Bowers, Clinton, and Zisman reported no change in μ_s or μ_k in the temperature range of 25° to 121°C.[3]

To the best of our knowledge, only one study has been made previously in which a temperature range extending below room temperature has been used. This was the work of King and Tabor in which the coefficient of friction was measured from −80°C to +100°C using a special glass apparatus inserted in a Dewar flask.[4] The only change in μ which they found was an increase from 0.1 to 0.2 as the temperature was lowered through −50°C. In that work fresh surfaces were used. As noted in the Introduction, such surfaces could give low values for μ which would not necessarily agree with values obtained on "worn" surfaces.

One of the purposes of the present investigation was to determine whether or not a change in the coefficient of friction for Teflon sliding on Teflon takes place at a temperature corresponding to that of the known room temperature phase transition. In order to avoid ambiguous results it was necessary to separate the effects due to conditioning of the surface and those due to temperature. A "worn" track (as well as a worn rider) was therefore used in the subsequent experiments.

III. APPARATUS AND MATERIALS

A. Apparatus

The friction apparatus has been described previously.[11] Briefly, it consists of a rider under controlled force bearing against a magnetically driven rotating cylinder. The rider, sliding freely in a bushing held in a phosphor bronze holder, moves tangentially due to frictional force during rotation of the cylinder. This force is measured by means of wire resistance strain gauges attached to a flexible section of the holder. The output of the strain gauge bridge circuit is applied to a G-E photoelectric recorder, thus producing a continuous and permanent record of the frictional behavior.

A stainless steel bell jar enclosing the main part of the apparatus enabled the experiments to be carried out in an atmosphere of dry air. A continuous flow of air was passed through two towers of sulfuric acid and then through the enclosure.

B. Materials

The Teflon specimens were prepared from fully sintered extruded rods made by the Ethylene Chemical

[6] H. A. Rigby and C. W. Bunn, Nature **164**, 583 (1949).

‡ The phase transition in Teflon was first brought to the attention of one of the authors (DGF) by Dr. J. D. Hoffman now at the National Bureau of Standards.

[7] Quinn, Roberts, and Work, J. Appl. Phys. **22**, 1085 (1951).

[8] Furukawa, McCoskey, and King, J. Research Natl. Bur. Standards **49**, 273 (1952).

[9] C. E. Weir, J. Research Natl. Bur. Standards **50**, 95 (1953).

[10] C. W. Bunn and E. R. Howells, Nature **174**, 549 (1954).

[11] D. G. Flom, Rev. Sci. Instr. **26**, 1 (1955).

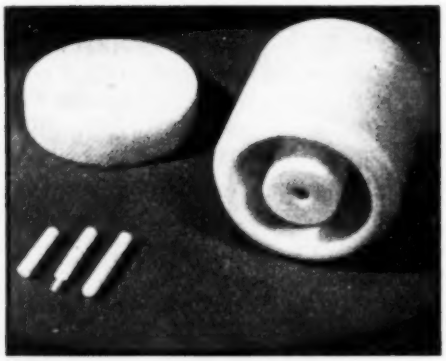

FIG. 1. Teflon cylinder (with cap) and Teflon riders.

Corporation. The riders were rods 150 mils in diameter ½ to 1 inch in length (Fig. 1). Plain cylindrical rods were used although it was found that similar results could be obtained with the hemispherically ended rods. The Teflon cylinder employed in most of this work was a two inch diameter cylinder partially hollowed out and fitted with a screw cap at the open end. This arrangement enabled the cylinder to be filled with dry ice for the runs below room temperature. The riders and cylinders were machined on the lathe with the occasional use of water as a cutting fluid.

Different methods of cleaning the Teflon specimens were tried including the use of detergents, benzene, *n*-hexane, and acetone. No difference was noted in the frictional properties of the variously treated surfaces and acetone was adopted.

IV. EXPERIMENTAL PROCEDURE AND RESULTS

As an indication of the type of deformation occurring at the contact interface the relationship between normal load and frictional force was determined, the load being varied by the addition of known weights to the push-rod assembly. As shown in Fig. 2, the coefficient of friction was independent of load in accordance with Amonton's law at both high and low speeds throughout a range of 20 to 210 grams. The increase in coefficient of friction below a load of 1 gram as reported by Shooter and Tabor was not checked.[2] A constant normal load of 108 grams was used in the rest of the experiments.

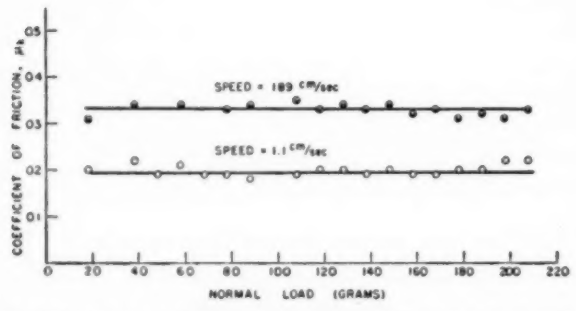

FIG. 2. Variation of friction with load for Teflon sliding on Teflon. Surfaces "worn in" by sliding at high speed.

A. Effect of High-Speed Sliding

During the initial experiments in which the effect of load was determined, it was found that if clean, newly prepared surfaces were used at low sliding speeds (1.1 cm/sec or less) the coefficient of friction was very low (0.05 to 0.08), in agreement with previous work in other laboratories. Furthermore, if the same low speed of sliding was maintained, μ_k remained low for at least 4100 traversals over the same track.

On increasing the sliding speed, the friction also increased; as will be discussed presently, it became necessary to study the relation between speed and friction in greater detail. At a speed of 189 cm/sec the coefficient of friction was found to be in the range of 0.32 to 0.36. The important observation was then made that if the coefficient of friction was measured at low speed following the high-speed sliding (allowing sufficient time for thorough cooling), the original low speed value for μ_k was no longer obtained. The increase was substantial, in the order of two- to threefold, and was irreversible in the sense that only by refinishing the surfaces with a sharp tool could the original low friction be restored.

TABLE I. Effect on high-speed sliding on the friction of Teflon on Teflon.

Sliding speed (cm/sec)	Coefficient of friction, μ_k	
	Fresh track	Tracks worn in by sliding at 189 cm/sec
1.1	0.07	0.19
8.0	0.13	0.22
189	...	0.32

A typical set of data demonstrating the effect is presented in Table I.

The types of friction curves obtained before and after high speed sliding are shown in Figs. 3 and 4, respectively, the average coefficient in Fig. 3 being slightly higher than is usually obtained on a clean, newly machined surface. These experiments clearly demonstrate an irreversible change in coefficient of friction with sliding.

However, the mechanism underlying the change in friction is not clear. It is probable that at the contact there is some localized heating and/or viscous flow of noncrystalline polymer. Surface degradation of the polymer might then take place. Apart from this, however, there is the possibility that orientation of the polymer at the rubbing surface with prolonged sliding may be important. Teflon films have been shown by Hanford and Joyce to be highly oriented during experiments in which thin sections of the polymer have been cold drawn as much as 400%.[12] A similar orientation as a consequence of sliding could presumably

[12] W. E. Hanford and R. M. Joyce, J. Am. Chem. Soc. **68**, 2082 (1946).

alter the strength properties of Teflon in addition to modifying its surface energy.

Measurements of friction between Teflon and metallic surfaces have not been made in this study but one would expect an irreversible increase in μ_k, if present in such a system, to be less pronounced.

B. Effect of Temperature

In the work designed to test the effect of temperature on the friction of Teflon, a dry air atmosphere was used in order that condensation on the cylinder would not occur below room temperature.§ The procedure used was as follows: The partially hollowed-out cylinder was filled with dry ice and the screw cap was put on. The cylinder was next placed on the shaft of the apparatus and the whole was enclosed with the bell jar through which dry air was then passed, gaseous CO_2 being removed as the dry ice sublimed. By carrying out these operations quickly, condensation was avoided. The measurement of the temperature of the cylinder was then made, followed by setting the cylinder in rotation at a predetermined speed, lowering the rider

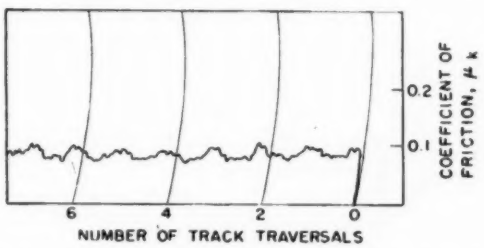

FIG. 3. Friction of Teflon sliding on Teflon at 1.1 cm/sec. Surfaces newly machined.

on to the cylinder, and measuring the frictional force. The rider was then lifted off the cylinder, rotation of the cylinder stopped, and the procedure repeated at successively higher temperatures as the cylinder warmed up.

For the measurements above room temperature a heater consisting of a glass tube wound with Nichrome wire was positioned to enclose the cylinder.

The temperature of the cylinder was measured in two ways, both of which can be considered to yield only approximate results. In one method a 50-mil copper-copnic thermocouple was held against the surface by means of a flexible holder so that the end of the thermocouple was pressed firmly against the surface. In the other method a thermocouple consisting of copnic wire within a 20-mil copper sheath was imbedded in a small hole in the cap of the cylinder. This thermocouple fitted loosely in the hole but was pressed against the cylinder so that it would remain in place while the

§ Preliminary measurements at room temperature over a wide range of speeds revealed that the friction of Teflon in an atmosphere of dry nitrogen was the same as in dry air.

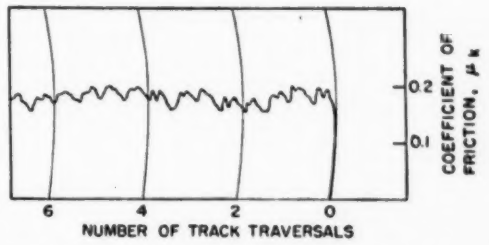

FIG. 4. Friction of Teflon sliding on Teflon at 1.1 cm/sec. Surfaces "worn in" by sliding at high speed.

cylinder was rotating. Each of these methods of temperature measurement gave the same result.

The temperature of the rider was also measured by imbedding a small thermocouple in a hole in the rider about $\frac{1}{16}$ in. from the rubbing surface. At the lower temperatures of the cylinder the temperature of the rider was approximately $3\frac{1}{2}°$ above that of the cylinder.

The results (Fig. 5) clearly indicate a change in coefficient of friction at a temperature of 15.5 to 17.5°C for the low speed and at a temperature of 16.4 to 19.0°C for the high speed. As mentioned previously, the bulk temperature of the rider was perhaps $3\frac{1}{2}°$ higher than that of the cylinder. In view of this, it can be concluded that the inflection in the friction curve in Fig. 5 is almost certainly a consequence of the room temperature transition. Both above and below the temperature of the inflection the coefficient of friction μ_k was found to be essentially independent of temperature.

C. Effect of Sliding Speed

In addition to the *irreversible* effect of previous sliding speed on the coefficient of friction for Teflon on Teflon, as already described, a *reversible* dependency of the friction on sliding speed was also found. This is graphically depicted in Fig. 6 at two different temperatures, one below and one above the room temperature transition point. That this speed dependence was at least partially due to a heating effect was indicated by the fact that following a high-speed run there would be a time lag of two to three minutes before the usual reversible low-speed friction could be obtained.

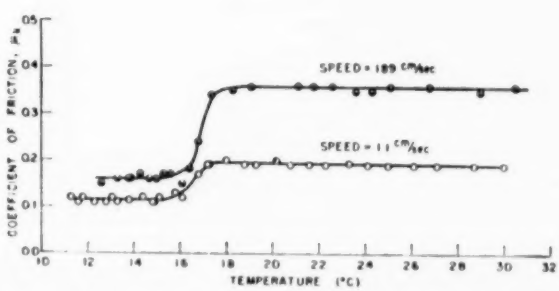

FIG. 5. Friction of Teflon sliding on Teflon as a function of temperature. Surfaces "worn in" by sliding at high speed.

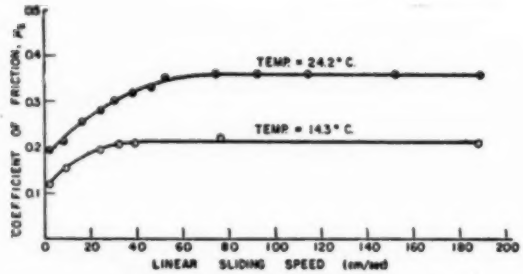

FIG. 6. Dependence of friction on speed for Teflon sliding on Teflon. Surfaces "worn in" by sliding at high speed.

D. Wear

The volume wear of a Teflon rider sliding on a Teflon cylinder in air at room temperature was measured using riders of different geometry such as the ones pictured in Fig. 1. The magnitude of wear was found to be independent of rider geometry and independent of sliding speed at the two speeds used (95 and 189 cm/sec). The wear was dependent on distance of sliding, however, the approximate constant wear being 4×10^{-11} cc per cm linear travel at a constant normal load of 108 grams. Although no wear measurements were made at very low sliding speeds, there were indications that under these conditions the rate of wear might well be a function of sliding speed.

V. CONCLUSION

Our study of the friction of Teflon sliding on Teflon has revealed two new and important facts concerning this polymer: (1) The coefficient of friction μ_k is low (0.05 to 0.08), in agreement with previous work in other laboratories, providing that low speeds and a fresh track are used. On surfaces worn in by high speed sliding, however, the coefficient of friction is permanently higher (two- to threefold) even at low speed. (2) With increasing temperature of one of the specimens, the coefficient of friction for Teflon on Teflon undergoes a marked increase in the range of 16 to 18°C. This behavior may be directly correlated with the phase transition in Teflon which occurs at 20°C.

In addition to the above facts, it has been found that the friction of Teflon increases with increasing sliding speed and attains a steady-state value at a speed within the range of 40 to 70 cm/sec depending upon the temperatures of the rubbing specimens.

Wear measurements of Teflon sliding on Teflon have shown the wear to be dependent on distance of sliding but independent of rider geometry and of sliding speed at speeds of 90 and 189 cm/sec.

VI. ACKNOWLEDGMENTS

The authors wish to acknowledge helpful discussions during the course of this work with Dr. J. D. Hoffman and Mr. R. H. Savage.

JOURNAL OF APPLIED PHYSICS VOLUME 26, NUMBER 9 SEPTEMBER, 1955

Glass Transitions in Polymer-Plasticizer Systems

L. BREITMAN
Research and Development Division, Polymer Corporation Ltd., Sarnia, Ontario, Canada
(Received May 2, 1955)

Glass temperatures (T_g) of pure and plasticized elastomers have been obtained from dilatometric measurements and from the temperature dependence of angular response to torsional stress. The depression of T_g by a diluent, determined by either method, is a convenient measure of its plasticizing ability. Some compounds which are normally crystalline above T_g of the pure polymer, but nevertheless compatible with the polymer, depressed the glass temperature. The polymer-diluent compatibility at low temperatures results either from supercooling, the depression of the melting point of diluent by polymer, or possibly a combination of both phenomena. T_g decreased as the diluent loading increased to a more or less well defined limit, beyond which further dilution had negligible effect. For diester type plasticizers both $\Delta T_{g\max}$ and the limiting diluent concentration were linear functions of compatibility, as defined by the extent to which standard polymer vulcanizates were swollen by plasticizer. The viscosities and apparent activation energies for flow (E_v) of hydrocarbon oils correlated with their low temperature plasticizing efficiencies. Pour points and glass temperatures may also be significant properties of the diluents. It is concluded that low E_v and high solvency for polymer are desirable properties for low temperature plasticizers.

AN elastomer, on cooling, is transformed within a fairly narrow temperature range from a relatively elastic, readily processed material to a hard, brittle glass-like mass. The "glass transition" region of a polymeric system serves to define a temperature below which rubber-like properties cannot exist. Transition phenomena in polymers are discussed by R. Boyer[1] in a review with an extensive bibliography to 1952.

[1] R. Boyer, Changements de Phases, Societé de Chimie Physique, deuxième Réunion Annuelle tenue en Commun avec la Commission de Thermodynamique de l'Union Internationale de Physique, Paris (June 2–7, 1952).

In this study it was desired to ascertain, in broad outline, the properties of a diluent which promote flexibility in elastomeric blends by postponing the glass transition to lower temperatures.

EXPERIMENTAL

Of the properties which may be measured to determine a glass temperature, relative volume was selected for its simplicity and convenience. The dilatometer designed by Bekkedahl and Wood[2] was used for pure polymers and their blends with diluents. A glass bead at the neck of the bulb prevented clogging of the capillary by polymer and a glass plug served to avoid degradation of the polymer and ignition of diluent when the bulb was sealed off. A silicone oil (G.E. silicone oil 9981-LTNV-20) was chosen as confining fluid because of its low swelling power and its linear V-T relation to at least -100°C. With but two exceptions noted elsewhere in this paper the miscibilities of the silicone oil with the diluents were so low as to preclude appreciable extraction of the latter from blends with polymer.

Table I. Ester plasticizers in GR-S.

Diluent	Vol. increase on swelling of vulcanizate %	Max ΔT_g °C	$(\delta_{GR\text{-}S}-\delta_{dil})^{2}$ [a,b]
Methyl phthalyl ethyl glycollate[c]	1.5	2	3.8
Dicarbitol phthalate[d]	1.6	2.5	4.5
Tributoxy ethyl phosphate[d]	17.7	16	0.1
Dibutyl phthalate[e]	33.1	24	0.7
Dioctyl adipate[d]	50.0	37	0.0
Dioctyl sebacate[f]	51.7	38	0.0
Dibutyl sebacate[f]	55.2	9	0.0

[a] $\delta_{GR\text{-}S}$ taken as 8.6.
[b] δ_{dil} (diluent) calculated from molar attraction constants [P. A. Small, J. Appl. Chem. 3, 71 (1953)].
[c] Monsanto Chemical Company.
[d] Ohio Apex, Inc.
[e] Carbide and Carbon Chemical Company.
[f] Resinous Products and Chemicals Company.

Filling of the dilatometer with the silicone oil was accomplished by small increments under vacuum, except when the diluent was too volatile. With care, most air pockets could be eliminated by alternate cooling and gentle warming. The presence of some air was tolerable; it was unnecessary to calculate specific volumes as the determination of a glass temperature could be made from direct dilatomer readings. A U-type dilatometer was used for measurements on liquids less dense than the confining fluid. Temperature control was achieved by immersing the dilatometer in a well stirred Dewar flask containing methanol, cooled by the addition of dry ice or liquid nitrogen as required. Temperatures were determined with a platinum resistance thermometer in a bridge circuit with a sensitive galvanometer as detector. The height of the liquid level could be estimated to within 0.2 mm on a scale fixed to the capillary of the dilatometer. Unless otherwise specified, ten to fifteen minutes were allowed to elapse at each temperature before a volume reading was made. The precision of the T_g determinations is estimated as ± 1°C.

Several measurements of low temperature flexibility were also made using a modified Gehman[3] test. A vulcanized polymer containing the plasticizer and 50 parts Philblack 0 per hundred of blend was subjected to torsional stress by means of a suspended wire clamped to its end; the angular response was measured after ten seconds.

The source and purity of the diluents are recorded in Tables I, II, III, and IV. These materials were used as received. Blends were prepared by the addition of diluent to polymer on a cold mill to facilitate rapid dispersion. Mixtures containing in excess of 15 parts of diluent with a melting point higher than 130°C. (Tables II, III,

Table II. High-melting compounds in butyl.

Diluent	Melt. point °C	Loading wt diluent per hundred polymer	Glass temperature °C
...	...	nil	−74.0
Adipic acid[a]	151	10	−75.8
Sebacic acid[b]	153	50	−72.0
Succinic acid[c]	185	30	−73.0
n-octadecanol[c]	59	20	−74.5
n-decanol[c]	−6	30	−73.0
Ethylene glycol[d]	−17	10	−75.5
Mannitol[a]	166	30	−72.0
Stearic acid[c]	69.4	10	−73.3
Capric acid[a]	31.5	10	−73.0
		50	−72.0
Dibutyl sebacate	−20	14	−73.5
		39	−74.0
n-octanol[c]	−16	10	−77.5
		30	−79.5
Valeric acid[d]	−34.5	10	−78.0
		30	−84.0

[a] Reagent grade, Matheson Company, Inc.
[b] Practical grade, Matheson Company, Inc.
[c] Reagent grade, Eastman Kodak Company.
[d] "Purified," Central Scientific Company, Toronto.
[e] National Bureau of Standards.

Table III. High-melting compounds in nitrile.

Diluent	Melt. point °C	Loading wt diluent per hundred polymer	Glass temperature °C
...	...	nil	−32.5
Sebacic acid	133	5	−33
Succinic acid	185	30	−29.3
Mannitol	166	30	−32.5
Stearic acid	69	10	−32.5
n-octadecane	27	5	−28.5
Valeric acid	−34.5	10	−41.3
		30	−52.5
Hexachloro-butadiene[a]	−22	42	−41

[a] Hooker Electrochemical Company.

[2] N. Bekkedahl and L. A. Wood, Ind. Eng. Chem. 33, 381 (1941).

[3] Gehman, Woodford, and Wilkinson, Jr., Ind. Eng. Chem. 39, 1108 (1947).

TABLE IV. High-melting compounds in GR-S.

Diluent	Melt. point °C	Loading wt diluent per hundred polymer	Glass temperature °C
...	...	nil	−62.5
Adipic acid	151–3	15	−61.0
Succinic acid	133	5	−61.0
n-octadecanol	59	50	−61.5
n-octanol	−16.3	30	−62.5
Ethylene glycol	−12	10	−60.0
Mannitol	166	30	−63.5
Stearic acid	69.4	30	−60.0
Capric acid	31.5	30	−62.5
Valeric acid	−34.5	30	−75.5
		10	−67.5

and IV) were generally not homogeneous. After some time separation of solid was evident at about 25°C. The remaining blends appeared to be true solutions at room temperature. The polymers were Polymer Corporation Limited production samples. GR-S was a high molecular weight butadiene-styrene copolymer obtained at 72% conversion from a 72/28 butadiene/styrene charge ratio at 5°C. The composition of the nitrile and butyl rubbers were 68/32 butadiene/acrylonitrile and 98/2 isobutylene/isoprene, respectively. All dilatometric glass temperatures reported here refer to unfilled, uncured polymers and blends.

RESULTS AND DISCUSSION

For our purposes the diluents can be conveniently classed as diester plasticizers, crystalline solids, and hydrocarbon oils.

1. Ester Plasticizers

Figure 1 presents experiments volume-temperature data for a typical compatible system, dioctyl phthalate-GR-S. The curves consist of the usual two linear segments intersecting at T_g. Larger scale plots sometimes revealed a curved transition region; the extrapolations to a point of intersection then gave the characteristic temperature.

The effect of plasticizer concentration in two typical GR-S compatible systems is illustrated by Fig. 2. The lower curve for dibutyl phthalate shows the limiting or "saturation" effect of high plasticizer concentrations. This behavior was apparent in every system investigated at sufficiently high diluent loadings. The saturation effect in dioctyl phthalate-GR-S blends would presumably be evident at higher plasticizer concentrations. The deviation of the glass temperatures at zero plasticizer concentration is probably a reflection of differences in nonpolymer content, mostly soap, between two production samples of the copolymer.

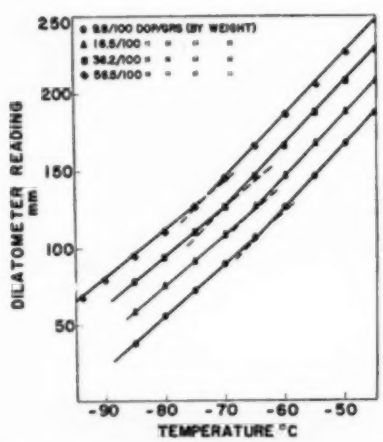

FIG. 1. Dioctyl phthalate in GR-S.

Additional data for a series of ester blends, including certain literature values,[4] were analyzed. The properties of interest for each system were: the maximum depression of the glass temperature, the concentration of diluent at which a saturation effect is evident, and the compatibility of the two components. The data in Table I illustrate the relationship between compatibility and the maximum effect on the glass temperature. The second column gives the maximum experimental volume increase of a standard vulcanizate swollen at 55°C in an excess of each ester. According to the Flory-Rehner theory[5] of swelling of polymer networks the magnitude of the volume increase for a fixed degree of cross linking—assured by the use of a standard vulcanizate—is a measure of solvent-polymer interaction. Specifically, the interaction parameter is related to the heat of solution which, at least in the simplest cases, is proportional to the square of the difference between the so-called solubility parameters, δ, for the polymer and the swelling agent. The best solvent is one for which this difference is least. The parameters of the esters were calculated from their structures and the scheme of molar attraction constants proposed by Small.[6] It is observed from the data in Table I that there is rough agreement between experimental and theoretical estimates of compatibility on the one hand, and between $\Delta T_{g\max}$ and compatibility on the other. Dibutyl sebacate does not fit the pattern

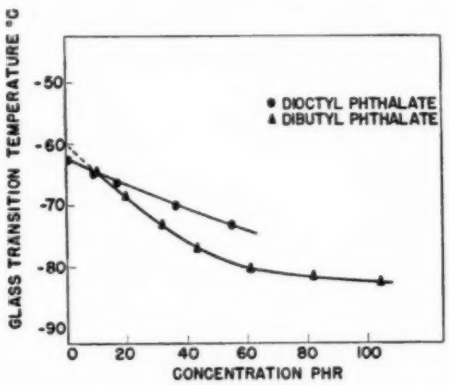

FIG. 2. Typical GR-S compatible systems.

[4] D. A. Henderson and L. A. McLeod, Trans. Inst. Rubber Ind. **30**, 115 (1954).
[5] P. J. Flory and J. Rehner, Jr., J. Chem. Phys. **11**, 512 (1943).
[6] P. A. Small, J. Appl. Chem. **3**, 71 (1953).

established by the other esters and will be considered in another section of this paper.

The curves of Fig. 3 show a linear relationship between the maximum depression of the glass temperature of uncured polymers and (1) volume increase on swelling of the corresponding vulcanizate and (2) the ester concentration beyond which T_g is not appreciably changed. It appears, therefore, that the saturation effect at high ester loadings is closely related to the compatibility of the components of the blend. Whether actual phase separation of excess diluent, or "sweating out," occurs at the saturation concentration is not known. The glassy state (i.e., at or below T_g) may be considered[7] as one in which the rate of relative motion of the kinetic units has fallen to a value of the same order of magnitude as the experimental time-scale. In a pure polymer the segmental jump rate and its temperature dependence are determined by structural details, intermolecular, and intramolecular forces which

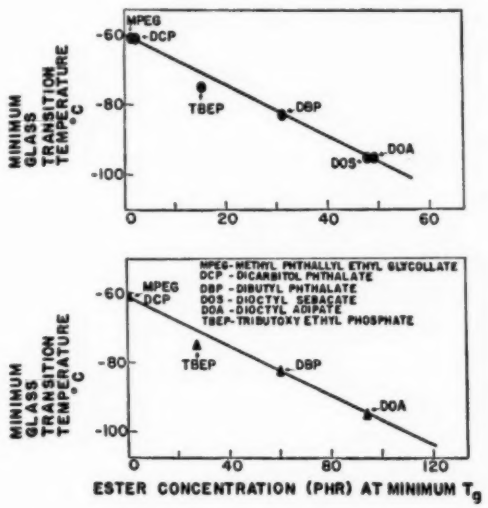

FIG. 3. Effect of ester plasticizers on GR-S.

govern local frictional resistance. The effect of plasticizer is to replace polymer segment—segment contacts by plasticizer—segment associations to an extent dictated by the plasticizer concentration and its solvating ability. If phase separation does not occur, saturation presumably corresponds to the plasicizer concentration beyond which local frictional resistance to segmental mobility is not materially diminished. Jenckel[8] has determined glass temperature by refractive index measurements on several polystyrene-plasticizer blends over very wide concentration ranges. His results indicate that if the plasticizer has sufficient solvent ability to ensure complete miscibility in all proportions with polymer, and if the plasticizer itself undergoes a glass transition, then T_g for the blends can vary continuously between the glass temperatures of the pure

[7] See, for example, F. Bueche, J. Chem. Phys. **20**, 1959 (1952).
[8] E. Jenckel, Kunststoffe **45**, 3 (1955).

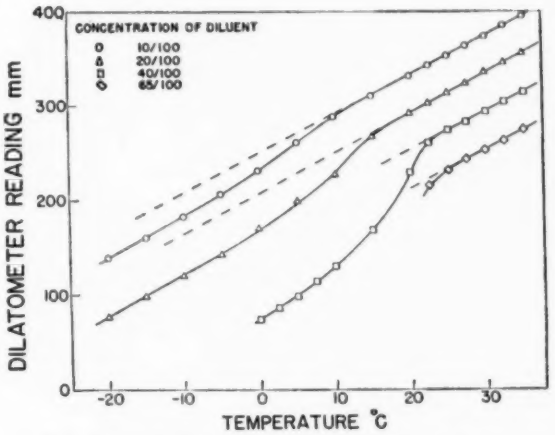

FIG. 4. Crystallization of octadecane in GR-S.

components. In such systems the glass temperature of the pure diluent appears to be the significant property.

2. Crystalline Solids

Volume-temperature measurements were made on blends of GR-S, nitrile, and butyl rubbers with a variety of compounds including carboxylic acids, alcohols, and hydrocarbons. Typical results are shown in Tables II, III, and IV. With the exceptions of dibutyl sebacate, valeric acid, and hexachlorobutadiene the diluents were high melting solids which crystallized readily and effected virtually no depression of the glass temperature in blends. Evidence for crystallization in octadecane-GR-S blends is provided by the nature of the volume-temperature curves of Fig. 4. Similar curves were obtained for butyl diluted with varying amounts of dibutyl sebacate. The glass transition temperatures of these blends are the same as for pure polymer, completely independent of the diluent concentration (see Fig. 5). Failure to depress the glass temperature is attributed to the crystallization of the diluent: at sufficiently low temperatures, though still above T_g,

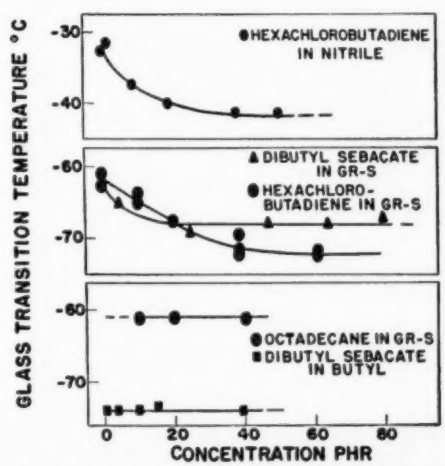

FIG. 5. Effect of crystallizing diluents in polymers.

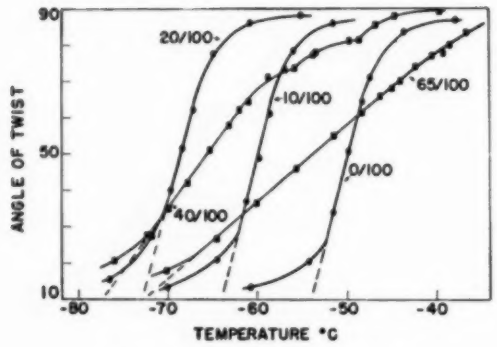

FIG. 6. Dibutyl sebacate in GR-S.

the blends are two-phase systems composed of essentially pure polymer and pure crystalline diluent. Even a fairly high melting diluent, however, may exhibit low temperature plasticizing ability if it is prone to supercool.

The plasticizing ability for GR-S of bidutyl sebacate, which crystallizes readily from its blends with polymers[4,9] is on the other hand attributed to the depression of the freezing point by polymer. This effect is qualitatively evident in Fig. 4: the higher the polymer concentration the lower the initial crystallization temperature. The system polymer-diluent is complete analogous to binary solutions of small molecules and can be treated by the thermodynamics appropriate to polymer solutions.[10] It can be shown[11] that

$$\Delta\bar{F}_1=0\simeq RT[\ln(1-v_2)+v_2+\chi v_2^2+\Delta H_f\cdot\Delta T/T_f RT] \tag{1}$$

relates the freezing point depression, $\Delta T=T_f-T$, of crystalline diluent to the volume fraction, v_2, of amorphous polymer in solution with the liquid diluent. ΔH_f is the heat of fusion of the solid at its normal (absolute) freezing temperature T_f, χ is the interaction parameter for the polymer-liquid pair, and $\Delta\bar{F}_1$ is the partial molar free energy of transfer of liquid diluent from the solution of composition v_2 to the crystalline solid at the temperature T.

This equation has been applied with quantitative success to the system azobenzene-natural rubber. There is excellent agreement between the composition dependence of the freezing point calculated from Eq. (1) and that reported in the literature.[12]

The low temperature plasticizing ability of some normally solid diluents can now be explained. It is necessary that sufficient diluent, as predicted by Eq. (1), be in the liquid state below the glass transition temperature of pure polymer. This condition is apparently fulfilled by the polymer-diluent pairs shown in the upper curves of Fig. 5 but not by the other two blends. The leveling off of the T_g *vs* diluent concentration curves is attained at a temperature below which, regardless of the amount of diluent added, separation of excess solid leaves insufficient liquid to further depress T_g.

Results which may be similarly interpreted have been obtained from Gehman tests on blends of GR-S with varying amounts of dibutyl sebacate. In Fig. 6 it is seen that ten and twenty parts of the ester per hundred polymer shift the sigmoidal curves and the extrapolated freeze points by about ten and twenty degrees, respectively. At higher loadings there is no improvement in low temperature properties. Furthermore, the sigmoidal curves have become distorted in a manner characteristic of crystallizing systems. The arcs on one of these curves (4.0/100) reflect the time-dependence of the crystallization. A smoother plot was obtained for the sample containing 65 parts of the ester when a standardized thermal treatment was adopted: after each measurement the test sample was brought to room temperature and permitted to relax for fifteen minutes. The ineffectiveness of high dibutyl sebacate concentrations, i.e., greater than about 20 parts per hundred, can again be attributed to the separation of excess solid at the low temperatures of these experiments.

3. Hydrocarbon Oils

Several hydrocarbons, some of which were obtained from crude oil as cuts in the processing oil range, were investigated with the U-type dilatometer. The data, some of which are plotted in Fig. 7, reveal breaks in the volume-temperature curve just as for polymers in the glass transition region. The linear segment of the high temperature range corresponds to the normal volume contraction on cooling of the liquid. At lower temperatures the volume decrease corresponds to the normal contraction of the oil in the glassy state. The change in

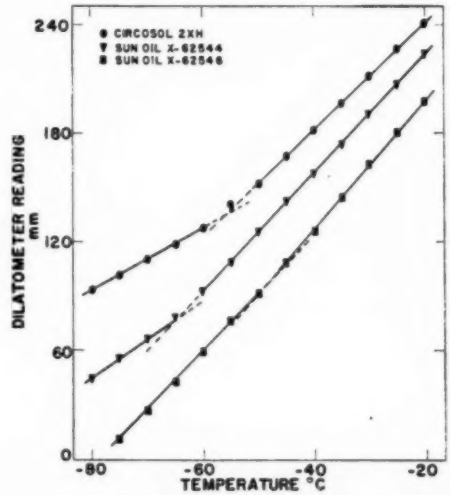

FIG. 7. Glass transitions in oils.

[9] Fletcher, Gent, and Wood, Third Rubber Technology Conference, London (June 1954).
[10] P. J. Flory and W. R. Krigbaum, Ann. Rev. Phys. Chem. **2**, 383 (1951).
[11] L. Breitman, J. Polymer Sci. **17**, 425 (1955).
[12] G. Bruni, Giorn. chim. ind. ed appl. 51 (February, 1921); Chem. Abstracts **15**, 2018 (1921).

slope of the volume-temperature curve for Sun Oil X-62546 at about −48°C is smaller than the corresponding changes for the other oils. Thus, though the volume data could be reproduced at will in successive cooling experiments, there is some uncertainty in this T_g assignment. The dilatometer readings for two oils, Sundex 53 and Sun Oil X-62542, were markedly time-dependent at temperatures, some ten to twenty degrees above T_g. Constant readings were obtained within about fifteen minutes at all other temperatures, even below T_g. The glass temperatures were readily located by extrapolation of accurately linear segments of the volume-temperature curves to points of intersection.

Heating experiments were also conducted, starting at the lowest temperature attained in the cooling cycle. On warming the sample about twenty degrees conchoidal fractures, characteristic of glasses, developed and were accompanied by audible "clicks." After cooling to the initial temperature a higher dilatometer reading was obtained because of the voids formed on fracture. These phenomena strongly suggest that the oils are obtained in a glassy state at low temperatures.

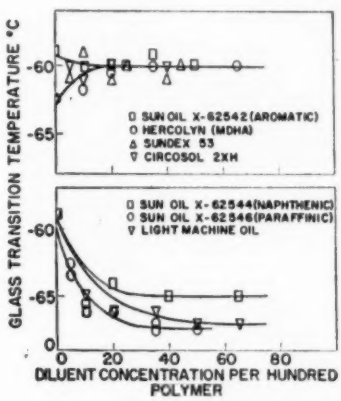

FIG. 8. Blends of commercial oils with GR-S.

Figure 8[13] shows the effect of concentration of these oil type diluents on the dilatometric T_g of GR-S blends. Compounds shown in the upper section of this figure have virtually no plasticizing ability at low temperatures; the other oils can postpone the transition by 5 to 9 degrees.

Flexibility tests gave results completely analogous to those obtained by dilatometry. Figure 9 illustrates the plasticizing action of Sun Oil X-62546 at various loadings in GR-S. Extrapolation of the linear portions of the angular twist-temperature curves to zero twist gave the so-called Gehman freeze point. Figure 10, in which freeze points are plotted against oil concentration, may be compared with the corresponding dilatometric T_g *vs* concentration curves shown in Fig. 8.

[13] "Paraffinic," "naphthenic," and "aromatic" are relative terms, denoting the preponderance of straight chain, naphthenic, or conjugated ring structures in the molecular mixture. The "paraffin" oil, for example, is dewaxed but contains a large fraction of carbon atoms in straight chains attached to cyclic nuclei, conjugated or otherwise.

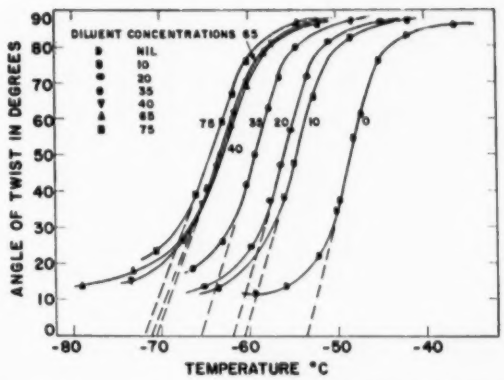

FIG. 9. Gehman curves for sun oil X-62546/GR-S blends.

An attempt was made to correlate low temperature behavior of GR-S blends with some physical properties of the hydrocarbon oils. Diluents, ranging in consistency from a heavy processing oil, X-62542, to a light solvent, Iosol 2232, are arranged in Table V in order of increasing low temperature plasticizing ability. There appears to be a trend toward greater plasticizing ability with decreasing glass temperature and decreasing pour point of the pure diluent, and also with increasing compatibility of the oil-polymer pair as measured by the volume increase on swelling of vulcanizates. The most consistent correlation however exists between the data in the three columns on the right in Table V: the viscosity and its temperature coefficient on the one hand and the maximum depression of the glass temperature on the other. The relationship suggests a mechanical interpretation of plasticizing action. Effective diluents are those providing environments which are less resistant to the motion of polymeric segments than those comprising pure polymer. The temperature coefficients of viscosity of the first four oils in this table correspond to apparent activation energies of 16.5 to 11.5 kilocalories per mole; the other, more effective, diluents have activation energies in the range 11 to 3 kilocalories.

SUMMARY

A summary of the investigation with the three types of diluent can be made with reference to Table VI.

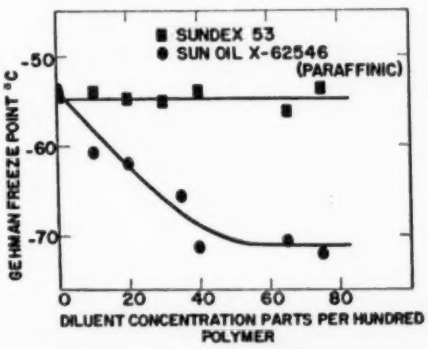

FIG. 10. Freeze resistance of GR-S blends.

TABLE V. Physical properties of oils: correlation with ΔT_g of GR-S blends.

Oil	T_g of oil °C	Pour point °F	Vol. increase on swelling GR-S %	Viscosity (Saybolt sec) 100°F	Viscosity (Saybolt sec) 210°F	Δ(log viscosity)[a] / Δ(1/T)	Max ΔT_g °C
X-62542[b]	−27.5	55	29.7	14 500	178	3.63×10^3	1
Hercolyn[c]	−37	30	48.1	3930	90.9	3.16	−2.5
Sundex 53[b]	−27.5	51	90.6	2715	87.0	2.90	−2.5
Circosol 2XH[b]	−56	20	77.2	1815	90.4	2.53	−2.5
X-62544[b]	−65	0	58.2	1260	78.5	2.38	6
Light machine oil[d]	−40[f]	−8	90.6	271.5	55.7	1.64	8
X-62546[b]	−48[f]	+5	81.7	213.2	53.1	1.63	8.5
Diesel fuel[d]	<−60	+5	215	3.90[g]	1.39[g]	0.85	>25[j]
Iosol 2232[e]	<−90	···	265	0.695[g]	0.950[g, h]	0.69[i]	>30[j]

[a] From kinematic viscosities at 100° and 210°F.
[b] Sun Oil Company.
[c] Hercules Powder Company.
[d] Imperial Oil Ltd., Sarnia.
[e] Imperial Oil Ltd., Toronto.
[f] Uncertain.
[g] Viscosity in centistokes.
[h] Viscosity at 68°F.
[i] From kinematic viscosities at 68° and 100°F.
[j] The diluents were extracted by the confining fluid; these values are therefore lower limits.

TABLE VI. Viscosity and compatibility effect on ΔT_g of GR-S.

Diluent	Δ(log visc.)[a] / Δ(1/T)	Vol. increase on swelling GR-S %	Max ΔT_g[b] °C
Hydrocarbon	$2.5\rightarrow3.6\times10^3$	30→77	nil or small
Oils	1.6→2.4	59→82	6→9
Dibutyl sebacate	0.86	110	9
Tributoxyl ethyl phosphate	1.02	36	16
Dibutyl phthalate	1.02	66	24
Dioctyl adipate	1.00	100	37
Dioctyl sebacate	1.08	104	38
Hydrocarbon oils	0.69→0.85	215→265	>25→30

[a] Kinematic viscosities at 100° and 210°F.
[b] Depression of glass transition temperature.

Hydrocarbon oils are more effective low temperature plasticizers the lower their temperature coefficient of viscosity. Dibutyl sebacate is representative of crystallizing diluents. Such compounds are ineffective low temperature plasticizers unless, (a) at equilibrium, favorable thermodynamic parameters permit their existence as liquids in the polymer, or (b) the plasticizers tend to exist as the nonequilibrium, supercooled, liquids in the transition temperature region of the polymer. Particularly desirable are liquids with low apparent activation energies of viscosity and high miscibility with polymer. The four ester plasticizers, tributoxy ethyl phosphate, dibutyl phthalate, dioctyl adipate, and dioctyl sebacate, have temperature coefficients of viscosity corresponding to a virtually common activation energy of 4.5 kilocalories. Here, the magnitude of diluent-polymer interaction, as indicated by volume increase measurements, dictates the order of effectiveness of the ester.

ACKNOWLEDGMENTS

The author appreciates the permission extended by Polymer Corporation Limited to publish these data. The dilatometric measurements were made by Mr. R. L. Arblaster. Gehman measurements were made by Mr. J. E. Durley under the supervision of Mr. A. C. MacLeod. The author is indebted to Dr. L. A. McLeod and Dr. H. Leverne Williams for helpful discussions.

JOURNAL OF APPLIED PHYSICS VOLUME 26, NUMBER 9 SEPTEMBER, 1955

Proton Magnetic Resonance in Polyamides

W. P. SLICHTER
Bell Telephone Laboratories, Inc., Murray Hill, New Jersey
(Received April 28, 1955)

The proton magnetic resonance absorption has been observed in several linear polyamides from 77°K to 400°K. The absorption line narrows gradually with increasing temperature up to about 280°K. A marked decrease in line width with increasing temperature occurs over a span of 20 or 30 degrees within the range of 280 to 400°K, and is presumed to result from the onset of rotation of chain segments. In a series of polyamides possessing an even number of carbon atoms between polar groups, this transition occurs at a lower temperature as the hydrocarbon portions are made longer (polydecamethylene octadecanediamide compared to polyhexamethylene adipamide). In the copolymer polyhexamethylene adipamide-sebacamide, the transition region is at a lower temperature than in the pure adipamide or pure sebacamide. The x-ray diffraction studies on polyamide fibers show that the chain packing becomes more symmetrical over these same temperatures. The resonance results are interpreted in terms of simple models.

I. INTRODUCTION

NUCLEAR magnetic resonance techniques have proved useful for the study of molecular structure, and especially for the investigation of motions of nuclei.[1] This report relates to the application of proton magnetic resonance techniques to the study of solid linear polyamides, with the aim of augmenting what is known of molecular structures and motions from x-ray diffraction and dielectric studies.

II. EXPERIMENTAL

The resonances were observed with a Pound-Knight-Watkins spectrometer[2]; the details of the apparatus are given elsewhere.[3] The magnet had a field inhomogeneity of about 0.3 gauss. The cryostat was similar to that used by Gutowsky.[4] Temperature changes between successive runs amounted to 25° or less. With each temperature change, a period of at least 30 minutes was allowed for temperature equilibration in the polymer.

The lateral spacings between polymer chains in fibers were measured, as a function of temperature, with the aid of an electrically heated oven mounted on the spectrogoniometer of a type XRD-3 General Electric x-ray diffraction unit. The oven was equipped with windows of 0.5-mil aluminum foil, to permit passage of the beam. Dry nitrogen was fed slowly into the oven to keep the polymer from oxidizing. Temperature regulation, deviating less than a degree, was provided by a thermistor-actuated electronic controller.

The polyamides were synthesized from the appropriate diamines and dibasic acids by the methods of Carothers,[5] or when possible were obtained commercially. The molecular weights were not measured, but were obviously high. The specimens were annealed to high crystallinity.[6] Apart from this heating, no attempt was made to desiccate the samples. For the resonance studies, the samples were in the form of chips of unoriented material, contained in small test tubes and inserted into the rf coil. There was about 0.5 gram of polymer within the coil. Temperature was measured with a copper-constantan thermocouple, with one junction in contact with the polymer.

III. LINE-WIDTH CHANGES

Figure 1 is a plot of resonance line width as a function of temperature for nylon 6–10.[7] The curve is typical of the nylons studied. The points were taken over several temperature cycles. No hysteresis was apparent on the time scale of these experiments. As is shown, the field inhomogeneity sets a lower limit on the measurement of line width.

The over-all features of this curve are comparable to those found with other polymers.[8] The gradual narrowing of the resonance curve is attributed here, as in previous studies, to the development of thermal motion.[9] The marked narrowing of the line is generally presumed to come from the onset of extensive chain rotation. In this case, though, the pronounced narrowing occurs at temperatures higher than in most previous

[1] H. S. Gutowsky and G. E. Pake, J. Chem. Phys. **18**, 162 (1950); J. G. Powles and H. S. Gutowsky, *ibid.* **21**, 1695, 1704 (1953); G. B. Benedek and E. M. Purcell, *ibid.* **22**, 2003 (1954). See also G. E. Pake [Am. J. Phys. **18**, 438, 473 (1950)] for a summary of work before 1950.

[2] R. V. Pound and W. D. Knight, Rev. Sci. Instr. **21**, 219 (1950); G. D. Watkins, thesis, Harvard University (1952).

[3] Shulman, Mays, and McCall, Phys. Rev. (to be published).

[4] Gutowsky, Meyer, and McClure, Rev. Sci. Instr. **24**, 644 (1953).

[5] W. H. Carothers, U. S. Patents 2,071,250 (1937) and 2,130,523 (1938).

[6] Fuller, Baker, and Pape, J. Am. Chem. Soc. **62**, 3275 (1940).

[7] As is conventional, a polyamide (or nylon) is identified by a pair of figures; the first tells the number of carbon atoms in the constituent diamine, and the second tells the number of carbons in the dioic acid. Thus polyhexamethylene sebacamide is nylon 6–10.

[8] R. Newman, J. Chem. Phys. **18**, 1303 (1950); Holroyd, Mrowca, and Guth, Phys. Rev. **79**, 1026 (1950); Holroyd, Codrington, Mrowca, and Guth, J. Appl. Phys. **22**, 696 (1951); H. S. Gutowsky and L. H. Meyer, J. Chem. Phys. **21**, 2122 (1953); Honnold, McCaffrey, and Mrowca, J. Appl. Phys. **25**, 1219 (1954); E. M. Banas and B. A. Mrowca, Bull. Am. Phys. Soc. **30**, No. 2, 25 (1955).

[9] It should be recalled (see Gutowsky and Pake[1]) that frequencies of motion amounting only to tens of kilocycles produce a noticeable narrowing of the resonance line width, and that such frequencies are very low in thermodynamic terms.

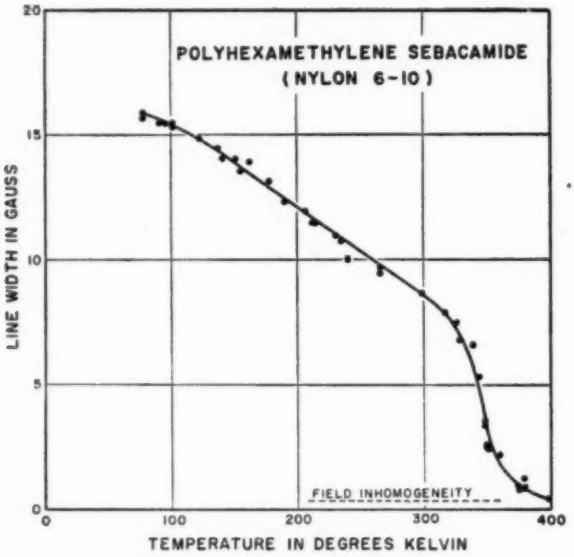

FIG. 1. Variation of resonance line width with temperature in nylon 6–10.

studies,[10] indicating greater constraints upon chain rotation than in most polymers studied to date. Further, the line width at low temperatures is greater than has generally been found. Finally, the line width appears to be still increasing with decreasing temperature at 77°K, whereas with other polymers[8] the line width usually levels off to a constant "rigid lattice" value at a higher temperature. This trend in line width suggests the persistence of a significant amount of motion at quite low temperatures.

In Fig. 2, the line width is shown as a function of temperature for three polyamides, nylons 6–6, 10–10, and 10–18. These compounds are all "even-even" polyamides, i.e., they have an even number of carbon atoms in both amine and acid. X-ray fiber patterns taken at room temperature[11] show that the lateral chain-chain packing is asymmetrical, and is the same in these compounds. Furthermore, the polar groups occurring regularly along each chain interact with the groups on neighboring chains to form layers of dipoles which are tilted with respect to the chain axes. Thus, the crystalline content is triclinic in form. With nylons 10–10 and 10–18, and to a lesser degree with 6–6, the monoclinic form, with the dipolar planes normal to the chain axes, is mixed with the triclinic.[12] It should be added that in the odd-odd polyamides, the chain packing is symmetrical (i.e. hexagonal) and less compact, and the dipole layers are normal to the chains.[11]

It is seen, in Fig. 2, that in these compounds of similar chain packing, the marked narrowing of the resonance occurs at lower temperatures as the hydrocarbon portions are made longer and the concentration of polar groups is decreased (nylon 10–18 compared to nylon 6–6). The measured absorption comes primarily from the methylenic hydrogens, and scarcely at all from the amido hydrogens, but it appears that the polar groups affect the motion of the hydrocarbon segments.

Copolyamides have been shown[11] to have depressed melting points and reduced elastic moduli, as compared with the related monopolyamides. This behavior has been attributed to the disorder in the dipolar array wrought by copolymerization. In Fig. 3, a comparison is made of the line-width temperature curves of nylon 6–6, nylon 6–10, and the copolyamide 6–6:6–10. The latter was synthesized with the diamine and with equimolar parts of adipic and sebacic acids. It appears from Fig. 3 that the partial disordering of dipoles causes a lowering in the temperature at which the motion of the hydrocarbon segments becomes appreciable.

IV. SECOND MOMENTS FOR RIGID CHAINS

For a comparison between theory and experiment, it is useful to deal with the second moment of the absorption line.[13] It is possible to calculate second moments for a number of systems of stationary[14] and moving[15] nuclei. We consider first the case of motionless

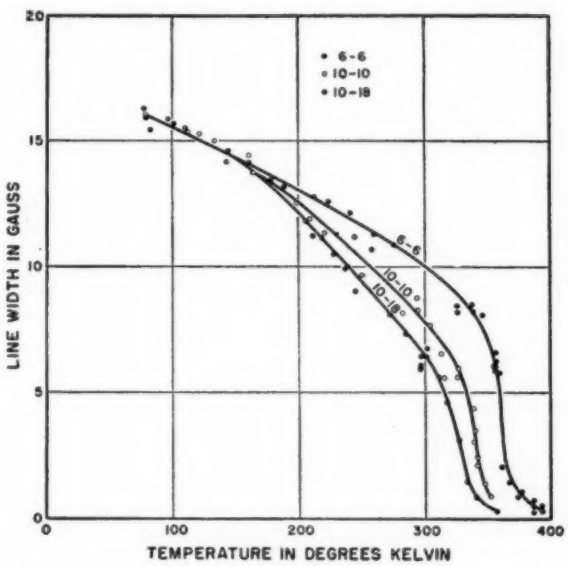

FIG. 2. Variation of resonance line width with temperature in nylons 6–6, 10–10, and 10–18.

[10] An exception appears in the work on polystyrene reported by Holroyd *et al.*[8] In that compound, however, the bulkiness of the phenyl group unquestionably sets the polymer apart, in regard to molecular motion, from linear macromolecules in which the substituents are small.

[11] Fuller, Baker, and Pape[6]; W. O. Baker and C. S. Fuller, J. Am. Chem. Soc. **64**, 2399 (1942); C. S. Fuller and W. O. Baker, J. Chem. Ed. **20**, 3 (1943); F. Ecochard, J. chim. Phys. **43**, 113 (1946); C. W. Bunn and E. V. Garner, Proc. Roy. Soc. (London) **A189**, 39 (1947).

[12] Fuller and Baker[11]; Bunn and Garner[11]; W. O. Baker and N. R. Pape, 122nd Meeting of The American Chemical Society, (September, 1952).

[13] J. H. Van Vleck, Phys. Rev. **74**, 1168 (1948).

[14] Gutowsky, Kistiakowsky, Pake, and Purcell, J. Chem. Phys. **17**, 972 (1949); also, G. E. Pake.[1]

[15] H. S. Gutowsky and G. E. Pake.[1]

polyamide molecules, with chain axes having no preferred orientation in space. For the calculation, it is assumed that the chain is fully extended, and that bends are gradual on a scale of five or so bond lengths along the chain. The data of Bunn and Garner[11] are adopted for the positions of chain atoms and amide groups. The C−C and C−H bonds are assumed to be distributed tetrahedrally, and the C−H distance is taken[16] as 1.094 A. Let the polyamide be represented as $-[NH(CH_2)_mNHCO(CH_2)_nCO]_p-$. Then the intramolecular contribution to ΔH_2^2, the second moment expressed in terms of magnetic field, is found to be $[18.5-22.7/(m+n+1)]$ gauss^2. In obtaining this relationship, one must require, for an error of no more than about a percent, that m, $n \geqq 5$. This expression is graphed in the top curve of Fig. 4. The limiting value for a polyamide with negligible dipole content, i.e., for a polymethylene, is shown by the dashed line. The latter value agrees with Andrew's[17] figure for a motionless long-chain n-alkane.

When either m or n is less than 5, the value of ΔH_2^2 is quite sensitive to the detailed chemical structure, and the general expression of the preceding paragraph is no longer accurate. It is therefore necessary to calculate ΔH_2^2 separately for each compound. For chemical reasons, many of these highly polar nylons have never been successfully synthesized. For two known compounds, nylons 4–6 and 6–6, the theoretical values of intramolecular ΔH_2^2 have been separately calculated, and are plotted in Fig. 4, to show the deviations which occur when the dipoles become populous. However, the highly polar compounds undoubtedly have distorted

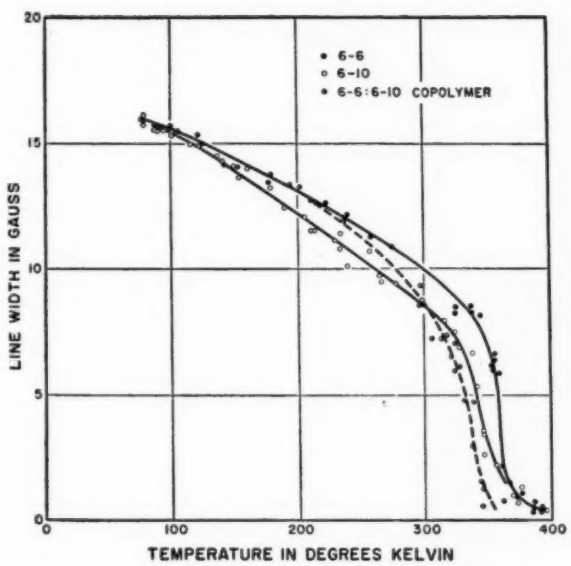

FIG. 3. Variation of resonance line width with temperature for nylon 6–6, nylon 6–10, and the copolymer 6–6:6–10.

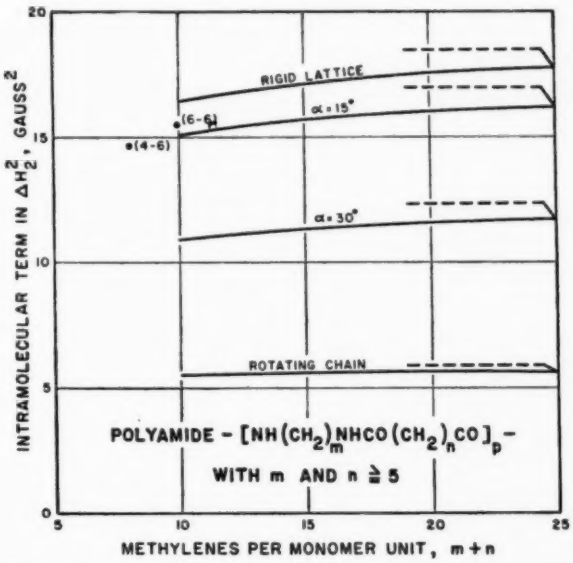

FIG. 4. Intramolecular contribution to the calculated second moment as a function of the number of methylene groups in the polyamide.

chains,[18] rather than extended chains, so that for a reliable calculation of ΔH_2^2 the positions of the chain atoms would have to be found for each compound by x-ray methods.

The contribution of the "foreign" nucleus, nitrogen, to the proton resonance is perceptible in the highly polar compounds, but is insignificant for $m+n$ greater than about 12.

Taking the room temperature data for atomic positions,[11] and applying corrections to allow for the contraction at liquid nitrogen temperature observed by x-ray diffraction (see below), the intramolecular contribution to the rigid lattice value of ΔH_2^2 in an even-even polyamide is found to be 9.7 gauss^2. Here the contribution of amido protons and nitrogens is negligible, practically speaking. Hence, for even-even polyamides, the total second moment is $[28.2-22.7/(m+n+1)]$ gauss^2 for a rigid lattice.[19] To the writer's knowledge, there have been no studies of detailed atomic coordinates in the odd-odd polyamide structures. Since the chains are more loosely packed than in the even-even series, the second moments ought to be somewhat smaller than the value just stated.

Table I compares the experimental second moments of several polyamides at liquid nitrogen temperature and at room temperature. The values at 77°K are in reasonable agreement with the foregoing calculation for a rigid lattice, and show the expected trend with increasing monomer size. It is felt that the experimental uncertainty is between 1 and 2 gauss^2, and that

[16] G. Herzberg, *Infrared and Raman Spectra of Polyatomic Molecules* (D. Van Nostrand Company, Inc., New York, 1945), p. 440.

[17] E. R. Andrew, J. Chem. Phys. **18**, 607 (1950).

[18] Fuller and Baker[11]; Bunn and Garner.[11]

[19] It should be remarked, though, that the lattice may not indeed be "rigid" at the liquid nitrogen temperature. The trends of line width with decreasing temperature have already been discussed. The second moment at liquid helium temperature might therefore be significantly greater than the value given above.

TABLE I. Experimental second moments.

Nylon	77°K	298°K
6–6	26 gauss^2	18 gauss^2
5–7	26	16
7–9	26	13
8–8	27	14
6–10	28	15
10–10	28	15
10–18	28	13

therefore this trend is probably real. This rather large uncertainty in experimental second moments comes from the fact that ΔH_2^2 is especially affected by the shape of the outer portions of the resonance curve, where the absorption is small and somewhat ambiguous. It is seen that the values at 298° decrease in general as the dipolar content of the material decreases. This trend is in accord with the earlier interpretation, that the dipolar association hinders the motion of the hydrocarbon segments.

V. SECOND MOMENTS FOR CHAINS IN MOTION

It is now assumed that the protons are engaged in classical rotation about the chain axes which, as before, show no preferred orientation in space.[15] It is again assumed that the chain is extended and comparatively unbending; and further that the classical rotation occurs uniformly, without twisting, on a scale of five or so bond lengths along the chain. Then the intramolecular term for ΔH_2^2 is $[5.9-4.7/(m+n+1)]$ gauss^2. As is seen in the bottom curve of Fig. 4, there is little variation with m and n.[20]

The intermolecular term for the rotating chain follows from Andrew's[21] treatment. His derivation considers the nuclei to be rotating uniformly, with no phase coupling between rotating chains. His treatment is strictly valid only for nuclei which rotate in the same plane in neighboring chains, but as an approximation he includes nuclei which depart somewhat from coplanarity. Proceeding in the same fashion here, the intermolecular term turns out to be 3.0 gauss^2. Hence the total second moment is $[8.9-4.7/(m+n+1)]$ gauss^2 if all the chain segments rotate.[22]

The experimental second moments at room temperature listed in Table I are all appreciably larger than the previously predicted values. One may conclude, then, that the observed reduction from the rigid lattice value corresponds to the rotation of some, but not all, of the chain segments. Actually, the picture must be more complex than this. It is unlikely that rotation occurs uniformly over sizeable lengths of the chain. Particularly in polyamides, studies of the dielectric behavior[23] show that the dipolar relaxation, viewed in terms of reaction kinetics, is characterized by a large activation energy (22.3 kcal). Rotational motion in polymeric hydrocarbons, studied by proton magnetic resonance, seems to be determined by much lower energies. Thus, for polyethylene[24] the activation energy is about 4 kcal, and for a molecule as unsymmetrical in cross section as natural rubber,[24,25] the activation energy is about 13 kcal. To be sure, a detailed comparison of the results of dielectric measurement and nuclear resonance is probably unjustified, but the large differences in these energies ought to be significant. One would expect, then, that the greater restriction experienced by the dipolar portions is conveyed to the adjacent paraffinic regions. Only at rather high temperatures, if at all, should it be a good approximation to speak of uniform motion along the chain segments.

This approximation of uniform motion is continued, nevertheless, to allow treatment of rotational oscillation, the case intermediate between the fixed lattice and the rotating chain. Andrew[26] has considered the effect of classical harmonic rotational oscillation upon the second moment. If the angular amplitude of oscillation is α, an application of Andrew's method to the present problem yields intramolecular terms of $[17.0-21.2/(m+n+1)]$ gauss^2 for $\alpha=15°$ and $[12.3-15.4/(m+n+1)]$ gauss^2 for $\alpha=30°$.[27] These

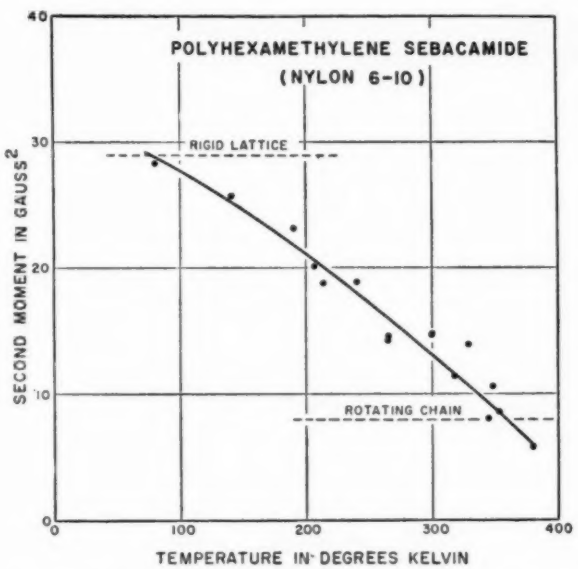

FIG. 5. Experimental second moment for nylon 6–10 as a function of temperature, with calculated values for the rigid lattice and the rotating chain.

[20] Andrew[17] predicts an intramolecular second moment of 6.8 gauss^2 for a long-chain n-alkane, whereas the present work predicts 5.9 gauss^2. The reason for this disparity is unknown.

[21] E. R. Andrew,[17] Appendix II.

[22] It should be remarked that the nuclear resonance measurement fails to distinguish between continuous classical rotation and jump-wise rotation occurring at the same frequency.

[23] W. O. Baker and W. A. Yager, J. Am. Chem. Soc. **64**, 2171 (1942).

[24] L. H. Meyer, thesis, University of Illinois (1953).

[25] Gutowsky and Meyer.[3]

[26] E. R. Andrew,[17] Appendix I.

[27] It is doubtless naive to consider that harmonic motion still exists when α is as large as 30°.

expressions are also plotted in Fig. 4. One may presume that the intermolecular term for rotational oscillation is reduced proportionately from its rigid lattice value.

A detailed model of the hydrocarbon motion would involve a more complex potential energy function[28] than the simple sinusoidal functions conventionally used to describe hindered internal rotation, and in particular would demand that a temperature-dependent function be set up. Approaches to this problem[29] have been only semiquantitative in even the simplest systems. There seems to be little merit now in a more detailed treatment of the complex hindrances in polyamides. Nor will there be a discussion of other imaginable classes of motion, such as flexing, and lateral and longitudinal translation in the solid, all of which would reduce the second moment.

Figure 5 shows the variation of the experimental second moments with temperature for nylon 6–10. A smooth curve has been drawn through the points. The horizontal dashed lines show the theoretical values of ΔH_2^2 for the rigid lattice and for uniform rotation of chain segments. One would expect the experimental second moment to continue to decrease with increasing temperature, as classes of motion other than rotation became more and more important. In fact, the motion at the higher temperatures used here must have consisted of a composite, not merely of rotation alone. But viewing the motion as only rotational, the present treatment indicates that substantially all the chain segments in nylon 6–10 are rotating at a temperature of about 360°K, over 100° below the melting point.

It is seen that the curve is nearly linear. The total energy of a harmonic oscillator is proportional to the square of the amplitude of motion, and the mean energy per oscillator of a collection of harmonic oscillators is proportional to temperature. Hence, if we presume that the motion is representable as a system of independent oscillators, with the second moment decreasing linearly from the rigid lattice value with increase in the square of oscillation amplitude,[26] then it follows that one would expect the second moment to decrease linearly with increasing temperature.

VI. COMPARISON OF PROTON RESONANCE DATA WITH X-RAY DIFFRACTION STUDIES

The hydrocarbon chain, in its extended form, is ribbon-like in its over-all shape[30] at room temperature, rather than tube-like. Accordingly, the packing of chains in crystals is lower in symmetry than the hexagonal structure. With thermal agitation at high temperature, though, the chains tend to become statistically circular in cross section, and the packing shifts toward the symmetrical hexagonal form. High-temperature x-ray diffraction studies of large paraffin molecules[31] and polyethylene[32] have shown the shift toward greater symmetry, but melting occurred before hexagonal packing was reached.

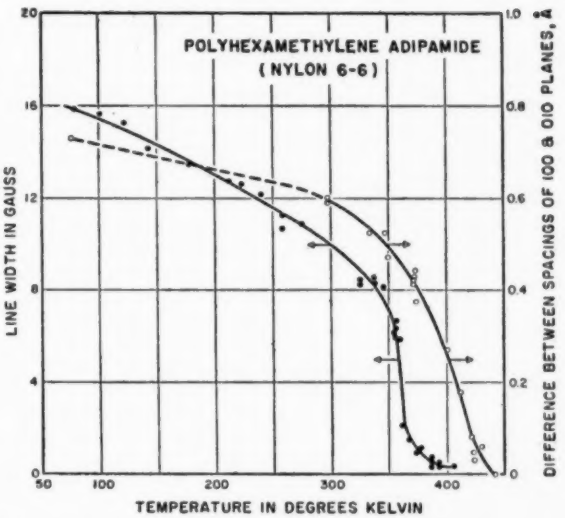

FIG. 6. Temperature dependence of resonance line width and of the difference between the 100 and 010 spacings, for nylon 6–6.

In the present work, studies of fibers of several even-even polyamides, ranging from nylon 10–18 to nylon 6–6, show that the symmetrical packing is achieved 50° to 100° below the melting point. In Fig. 6, the difference between the spacings of the 100 and 010 planes is graphed, as a function of temperature, for nylon 6–6. These spacings coalesce when molecular motion causes the packing to become hexagonal. In the same figure, the proton resonance line width is shown for the same compound. It is seen that the temperature region for the approach to symmetry in packing corresponds to the region in which the resonance studies show that the chain motion becomes appreciable.

VII. ACKNOWLEDGMENTS

It is a pleasure to express appreciation to D. W. McCall and K. H. Storks for some valuable discussions, to J. M. Mays for the use of his nuclear resonance apparatus, and to R. F. Westover for preparing the figures.

[28] See R. J. Meakins and J. W. Mulley, J. Chem. Phys. **21**, 1934 (1953).

[29] L. Pauling, Phys. Rev. **36**, 430 (1930); R. H. Fowler, Proc. Roy Soc. (London) **A149**, 1 (1935).

[30] A. Müller, Proc. Roy. Soc. (London) **A120**, 437 (1928).

[31] A. Müller, Proc. Roy. Soc. (London) **A127**, 417 (1930); **138**, 514 (1932).

[32] C. W. Bunn and T. C. Alcock, Trans. Faraday Soc. **41**, 317 (1945).

Unilateral Compression of Rubber

MICHAEL J. FORSTER
Chemical and Physical Research Laboratories, Firestone Tire and Rubber Company, Akron 17, Ohio
(Received April 29, 1955)

One-dimensional compression measurements have been made on samples of natural rubber gum stock. The experimental stress-strain curve and the theoretical relation $f=G(L-1/L^2)$ agreed quite well over the entire range (0%–32%) studied. No hysteresis loop was evident.

The friction at the faces of the sample was eliminated by a new method of lubrication. The sample essentially floated between two thin films of a liquid which flowed under pressure between the sample and compressing plates allowing uniform lateral expansion of the sample.

INTRODUCTION

ATTEMPTS to obtain stress-strain relationships, modulus, and Poisson's ratio of rubber by one-dimensional compression have never been very successful because of the friction between the sample faces and the compressing plates. Because this friction seriously impedes the expansion at the face of the sample, the sample does not undergo uniform lateral expansion as it is compressed longitudinally. The uneven lateral expansion or "barreling" results in errors in the measurement of modulus and stress and makes it impossible to measure Poisson's ratio.

Ariano[1] reported but little success in overcoming this friction by using as a lubricant a mixture of glycerol and graphite. A higher degree of lubrication was achieved by Kimmich[2] who used petrolatum in a study of the effect of shape on compressive stress. Other investigators, feeling that even the best of lubricants would not entirely eliminate the friction, by-passed this difficulty by assuming that a two-dimensional extension was equivalent to a one-dimensional compression. Sheppard and Clapson[3] and Treloar[4] used inflated balloons to provide the two-dimensional stretch, confining their measurements to a small section of the surface over which the degree of stretch was assumed constant. A thin sheet of rubber was used by Russell[5] in a similar bilateral stretch experiment, air pressure again providing the stretching force.

Very little work on one-dimensional compression has been done however since the development of the statistical theories[6,7] of rubber-like elasticity, and, with the exception of Treloar's two-dimensional stretch experiments,[4] no attempts have been made to correlate experimental and theoretical compression stress-strain data. It should therefore prove interesting to compare true one-dimensional compression data with theory as well as with one-dimensional compression data obtained in bilateral stretching.

[1] R. Ariano, Rubber Chem. and Technol. **11**, 561 (1938).
[2] E. G. Kimmich, Rubber Chem. and Technol. **14**, 407 (1941).
[3] J. R. Sheppard and W. J. Clapson, Ind. Eng. Chem. **24**, 782 (1932).
[4] L. R. G. Treloar, Trans. Inst. Rubber Ind. **19**, 201 (1944).
[5] G. C. Russell, Trans. Inst. Rubber Ind. **9**, 283 (1934).
[6] E. Guth and H. M. James, Ind. Eng. Chem. **33**, 624 (1941).
[7] L. R. G. Treloar, Trans. Faraday Soc. **39**, 241 (1943).

APPARATUS AND METHOD

In order to attain the high degree of lubrication required for direct compressive tests, a method of lubrication was devised which causes a liquid to be forced between the sample faces and the compression plates at all compressive strains. Figure 1 shows how this was accomplished. Sixty-four small holes (0.0135 inch or 0.0343 centimeter in diameter) were drilled through each plate B, so that the lubricant could pass from the chambers D behind the plates to the faces of sample A. The chambers D in turn are connected by means of the tubes C to a hydraulic pump which supplies the lubricant under pressure. A gauge in the line C allows measurements of the lubricant pressure. In addition to the holes, each plate has a small pin at its center to prevent lateral motion of the sample.

Compression of the sample is achieved by motion of the left plate which, along with its lubricant chamber, is mounted in the bronze bearing H. The screw K causes the left plate to slide along in the sleeve J, which was carefully machined to prevent lateral motion. Measurements of the amount of compression are made possible by the dial gauge L, whose foot M engages the bronze bearing.

Similarly, measurement of the lateral expansion of the sample is made by means of a dial gauge. The foot O presses gently against the side of the sample and transmits its motion to the gauge N. Because centering of the sample on the plates cannot be checked, measurements of the diameter rather than the radius are taken.

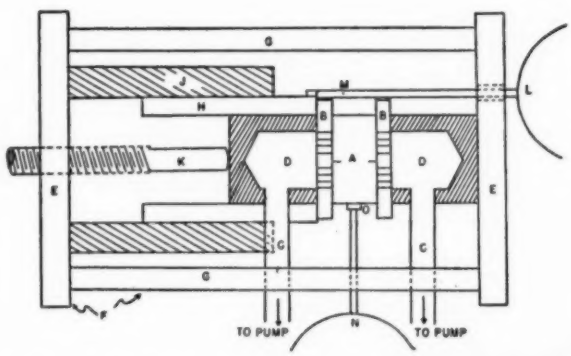

FIG. 1. Unilateral compression apparatus—cross-sectional view.

The large forces involved in compression of the rubber require a sturdy mounting for the compression plates. The frame of the apparatus consists of two steel plates E (1.27 centimeters or $\frac{1}{2}$-inch thick), held together by four steel rods G, having a diameter of 0.95 centimeter or $\frac{3}{8}$ inch.

The samples used in the experiments were cylindrical in shape, having a diameter of 4.0 centimeters and a height of 1.9 centimeters. Before testing, the height and diameter of the sample were measured, the sample was centered on the compression plates, and the left plate driven to the right until each compression plate made contact with its corresponding sample face. After initial readings of the height and diameter were obtained from the dial gauges, the sample was compressed about 32% in steps of 2 to 3%. At the end of each compression step, the sample was lubricated by opening a valve which allowed the lubricant (glycerine) to flow through the compression plates to the sample faces. During the lubrication, the sample was rotated through a small angle and then returned to its original position in order to insure perfect freedom of the surfaces. The sample at this time essentially floated between two thin films of glycerine. After the lubricant valve was closed, 5 minutes were allowed before any measurements were taken. This delay permitted the excess lubricant to drain from between the sample faces and the compression plates and enabled the lubricant pressure to come to equilibrium before it was measured. Since the equilibrium lubricant pressure was that at which the lubricant no longer flowed to the surfaces of the sample, it was also the same as the stress on the sample. The stress with respect to the actual cross section could therefore be read directly. At the same time that the lubricant pressure attained equilibrium, the sample height and diameter were measured in order to determine the strain and lateral expansion, respectively. At this stage, the sample was also examined for signs of barreling by placing a straight edge against the side of the cylinder.

RESULTS AND DISCUSSION

Measurements of stress, strain, and lateral expansion were made on a natural rubber gum vulcanizate.* The stress-strain curves obtained are shown in Fig. 2. The stress referred to the actual cross section was obtained directly by experiment. The stress referred to the original cross section was calculated from the stress based on the actual cross section and the lateral expansion. Measurements made on both the increasing and decreasing parts of the strain cycle fell on the same curve so that no hysteresis was observed in the range studied.

The theoretical stress-strain curve showed very good agreement with the experimental curve of the stress based on the original cross section. A value of 5.6 kg/sq cm was used for the shear modulus. Treloar[4] showed similar agreement between his experimental data and

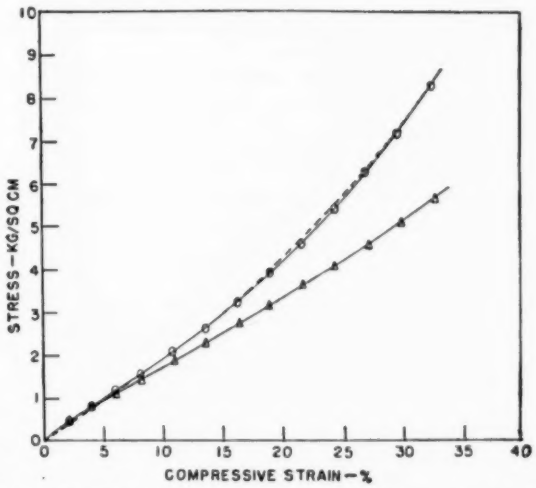

FIG. 2. Stress-strain curves for natural rubber gum vulcanizate. △ is stress referred to actual cross section; ○ is stress referred to original cross section; – – – is theoretical curve $f=G(L-1/L^2)$.

the same equation when he used a shear modulus of 4.0 kilograms per square centimeter. An analysis of the compressive stress-strain data of Sheppard and Clapson[3] revealed that they, too, could be represented by the theory if G were given the same value of 4.0 kilograms per square centimeter. This is rather remarkable agreement, even though both investigators used similar 8% sulfur compounds.

In these experiments and accelerated stock containing 2.5% sulfur was used. This could account for the relatively large value obtained for the shear modulus although a part of the increase in modulus (over that fitting data of Sheppard and Clapson and of Treloar) might be attributable to the difference in experimental methods.

Now although the experimental and theoretical compression curves have been shown to agree quite well, a close examination reveals a definite difference in their shapes. The experimental curve has a knee at low compressive strains, which gives the curve the sigmoidal shape typical of elastomers in extension. In a relatively early paper Ariano[8] discusses the sigmoidal shape of extension curves, but reports that his compression curves showed no point of inflection, being hyperbolic in nature. This was probably due to the absence of a lubricant in Ariano's experiments, since the experimental curves obtained by Sheppard and Clapson in two-dimensional extension, where friction was entirely eliminated, were sigmoidal in shape. The same was found true of Treloar's work when a curve was drawn through the experimental points. Thus there seems to be little doubt that the sigmoidal shape will be obtained as long as adequate means for lubricating the sample faces are provided.

The natural rubber gum vulcanizate used in these experiments showed no signs of barreling so that the volume change on compression could be calculated from

* See Appendix for recipe and curing time.

[8] R. Ariano, India-Rubber J. **76**, 207 (1928).

the strain and lateral expansion measurements. The volume, determined from these measurements, increased slightly at low compressive strains and did not become less than the original volume until the strain was increased to 13%. This initial increase in volume appeared to be real but because of its unexpected nature should be checked further before its final acceptance.

ACKNOWLEDGMENTS

The author wishes to thank Dr. E. E. Hanson and Dr. J. W. Liska for their helpful suggestions and the Firestone Tire and Rubber Company for permission to publish this work.

APPENDIX

Natural Rubber Test Recipe

Smoked sheet	100
Stearic acid	1
Zinc oxide	5
Sulfur	2.5
Benzothiazyl disulfide	1
Phenyl beta naphthylamine	1
Cured 60 minutes at	280°F

JOURNAL OF APPLIED PHYSICS VOLUME 26, NUMBER 9 SEPTEMBER, 1955

Apparatus for Making Simultaneous Stress and Birefringence Measurements on Polymers

E. F. Gurnee, L. T. Patterson, and R. D. Andrews
Physical Research Laboratory, The Dow Chemical Company, Midland, Michigan
(Received May 16, 1955)

An instrument has been constructed to allow simultaneous measurements of stress and birefringence in polymer samples to be made as a function of time and temperature. The stress is measured by attaching one end of the sample to a cantilever beam near the fulcrum; the small deflection of the beam is indicated by means of a differential transformer, which in turn is attached to an automatic recorder.

The birefringence is measured with a Senarmont compensator (quarter-wave plate method). Measurements can be made either manually or with a continuously rotating analyzer. This latter method permits the automatic recording of the birefringence and is also adaptable to the study of rapid birefringence changes. The sample is housed in a copper pipe surrounded by a thermostatically controlled liquid bath.

Some data are presented showing the use of this apparatus in measuring birefringence and stress changes during stress relaxation experiments (sample held at constant elongation), birefringence changes during creep under constant load, and stress-optical coefficients.

INTRODUCTION

AN IMPORTANT method for investigating polymeric materials is by means of stress relaxation experiments. A sample of polymer is given a rapid extension to a fixed elongation, and the stress in the sample is measured as a function of the time. This stretching of the sample introduces an optical anisotropy in the polymer which decays as the stress relaxes; consequently, it is also desirable to be able to measure the birefringence decay during the stress relaxation experiment, since this provides valuable additional information on the molecular nature of the relaxation process.[1]

The apparatus described in this paper was primarily designed to make simultaneous measurements of the stress and birefringence during stress relaxation experiments carried out at constant temperature. In addition, however, it is suitable for other stress-optical studies such as the determination of stress-optical coefficients, measurement of birefringence changes during creep, etc.

[1] R. S. Stein and A. V. Tobolsky, Textile Research J. 18, 201, 302 (1948).

DESCRIPTION OF THE APPARATUS

A block diagram of the equipment is shown in Fig. 1. The temperature is maintained at a constant value by an oil bath with copper coil heaters controlled by a mercury thermostat. Toward one end of the bath, and opening to the outside, are two intersecting copper pipes: the vertical pipe serves as an air chamber for the sample, and the horizontal pipe allows a beam of light to be passed through the sample for the birefringence measurements. The temperature in the sample chamber is measured with a thermocouple and recorded on a 0–60°C Brown strip-chart recorder. The zero of this recorder can be set at any temperature by means of a bucking voltage supplied by a hand potentiometer. The recorder can be read to the nearest 0.1°C; in any given run the maximum recorded deviation from the desired temperature is about ±0.2°C.

The sample is usually a flat strip between $\frac{1}{2}$ in. and 1 in. wide, approximately $\frac{1}{10}$ in. thick, and about 6 in. long. The upper end of this sample is clamped to a connecting rod which is suspended from a cantilever beam by means of a ball joint. The stress in the sample causes a small deflection of this beam which moves the core of

a differential transformer fastened to the tip of the beam. The output of this transformer is balanced by that of another differential transformer which replaces the slidewire in a Brown-chart recorder. The range for the stress measurements is changed by replacing the cantilever beam with one of a different cross section; the total deflection of the beam is kept small in order not to exceed its elastic limit, and to limit operations to the linear portion of the differential transformer.

Since the stress relaxation is of a roughly exponential form, it is desirable to have a fast chart speed at the beginning of the experiment for greater accuracy in reading time values, and a slow speed at the end to avoid unwieldy lengths of chart paper. This is accomplished by means of a solenoid-actuated clutch that permits chart drive either direct from the motor or through a 100:1 gear reducer.

The bottom of the sample is clamped to a connecting rod which runs through a vertical guide. This rod can be fastened to a lever system for applying large stresses to the sample. Smaller stresses can be applied by hanging weights directly from the rod. Stops are available for holding the sample at a fixed extension.

The birefringence is measured by determining the optical retardation by means of a Senarmont compensator, modified to permit automatic recording. Automatic recording of birefringence changes has several advantages: (1) rapid changes can be studied, (2) measurements can be made at extremely short times from the beginning of an experiment, (3) the order of the retardation is tabulated and, (4) there is no ambiguity in the sign of the birefringence.

The light source is a mercury arc lamp (G.E. AH–3) operating at 0.3 ampere dc, and requiring a firing potential of about 500 volts dc. The use of a dc supply, rather than the more customary ac, avoids undue 120 cycle modulation in the final output of the photocell. A green filter is used to obtain monochromatic light (5461 A). The polarizer and analyzer are constructed with Polaroid disks, rather than Nicol prisms, in order to obtain a large aperture at a reasonable cost. The incomplete polarization in the violet region causes no difficulty since that part of the spectrum has been removed by the green filter.

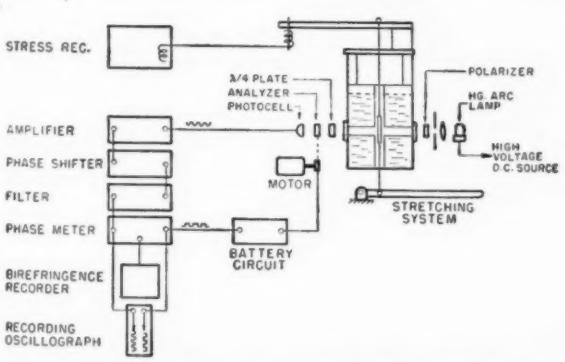

FIG. 1. Block diagram of the stress relaxation equipment and associated circuits for measuring birefringence.

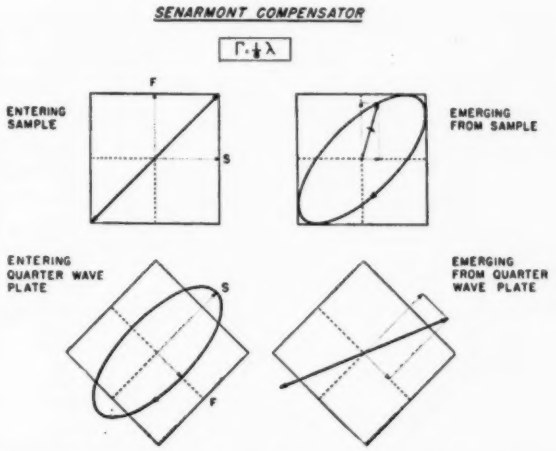

FIG. 2. This diagram indicates how the sample and the quarter-wave plate rotate the plane of polarization of the light from the polarizer.

The operation of this type of compensator[2] is illustrated in Fig. 2 which has been drawn for the case where the sample has an optical retardation of $\frac{1}{8}$ wavelength. The original plane of polarization of the light makes an angle of 45° with the fast and slow axes of the sample. After passing through the sample, this plane polarized light has become elliptically polarized; the major and minor axes of this ellipse also make a 45° angle with the fast and slow axes of the sample. This ellipse, which arises from 2 equal components $\frac{1}{8}\lambda$ (45°) out of phase, can also be considered as the resultant of two plane polarized components of unequal amplitudes 90° out of phase, one of the components being parallel to the slow axis and the other parallel to the fast axis of a quarter-wave plate. The quarter-wave plate removes the 90° phase difference between these two waves and consequently the amplitudes can be added as vectors.

The light output from the quarter-wave plate is thus plane polarized, the azimuth angle of this plane depending on the optical retardation through the sample. Consequently, by continuously rotating the analyzer, the intensity of light transmission through the analyzer varies sinusoidally with time, and with a phase which varies with the optical retardation of the sample. This light is readily converted to an electrical voltage by means of a photocell and then amplified. The phase of this voltage is observed by comparison with a reference square-wave voltage obtained from a commutator that is synchronously rotated with the analyzer. The frequency of the sine wave and the square wave is approximately 6 cps.

The phase shift is measured with an electronic phase meter that gives a dc output of 0–200 microamperes, corresponding to a phase shift of 0–360 degrees, which

[2] H. S. Bennett, *McClung's Handbook of Microscopical Technique*, R. McC. Jones, Editor (Paul B. Hoeber, Inc., New York, 1950), third edition, Chap. IX.

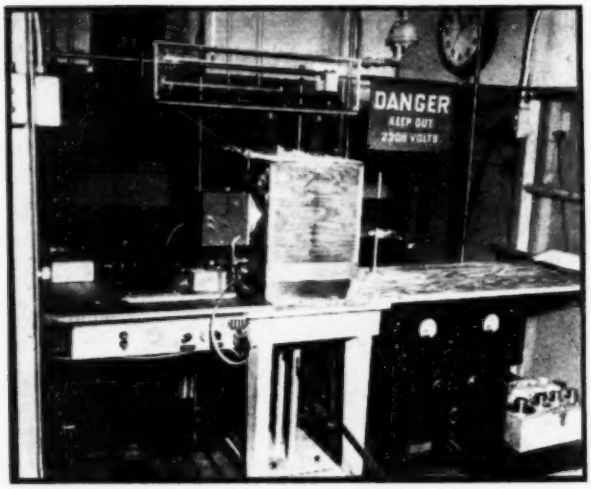

FIG. 3. Photograph of the stress relaxation equipment.

can be read on an ammeter calibrated in degrees phase shift. A modified Brown recorder provides a record of the output of the phase meter. For short-time measurements (<6 sec), the outputs from the photocell and the commutator are fed directly to a dual channel recording oscillograph and the phase shift is measured directly from the oscillograph traces.

For experiments involving slow birefringence changes over a period of several days, it is more satisfactory to replace the continuously rotating analyzer with the usual manual analyzer and not use the birefringence recording system.

A photograph of the apparatus is shown in Fig. 3, while Fig. 4 gives a view of the recorders and the auxiliary electronic equipment for the measurement of the birefringence.

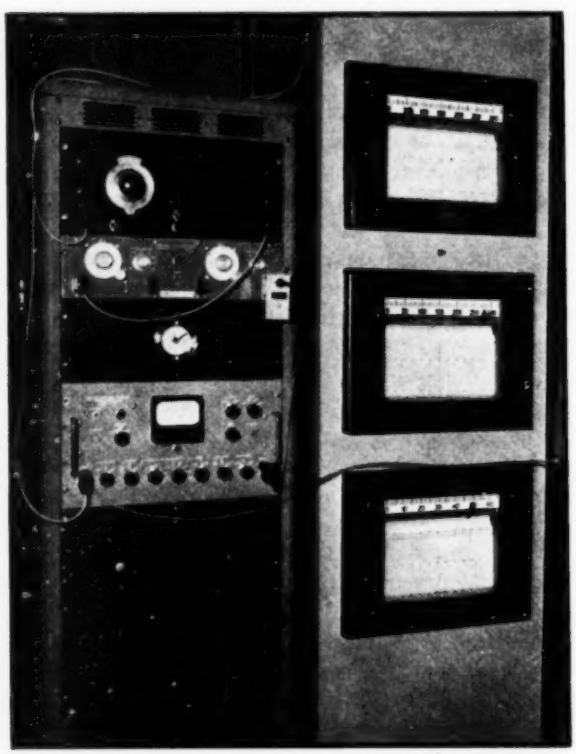

FIG. 4. Photograph of the electronic equipment for the birefringence measurements, and the recorders for recording birefringence, stress, and temperature.

TYPICAL RESULTS OBTAINABLE WITH THIS EQUIPMENT

Some results will now be given to illustrate the use of this apparatus. These experiments were made with samples cut from an extruded sheet of Dow polystyrene.

Figure 5 is a sketch of the recorder traces obtained from a typical stress relaxation experiment. One recorder width on the birefringence chart corresponds to an optical retardation of one wavelength. The order of the retardation remaining at the end of the run is determined by some auxiliary method (usually with the Berek compensator and a polarizing microscope after removal of the sample from the apparatus); it is then possible to count back to determine the order of each of the chart peaks. We thus have an effective expansion of the chart width by a factor of the highest order of retardation (number of wavelengths) obtained, which may be as high as 25, and consequently the birefringence measurements are extremely accurate. A break can be observed in about the center of the upper traces in Fig. 5 at the point where chart speed was changed.

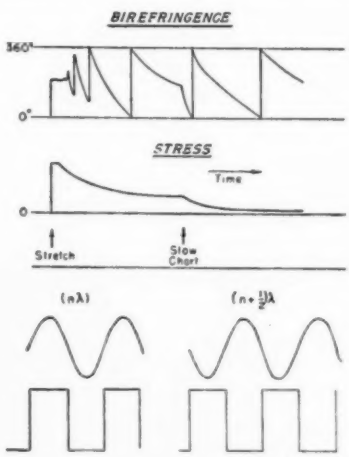

FIG. 5. Sketch of typical traces from the birefringence and stress recorders (top), and sections of traces from the recording oscillograph for short-time birefringence measurements (bottom).

Since the recorders and phase meter cannot follow the changes during the first six seconds or so, we rely on recording oscillograph traces for these very short times. Traces of this sort, corresponding to retardations of an integral and half-integral number of wavelengths, are also shown in Fig. 5. The sine wave is the output from the photocell which appears on one channel of the oscillograph, and the square wave is the reference signal from the commutator which appears on the other channel.

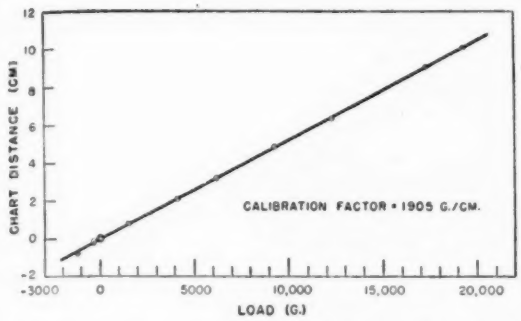

FIG. 6. Calibration curve for one of the cantilever beams.

The stress chart actually indicates the deflection of the beam which must be calibrated against known weights. The calibration curve is shown in Fig. 6, and turns out to be quite linear.

It has become a habit to refer to these measurements as "stress" and "birefringence" when in reality they are "force" and "optical retardation." Since these terms are readily related, however, this should cause no confusion.

Typical stress relaxation and birefringence decay data at three different temperatures are shown in Figs. 7 and 8. The accuracy of these data is quite satisfactory if one considers the fact that the ordinate scales here are linear rather than logarithmic. The stress accuracy, also, has been improved considerably since these measurements were made through stabilization of the temperature of the cantilever beam by addition of the Plexiglas housing shown in Fig. 3.

In Fig. 9 we show similar data in which the birefringence has been recorded from the beginning of the stretching of the sample using the recording oscillograph. For stress relaxation experiments it is desirable to stretch the sample much faster than the 6 sec used here: ideally the stretching should be instantaneous.

In addition to its use in obtaining relaxation data, this equipment has proved useful in stress-optical studies in the glassy state. Figure 10 is a plot of the change in birefringence against the applied stress at

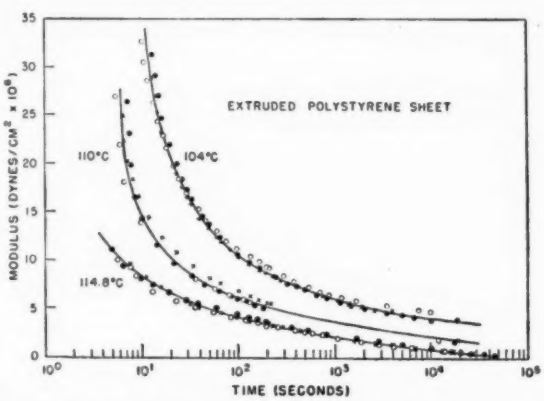

FIG. 7. Polystyrene stress relaxation data for three different temperatures. Three duplicate runs are shown at each temperature. Stress is plotted as modulus (stress/strain).

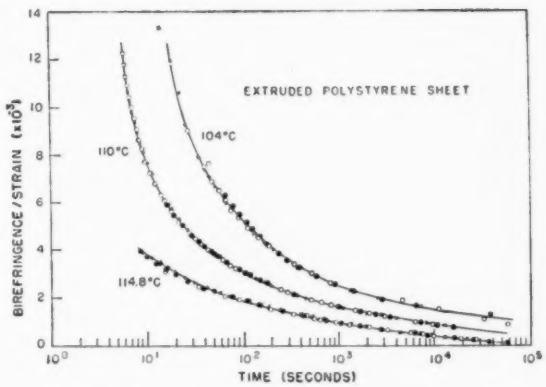

FIG. 8. Birefringence decay curves for the experiments shown in Fig. 7.

40°C for the same extruded polystyrene. Notice that this birefringence is positive while that obtained by stretching at higher temperatures (above the transition temperature) is negative. The stress-optical coefficient obtained from the slope of this graph is +8.81 brewsters (1 brewster = 10^{-13} cm²/dyne).

The effect of time on this stress-optical coefficient has also been determined as shown in Fig. 11. The curve marked "creep" represents the change in the apparent stress-optical coefficient (ratio of birefringence to stress) under a given constant stress (7.15×10^7 dynes/cm²) at 40°C. The relaxation curve is obtained by applying the same initial load and immediately clamping to hold at constant length. The stress in the time interval of this experiment decayed about 37%.

DISCUSSION

The experimental results that have been given in this paper simply illustrate some of the types of measurement that can be carried out with the stress-optical equipment that has been constructed and consequently no theoretical interpretations are presented.

A complete description of the electronic circuits has been avoided since that would require a discussion

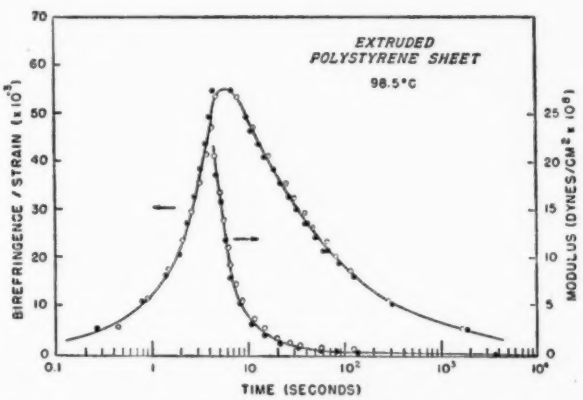

FIG. 9. Stress relaxation and birefringence change for two samples of polystyrene that were stretched slowly (6 sec). Note that the birefringence can be followed right through the stretching.

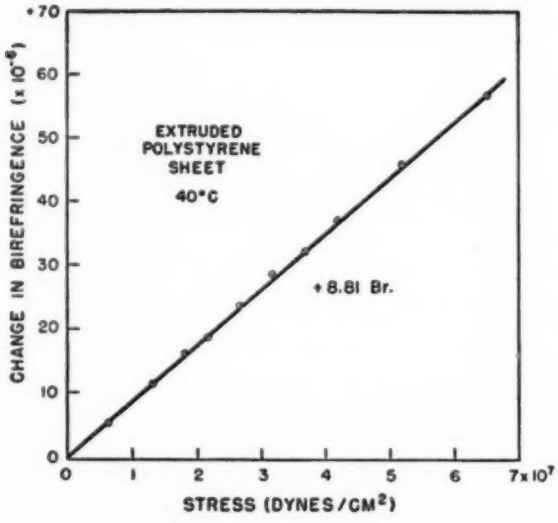

FIG. 10. Stress-optical coefficient for polystyrene at 40°C.

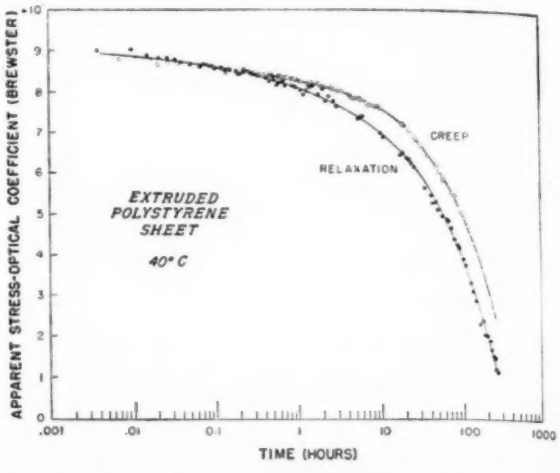

FIG. 11. Change in stress-optical coefficient as a function of time during a relaxation experiment compared with similar data for a creep experiment.

considerably longer than seemed desirable here. To partly make up for this lack of detail, we will now point out several of the problems that arose in the construction of the equipment.

As far as stress measurements are concerned, the biggest problem was room temperature variation. By operating in a constant temperature room (±2°C), shielding the beam from drafts, and keeping the stress recorder at approximately constant temperature by operating its amplifier continuously, the external temperature effects were reduced to a suitable level. In addition, a linear correction for the stress reading has been developed to correct for temperature variations, although in most cases is not not needed. Temperature variations seem to affect principally the stress recorder itself, and the correction required is determined from the position of the stress trace with the secondary of the differential transformer on the cantilever beam shorted out (zero input into recorder). It was also necessary to eliminate the effect of building vibrations with a small oil dashpot attached to the cantilever beam.

The birefringence measurements were subject to the disturbing influence of stray 60-cycle voltages in spite of all attempts to maintain a high "signal to noise" ratio. This problem was finally solved by inserting an electronic filter just before the phase meter.

The strain is determined by measuring the final separation of two marks on the sample that were originally 10 cm apart. While this method is accurate for fairly large strains, it is probably the main source of error for experiments done with 10% or less strain. It is anticipated that a new strain measuring procedure will be used to reduce this error for experiments near the glassy state.

In conclusion, we should mention that many of the ideas and problems involved in the construction of this equipment could have been solved in various ways. For example, it might be more desirable to use a photomultiplier tube and avoid the several stages of electronic amplification that we have been forced to use in the birefringence circuits. The methods used represent a certain amount of personal taste that was often influenced by equipment immediately available.

JOURNAL OF APPLIED PHYSICS VOLUME 26, NUMBER 9 SEPTEMBER, 1955

Effects of Attenuating Materials on Detonation Induction Distances in Gases*

MARJORIE W. EVANS, FRANK I. GIVEN, AND WILLIAM E. RICHESON, JR.
Stanford Research Institute, Menlo Park, California

(Received January 5, 1955)

The effectiveness of acoustic absorbing wall materials in delaying the onset of detonation in gases is explored. Experiments are reported for stoichiometric H_2-O_2 mixtures in two-inch diameter cylindrical tubes. The results show that the detonation induction distance may be increased by as much as a factor of two by making the walls of the tube of porous sintered bronze.

DETONATION INDUCTION IN GASES

THE initiation by shock waves of detonation in gases has been extensively explored experimentally.[1–6] The shock waves may be created by detonation of a solid explosive,[4] by the breaking of a diaphragm separating a high pressure and a low pressure chamber, the former containing an inert gas, the latter a detonable gas,[5] or by shock waves formed from detonation waves originating in a different detonable mixture.[2,3] As summarized by Berets, Greene, and Kistiakowsky,[3] very intense shocks appear to start the detonation instantly and may overdrive it initially beyond its steady-state velocity, weaker shocks may cause ignition which eventually leads to detonation, and still weaker shocks may produce no ignition.

A related problem is the transition in gaseous systems from a deflagration to a detonation. This also has been the subject of extensive experimental work, by means of which it has been established that detonation results from the coalescence of a deflagration front with a shock wave.[4,7,8] The circumstances controlling the transition to detonation have been examined by several workers.[9–12]

Hydrodynamic reasoning shows that in the development of detonation from a deflagration originating at one end of a closed cylindrical tube, a precompression wave is sent out into the unburned gas ahead of the reaction front, pushing the unburned gas forward with a velocity sufficient to insure that the gas comes to rest when the deflagration passes over it.[11] It is reasoned by extension from this argument that during the deflagrative course of the process the strength of the precompression wave is increased so that its speed equals that of a detonation, its strength becoming comparable to the strength of the detonation. It is then necessary, as the final step of the transition, either that the deflagration overtake the shock wave with resulting coalescence forming a detonation, or that the precompression shock have a strength sufficient to form a detonation ahead of the deflagration in the unburned gas. The former case has been analyzed by Oppenheim,[12] the latter by Manson.[10] Both cases have been observed experimentally.

Thus for given conditions of geometry, composition, and spark energy, the time or distance required to form a detonation wave is equal to the time or distance required to form a precompression shock of requisite strength. Given a method of attenuating a precompression wave and thus delaying the buildup of shock strength, one should be able to increase the distance required to form a detonation wave. Such a method of attenuation is offered by acoustic attenuating wall materials, since it has been shown by acoustic experiments that when a plane wave travels down a circular tube which is lined with an absorbing material, energy is fed from the plane wave laterally into the material.[13] This paper reports the results of experiments designed

TABLE I. Acoustic properties of porous sintered bronze.[a]

Grade	Frequency (cps)	Surface impedance ratio	Attenuation coefficient in material (db/cm)
MH-28 (coarse)	5000	$3.2-j1.2$	4.8
	7000	$3.2-j1.0$	5
	9000	$2.2-j1.5$	5.3
MH-100 (fine)	5000	$5+j1$	7.2
	7000	$4.6+j0$	8.5
	9000	$2.7+j2.1$	12

[a] Measurements were supplied by Soundrive Engine Company.

* This research was supported by Soundrive Engine Company, Los Angeles, California.

[1] W. C. F. Shepherd, *Third Symposium on Combustion, Flame, and Explosion Phenomena* (Williams and Wilkins, Baltimore, Maryland, 1949), p. 301.

[2] Berets, Greene, and Kistiakowsky, J. Am. Chem. Soc. **72**, 1080–86 (1950).

[3] Berets, Greene, and Kistiakowsky, J. Am. Chem. Soc. **72**, 1086–90 (1950).

[4] Schmidt, Steinicke, and Neubert, Forsch. Gebiete Ingenieurw. **B17** (1951).

[5] J. B. Fay, Fourth Symposium on Combustion (Williams and Wilkins, Baltimore, Maryland, 1953), p. 50.

[6] A. J. Mooradian and W. E. Gordon, J. Chem. Phys. **19**, 1166–72 (1951).

[7] W. Payman and H. Titman, Proc. Roy. Soc. (London) **A152**, 418–45 (1935).

[8] Bone, Fraser, and Wheeler, Trans. Roy. Soc. (London) **A235**, 29–68 (1936).

[9] P. Laffitte, J. Chim. phys. **26**, 391–423 (1929).

[10] N. Manson, "Propagation des detonations et des déflagrations dans les melanges gazeux," L'Office National d'Etudes et de Recherches Aeronautiques, Inst. Franc. Petroles, Paris, 1947.

[11] R. Courant and K. O. Friedrichs, *Supersonic Flow and Shock Waves*, (Interscience Publishers Inc., New York, London, 1948), p. 204 *f*.

[12] A. K. Oppenheim, *Fourth Symposium on Combustion* (Williams and Wilkins, Baltimore, Maryland, 1953), p. 471.

[13] H. J. Sabine, J. Acoust. Soc. Am. **12**, 53–57 (1940).

TABLE II. Velocity data: one-inch fine liner (MH-100).

Experiment no.	1	2	3	4	5	6	7
Distance from spark (inches)				Velocity (m/sec)			
0–2.5	···	156	159	165	159	154	142
2.5–12.5	···	349	337	371	336	316	383
12.5–15	···	···	377	503	552	545	···
15–17.5	734	···	*1040*	677	···	583	*678*
17.5–20	*828*	*1300*	2890	*887*	*928*	770	2860
20–22.5	2870	2890	2890	2850	2890	*1048*	2860
22.5–25	2870	2890	···	2850	2890	2380	2350
25–27.5	2870	2890	···	···	2890	D	2860
27.5–30	2870	2890	···	···	2890	2910	2860
30–40	2780	2550	2890	···	2770	2840	···

to test the hypothesis that the distance required to form a detonation, herein called the detonation induction distance, x_d, can be increased by attenuating the precompression waves by making the walls of porous sintered bronze.

EXPERIMENTAL DETAILS

The combustion tubes were 6 ft in length, closed at both ends. The liners were hollow cylinders of 2-in. inside diameter and either 3- or 4-in. outside diameter, machined to fit snugly into their respective shells. The length of each cylinder was 3 in. and the complete liner was made by packing the small cylinders into the shells.

Two grades of sintered bronze were used, MH-28 (coarse) and MH-100 (fine), the designation of grade being that of the manufacturer, the Asco Sintering Company. Microscopic examination of the liners showed that the diameter of the spheres in the MH-100 fine sintered bronze was 0.27 mm, while that in the MH-28 coarse material ranged from 0.27 to 0.472 mm. The average diameter of the pores was computed to be 0.04 mm and 0.07 mm for fine and coarse material, respectively. The porosity was 40 to 50%. The acoustic properties of the materials as measured with a plane wave are given in Table I.

The detonable gas was 67.0±1% hydrogen in oxygen, with a nitrogen impurity of 0.3%. More accurate control of composition was not considered necessary for the experiments because of the relative insensitivity of detonation induction distance to composition, and the fact that x_d was determined only to ±1.25 in. The initial pressure in all experiments was one atmosphere. Ignition was by electric spark, the energy being 540±10 millijoules. The duration of the spark was of the order of one-half microsecond.

The position of the reaction zone as a function of time was recorded by means of ionization gaps and electronic amplification and recording equipment. Each gap consisted of a pair of special electrodes centered on the axis of the tube and polarized by a direct current potential of approximately 20 v. Ten gap stations were used with a spacing which could be adjusted so that within the neighborhood of the point of detonation initiation the gaps were placed at 2.5-in. intervals. Several gaps were placed after the point of initiation so that the detonation velocity was measured over several intervals. This permitted assurance that steady-state detonation was established.

TABLE III. Velocity data: 0.5-inch fine liner (MH-100).

Experiment no.	1	2	3	4	5	6	7	8	9
Distance from spark (inches)					Velocity (m/sec)				
0–2.5	161	171	166	163	158	161	160	166	161
2.5–5	237	237	247	237	262	238	242	239	223
5–7.5	453	3020	353	458	346	409	474	422	462
7.5–10	518	2160	321	366	342	329	407	422	384
10–12.5	756	642	···	673	624	565	731	1082	656
12.5–15	756	828	828	712	732	727	799	858	779
15–17.5	*2070*	583	713	*ND*	*ND*	*747*	*948*	*1915*	890
17.5–20	2770	*2570*	*2570*	3420	3210	D	D	2770	*2490*
20–30	2770	3200	2780	2970	3120	3080	3305	2770	···
30–40	2770	3100	2780	2850	2710	2750	2770	2770	3850

TABLE IV. Summary of detonation induction distance data.

Diameter and liner	x_d (inches from spark)	No. of experiments
2-in. ID-no liner	5–7.5	5
	10–12.5	10
3-in. ID-no liner	5–7.5	4
4-in. ID-no liner	7.5–10	3
2-in. ID-0.5″ fine	15–17.5	6
	17.5–20	3
2-in. ID-1″ fine	15–17.5	2
	17.5–20	5
2-in. ID-0.5″ Coarse	12.5–15	6
	17.5–20	1
	20–22.5	5
	22.5–25	4
	25–27.5	2
2-in. ID-1″ Coarse	15–17.5	1
	20–22.5	1
	22.5–25	3
	25–27.5	1

A small portion of the spark energy was used to trigger a sweep raster on an oscilloscope. On the arrival of a flame front at an ionization gap, the gap became conductive. This conduction was converted into signal pips which were superimposed upon the calibrated sweep raster. In order to simplify trouble-shooting, even-numbered gaps produced upward pulses, odd-numbered gaps produced downward pulses. The detonation induction distance was determined by computing the velocity of the reaction front between successive stations. The transition was assumed to occur within the 2.5-in. interval preceding that interval for which the detonation velocity was observed.

The value for the steady-state detonation velocity for 67% hydrogen in oxygen is given by Berets, Greene, and Kistiakowsky as 2830 meters/second.[2] This value was confirmed within our measurement precision of 5%. An initial overshoot of the velocity persisting for several inches was noted in about 40% of the experiments as an apparently random effect.

Tables II and III give typical sets of velocity data, for the one-inch and one-half-inch fine liners, respectively. The position of the beginning of detonation is italicized. The symbol D indicates that although detonation was clearly occurring, the velocity could not be accurately calculated because of the overlay of pips at a reversal point on the raster. Similarly ND indicates that detonation was clearly not occurring. Missing data is the result of overlay of pips or failure of an ionization gage. Initial overshoot may be observed in No. 4, 5, 6, 7, and 9 of Table III. In No. 2 of Table III detonation momentarily occurred at 2.5–5 in., but quickly reverted to deflagration. This phenomenon was observed on one other occasion.

A summary of the detonation induction distance data for all tube diameters and wall conditions is shown in Table IV.

CONCLUSIONS

The results displayed in Table IV show that the acoustic absorbing properties of porous sintered bronze walls have a pronounced effect on detonation induction distance, the mechanism being that of attenuation of precompression waves. A rough median may be cited as representative of the relative effect of the various liners on x_d. For tubes with plain steel walls x_d showed a median of 7.5 to 10 in. With the fine liners the values for x_d fell in the range of 15–20 in., and with the coarse liners the median value was 20–25 in.

The authors take pleasure in acknowledging their indebtedness to Soundrive Engine Company for support of this research, to Dr. Vincent Salmon for his contributions to the acoustic aspects, and to James S. Arnold for his help in solving the experimental problems.

JOURNAL OF APPLIED PHYSICS VOLUME 26, NUMBER 9 SEPTEMBER, 1955

Small Particle X-Ray Scattering by Fibers. II. Radial Distribution of Microcrystallites

A. N. J. HEYN*
Clemson College, Clemson, South Carolina
(Received March 17, 1955)

Radial distribution functions of the microcrystalline particles in fibers are derived from the x-ray scattering at small angles. Particle distribution functions are obtained by application of the method of Fourier synthesis to the x-ray data, by inversion of the intensity scattered under conditions where interparticle interference plays a part.

Different distribution curves are obtained with different fibers, investigated under the same conditions.

The distribution curves obtained with the same fiber investigated under different conditions of swelling, are consistent with the wider separation of the particles at higher degrees of swelling. A quantitative explanation is thus given of the differences between the scattered intensities at different degrees of swelling.

The degree of crystallinity is calculated from the distribution curves, so obtained, in combination with the particle sizes determined in preceding papers.

INTRODUCTION

In previous communications,[1] the scattering of fibers under different conditions of swelling was found to show large differences. The differences were qualitatively explained as being due to interparticle interference. In the more densely packed conditions, this effect plays the greatest part, it decreases at higher degrees of swelling and finally disappears completely if the swelling is far enough increased, under which conditions only independent particle scattering would remain.

The conditions for obtaining independent particle scattering have been analyzed in the preceding paper[1] in which it was shown in detail how, by suitable experimental conditions, pure independent scattering by isolated particles can be separated from the effect of interparticle interference. From the scattering obtained under such conditions, the *size* (diameter or radius of gyration) and *shape* of the scattering particles (microcrystallites) were derived.

Under normal conditions, however, interparticle interference plays an important part in the scattering by fibers, which effect causes the independent scattering curves to be profoundly changed. In the present paper the effect of interparticle interference is quantitatively studied and the method of Fourier synthesis is applied to the experimental data for deriving the radial distribution of particles, in analogy with the procedure used in liquids.

The use of this method for determining the distribution of atoms in liquids, was originally proposed by Zernicke and Prins[2] and developed by Debye and Menke.[3] Warren and Gingrich[4,5] and co-workers

* Professor of Natural and Synthetic Fibers, School of Textiles.

[1] A. N. J. Heyn, J. Appl. Phys. **26**, 519–526 (1955); see also Am. Chem. Soc. **70**, 3138 (1948); Textile Research J. **19**, 163–72 (1949); J. Am. Chem. Soc. **72**, 2284–5 (1950a); J. Am. Chem. Soc. **72**, 5768–9 (1950b); Nature **172**, 1000 (1953); Textile Research J. **23**, 782–87 (1953).

[2] F. Zernicke and T. H. Prins, Z. Physik **41**, 184–94 (1927).

[3] P. Debye and H. Menke, Physik. Z. **31**, 797 (1930); Ergebn. tech. Röntgenk **2**, 1 (1931).

[4] B. E. Warren, J. Chem. Phys. **2**, 551 (1934); J. Appl. Phys. **8**, 645 (1937); Hultgren, Gingrich, and Warren, J. Chem. Phys. **3**,

employed the method in the study of the atomic distribution functions in a great number of liquid elements, liquids, and noncrystalline solids, like carbon black and glass. Other authors[6] have later studied more complicated liquids. Debye and Bueche[7] used the same principle to light scattering by inhomogeneous substances. In a theoretical treatise, Oster and Riley[8] proposed the same procedure for x-ray scattering by small particles. Such radial distribution analysis has so far not been carried out for small particle scattering.

The results will be tested by investigating whether the distribution functions obtained under different degrees of swelling are consistent with the different separation of particles, which goes together with different swelling. If this will prove to hold, a quantitative explanation would conversely be given of the differences between the scattering of fibers at different degrees of swelling, and of the maxima and minima which may occur under certain conditions in the scattering curves.

THEORETICAL PART

Determination of Radial Distribution Function

In the preceding paper, the following theoretical equation has been used for particle scattering under conditions where interparticle interference plays a part:

$$I_n = N\phi^2(kR)\left[1+\int_0^\infty 2\pi r(\rho(r)-\rho_0)J_0(kr)dr\right]. \quad (10)$$

The contribution from interparticle interference is represented by the function under the integral sign, which will be termed $G(kr)$:

$$\int_0^\infty 2\pi r(\rho(r)-\rho_0)\cdot J_0(kr)dr = G(kr). \quad (10a)$$

The function $G(kr)$ contains the radial density function of scattering material $\rho(r)$ which will be determined in the following.

This function can be obtained in a straightforward way by inverting the experimental intensity function by means of the Fourier integral theorem.

If I_i denotes the angular distribution of intensity for independent scattering [the function $\phi^2(kR)$] and I_n that for nonindependent scattering [the function of Eq. (10)], and if $(I_n/I_i)-1$ is written $i(k)$, then $G(kr)=i(k)$ and Eq. (10) can be written:

$$i(k) = \int_0^\infty 2\pi r(\rho(r)-\rho_0)\cdot J_0(kr)dr. \quad (11)$$

This integral equation can be solved by the application of the Hankel inversion theorem[9]:

$$2\pi(\rho(r)-\rho_0) = \int_0^\infty ki(k)J_0(rk)dk. \quad (12)$$

For the determination of this density function, the function $i(k)=(I_n/I_i)-1$ must be known, and therefore the curves I_i for independent scattering, and I_n for nonindependent scattering. These curves are available from experiment, but are obtained in relative intensities.

The problem of correlating the two curves is discussed in the experimental part.†

Theoretical Analysis of the Effect of Interparticle Interference

The function $G(kr)$ is a composite of two simpler functions, the radial density function $2\pi r(\rho(r)-\rho_0)$, and a zero Bessel function, $J_0(kr)$. [See Eq. (10a).]

The Distribution Function, $g(r)$

The radial density function $2\pi r(\rho(r)-\rho_0)$ in which ρ_0 is the mean density of particle centers in the equatorial plane throughout the sample and $\rho(r)$ the density in this plane at distance r from the center of any reference particle, can also be written: $2\rho_0(g(r)-1)$, in which $g(r)$ is the radial distribution function. The number of centers found within radii r and $r+dr$ is, therefore, $2\pi r\rho_0 g(r)dr$. The lowest possible value of r is apparently $2R$, if R is the average radius of particles.

One of the obvious properties of this function is that it has pronounced maxima and minima if some periodicity exists in the distribution of the particles; this is generally the case at closer packing. The distance of the first maximum is termed r_{max}. The subsequent maxima are steadily lower and thus the curve rapidly converges toward the mean density value ρ_0 for larger

351–355 (1935); Warren, Krutter, and Morningstar, J. Am. Chem. Soc. **19**, 202 (1936); G. L. Simard and B. E. Warren, J. Am. Chem. Soc. **58**, 507 (1936); J. Biscoe and B. E. Warren, J. Appl. Phys. **13**, 364 (1942). B. E. Warren and N. S. Gingrich, Phys. Rev. **46**, 248–251 (1934).

[5] N. S. Gingrich, Phys. Rev. **59**, 290–292 (1941); Revs. Modern Phys. **15**, 90–119 (1943); A. Eisenstein and N. S. Gingrich, Phys. Rev. **58**, 307 (1940); **62**, 261 (1942).

[6] T. Katzoff, J. Chem. Phys. **2**, 841–851 (1934).

[7] P. Debye and A. M. Bueche, J. Appl. Phys. **20**, 518–525 (1949).

[8] G. Oster and D. C. Riley, Acta Cryst. **5**, 1–6 and 273–276 (1952).

[9] I. N. Sneddon, *Fourier Transforms* (McGraw-Hill Book Company, Inc., New York, 1954), pp. 62–65.

† In a study of atomic distribution functions, Finbak[15] emphasises that the lower intensities at large angles (of which the exact measurement is besides difficult) have a disproportionate influence on the distribution curve. He avoids this difficulty by introducing an "*electronic*" radial distribution function in which the difference I_n-Nf^2 (corresponding to I_n-I_i in the present case) is used instead of the proportion of these same quantities, I_n/Nf^2-1. Systematic errors resulting from inaccurate measurements of intensity in this range are thus greatly reduced.

In small particle scattering, the intensity falls much more rapidly with angle than in atomic scattering, so that the above considerations are even more important. For this reason less weight will be assigned in the experimental analysis to the low intensities at larger angles.

The use of the Finbak equation, modified for cylindrical symmetry by the author, was not found, however, to offer special advantages or to give essentially different results in the present case of small particle scattering.

values of r. If the particles are not closely and regularly packed, the maxima and minima are less pronounced and the curve is flatter and finally approaches a horizontal straight line, corresponding to ρ_0, as has been discussed in the preceding paper.

The Bessel Function, $J_0(kr)$

This function, which represents the scattered amplitude from a ring of material at a radius r around the origin center in the equatorial plane, is likewise represented by a converging fluctuating curve. It has an initial maximum $kr=0$, passes through a zero value at $kr=2.4048$, has a first minimum for $kr=3.8317$, a second zero value for $kr=5.5201$, and a "first" maximum at $kr=7.0156$. Figure 1 gives a few curves as a function of the angle ϵ (which is proportional to k) for 3 values of r. It is seen that for larger values of r the maxima and minima are closer together.

The Function $G(kr)$

This function, which represents the effect of interparticle interference, combines the features of the density distribution function with those of the Bessel function. One single Bessel function, corresponds to every value of r in the density function. The *angular location* of the maxima, minima, and influctions of these single functions are determined by the charateristics of the Bessel function, their *magnitudes* by those of the distribution function. The distribution function will be found (in the experimental part) to have its main density fluctuations in the area from 0–150 A. It is seen from Fig. 1 that the J_0 curves corresponding to such values of r show, in general, about 2 or 3 waves in the interval between zero and 0.006 radian.

The $G(kr)$ function is the integral of all these single curves *for all possible values of* r. This curve will itself, therefore, also fluctuate and converge around zero value. This is illustrated in Fig. 1(D).

The $G(kr)$ function may be considered as being superimposed on the curve for independent scattering $I_i=N\phi^2(kr)$, which following Eq. (10) is multiplied by $1+G(kr)$ to yield the curve for nonindependent scattering. Its maxima, minima, and inflections, are, therefore, reflected in the latter curve. At angles for which the $G(kr)$ function is zero—i.e., somewhere between the maxima and minima of the latter curve—the intensities of the independent and nonindependent scattering curves will accordingly be equal. The coordinates at these angles can be used as points of reference for correlating the two scattering curves so as to express them in the same intensity units.

Approximation of particle distance from angular location of maximum, inflection, and minimum in the scattering curve.—The $G(kr)$ function, being the integral of an infinite number of single Bessel functions, is highly complex in nature, and the density distribution function which underlies it can only be obtained in a reliable way by means of a Fourier synthesis of the scattered intensity as discussed in Sec. 1.

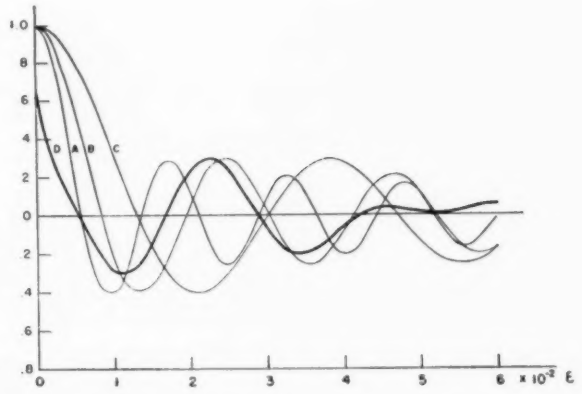

FIG. 1. $J_0(kr)$ curves for different values of r (in A units). (A) $r=100$; (B) $r=70$; (C) $r=45$; (D) average curve of $r=70$ plus $r=80$ minus $r=45$.

In the distribution analysis of fluids, the earlier investigators (Ehrenfest,[10] Keesom and de Smedt[11] Stewart[12] and in one case also Warren,[13] however, endeavored to obtain an answer by assuming a simplified situation in which the integral is substituted by the single function.‡ This amounts to the assumption that the atoms act in pairs, as in diatomic gases. Since in liquids each atom actually acts with *all* of the others, the results can at best be considered as very rough approximations which may be applied under very special conditions only.

In small particle scattering, such a simplified situation would correspond to a concentration of scattering material only at *one* definite distance r_{max} from the origin center. Under this assumption, the $G(kr)$ function for fibers would have maxima and minima identical with those of the single function $J_0(kr_{max})$. The distance r_{max} could then conversely be associated with the maxima and minima and inflections of the $G(kr)$ function and hence with the maxima and minima of the experimental scattering curve by the following

[10] P. Ehrenfest, Proc. Koninkl. Akad. Amsterdam **17**, 1184 (1915).

[11] W. H. Keesom, Physics **2**, 1181 (1922); **5**, 125 (1924); W. H. Keesom and J. de Smedt, Proc. Koninkl. Akad. Amsterdam **25**, 118–124 (1922); **26**, 112–115 (1923).

[12] G. W. Stewart, Revs. Modern Phys. **2**, 116–122 (1930); Trans. Faraday Soc. **29**, 982–983 (1933); G. W. Stewart and R. W. Morrow, Phys. Rev. **37**, 232–244 (1927).

[13] B. E. Warren, Phys. Rev. **44**, 969–973 (1932).

‡ In atomic scattering for liquids, the ("three-dimensional") function $\sin(kr)/kr$ takes the place of the ("two-dimensional") Bessel function used in this paper in connection with the cylindrical symmetry of fibers. The coefficient in the original Keesom equation $\lambda=0.814\times 2r\sin\theta$, corresponds to the first maximum of this function. The ("one-dimensional") function $\cos(kr)$ applies to complete crystalline packing and can be rewritten as Bragg's equation, in which the coefficient is unity. The use of Bragg's equation in liquid scattering, as, for instance, done by Stewart[12] in the earlier years, introduces another simplification which corresponds to a nearly fully crystalline periodicity, or *cybotactic* condition, which this author accepts for liquids.

equations:

first maximum: first inflection: first minimum:

$$kr_{max}=7.0156 \quad kr_{max}=5.5201 \quad kr_{max}=3.8317 \quad (15)$$

which can be rewritten in analogy to Bragg's equation:

$$n\lambda=0.895\cdot 2r\sin\theta \quad n\lambda=1.140\cdot 2r\sin\theta$$
$$n\lambda=1.640\cdot 2r\sin\theta \quad (16)$$

in which r is the average distance of neighboring particle centers from a reference particle and the wavelength of the radiation. For small angles, $2\sin\theta$ may be taken equal to the scattering angle in radians.[2]

The real situation in small angle scattering by fibers is less simple; the distribution functions, determined in the experimental part of this paper, show that important inhomogenities of density occur also at other distances than r_{max}, just as in liquids. Therefore, contributions from other distances than r_{max} have also to be taken into account. These other contributions will to a larger or smaller extent—depending on the distribution function—influence and shift the location of the intensity maxima and minima originating from the high density peak at r_{max}. The deep minimum, expecially which generally occurs at the beginning of the particle distribution curve, may largely influence the location of these maxima and minima. (See Fig. 1.) Only if the concentration of scattering matter at r_{max} is extremely high and if the initial minimum is less pronounced (as in dense packing), can a reasonable correlation between r_{max} and the maximum of the scattered intensity be expected.

It will be investigated in the experimental part whether under certain conditions the above approach will have some value for a quick approximation of the average particle distance in fibers.

EXPERIMENTAL PART

Features of Experimental Scattering Curves

The scattering diagrams were obtained with the technique described in the preceding paper[1] in which the diagrams and curves of different fibers have already been published and discussed. The diagrams of Fortisan rayon are given here as an example. Figure 2 shows the diagrams of this fiber at different degrees of swelling. A is the diagram of the dry fiber; B and B′ of the water swollen fiber, and C of the highly swollen fiber in which interparticle interference is almost completely absent. The distribution of scattered intensity corresponding to these cases is represented by the curves in Fig. 3.

The intensity distribution of Fortisan in the water swollen condition B shows a clear minimum and maximum which has already been *qualitatively* explained in foregoing papers[14] as being due to interparticle interference. The maxima and minima were namely

[14] A. N. J. Heyn, Nature **172**, 1000 (1953); Textile Research J. **23**, 782–87 (1953).

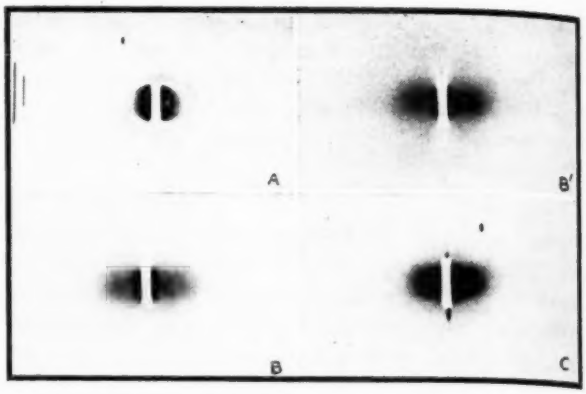

FIG. 2. Small angle x-ray scattering by Fortisan.[14] (A) Fortisan in the dry state; (B) (B′) Fortisan swollen in water; (C) Fortisan swollen beyond the water swollen condition. Note limited scattering area in A; larger area and presence of maximum in B and B′; and high intensity and absence of a maximum in C. Original size; sample distance 20 cm.

found to become less pronounced and to shift slightly at higher degrees of swelling where interparticle interference plays a smaller part and finally to disappear completely. This is illustrated by curve A, Fig. 3, of the highly swollen fiber. This curve shows an inflection only and approaches the curve for independent scattering I. In the majority of cases investigated, distinct maxima and minima are not observed in the scattering curves. The curves of jute (Fig. 4), for instance, do not show any maxima and minima; the curve of the water-swollen fiber B shows only an inflection (like Fig. 3, A).

No fundamental difference exists, however, between these nonindependent scattering curves of varying shapes. This follows from the smooth and gradual transition of the different types of curves into each other and finally into the independent scattering curves with increased swelling, as described in previous papers,[14,1] and also from theory.§

Correlating of Curves

For the determination of the distribution function, the function $i(k)=(I_n/I_i)-1$ must be known. The curves I_i for independent scattering and I_n for nonindependent scattering are obtained from experiment only in *relative* intensities, due to the differences in absorption under different conditions. The curves cannot be directly correlated, therefore.

It was possible to correlate the curves by introducing a correction factor for absorption under different conditions of swelling (the absorption in different *directions* of scattering may be assumed to be the same within the narrow angular region of scattering, contrary to what is the case in atomic scattering). For this purpose,

§ The deviation of the nonindependent scattering curve from the smooth, bell-shaped independent scattering curve is namely determined by the shape of the $i(k)$ curve. If the latter curve has intensive maxima and minima, clear maxima and minima will be imposed on the first curve; otherwise, more or less distinct inflections will only result.

the transmitted radiation was directly measured with a Geiger counter. The intensity of the primary beam was reduced in all cases with the same absorbing screen; a difficulty was the accurate stabilization of the original beam. In later experiments, the exposures were, therefore, standardized by means of a nickel foil placed in part of the transmitted beam. The 111 reflection of the nickel was photographed on the same film along with the complete exposure of the sample, thus providing a measure for the exposure at 0 angle.

In addition, an *indirect* method was also followed for correlating the curves by "fitting." Since, according to theory, the I_n curve fluctuates *around* the I_i curve and converges (so that the functions closely agree at larger angles), a conversion factor for "fitting" the curves can be indirectly found from the intensities at larger angles.‖ In the present case of small angle scattering it proved more desirable,‖ however, to use the more central part of the curve for fitting. This was done in the following way.

At angles where the $G(kr)$ function has zero value, the two curves will have the same ordinate (and hence cross-over). These angles correspond roughly to the inflections between neighboring maxima and minima. The inflections can thus be used as correlation (identity) points for the two curves. This method is used in Fig. 3. If a more correct fitting is desired the method proposed for curve "fitting" in atomic distribution analysis by

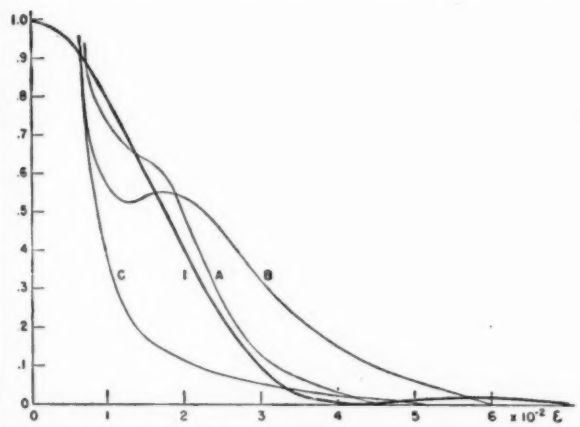

FIG. 3. Normalized distribution of intensity in small angle scattering by Fortisan. (I) Theoretical curve for independent scattering; (A) fiber swollen beyond the water swollen state; (B) fiber swollen in water; (C) fiber in dry state.

‖ This is the main method in the analysis of atomic distribution functions, where the atomic scattering function (which is taken from tables) corresponds to the I_i function. It is customary to "fit" the curves here at very wide angles where the two functions are known to closely agree. Since the intensities at these angles are low and less accurately measured, this cannot be done with great accuracy. Hultgren, Gingrich, and Warren,[4] describe a method for fitting their entire length, but this method is very cumbersome. Gingrich[5] and Finbak[15] have discussed the results of inaccurate curve fitting.

In small particle scattering, the intensity falls much more rapidly with angle than in atomic scattering so that the fitting should be mainly done here with the more central part of the scattering curve. (See also reference †.)

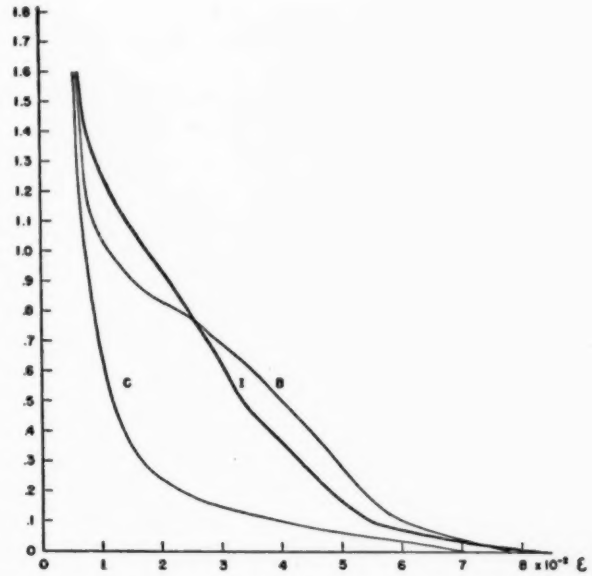

FIG. 4. Distribution of intensity in small angle scattering by jute; intensities in same arbitrary units for all curves. (I) Theoretical curve for independent scattering; (B) fiber swollen in water; (C) fiber in the dry state.

Hultgren, Gingrich, and Warren[4] can be applied. Instead of the experimental curve, the theoretical normalized independent scattering curve is further often used as is customary in atomic distribution analysis. An advantage is that all other curves correlated, will thus also be normalized.

Figure 3 represents the correlated intensity curves of Fortisan. I is the normalized theoretical, independent scattering curve for a particle size, $R=22.5$ A (determined in the preceding paper); B is the experimental curve of the same fiber swollen in water; A the curve after swelling beyond the water swollen condition (e.g., 5% sodium hydroxide); and C the curve of the dry fiber. Curves B and C have been converted by using the inflection point as point of identity. The point of reference in curve C was taken at a slightly smaller angle than in curve B and had to be estimated since no inflection point occurs in this curve.

The correlated intensity curves of jute are given in Fig. 4.

Graphical Integration

After the scattering curve has thus been converted into the same units, the further procedure amounts to evaluating the integral of Eq. (11). This is done graphically in the following way: (1) the function $(I_n/I_i)-1$ is plotted *versus* k. (2) A *possible* value of r is chosen and the curve $ki(k)\cdot J_0(kr)$ is plotted as a function of k. (3) The area under this curve is determined (the part which lies below the abscissa must be subtracted from the part which lies above it). This area is proportional to $\int_0^\infty ki(k)\cdot J_0(rk)dk$, for the single r. (4) The same is done for other possible values of r

and the areas under the various curves are plotted *versus* r. The latter curve is the density function, $2\pi(\rho(r)-\rho_0)$.

The Fourier transformation requires that the intensity of the scattering be known from $k=0$ until $k=\infty$. The experimental intensity is only known, however, between finite limits. This change of limit might cause small errors in the distribution function. The part at larger angles, on the other hand, has a disproportionate influence and may cause spurious peaks to occur in the distribution function, if the measurements in this part of lower intensity are not very accurate.[1] The neglecting of the part at larger angles will, therefore, rather improve the results. In the present paper, the limits were generally from 0.005 until 0.06 radian (in Fortisan, e.g., 0.005–0.0275 radian corresponding to the main area of small angle scattering in this fiber).

DISCUSSION OF RESULTS

General Features of Distribution Functions

The distribution functions calculated for the different fibers are given in Figs. 5 and 6. In these figures, A is the distribution function for the dry fiber, B the fiber swollen in water, and C the fiber swollen beyond the water swollen condition.

The distribution curves show the general features discussed in the theoretical part. They are very simple and show great similarity. The curves fluctuate and converge towards zero value. A fully smooth transition is found between subsequent maxima and minima. This is to be expected since the distribution curves are statistical curves, representing the *density of particle centers averaged over all directions in the equatorial plane, and around any particle.*

The initial traject between $r=0$ and $r=2R$ has no direct physical significance since no particle centers can be present within this interval; this part of the curve is therefore indicated by a dotted line. The curve continues the same direction here as it had just outside this interval. This differs from the findings in atomic distribution analysis where the curve theoretically follows the abscissa and where spurious maxima, which are often found in experiment, have been ascribed to systematic errors resulting from incorrect curve fitting, due to inaccurate intensity measurements at larger angles (Debye and Menke,[3] Finbak[15]). Such irregularities are in that case also found in the significant part of the curve (Finbak[15]). Such irregularities are not found, however, in the present particle distribution curves of which the general appearance is extremely regular and in this respect better than of any atomic distribution function reported. The possibility of incorrect fitting appears improbable therefore. (This conclusion is further substantiated by the fact that the angular locations of the maxima in "electronic" distribution functions of the same fibers—not further discussed in this publication—are the same as in the present distribution function. See footnote †.)

[15] C. Finbak, Acta. Chem. Scand. **3**, 1279 (1949); **3**, 1293 (1949).

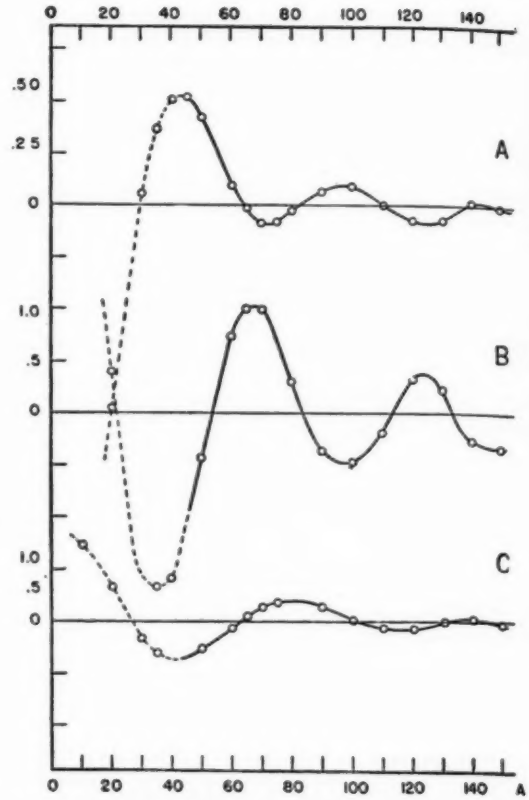

FIG. 5. Radial distribution functions of particle centers for Fortisan rayon. (A) dry fiber; (B) fiber swollen in water; (C) fiber swollen beyond the water swollen state. Abscissa: Distance from origin in A; Ordinate: Units marked on *right* side of axis designate $2\pi(\rho(r)-\rho)_0$; each division equals 5 units if ρ is given in number of centers per (100 A)^2. Same units for A, B, and C. Units marked on *left* side of axis designate absolute values of $g(r)-1$. The units for A, B, and C are different and are only marked on part of the positive axis for each case.

Radial Distance of Maxima and Minima of Density

Fortisan

The distribution curves found with Fortisan are given in Fig. 5. With dry Fortisan, A, the first maximum of density of particle centers, is found at a distance of $r=45$ A. This means that the particles, if they are assumed to have cylindrical shape, must touch each other in the dry fiber, since their "radius" was found to be 22½ A. This follows also from other data; namely, the fiber is known to have almost 100% crystallinity so that amorphous material does not take any space between the microcrystallites. These facts together point conversely to the conclusion that the "radius" determined must indeed be attributed to nearly cylindrical particles and must not merely be considered as a measure of the radius of gyration of particles of unknown shape. If the particles were not of cylin-

drical, but, for instance, of lamellar shape, a different spacing than 45 A would more probably result at closest packing for the same radius of gyration. The first maximum in the dry condition is followed by a minimum of 72 A, a second maximum at 98 A, and a second minimum at 135 A.

With the water swollen fiber B, the first maximum occurs at a distance of 68 A. This is in good agreement with the moving apart of the microcrystallites upon swelling. This maximum is followed by a minimum at 97 A and a second maximum at 123 A. The location of the second maxima is in agreement with what can be expected, if a roughly hexagonal packing is assumed. [See Fig. 7(B) in which the calculated second minimum lies at 97.5 A and the second maximum at 127 A.]

With the highly swollen fiber, C, a first maximum is found at 80 A followed by a first minimum at 115 A after which the curve is nearly horizontal.

In the water swollen condition B, the maxima and minima are more intense than in the other conditions (A and C). The flatter maxima and minima in the other curves can be explained by the more irregular packing resulting from high swelling in condition C, and the very close packing of particles of not fully uniform size in the dry condition A.

Fiber G

The distribution curves of fiber *G* are very similar to those of Fortisan. With the dry fiber, the first maximum is found at 47 A; with the water swollen fiber at 74 A.

Jute

The distribution functions of jute (Fig. 6) are different from those of the foregoing fibers. With the dry fiber, an intense first maximum is found at 35 A

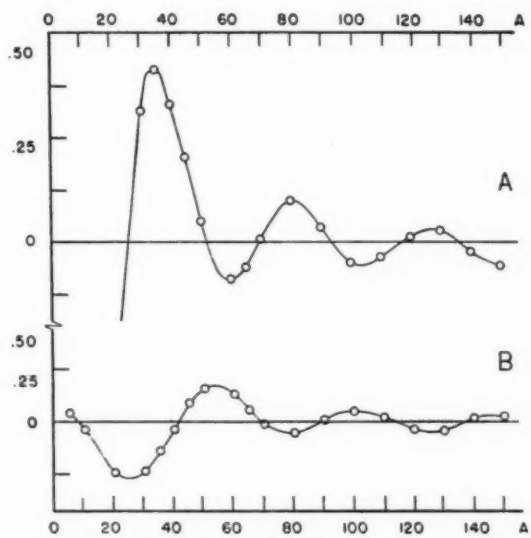

FIG. 6. Radial distribution functions of particle centers for jute. (A) Dry fiber; (B) fiber swollen in water. Abscissa: see same under Fig. 5. Ordinate: see same under Fig. 5.

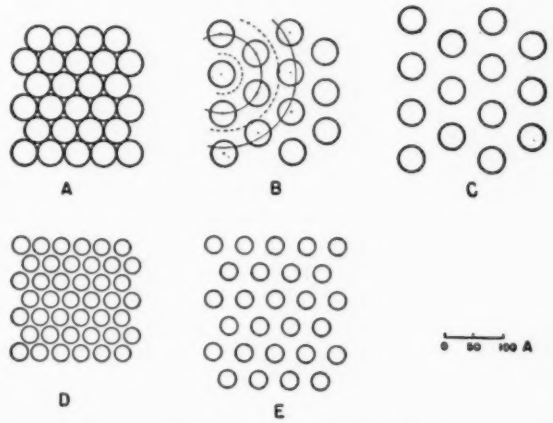

FIG. 7. Schematical representation of size and distribution of microcrystallites in Fortisan rayon (above) and jute (below). (A) Fortisan dry; (B) same swollen in water; (C) same swollen beyond the water swollen state; (D) jute dry; (E) jute swollen in water (scale 100 A). The circular and equal cross section of the microcrystallites is schematical; their shape and size will actually more or less deviate from this average. The concentric circles in (B) correspond to the calculated (and experimental) first minimum, first maximum, second minimum and second maximum of density of particle centers around each particle.

and with the water swollen fiber at 53 A. The maxima of the water swollen fiber are much less intense than those of the dry fiber. This differs from what was found in rayons, where the situation is reversed.

The location at 35 A of the first maximum in the dry condition indicates that the particles do not completely touch each other in the dry state (as in Fortisan) since their diameter was found to be 28 A units. The space between the particles is filled up by amorphous cellulose and lignin. This may allow a more regular packing which, in turn, may account for the above-mentioned more intense maximum in this condition.

Figure 7 is a schematic representation comparing the size and distribution of the microcrystallites in Fortisan, rayon, and jute.

Absolute Density Values

The ordinates y of the distribution curves of Figs. 5 and 6 represent the absolute density of particle centers, $2\pi(\rho(r)-\rho_0)=2\pi(g(r)-1)\rho_0$, in absolute values and, hence, gives the distribution function $g(r)-1$ in relative values. By dividing these values by 2π, the deviation of densities from the over-all density throughout the sample is obtained in absolute values, and by dividing these latter values by ρ_0, the distribution function $g(r)-1$ can be obtained in absolute values.

For the latter purpose, it is necessary to know ρ_0. This value can be calculated from the statistical distance of neighboring particle centers (location of of first maximum in distribution curve). If a hexagonal packing is assumed, the density ρ_0 of particle centers per square A equals then $1/(\frac{1}{2}V3r_{max}^2)$ and $g(r)-1$ equals $y\frac{1}{2}V3r_{max}^2/(2\pi)$. For the samples of Figs. 5A, B, C, and 6A, B the center density is thus found to be

TABLE I. Particle distance in Fortisan and fiber *G* rayons at different degrees of swelling.

Condition	From first maximum of distribution curve	From minimum of the scattering curve	From inflection of the scattering curve	From maximum of the scattering curve
		Fortisan		
Normal swelling in water (B)	68	72	84	90
Swollen beyond the water swollen state (C)	80	81	96	111
		Fiber *G*		
Normal swelling in water (B)	74	78	90	95.5

respectively: 5.96, 2.50, 1.80, and 9.43, 3.96 per (100 A)^2. The values of the distribution function at the first maximum are found to be, respectively: 0.28, 0.68, 0.18, and 0.28, 0.13. The latter values multiplied by ρ_0 give the absolute density at the first maximum: in the case of Fig. 5B, the density at the first maximum is, for instance, 68% above the over-all density of 2.5 which is in total 4.2 centers per (100 A)^2. In a similar way, the absolute density at the minima or at any other distance from a reference center can be directly calculated for the distribution curves.

Approximation of Particle Distance from Minimum and Maximum of Scattering Curves

The particle distance was calculated by the approximation formulas of Eq. (15) and Eq. (16) for two cases in which distinct minima and maxima occured in the scattering curve, namely, Fortisan and fiber *G* rayon. In the theoretical part, it has been pointed out already that these equations have only limited value and that they can be only applied under certain conditions and for a quick approximation.

In Table I, the values obtained with these formulas are compared with the values which follow from the distribution curves (distance of first maximum of distribution curve). It is seen from this table that the best agreement is obtained when the distance is calculated from the *minimum* of the scattering curve and that the largest differences (about 30%) occur if the approximation is made from the *maximum* of the distribution curve.

Degree of Crystallinity

The results obtained with the dry fiber furnish a direct measure for the degree of crystallinity, the proportion between crystalline and amorphous material. This proportion follows from the diameter and the center-to-center distance of the microcrystallites in the dry state. If it is assumed that all space between the crystallites is filled with amorphous material and that no interspaces exist, this is given by the ratio $\pi R^2 \div (2r)^2$, (a); if the interspaces at closest packing (where the microcrystallites touch each other) are assumed to be empty, it is given by $R^2 \div r^2$, (b).

For Fortisan, the following values can be calculated: 100% (b) or 78.5% (a) and for jute 64% (b) or 50.3% (a).

General Conclusion

The above findings complement those of preceding papers[1] on the high regularity of the microcrystalline (or supermolecular) structure of natural and artificial cellulose fibers. In previous papers the great uniformity in *size* of the microcrystallites had been concluded. From the results of the present paper the great regularity of their *distribution* in space can be concluded. The *quantitative* determinations show further that size and distribution of microcrystallites vary with the type of the fiber and that their density of distribution varies in the same fiber, as required, with the degree of swelling. The results fully confirm the conclusion of the preceding paper about the role of interparticle interference and its experimental elimination. With increased swelling the distribution curves flatten more and more out and finally approach a straight horizontal line. From this moment on, interparticle interference no longer plays a part, and independent particle scattering prevails.

ACKNOWLEDGMENTS

The author is indebted to the Claude W. Kress Research Foundation of Clemson College for a grant for equipment, used in this study and the DuPont de Nemours and Celanese Corporation for samples of fiber *G* and Fortisan.

A Semiempirical Expression for the First Townsend Coefficient of Molecular Gases

R. W. Crowe, J. K. Bragg,* and J. C. Devins
General Electric Research Laboratory, Schenectady, New York

(Received January 29, 1955)

The general utility of an approximate expression for the first Townsend coefficient of a gas, derived several years ago by Druyvesteyn and Penning, has been tested by introducing into the theoretical treatment somewhat more realistic assumptions regarding the relevant scattering cross sections of the gas molecule. It has been demonstrated by numerical calculations that the functional dependence of the Townsend α upon the electric field and the gas pressure is, within certain limits, insensitive to the assumed energy dependence of the elastic and inelastic cross sections. The functional form of the inelastic cross section does, however, influence the way in which the ionization energy of the gas molecule enters in the exponential part of the expression.

I. INTRODUCTION

THE starting point for all calculations of the first Townsend coefficient of a gas is the determination of the distribution in energy, $W(\epsilon)$, of conducting electrons in the presence of an electric field, E. The success of such a determination requires, among other things, an accurate knowledge of certain physical properties of the gas molecules, such as their elastic, excitation, and ionization cross sections. In general, these properties are not well understood either upon theoretical or experimental grounds. As a result, complete theoretical discussions of the conduction process have been limited to very special cases involving some of the rare gases, for which fairly thorough experimental studies of the relevant cross sections have been carried out.[1–3] Because of the highly complex nature of the resulting distribution function, a numerical procedure must be used to calculate the Townsend α for these gases.

In 1940, Druyvesteyn and Penning[4] attempted to simplify the problem in order to obtain a more general and useful expression for α. By assuming an elastic cross section independent of energy and an average value of the inelastic cross section, they derived an expression for the distribution function from which they were able to show that

$$\alpha/P \approx (A_0 E/P)\exp(-B_0 P/E), \qquad (1)$$
$$B_0 = (3\sigma_i\theta)^{\frac{1}{2}}(\epsilon_i - \epsilon_e)(N_a/P),$$

at low values of E/P. In this expression A_0 is a constant characteristic of the gas, σ_0 is the assumed inelastic cross section, θ is the elastic cross section, ϵ_e and ϵ_i are the thresholds for electronic excitation and ionization, N_a is the number of gas molecules per unit volume, and P is the gas pressure.

Recently, we have become interested in trying to correlate sparking potentials of gases with molecular structure, a procedure that obviously requires some knowledge of the manner in which molecular properties influence α. Thus it seemed of interest to determine, if possible, the general utility of Eq. (1). The procedure adopted in the present work was to introduce into the theoretical treatment somewhat more realistic assumptions regarding the energy dependence of the elastic and inelastic cross sections of the gas molecule. Such a procedure should provide a test of the sensitivity of the result to the assumed cross sections.

II. DISTRIBUTION OF ELECTRONS IN ENERGY

The present work follows the derivations of Smit[1] and Druyvesteyn.[2] If we ignore the term involving electron energy loss produced by elastic scattering, the differential equation relating $W(\epsilon)$ to ϵ, as derived by Smit, reduces to[5]

$$dW/d\epsilon - W/2\epsilon + G/a\epsilon^{\frac{1}{2}} = 0, \qquad (2)$$
$$a = e^2E^2/3N_a\theta,$$
$$G = N_a\int_\epsilon^\infty x^{\frac{1}{2}}\sigma(x)W(x)dx.$$

In this equation, σ is the sum of the scattering cross sections for all excitation and ionization processes. The solution of Eq. (2) depends upon the assumptions made regarding the dependence of σ and θ upon ϵ. For the sake of simplicity we consider inelastic collisions involving only electronic excitation and ionization of the gas molecule.

A. θ Independent of ε

If we assume that θ is independent of ϵ, then in the range of energy below ϵ_e,

$$W(\epsilon) = \epsilon^{\frac{1}{2}}[C_1 - (G_0/a)\log\epsilon], \quad \epsilon < \epsilon_e, \qquad (3)$$
$$G_0 = N_a\int_{\epsilon_e}^\infty x^{\frac{1}{2}}\sigma(x)W(x)dx.$$

* Present address: Operations Research, Inc., 8485 Fenton Street, Silver Spring, Maryland.

[1] J. A. Smit, Physica **3**, 543 (1936).

[2] M. J. Druyvesteyn, Physica **3**, 65 (1936).

[3] J. Abdelnabi and H. S. W. Massey, Proc. Phys. Soc. (London) **A66**, 288 (1953).

[4] M. J. Druyvesteyn and F. M. Penning, Revs. Modern Phys. **12**, 87 (1940). See their Eq. (43).

[5] We have calculated $W(\epsilon)$ numerically for an idealized system that included the influence of elastic scattering. The results were, provided E/P was not too low, almost identical to those obtained from the following equations throughout the energy range of interest.

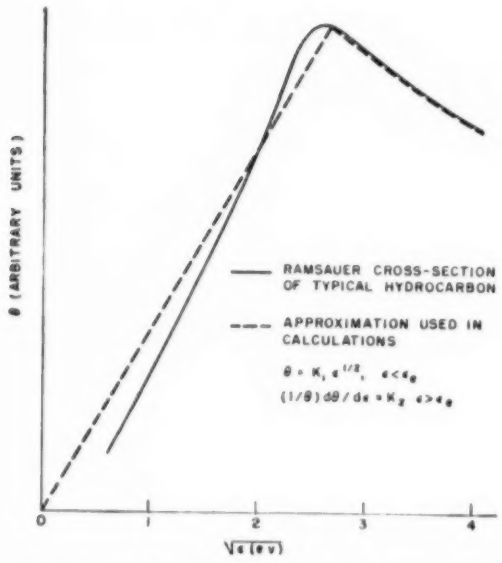

FIG. 1. Variation of the total scattering cross section of a typical hydrocarbon molecule with electron energy.

By differentiating Eq. (2) in the range $\epsilon > \epsilon_e$, and ignoring $\frac{1}{4}\epsilon^{-2}$ in favor of $N_a\sigma/a$,[6] we obtain the well-known Druyvesteyn expression[2];

$$d^2W/d\epsilon^2 - N_a\sigma W/a = 0, \tag{4}$$

the solution of which is determined by the functional dependence of σ upon ϵ. If we assume, as an approximation, that σ is of the form, $\sigma = \sigma_0(\epsilon - \epsilon_e)$, the solution is a Hankel function.

$$W(\epsilon) = C_2 i^{\frac{1}{3}} \beta^{\frac{1}{2}} H_{\frac{1}{3}}^{(1)}(2i\beta^{\frac{1}{2}}/3), \quad \epsilon > \epsilon_e, \tag{5}$$
$$\beta = (3N_a^2\sigma_0\theta/e^2E^2)^{\frac{1}{3}}(\epsilon - \epsilon_e),$$
$$i = (-1)^{\frac{1}{2}}.$$

To normalize the distribution, Eqs. (3) and (5) must be joined at ϵ_e and the result integrated.

B. θ Dependent Upon ε

The Ramsauer cross sections of most of the rare gases,[7] as well as those of the aliphatic hydrocarbons,[8] vary with ϵ in a manner similar to that shown schematically in Fig. 1. We can approximate this dependence by assuming that

$$\theta = K_1\epsilon^{\frac{1}{2}}, \quad \epsilon < \epsilon_e$$
$$(1/\theta)d\theta/d\epsilon = K_2, \quad \epsilon > \epsilon_e \tag{6}$$

where K_1 and K_2 are constants for a given gas. For this model, integration of Eq. (2) yields,

$$W(\epsilon) = \epsilon^{\frac{1}{2}}(C_3 - 2G_0\epsilon^{\frac{1}{2}}/d), \quad \epsilon < \epsilon_e, \tag{7}$$
$$d = e^2E^2/3K_1N_a.$$

[6] This simplification is justified provided E/P is not too high.
[7] C. Ramsauer and R. Kollath, Ann. Physik **3**, 536 (1929).
[8] H. S. W. Massey and E. H. S. Burhop, *Electronic and Ionic Impact Phenomena* (Oxford University Press, London, 1952), p. 208.

Now Smit[1] has noted that K_2 for helium is equal to about -0.02. We have examined the Ramsauer cross sections of the hydrocarbon gases and have found that K_2 varies from -0.028 to -0.015 throughout the series from methane to pentane. If we assume that $K_2 = -0.02$ for a typical gas, differentiation of Eq. (2) in the range $\epsilon > \epsilon_e$ (again ignoring $\frac{1}{4}\epsilon^{-2} - 0.01/\epsilon$ in favor of $N_a\sigma/a$) yields the equation,

$$d^2W/d\epsilon^2 + 0.02dW/d\epsilon - N_a\sigma W/a = 0, \tag{8}$$

the solution of which may be written,

$$W(\epsilon) \approx C_4 i^{\frac{1}{3}} \rho^{\frac{1}{2}} \exp[-0.01(\epsilon - \epsilon_e)] \times H_{\frac{1}{3}}^{(1)}(2i\rho^{\frac{1}{2}}/3), \quad \epsilon > \epsilon_e, \tag{9}$$
$$\rho = (3N_a^2\sigma_0\theta/e^2E^2)^{\frac{1}{3}}(\epsilon - \epsilon_e) + 10^{-4}(3N_a^2\sigma_0\theta/e^2E^2)^{-\frac{1}{3}},$$
$$\theta = \theta(\epsilon_e)\exp[-0.02(\epsilon - \epsilon_e)].$$

Comparison of Eq. (9) with Eq. (5) shows that, except for very large ϵ, the introduction of a mean free path whose energy dependence approximates that observed experimentally, has only a minor influence on the shape of the distribution function in the range $\epsilon > \epsilon_e$. Examples of the normalized distribution functions for the two models are shown in Fig. 2.

III. THE FUNCTIONAL FORM OF α

By definition, the Townsend α is given by

$$\alpha = (1/vN)dN/dt$$
$$= (N_a/v)(2/m)^{\frac{1}{2}} \int_{\epsilon_i}^{\infty} x^{\frac{1}{2}}\sigma_i(x)W(x)dx, \tag{10}$$

where v is the electron drift velocity, m is the electron mass, and σ_i is the cross section for ionization. In order to calculate α, either Eq. (5) or Eq. (9) must be introduced into Eq. (10). However, we can obtain certain information about α without resorting to

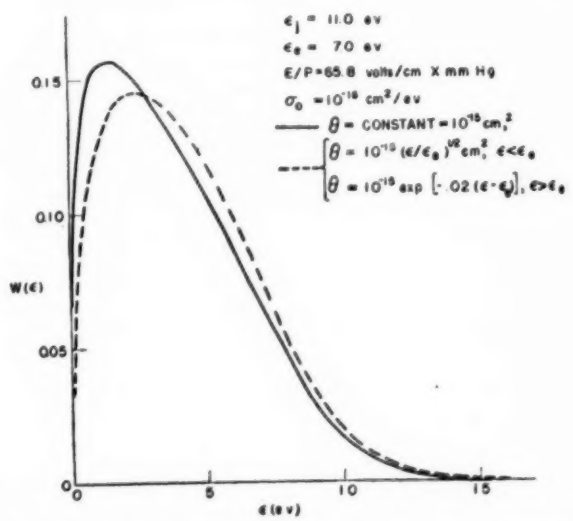

FIG. 2. The influence of an energy dependent mean free path upon the shape of the distribution function.

numerical calculations. By use of the asymptotic expansion of the Hankel function, it can be shown that the exponential variation of α ought to be of the form,

$$\exp[-(1/kT)(4\sigma_0\theta/3)^{\frac{1}{2}}(\epsilon_i-\epsilon_e)^{\frac{1}{2}}(P/E)],$$

where k is the Boltzmann constant and T is the absolute temperature. For the case where Eq. (9) is used, θ should have some average value above that at ϵ_e. Note that this result is nearly the same as the exponential part of Eq. (1). The essential difference arises from the slightly different assumption made regarding the functional form of σ. In fact, it can be demonstrated that, as one writes σ to successive powers (σ_0, $\sigma_0(\epsilon-\epsilon_e)$, $\sigma_0(\epsilon-\epsilon_e)^2\cdots$), the exponent of $(\epsilon_i-\epsilon_e)$ advances by intervals of $\frac{1}{2}$; i.e., $(\epsilon_i-\epsilon_e)$, $(\epsilon_i-\epsilon_e)^{\frac{1}{2}}$, $(\epsilon_i-\epsilon_e)^2\cdots$.

The approximations employed in developing the foregoing expression for the exponential variation of α with E/P are sufficiently severe to obscure a possible pre-exponential dependence upon E and P. In order to investigate such a dependence, and incidentally to support the approximate expression for the exponential factor, we have carried out numerical calculations for the two models discussed in the previous sections. For these calculations it was assumed that $v\approx k_eE/P$, where k_e is independent of E/P. σ_i was approximated by the expression, $\sigma_i=b(\epsilon-\epsilon_i)$. The remaining conditions were chosen such that the range of E/P considered should correspond approximately to that which is significant to most discharge phenomena.

The results of the calculations are shown in Fig. 3 in the form of plots of $\log\alpha/E$ *vs* P/E. Note that the calculated points fall on straight lines, suggesting that

$$\alpha/P\approx(AE/P)\exp(-BP/E),$$
$$B=(1/kT)(4\sigma_0\theta/3)^{\frac{1}{2}}(\epsilon_i-\epsilon_e)^{\frac{1}{2}}, \tag{11}$$

which is of the same general form as Eq. (1). The slope of Curve I in Fig. 3 is within 5% of that predicted by Eq. (11). The slope of Curve II agrees with the predictions of Eq. (11) if one assigns a value to θ in the latter close to that at ϵ_i.

We can generalize our results by saying, (1) that the functional dependence of α upon E and P is not appreciably affected by *certain* variations in the energy dependence of the cross sections involved, and (2) that the functional form of the inelastic cross section influences the way in which the ionization and excitation energies appear in the exponential part of the expression.

It has already been pointed out that inelastic collisions involving excitation of molecular vibrations and rotations have been neglected in the present work. The applicability of Eq. (11) for molecular gases necessarily implies that such processes exert little or no influence on the functional form of α. To be sure they will become increasingly important at very low electron energies, and may very well alter the shape of the distribution in this region. However, the exponential variation of α with E/P, which involves only the high-energy tail of the distribution, should not be appreciably affected by their inclusion. In principle, there is no limit to the number of individual scattering mechanisms that can be included in the equations leading to the determination of $W(\epsilon)$. However, the inclusion of each specific mechanism will lead to the appearance of certain molecular parameters in the expression for α. In order that the derived expression for α be useful for correlative purposes, it is desirable to keep the number of these adjustable parameters at a minimum. Consequently, we have chosen to include only those processes which we believe to be most important in the range of E/P significant to most discharge phenomena.

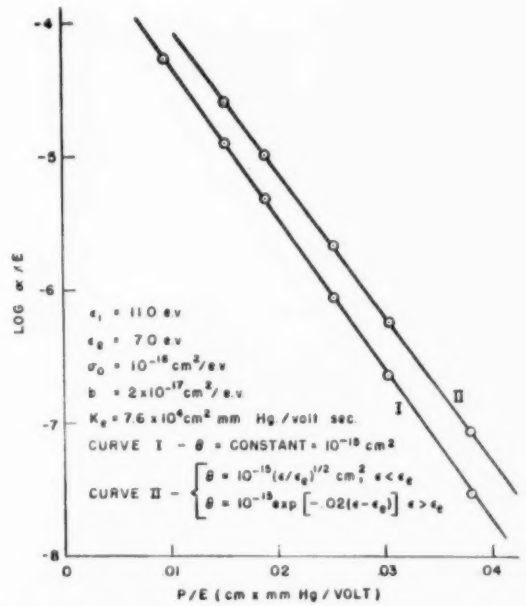

FIG. 3. The calculated dependence of $\log\alpha/E$ upon P/E for a hypothetical gas. Curve I—θ independent of ϵ, Curve II—θ dependent upon ϵ.

IV. APPLICATION TO ELECTRIC BREAKDOWN

By combining Eq. (11) with the Townsend criterion for electrical breakdown, one obtains an expression relating the uniform-field sparking voltage, V_s, to the product of the gas pressure and the electrode separation, $P\delta$;

$$V_s=BP\delta/[\log V_s+\log(A/r)], \tag{12}$$
$$r=\log(1+1/\gamma),$$

where γ is the secondary ionization coefficient. Because γ does not vary strongly with E, r can usually be assumed constant for a given gas. Thus we are provided with a means of determining the exponential factor, B, in Eq. (11) without restoring to the rather difficult measurement of pre-breakdown current.

In order to determine the composite cross section, $(\sigma_0\theta)^{\frac{1}{2}}$ from breakdown measurements, we must have

some information about the energy difference $(\epsilon_i - \epsilon_e)$. Unfortunately, such information is rarely available. However, this energy difference should be nearly proportional to ϵ_i for gases of similar molecular structure and composition. In fact, sparking potentials for a series of such gases should provide information about the influence upon $(\sigma_0\theta)^{\frac{1}{2}}$ of small changes in molecular structure. With this possibility in mind, we are now measuring the sparking potentials of a wide variety of hydrocarbon gases. The results will be published shortly.

The authors wish to express their appreciation to Miss Virginia Thomas of this Laboratory for carrying out the tedious calculations reported here.

JOURNAL OF APPLIED PHYSICS VOLUME 26, NUMBER 9 SEPTEMBER, 1955

Measurement of Susceptibility Tensor in Ferrites*

J. O. Artman and P. E. Tannenwald
Lincoln Laboratory, Massachusetts Institute of Technology, Cambridge, Massachusetts

(Received January 15, 1955)

Experimental techniques for measuring the magnetic susceptibility tensor components in microwave cavities are described. General expressions for the perturbation of microwave cavities by the magnetic properties of ferrites are developed. Experimental results are given for Ferramic 1331 measured at 9165 Mcps. Since these results indicate that both the real and imaginary parts of the tensor components χ and κ are approximately equal to each other in the resonance region, only measurement of the diagonal components may suffice to specify the complete tensor. However, whenever the small differences between χ and κ are desired, measurement of the tensor susceptibility in a degenerate cavity will be necessary. An attempt has been made to compare the experimental results with the Bloch-Bloembergen magnetic resonance theory as applied to circularly polarized excitation.

INTRODUCTION

It is well known that ferromagnetic materials become anisotropic upon application of a magnetic field and that consequently the susceptibility of ferrites must be described by a tensor.[1] Since furthermore the susceptibility exhibits a dispersive as well as an absorptive character, each tensor component consists of a real and imaginary part. In the past many investigators have reported microwave cavity measurements of the imaginary part of the diagonal tensor component. However a determination of all four components is of general interest to provide a comparison between theory and experiment. Furthermore, nonreciprocal components[2,3] such as the Faraday rotator depend on terms involving combinations of the diagonal and off-diagonal components of the susceptibility tensor.

It is the purpose of this paper to describe the experimental techniques used for measuring the tensor components in microwave cavities[4] and to develop the general expressions for the perturbation of microwave cavities due to the magnetic properties of ferrites.

PHYSICAL DESCRIPTION

The study of the microwave behavior of ferrites in cavities has become a standard technique in recent years. Briefly, the sample is introduced into the cavity and the resulting perturbing effects on the cavity Q and resonance frequency upon application of a dc magnetic field are noted. The prime requisite for examining the tensor properties is that the cavity be degenerate in two suitably chosen orthogonal linear modes.

Figure 1 shows the effect of introducing a small ferrite sample into such a degenerate cavity in a region of maximum rf H and zero E fields and applying a dc magnetic field perpendicular to the microwave H vector. The dips represent the cavity resonance absorption as seen on an oscilloscope by observing the microwave signal reflected from the cavity. The horizontal axis is proportional to the microwave frequency. As the dc magnetic field is applied, the single resonance is seen to split into two.

In order to understand what happens as the dc field is varied, one must look at the behavior of the electron spins in the ferrite. When a large steady magnetic field is applied to a ferromagnetic material, the unpaired

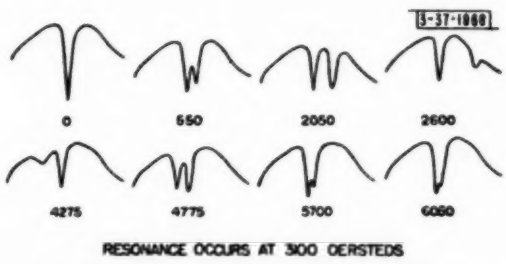

FIG. 1. Splitting of modes in degenerate cavities.

* The research in this document was supported jointly by the Army, Navy, and Air Force under contract with the Massachusetts Institute of Technology.

[1] D. Polder, Phil. Mag. **40**, 99 (1949).
[2] C. L. Hoga, Bell System Tech. J. **31**, 1 (1952).
[3] Lax, Button, and Roth, J. Appl. Phys. **25**, 1413 (1954).
[4] First reported by the authors in Phys. Rev. **91**, 1014 (1953).

electron spins tend to line up with the applied field, and consequently the resultant magnetic moment precesses about the field. The classical precessional motion would be quickly damped out by the crystal lattice unless energy is supplied by an oscillating magnetic field; the microwave radiation provides this oscillating field. Maximum energy is transferred from the microwave field to the electron spin system when the frequency of the microwaves equals the precession frequency of the electron spins. This is the condition of ferromagnetic (or gyromagnetic) resonance.

If the cavity is excited in one linear mode, the precessing electron spins will couple to this mode and in turn couple to and excite the orthogonal mode. Due to this ferrite-cavity interaction, the description of the cavity properties in terms of two orthogonal linear modes is no longer convenient. The linearly polarized excitation can be considered as the sum of two fields or modes circularly rotating in opposite senses. Initially the cavity is degenerate in these two rotating modes. However the precessing spins in the ferrite affect these two fields differently. One field rotates in the same sense as the precessing magnetic dipoles of the ferrite spins and interacts strongly with them; the resonant frequency and cavity Q of this mode are significantly modified, maximum reduction in Q occurring at ferrite resonance. The other mode, rotating in a sense opposite to that of the precessing magnetic dipoles, is hardly affected. These two circularly rotating modes are appropriate for description of the perturbed cavity.

We may designate that mode which rotates in the same direction as the electron spin precession as the "extraordinary mode." We shall show later from the theory that the frequency of this extraordinary mode at first increases with magnetic field; it then becomes negative beyond resonance, reappearing on the other side of the so-called ordinary mode. At approximately twice the resonance field the two modes appear to coalesce again. These features are displayed on the oscilloscope traces of Fig. 1.

In the following sections we shall derive the perturbation expressions for a degenerate cavity and subsequently describe the experimental arrangement. Some of the results and conclusions regarding measurements of the components are stated in the final section.

GENERAL PERTURBATION THEORY[5]

Degenerate Case

When the degeneracy of a resonant cavity is removed by insertion of a small ferrite sample, the two "natural" modes of oscillation characteristic of the perturbed cavity are right- and left-hand circularly rotating. This

[5] The treatment given follows in many respects that of B. Lax, Convention Record, Inst. Radio Engrs., 1953 National Convention, Part 10, pp. 70–74 and unpublished notes.

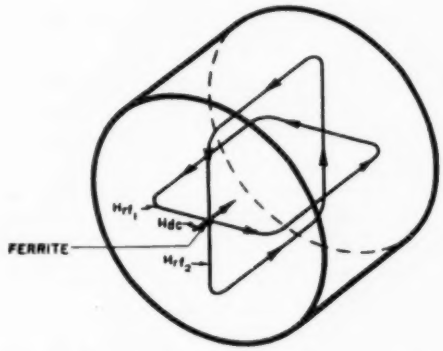

FIG. 2. Orthogonal rf H lines in degenerate cavity.

follows from the nature of the susceptibility tensor χ_m[6]:

$$\chi_m=\begin{pmatrix}\chi & -j\kappa\\ j\kappa & \chi\end{pmatrix}.$$

Consider a cavity that can support two orthogonal modes of oscillation, 1 and 2, as pictured in Fig. 2. The ferrite is placed on the axis of the cavity in a region of zero rf E. Choose axes in the orthogonal 1, 2 directions and let H_1, H_2 be the rf H mode amplitudes in these directions at the position of the ferrite. The relative magnitudes and phases of H_1 and H_2 are unspecified. A "natural" mode of oscillation $\begin{pmatrix}H_1\\ H_2\end{pmatrix}$ satisfies the following relation:

$$(H_1^* \quad H_2^*)\begin{pmatrix}\chi & -j\kappa\\ j\kappa & \chi\end{pmatrix}\begin{pmatrix}H_1\\ H_2\end{pmatrix}=\lambda(H_1^* \quad H_2^*)\begin{pmatrix}H_1\\ H_2\end{pmatrix},$$

or

$$(H_1^* \quad H_2^*)\begin{pmatrix}\chi-\lambda & -j\kappa\\ j\kappa & \chi-\lambda\end{pmatrix}\begin{pmatrix}H_1\\ H_2\end{pmatrix}=0,$$

where λ is some constant.

Solutions are given by

$$\begin{vmatrix}\chi-\lambda & -j\kappa\\ j\kappa & \chi-\lambda\end{vmatrix}=0.$$

Two solutions exist: $H_2=+jH_1$ corresponding to $\lambda=\chi+\kappa$ and $H_2=-jH_1$ corresponding to $\lambda=\chi-\kappa$. H_1 and H_2 are therefore equal in magnitude but due to the factor $(\pm j)$ are in quadrature in time as well as in space—i.e., the natural modes

$$\mathbf{H}_\pm=\begin{pmatrix}H\\ \pm jH\end{pmatrix}$$

are right- and left-hand circularly rotating modes.

[6] The permeability tensor μ_m is defined as $\mathbf{I}+\chi_m$.

$$\mu_m=\begin{pmatrix}\chi+1 & -j\kappa\\ j\kappa & \chi+1\end{pmatrix}=\begin{pmatrix}\mu & -j\kappa\\ j\kappa & \mu\end{pmatrix}.$$

For the case of the empty cavity resonating in the frequency ω_0, Maxwell's equations are:

$$\nabla\times\mathbf{H}_0=j\omega_0\epsilon_0\mathbf{E}_0,$$
$$\nabla\times\mathbf{E}_0=-j\omega_0\mu_0\mathbf{H}_0,$$

where $\mathbf{E}$ and $\mathbf{H}\propto e^{j\omega t}$.

In these and subsequent formulas the electromagnetic field and currents correspond to the rotating modes discussed previously.

If this cavity now contains a perturber located in a small volume Δv, the cavity will then resonate at a new frequency ω. The Maxwell equations in this case are:

$$\nabla\times\mathbf{H}=j\omega\epsilon_0\mathbf{E}+\mathbf{J}_e,$$
$$\nabla\times\mathbf{E}=-j\omega\mu_0\mathbf{H}-\mathbf{J}_m,$$

where $\mathbf{J}_e$ and $\mathbf{J}_m$ can exist only in the small volume Δv occupied by the perturber. If the perturber is a ferrite located in a region where $\mathbf{H}$ is circularly polarized, then $\mathbf{J}_m=j\omega\mu_0\chi_m\cdot\mathbf{H}_0$. $\chi_m\cdot\mathbf{H}$ represents the multiplication of the tensor χ_m into the vector $\mathbf{H}$, but, since $\mathbf{H}$ is circularly polarized, χ_m is then effectively the scalar $\chi\pm\kappa$. The relation between $\mathbf{J}_e$ and $\mathbf{E}$ generally is of a scalar nature: $\mathbf{J}_e=\sigma\mathbf{E}$.[7]

In accordance with the first-order perturbation theory, the two Maxwell equations are now combined, the approximations $\mathbf{E}\cong\mathbf{E}_0$, $\mathbf{H}\cong\mathbf{H}_0$ are made, and the appropriate boundary conditions are applied. These steps are carried out in detail in the Appendix A. The result yields the expressions for the complex frequency shift of the cavity in terms of the tensor components, the sample volume and the microwave magnetic field configuration:

$$\frac{\Delta\omega_\pm}{\omega_0}=\frac{[\chi\pm\kappa]H^2\Delta v}{2\int_v H^2d\tau}.$$

Since in general χ and κ are complex quantities, $\Delta\omega_\pm/\omega_0$ must also be a complex quantity. Thus $\chi=\chi'-j\chi''$, $\kappa=\kappa'-j\kappa''$ and the complex frequency change $\Delta\omega$ by definition is given by

$$\Delta\omega=\Delta\omega_r+j\Delta\omega_i=\Delta\omega_r+j\Delta\left(\frac{\omega_0}{2Q}\right).$$

Therefore the real and imaginary parts of the complex perturbation relation separate as follows:

$$\left(\frac{\Delta\omega_r}{\omega_0}\right)_\pm=-\frac{[\chi'\pm\kappa']H^2\Delta v}{2\int_v H^2d\tau},$$

$$\Delta\left(\frac{1}{2Q}\right)_\pm=\frac{[\chi''\pm\kappa'']H^2\Delta v}{2\int_v H^2d\tau}.$$

[7] B. Lax (see reference 5) discusses magneto-ionic media in which the electric properties are represented in terms of a tensor conductivity σ. For such media $\mathbf{J}_e=\sigma\cdot\mathbf{E}$.

Substitution of the appropriate fields for the circular TE_{11n} mode is carried out in Appendix B.

Nondegenerate Case

It is worthwhile to state briefly the result for the nondegenerate case. Only χ, the diagonal member of the tensor χ_m, contributes to the perturbation since the change in energy depends on

$$(H^*\quad 0)\begin{pmatrix}\chi & -j\kappa\\ j\kappa & \chi\end{pmatrix}\begin{pmatrix}H\\ 0\end{pmatrix}=\chi H^2.$$

The formulas derived for the degenerate case can be modified for a linearly polarized mode and applied to a nondegenerate cavity. κ does not appear in the equations.

The general relations for the change in frequency and change in Q are:

$$\frac{\Delta\omega_r}{\omega_0}=-\frac{\chi'H^2\Delta v}{2\int_v H^2d\tau},$$

$$\Delta\left(\frac{1}{2Q}\right)=\frac{\chi''H^2\Delta v}{2\int_v H^2d\tau}.$$

Substitution of the appropriate fields for the circular TE_{11n} and rectangular TE_{10n} modes is carried out in the Appendix B.

EXPERIMENTAL METHOD[8]

Linear Polarization Apparatus

The basic microwave apparatus is shown in Fig. 3. Energy from a frequency-modulated klystron is fed into a cavity, which is placed between the poles of an electromagnet. Both the power incident upon and reflected from the cavity are monitored by a pair of directional couplers terminated by crystals; forward

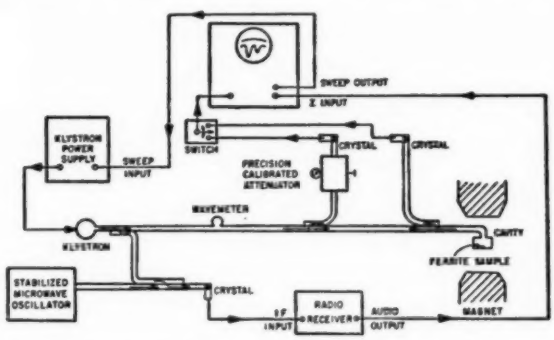

FIG. 3. Apparatus for measuring susceptibility of ferrites.

[8] Details are given by the authors in Technical Report Number 70, Lincoln Laboratory, M.I.T., September 1954.

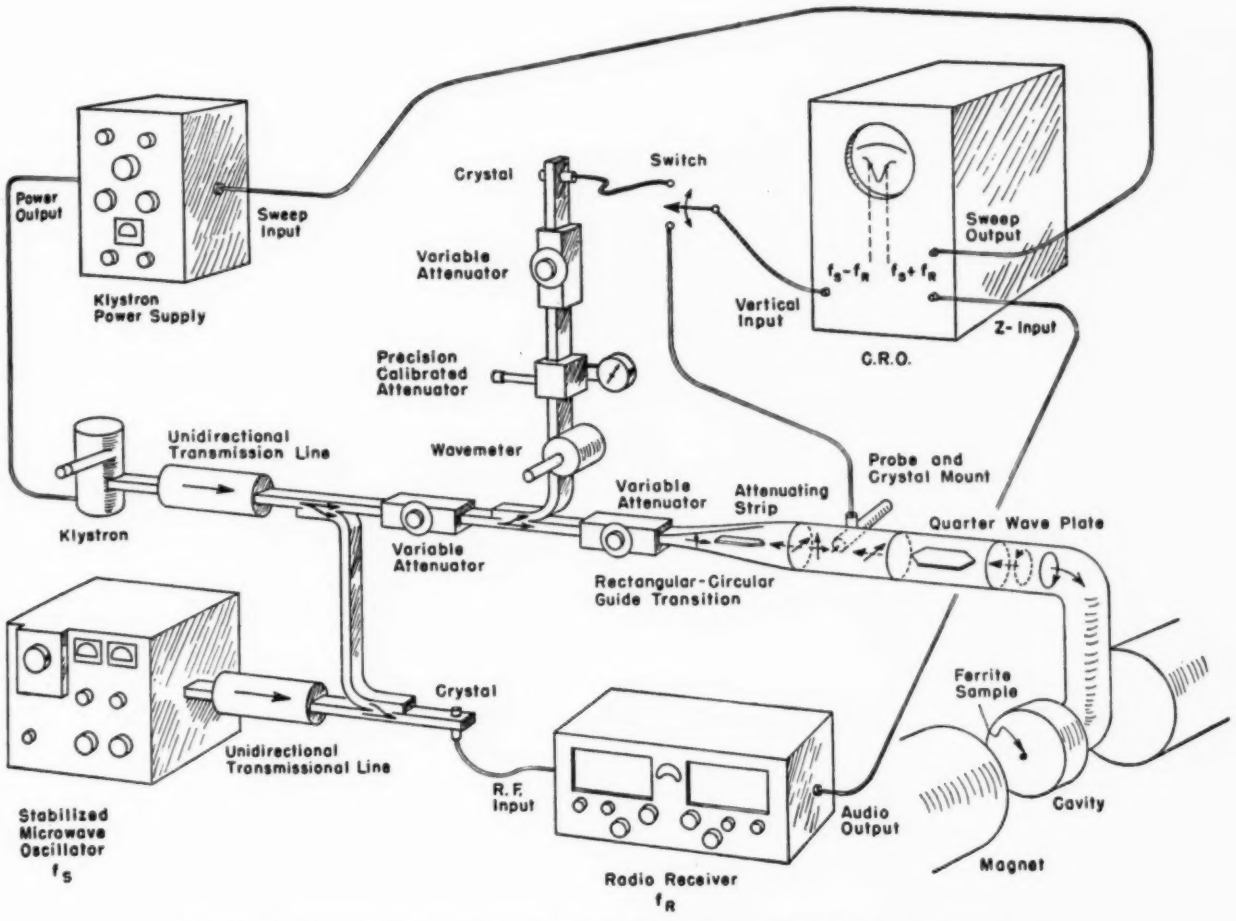

FIG. 4. Measurement of tensor permeability of ferrites using circularly polarized microwaves.

and reflected signals are alternately selected by an electrical switch and are viewed simultaneously on an oscilloscope. Frequencies are measured with a microwave wave meter. The reflection coefficient is immediately determined by noting the attenuation necessary to reduce the incident signal level to that of the reflected signal. The cavity Q is directly related to this reflection coefficient. The cavity properties are observed as the dc magnetic field is slowly increased from zero to and beyond ferrite resonance. The resulting split in cavity resonance will appear on the oscilloscope as shown in Fig. 1. Sets of frequency and Q measurements are made at various magnetic field settings in order to measure the variation of dispersion and absorption as a function of magnetic field.

If differences in frequency have to be measured more accurately than is feasible with a wave meter, a frequency stabilized microwave oscillator is available for reference purposes. Using conventional crystal heterodyning techniques, frequency differences as small as 0.02 Mcps between the cavity resonant frequency and stabilized reference oscillator can be determined by means of a tuned rf receiver.

Circular Polarization Apparatus

Although the mode-splitting of the degenerate cavity (Fig. 1) strikingly demonstrates ferrite tensor properties, exact measurement of these mode parameters is frequently not practical. The two split resonances often overlap sufficiently so as to make determination of individual mode characteristics difficult. However if the cavity is excited with circularly polarized radiation, each of the two modes can be viewed alone, depending on the sense of the incident polarization.

The circular polarization apparatus is shown in Fig. 4. Radiation is fed through the circular wave guide and is incident upon a quarter-wave plate. This plate, $\lambda_g/4$ in length and oriented 45 degrees with respect to the plane of the incident polarization, circularly polarizes the microwave. This polarized signal passes around a pair of polarization-compensated bends and excites the cavity. Radiation returning from the cavity is converted back into linearly polarized waves upon passage through the quarter-wave plate. This reflected signal returns polarized at 90 degrees to the original incident wave. The reflected signal is monitored by a probe and absorbed by a matched termination. The sense of

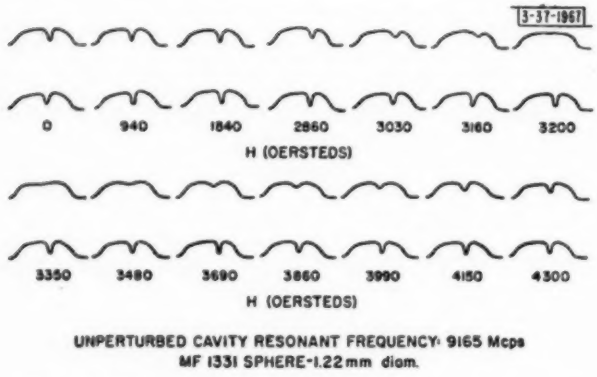

FIG. 5. Effect of ferrite perturbation on the contra-rotating modes in a degenerate cavity.

circular polarization with respect to the spin precession is reversed either by changing the orientation of the quarter-wave plate by 90 degrees or by reversing the dc magnetic field. The remaining details of the circular polarization system are similar to the more conventional wave guide system discussed previously. In Fig. 5, a sequence of oscilloscope trace photographs shows the behavior of the circularly rotating modes as the magnetic field is varied from zero to and beyond ferrite resonance.

Wall- and Size-Effect

We have found it necessary to take certain precautions with respect to sample position and size. We have observed that the measured susceptibility approaches an asymptotic value when the sample is moved away from the cavity end wall by approximately one or two sphere diameters.

Furthermore, it has long been known that the measured ferrite susceptibility apparently depends on the size of the sphere employed.[9] Spheres of 0.5 mm diameter or less turn out to be satisfactory; or, if larger spheres are used, the results must be extrapolated to zero sphere diameter.

RESULTS AND DISCUSSION

Tensor Components

The results of a typical run on a ferrite sphere at 9165 Mcps made with the circular polarization apparatus are shown in Fig. 6. The tensor components $\chi'+\kappa'$ and $\chi''+\kappa''$ are plotted against applied magnetic field. The quantities $\chi'-\kappa'$ and $\chi''-\kappa''$ were also measured and found to be very small. $\chi'-\kappa'$ is about 0.2 and $\chi''-\kappa''$ is about 0.01, both quantities being very insensitive to magnetic field variations. The units here are such that the relation between permeability and susceptibility is $\mu=1+\chi$.

It should be mentioned that the sample was mounted a small distance from the end wall, but we did not make measurements on a sufficient number of spheres to be able to extrapolate the susceptibilities to zero sphere diameter.

[9] Yager, Merritt, and Guillaud, Phys. Rev. **81**, 477 (1951).

Comparison with Theory

In this section we shall state the usual equation of motion which applies to a precessing spin vector, include the type of damping term first adopted for electron spin resonance by Bloembergen,[10,11] and then derive briefly the susceptibility tensor components when the exciting radiation is circularly polarized.

The equation of motion with damping is

$$\frac{d\mathbf{M}}{dt}=\gamma\mathbf{M}\times\mathbf{H}-\frac{\mathbf{M}}{T}.$$

$\mathbf{M}$ is the magnetization vector, $\mathbf{H}$ includes both dc and microwave magnetic fields, γ is the gyromagnetic ratio ($ge/2mc$), and T is the relaxation or damping time.

We apply the dc field in the z-direction and call it H and write for the circularly polarized microwave field $h=h_x+jh_y$. The magnetization in the z-direction is M and the precessing components are $m=m_x+jm_y$. m is understood to have a time dependence proportional to $e^{j\omega t}$; a choice of $+\omega$ will correspond to the circular polarization having the same sense as the precessing spins and $-\omega$ will correspond to the oppositely precessing spins.

Substitution into the equation of motion then yields

$$\frac{m_\pm}{h}=\frac{\gamma M}{\mp\omega+\gamma H+j/T}\equiv\frac{\chi\pm\kappa}{4\pi}.$$

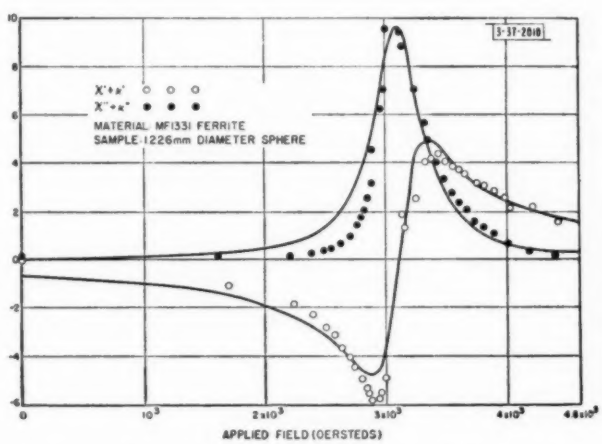

FIG. 6. Components of microwave susceptibility tensor.

[10] N. Bloembergen, Phys. Rev. **78**, 572 (1950).

[11] Other types of damping terms have been employed in the past, e.g., the Landau-Lifshitz type, which introduces the damping parameter α in the equation of motion: $d\mathbf{M}/dt=\gamma\mathbf{M}\times\mathbf{H}-(\gamma\alpha/|M|)[\mathbf{M}\times(\mathbf{M}\times\mathbf{H})]$. However, differences in line shape and resonance condition depend only in the second order on the type of damping term.

The result, when converted to the case of variable magnetic field rather than variable frequency, is

$$\chi'\pm\kappa'=\frac{4\pi M(H\mp H_0)}{(H\mp H_0)^2+(1/\gamma^2T^2)},$$

$$\chi''\pm\kappa''=\frac{4\pi M 1/\gamma T}{(H\mp H_0)^2+(1/\gamma^2T^2)},$$

$$\chi\pm\kappa=(\chi'\pm\kappa')-j(\chi''\pm\kappa''),$$

where $\omega=\gamma H_0$. $\omega=\gamma H_0$ is the usual resonance condition in an infinite medium or for a spherical specimen. The important cases where demagnetizing factors must be included will be discussed below.

Comparison between theory and experiment was made as follows. The theoretical expressions require insertion of two experimentally determined parameters —the resonance field H_0 and the half-width at half-height ΔH, which can easily be shown to be equal to $1/\gamma T$ to a good approximation. The solid lines in Fig. 6 are a plot of these expressions for $H_0=3115$, and $\Delta H=235$. The experimental points are indicated by circles and squares. $4\pi M$ was determined by requiring that the maximum experimental and theoretical values of $\chi''+\kappa''$ be equal. This results in $4\pi M=2270$, which falls in the range of saturation magnetizations normally encountered for Ferramic 1331.

The theory, as it stands, evidently does not describe the extraordinary susceptibilities ($\chi'+\kappa'$ and $\chi''+\kappa''$) accurately. The most pronounced discrepancies exist in the tails of the absorption and dispersion curves between ΔH and $3\Delta H$ on each side of resonance. To what extent this lack of agreement is due to the polycrystalline nature of the sample is not clear at present; an averaging process of the susceptibilities would have to be carried out over the various randomly-oriented crystallites. Asymmetry in resonance curves may in general be ascribed to dimensional effects. The tails of body resonances contribute asymmetrically to the observed gyromagnetic susceptibilities.

The ordinary susceptibilities ($\chi'-\kappa'$ and $\chi''-\kappa''$) were not plotted as a function of magnetic field because they remain approximately constant and are very small. However, a numerical comparison may be made at some point, say at resonance, using the same experimental parameters as in the foregoing. This is shown in Table I.

It should be pointed out that comparison between theory and experiment is not valid below the region where the sample is not completely magnetized, unless the theory is modified to take into account the partial magnetization. For the Ferramic 1331 sample used, saturation would occur at approximately $(4/3)\pi M=\frac{1}{3}\times 2270=750$ oersteds.

TABLE I.

	Experiment	Theory
$\chi'-\kappa'$	0.2	0.3
$\chi''-\kappa''$	0.01	0.01

CONCLUSIONS

This paper gives a detailed description of the interaction of microwave fields in cavities with ferrites. Both theory and experiment have been carried out. A degenerate cavity technique had to be developed in order to measure all four tensor components of the magnetic susceptibility.

The results indicate that both the real and imaginary parts of χ and κ are approximately equal to each other in the resonance region since $\chi'-\kappa'$ and $\chi''-\kappa''$ are very small compared to $\chi'+\kappa'$ and $\chi''+\kappa''$, respectively. A consequence of this result is that near resonance, where χ and κ are large numbers, only measurement of the diagonal components may suffice to specify the complete tensor. However, whenever the small differences between χ and κ are desired, measurement of the tensor susceptibility in a degenerate cavity will be necessary.

One important case where tensor measurements will prove to be of great value is in the region below ferromagnetic resonance where many of the present nonreciprocal devices operate. However here, as we have seen, the susceptibilities are small and are the result of contributions from the tail of the gyromagnetic resonance curve as well as other mechanisms associated with the initial susceptibility. A larger sample would give a more easily observable effect, and for such a case the sample could advantageously be in the shape of a disk.[12] Large spherical samples are more susceptible to dimensional effects than thin disks of the same volume. Furthermore in thin disks measurements can be made more easily of initial susceptibilities below magnetic saturation. We can see this by rewriting the complex susceptibilities so as to include demagnetizing factors:

$$\chi\pm\kappa=\frac{4\pi M}{[H+M(N_x-N_z)\mp H_0]+j\dfrac{1}{\gamma T}}.$$

N_x and N_z are the demagnetizing factors in the x- and z-directions, and $N_x=N_y$. Obviously a circularly symmetric sample must be used if the cavity is to be degenerate and is to support circularly polarized modes. The magnetic field is applied in the z-direction perpendicular to the plane of the disk. From the equation it is evident that for a disk the region between saturation and resonance is much extended in terms of the applied field. That is, saturation occurs at $H_s=4\pi M$ and resonance occurs at $H_r=H_0+4\pi M$, so that $H_r-H_s=H_0$. For a sphere, $H_s=(4/3)\pi M$ and $H_r=H_0$ so that $H_r-H_s=H_0-(4/3)\pi M$. If it is desired to study

[12] J. H. Rowen and W. von Aulock, Phys. Rev. **96**, 1151 (1954), are investigating the tensor susceptibility of disk-shaped specimens. These authors also point out the advantages of measuring the "intrinsic" susceptibility, which relates the internal H (rather than external H) and the internal B. See also our footnote 13.

the susceptibilities as the material magnetizes, then in a disk gyromagnetic resonance is separated more distinctly from other low-field effects contributing to the susceptibility.

ACKNOWLEDGMENTS

We wish to express our appreciation to Benjamin Lax for his original suggestion, helpful advice, and continued interest in this work.

APPENDIX

General Perturbation Formulas for the Degenerative Cavity

From the unperturbed and perturbed Maxwell equations in the text, we have

$$\int_{\text{cavity volume } v} \left[\begin{matrix}\mathbf{E}_0^*\cdot\nabla\times\mathbf{H}-\mathbf{H}_0^*\cdot\nabla\times\mathbf{E}\\ +\mathbf{E}\cdot\nabla\times\mathbf{H}_0^*-\mathbf{H}\cdot\nabla\times\mathbf{E}_0^*\end{matrix}\right]d\tau$$

$$=j(\omega-\omega_0)\int_v[\epsilon_0\mathbf{E}_0^*\cdot\mathbf{E}+\mu_0\mathbf{H}_0^*\cdot\mathbf{H}]d\tau \times\int_{\Delta v}(\mathbf{J}_e\cdot\mathbf{E}_0^*+\mathbf{J}_m\cdot\mathbf{H}_0^*)d\tau.$$

Using the identity $\nabla\cdot(\mathbf{a}\times\mathbf{b})=\mathbf{b}\cdot(\nabla\times\mathbf{a})-\mathbf{a}\cdot(\nabla\times\mathbf{b})$ and the Divergence theorem $\int_v\nabla\cdot\mathbf{F}d\tau=\int_s\mathbf{F}\cdot d\mathbf{A}$, the equation above is transformed to:

$$\int_v\left[\ \right]d\tau=\int_v[\nabla\cdot(\mathbf{E}_0^*\times\mathbf{H})+\nabla\cdot(\mathbf{E}\times\mathbf{H}_0^*)]d\tau$$

$$=\int_s[\mathbf{E}_0^*\times\mathbf{H}+\mathbf{E}\times\mathbf{H}_0^*]\cdot d\mathbf{A}.$$

The integral $\int_s[\ ]\cdot d\mathbf{A}$ is zero since the electromagnetic fields in the cavity must obey the surface boundary conditions: $\mathbf{E}_0\times d\mathbf{A}=0$, $\mathbf{E}\times d\mathbf{A}=0$. Hence,

$$(\omega-\omega_0)=\frac{j\int_{\Delta v}(\mathbf{J}_e\cdot\mathbf{E}_0^*+\mathbf{J}_m\cdot\mathbf{H}_0^*)d\tau}{\int_v(\epsilon_0\mathbf{E}_0^*\cdot\mathbf{E}+\mu_0\mathbf{H}_0^*\cdot\mathbf{H})d\tau}.$$

In accordance with first-order perturbation theory, the approximations $\mathbf{E}\cong\mathbf{E}_0$, $\mathbf{H}\cong\mathbf{H}_0$ are now made in this formula. For the particular case in which Δv is placed where $\mathbf{E}$ is zero, $\mathbf{J}_e$ is zero. Further $\mathbf{J}_m=j\omega\mu_0\chi_m\cdot\mathbf{H}_0$.[13]

[13] N. Bloembergen has pointed out [see also J. Appl. Phys. **23**, 1383 (1952)] that this definition of susceptibility does not correspond to the usual one since the local field at the sample is not the applied field H_0. However the Bloch-Bloembergen magnetic resonance equations are generally written so as to define a "susceptibility" just in this very manner, so that comparison of theory and experiment is valid. The distinction is trivial in paramagnetic resonance where the local and applied field are essentially the same.

Since the time averages of stored electrical energy and stored magnetic energy are equal, it follows that $\epsilon_0\mathbf{E}_0^*\cdot\mathbf{E}_0=\mu_0\mathbf{H}_0^*\cdot\mathbf{H}_0$.

Substituting and simplifying:

$$(\omega-\omega_0)=-\frac{\omega_0}{2}\frac{\int_{\Delta v}(\chi_m\cdot\mathbf{H}_0)\cdot\mathbf{H}_0^*d\tau}{\int_v(\mathbf{H}_0\cdot\mathbf{H}_0^*)d\tau},$$

$\int_{\Delta v}(\chi_m\cdot\mathbf{H}_0)\cdot\mathbf{H}_0^*d\tau$ is just the complex change in the stored cavity energy $\int_v(\mathbf{H}_0\cdot\mathbf{H}_0^*)d\tau$. Denoting $\omega-\omega_0$ by $\Delta\omega$, $\int_v(\mathbf{H}_0\cdot\mathbf{H}_0^*)d\tau$ by w, and $\int_{\Delta v}(\chi_m\cdot\mathbf{H}_0)\cdot\mathbf{H}_0^*d\tau$ by Δw, the above relation can be written concisely as $\Delta\omega/\omega_0=-\Delta w/w$. In the formula above, $\mathbf{H}_0$ will now be written simply as $\mathbf{H}$. Over Δv, $\mathbf{H}$ corresponds to a circularly polarized wave: $\mathbf{H}=1/\sqrt{2}(H\hat{\imath}_1\pm jH\hat{\imath}_2)$. Therefore

$$\chi_m\cdot\mathbf{H}=\begin{pmatrix}\chi & -j\kappa\\ j\kappa & \chi\end{pmatrix}\begin{pmatrix}\frac{H}{\sqrt{2}}\\ \pm j\frac{H}{\sqrt{2}}\end{pmatrix}=\frac{1}{\sqrt{2}}\begin{pmatrix}\chi H\pm\kappa H\\ j\kappa H\pm j\chi H\end{pmatrix}$$

and

$$(\chi_m\cdot\mathbf{H})\cdot\mathbf{H}^*=\tfrac{1}{2}[(\chi\pm\kappa)H^2+(\chi\pm\kappa)H^2]=(\chi\pm\kappa)H^2.$$

If Δv is small

$$\int_{\Delta v}(\chi_m\cdot\mathbf{H})\cdot\mathbf{H}^*d\tau=\int_{\Delta v}[(\chi\pm\kappa)H^2]d\tau=(\chi\pm\kappa)H^2\Delta v.$$

Hence the perturbation relation which results is:

$$\frac{\Delta\omega_\pm}{\omega_0}=-\frac{[\chi\pm\kappa]H^2\Delta v}{2\int_v H^2d\tau}.$$

Perturbation Formulas for Circular TE_{11n} Cavities

A degenerate right circular cylinder resonating in the TE_{111} mode is suitable for susceptibility tensor measurements. The spherical sample is placed at the center of the end wall and the dc magnetic field is applied perpendicular to the plane of the end wall. See Fig. 7. The TE_{111} cavity is also suitable for measurements of just the diagonal component of the susceptibility tensor. In order to do this the cavity must be made nondegenerate. For example the angular symmetry can be disturbed by coupling through an iris located on the side of the cavity. See Fig. 8.

In the degenerate case the perturbation expressions were:

$$\frac{\Delta\omega_\pm}{\omega_0}=-\frac{[\chi\pm\kappa]H^2\Delta v}{2\int_v H^2d\tau}.$$

The calculation of

$$\frac{H^2\Delta v}{2\int_v H^2 d\tau}$$

is the same in both cases.

The microwave H fields for the TE_{111} mode of the right circular cylinder are as follows:

$$H_\rho=\frac{k_3}{k}J_1'(k_1\rho)\cos\theta\cos k_3 z,$$

$$H_\theta=\frac{k_3}{k}\frac{J_1(k_1\rho)}{k_1\rho}\sin\theta\cos k_3 z,$$

$$H_z=\frac{k_1}{k}J_1(k_1\rho)\cos\theta\sin k_3 z.$$

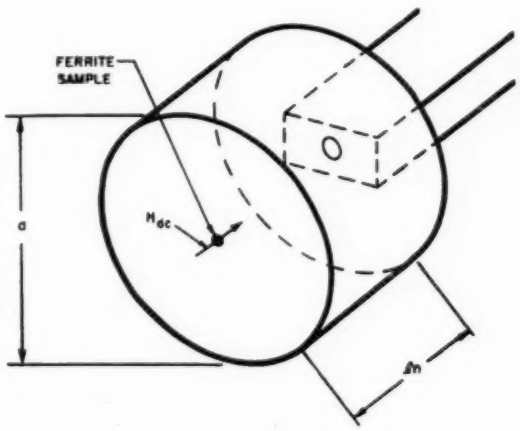

FIG. 7. Degenerate TE_{11n} cylindrical cavity.

See Fig. 9. The parameters appearing in the above equations are defined as follows:

$$k_1=\frac{2r_{11}}{a},\quad k_3=\frac{\pi}{L},\quad k^2=k_1^2+k_3^2,\quad \lambda=2\pi/k,$$

$$r_{11}=1.8412,\quad J_1'(r_{11})=0.$$

The perturbation expression becomes:

$$\frac{H^2(\rho=0,z=0)\Delta v}{2\int_v H^2 d\tau}=\frac{2\pi\Delta v}{L^3(J_0(r_{11}))^2\left[\frac{\pi^2a^2}{L^2}+4r_{11}^2\right]\left[r_{11}^2-1\right]}$$

$$=\frac{26.316\Delta v}{\left(\frac{\pi^2a^2}{L^2}+13.560\right)L^3}.$$

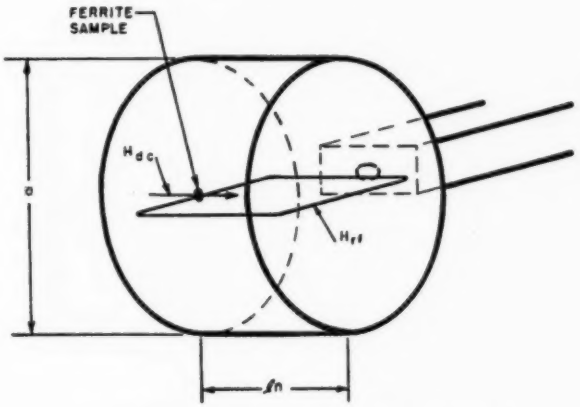

FIG. 8. Nondegenerate TE_{11n} cylindrical cavity.

In the more general case of a TE_{11n} cavity the perturbation expression is:

$$\frac{H^2(\rho=0,z=0)\Delta v}{2\int_v H^2 d\tau}=\frac{26.316\Delta v}{\left(\frac{\pi^2a^2}{l^2}+13.560\right)nl^3},$$

where $l=L/n$. Since $\Delta\omega=\Delta\omega_r+j\Delta(\omega_0/2Q)$ the final equations are:

Degenerate TE_{11n} Cavity

$$\left(\frac{\Delta\omega_r}{\omega_0}\right)_\pm=-\frac{26.316}{\left[\frac{\pi^2a^2}{l^2}+13.560\right]}(\chi'\pm\kappa')\frac{\Delta v}{nl^3},$$

$$\Delta\left(\frac{1}{2Q}\right)_\pm=\frac{26.316}{\left[\frac{\pi^2a^2}{l^2}+13.560\right]}(\chi''\pm\kappa'')\frac{\Delta v}{nl^3}.$$

Nondegenerate TE_{11n} Cavity

$$\frac{\Delta\omega_r}{\omega_0}=-\frac{26.316\chi'}{\left[\frac{\pi^2a^2}{l^2}+13.560\right]}\frac{\Delta v}{nl^3},$$

$$\Delta\left(\frac{1}{2Q}\right)=\frac{26.316\chi''}{\left[\frac{\pi^2a^2}{l^2}+13.560\right]}\frac{\Delta v}{nl^3}.$$

Perturbation Formulas for Rectangular TE_{10n} Cavities

A suitable nondegenerate cavity can also be constructed from a closed-off section of rectangular wave guide resonating in the TE_{10n} mode (see Fig. 10). The ferrite is placed at the center of the end plate at the point $x=a/2$, $y=b/2$, $z=0$. The dc magnetic field is applied perpendicular to the rf H field. The electro-

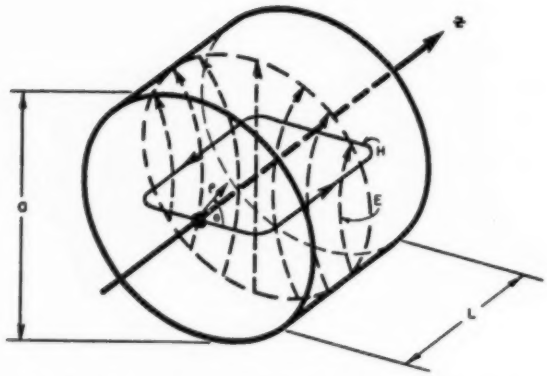

FIG. 9. Mode configuration in cylindrical TE_{111} cavity.

magnetic fields for the TE_{10n} mode are:

$$E_x=E_z=H_y=0,$$

$$E_y=\sin\frac{\pi x}{a}\sin\frac{\pi z}{l},$$

$$H_x=\frac{a}{(a^2+l^2)^{\frac{1}{2}}}\sin\frac{\pi x}{a}\cos\frac{\pi z}{l},$$

$$H_z=\frac{a}{(a^2+l^2)^{\frac{1}{2}}}\cos\frac{\pi x}{a}\sin\frac{\pi z}{l}.$$

At the point $(x=a/2, y=b/2, z=0)$ $H_x=a/(a^2+l^2)^{\frac{1}{2}}$, and all other electromagnetic field components vanish. Then,

$$\frac{H^2\Delta v}{2\int_v H^2 d\tau}=\frac{a^2\Delta v}{2\int_v\left(a^2\sin^2\frac{\pi x}{a}\cos^2\frac{\pi z}{l}+l^2\cos^2\frac{\pi x}{a}\sin^2\frac{\pi z}{l}\right)d\tau}$$

$$=\frac{2a^2\Delta v}{(a^2+l^2)V},\quad V=abnl.$$

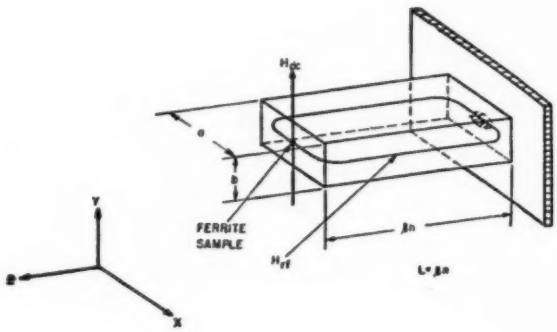

FIG. 10. Rectangular TE_{10n} cavity.

Since the free-space wavelength λ_0 equals $2al/(a^2+l^2)^{\frac{1}{2}}$:

$$\frac{H^2\Delta v}{2\int_v H^2 d\tau}=\frac{\Delta v}{V}\cdot 2\left[1-\left(\frac{\lambda_0}{2a}\right)^2\right].$$

Since

$$\frac{\Delta\omega_r}{\omega_0}=-\frac{\chi' H^2\Delta v}{2\int_v H^2 d\tau}\quad\text{and}\quad\Delta\left(\frac{1}{2Q}\right)=\frac{\chi'' H^2\Delta v}{2\int_v H^2 d\tau},$$

the perturbation formulas are:

$$\frac{\Delta\omega_r}{\omega_0}=-\chi'\frac{\Delta v}{V}\cdot 2\left[1-\left(\frac{\lambda_0}{2a}\right)^2\right],$$

$$\Delta\left(\frac{1}{2Q}\right)=\chi''\frac{\Delta v}{V}\cdot 2\left[1-\left(\frac{\lambda_0}{2a}\right)^2\right].$$

JOURNAL OF APPLIED PHYSICS VOLUME 26, NUMBER 9 SEPTEMBER, 1955

Tensile Strength of Plastics above the Glass Temperature*

F. BUECHE
Physics Department, University of Wyoming, Laramie, Wyoming
(Received May 6, 1955)

A theory is presented for the tensile strength of rubbery plastics under dynamic test conditions. It is found that a nearly universal curve may be plotted relating the tensile strength of rubbers to the time of application of the load in a simple creep test or to the shear rate in a conventional type tensile test. The dependence on chain length, degree of cross linking, and temperature is also predicted.

Experimental results for the tensile strength of poly butyl methacrylate in the range 30–95°C are presented. These are shown to agree with the theory within the experimental error. The experimental testing scale extends over a range of eight decades when use is made of a temperature–time superposition principle predicted by the theory.

By comparing the tensile creep and tensile strength curves for poly butyl methacrylate, it is possible to find the size of a segment as defined in the theory of viscoelasticity. One segment is found to contain about six monomer units.

INTRODUCTION

THE tensile strength of plastics has been a problem of major concern during the past several years. Although a great number of data are available, very little progress has been made towards finding a satisfactory molecular interpretation of them. Several correlating relationships have been found[1,2] but except in a very few instances these have been almost completely empirical in nature.

We propose to present here a molecular interpretation of the tensile strength of plastics above their glass temperature. In order to preserve the simplicity of the problem, we shall not attempt to give a completely accurate theory at this time. Rather drastic simplifications will be made but care will be taken to point out their consequences. It is to be expected that a more accurate theory will not alter the basic results found here. Our theoretical result will be tested by comparing it with pertinent experimental data and substantial agreement between theory and experiment will be found.

THEORY

Let us first consider what happens when a rubbery plastic is stretched. It has been shown that for a cross-linked material the deformation can be described adequately as the stretching of a network system under the action of viscous forces. It has further been shown that high molecular-weight materials which do not contain chemical cross links exhibit this same behavior also. A quantitative theory has been developed which shows that the entanglements of the linear polymer chains act as temporary cross links thereby giving rise to the observed network behavior.[3–5] If the molecular weight of the polymer is sufficiently high, the linear polymer is found to have the same elastic behavior as a cross-linked system. However, if the sample is held extended for a sufficiently long time the entanglements will eventually slip and the polymer will exhibit true viscous flow.

Because of the fact that a network structure is present in high molecular-weight linear polymers as well as in the truly cross-linked systems, it is possible to give a theory which will apply to both systems. Our theory for the tensile strength of plastics above their glass temperature will be based on the following molecular picture.

When a force is applied to a rubber, each network chain in the sample begins to elongate. The rate at which the chain elongates is controlled by the internal viscosity of the polymer and if one waits long enough the chains will elongate to an equilibrium length under the applied force. However, each network chain is placed under tension as it elongates, the tension in each chain being proportional to its elongation. This tension, if sufficiently large, will cause the chain to break and, when the rate of chain breakage has become large enough the sample will break. On the basis of this picture we can draw several qualitative conclusions which the theory will be shown to confirm. First, the strength of a rubber should be much greater under a fast than a slow test since in the former case the network chains are not able to elongate very far during the period of the test. Second, the sample should appear much weaker at high than at low temperatures under the same type of test. This follows because at high temperatures the chains can elongate more rapidly and thus will break in a shorter time. Third, the strength of the material will be increased by increasing the number of network chains per unit volume since the force applied to each will then be smaller. And last, there should be

* This work was made possible by a grant from The Research Corporation.

[1] See, for example, R. N. Haward, *Strength of Plastics and Glasses* (Interscience Publishers, Inc., New York, 1949) and P. J. Flory, *Principles of Polymer Chemistry* (Cornell University Press, Ithaca, New York, 1954).

[2] C. C. Hsiao, J. Appl. Phys. **23**, 1189 (1952).

[3] F. Bueche, J. Chem. Phys. **22**, 603 (1954).

[4] F. Bueche, J. Appl. Phys. **26**, 738 (1955).

[5] Ferry, Landel, and Williams, J. Appl. Phys. **26**, 359 (1955).

a minimum force for which the sample will break under a very slow test. This follows from the fact that if the sample has not yet broken by the time that the network has been fully elongated, the sample is not likely to break in a reasonable length of time, since the force on the network chains is already a maximum. We shall see that the quantitative considerations given in the following substantiate these conclusions.

To formulate a quantitative theory we must know how the network chains respond to stress. Let us first focus our attention upon segments i and $i+1$ of a network chain which contains N segments. If the center of the ith segment is displaced a distance x_i by the force, and segment $i+1$ by x_{i+1}, then the intervening segment will be stretched a distance $x_{i+1}-x_i$. This elongation may be shown to be accompanied by a tension in the segment equal to $(3kT/l^2)(x_{i+1}-x_i)$ where l is the length of a chain segment so defined that the chain itself has an equilibrium mean square end-to-end distance of Nl^2. It is the aforementioned tension in the segments which tends to break them and leads to tensile failure of the sample.

We now calculate how many segments break per unit time. In the absence of an external force, the rate of segment fracture will be

$$(dn/dt)=\omega\nu N \exp(-E/kT),$$

where ω is a segment oscillation frequency and E is an activation energy for fracture. We need not be more explicit about these quantities for the present purposes. The quantity ν is the number of active network chains per unit volume.

In the presence of an applied constant force an elastic energy

$$V_i=\tfrac{3}{2}(x_{i+1}-x_i)^2(kT/l^2) \qquad (1)$$

will be stored in each segment. The value of $x_{i+1}-x_i$ may be calculated using the methods of a previous paper,[4] and one finds

$$x_{i+1}-x_i=(4FR/3\pi^2\nu kT)\sum_{n\,\mathrm{odd}}^{N}(1/n^2)\times[1-\exp(-\beta t n^2/N^2)]\times\{\cos[(i+1)(n\pi/N)]-\cos(in\pi/N)\}+Fl/Y, \qquad (2)$$

where Y is Young's modulus and $\beta=3\pi^2kT/f_0l^2$. The quantity β is N^2/τ_1, where τ_1 is the characteristic chain response time used before.[4]

The symbols used in Eq. (2) are the same as in the previous paper.[4] However, the last term of the equation is new and represents the initial essentially instantaneous short-range deformation of the sample (i.e., the van der Waal's extension). This type of deformation is much smaller than the network type extension and has been neglected in previous calculations. We will find that it plays an important part in the present problem. It should also be emphasized that F in Eq. (2) is the initial force per unit area applied to the end of the tensile test sample. No correction to F is to be made for changes in cross section of the sample as it elongates under elastic conditions. However, F must be changed in order to compensate for cross-section changes resulting from pure viscous flow.

The reasons for these restrictions on F can be understood from the following qualitative considerations. First, under elastic extension, the load applied to the total cross section is being held by approximately the same number of chains regardless of the cross section area at any time during the stretching process. Thus, the force per chain is essentially constant throughout the test. Second, true viscous flow decreases the number of chains holding the load on any cross section in proportion to the change in cross-sectional area resulting from such flow. Consequently, the force on any given chain increases as viscous flow takes place.

We might also mention here that although Eq. (2) was derived only for the linear portion of the stress–strain curve, it has a wider range of validity in this case. This is the result of the fact that the nonlinearity encountered at moderate extensions results primarily from the lateral contraction of the sample as it stretches. Since we are only interested here in the longitudinal stretching of the chains, we can, to a good approximation, ignore this other complication. However, to be consistent we should multiply the right side of Eq. (2) by a factor near unity to take care of the fact that we are concerned only with the x directed chains. This factor is absorbed in the constant q which is introduced in the next paragraph.

Equations (1) and (2) are an oversimplification of the problem. They consider all chains to have identical expressions for $x_{i+1}-x_i$. We know that this cannot be true since there must always be a statistical distribution of chain lengths in the sample. It is clear that the more extended chains will have the most energy stored in them. It is a formidable task to take exact account of this effect. As an approximation to the true state of affairs we shall multiply $x_{i+1}-x_i$ in Eq. (2) by a factor q in order to compensate for the use of the average value of $x_{i+1}-x_i$. It is expected that q will be larger than unity since the more extended chains will be the most important for the present purposes. We then have

$$V_i=\tfrac{3}{2}q^2(x_{i+1}-x_i)^2(kT/l^2). \qquad (1b)$$

Since the elastic energy contributes to the total energy available to break the segment, we have that the rate of segment fracture is

$$(dn/dt)=\omega\nu\sum_{i=0}^{N}\exp[-(E-V_i)/kT].$$

This implies that all of the elastic energy contributes to the breaking of the segment. If such is not the case,

the error in this assumption will be absorbed in the constant q and will not impair the theory.

As a logical criterion for break we will stipulate that the sample will break when the segment fracture rate exceeds a certain critical value. It may be shown that the critical condition for sample failure is then given by the relation

$$\exp(\Phi^2)=\sum_i \exp[3q^2(x_{i+1}-x_i)^2/2l^2]. \qquad (3)$$

That is to say, if the right side of Eq. (3) exceeds the left side, the sample will break. The critical breaking parameter Φ contains the quantities ω and E/kT. It is a measure of the stability of the chain. For any stable chain molecule it turns out that Φ must be larger than about 4. Its exact value is of little consequence since it is apparent that Φ and q are approximately proportional and a change in one will be compensated by a change in the other.

It is now possible to use Eqs. (2) and (3) to compute a theoretical curve relating the time taken to break the sample to the applied load. If one neglects the initial small instantaneous deformation term in Eq. (2), a universal breaking curve for all amorphous, high molecular weight, or cross-linked polymers is obtained. This result is given in Fig. 1 and Table I. Actually the curve depends slightly upon the value of N which one chooses but this dependence is so small that the curves for N equal to 20 and 60 are identical for all practical purposes and the curve shown in Fig. 1 is their average. The figure shows that when $F/\nu kTN^{\frac{1}{2}}$ is plotted against log (βt), a single curve is obtained which should be the same for all rubbery plastics. From this fact it is apparent that differences in the tensile strength of various rubbers at the same temperature must be the result of differences in degree of cross linking, number of chains per unit volume, or variations in the quantity β. It should also be pointed out that the foregoing result was obtained assuming the applied force to act at the ends of the network chains. This is not consistent with the facts at short times. We have carried out a more exact calculation in Appendix I, and it is shown there that the consequences of our approximation are not very serious for the present purposes.

The theoretical result shown in Fig. 1 confirms the qualitative predictions made in the foregoing. In order to obtain a strong rubbery plastic, one should eliminate true viscous flow since it causes the cross-sectional area to decrease and as a result causes an apparent increase in F. We also note that if the number of cross links is increased by a factor p^2, the strength will increase by a factor p. An increase in the number of network chains per unit volume causes an identical increase in the strength of the plastic. These statements all presuppose the same value of βt. Obviously, one can increase the breaking strength of the polymer by using a fast test or by working at low temperatures.

TABLE I. Tensile strength as a function of time to break under a constant load.

$\log_{10}(\beta t)$	−0.40	0.00	0.50	1.00	2.00	2.50	∞
$(F/\nu kTN^{\frac{1}{2}})(q/\Phi)$	23.5	10.9	7.20	5.30	3.16	2.72	2.45

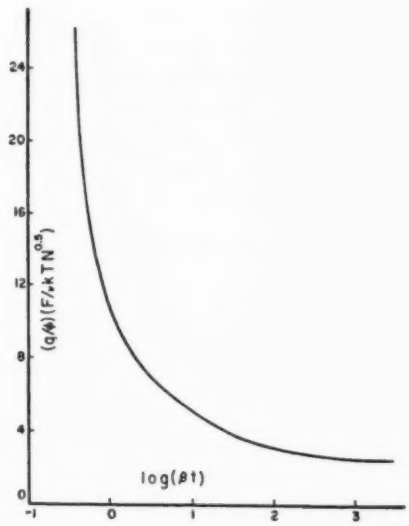

FIG. 1. Theoretical relationship showing the time taken to break a plastic under various loads ($\beta=3\pi^2kT/f_0l^2$).

EXPERIMENTAL

The polymer chosen for this work was an unfractionated sample of polybutyl methacrylate. It had been prepared by bulk polymerization without catalyst at 60°C. The reaction was carried to 10% conversion. The polymer had an intrinsic viscosity of 3.94 at 25°C in $CHCl_3$ and was therefore calculated to have a molecular weight of[6] 1.6×10^6. After the polymer had been purified by precipitation in methanol and subsequent drying, it was dissolved in chloroform and cast in the form of a film on a mercury surface. The films were dried at 125°C for several hours before use. It was found that this polymer had a glass temperature of about 8°C.

In order to ascertain the general mechanical properties of the polymer, the composite creep curve under very small elongations (<5%) was obtained by a technique described previously.[4] The result is shown in Fig. 2. It is seen that this polymer exhibits a plateau region characteristic of very high molecular-weight polymers. The final rise in the curve is the result of true viscous flow. It was found that the polymer had a tensile viscosity of 2.2×10^{11} poise at 92°C. The variation of the creep curve with temperature as found previously[4] was confirmed by this work.

It seemed of value to measure the variation in the creep curve as a function of applied load. One might expect that the curves at various loads would coincide if they were plotted in the form $(1/F)(\alpha-1/\alpha^2)$ *vs* $\log(t)$, where $\alpha=L/L_0$ since the kinetic theory of rubber-

[6] See Chem. Abstracts **46**, 10787i.

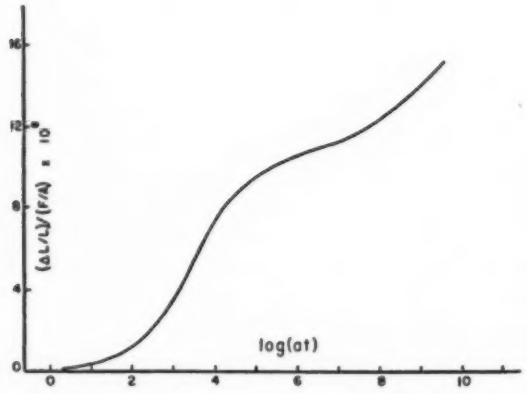

FIG. 2. Experimental compliance curve (cm²/dyne) for a sample of poly butyl methacrylate under small loads. t is in minutes and a is 1 min^{-1} at 30°C.

like elasticity predicts this function to be independent of load for long times. This is nearly true as is shown in Fig. 3. However, deviations occur near the breaking point of the sample (represented by the crosses).

The samples for the tensile strength measurements were prepared as already described in the form of thin films, 1.0 to 0.1 mm thick. They were cut into the shape of a dumbbell by the use of razor blades. The radius of curvature of the samples was about 20 cm and they were about 0.40 cm wide at the neck. All measurements were taken at constant temperature and low relative humidity employing previously described techniques.[4] The measurements were exceedingly simple and consisted of applying a known load to the sample and recording the time taken for the sample to break. It should be noticed that no correction was made for the change in cross section as the sample elongated. All data were considered valid except for the few cases when the sample broke at the clamp.

It is clear from the universal curve of Fig. 1 that a temperature-time superposition is valid for tensile strength data as well as for the more customary cases dealing with viscoelastic properties.[3,4,7] Our theoretical curve predicts that if the data are plotted in the form $\log(F/T\rho)$ *vs* $\log(a_T t)$, where ρ is the density of the polymer, the data at different temperatures can be made to coincide by proper choice of the constant a_T. This turns out to be true for our data which were obtained in the range 30–95°C. The composite curve reduced to $a_T = 1$ min^{-1} at 30°C is plotted in Fig. 4. It was further found that the factors a_T were identical within experimental error to those determined previously for this polymer using viscoelastic data.[4]

TEST OF THE THEORY

The theoretical strength curve may be tested by comparing plots to the same scale of our experimental data in the form $\log(F)$ *vs* $\log(t)$, and the theoretical relation in the form $\log(F/\nu kTN^{\frac{1}{3}})(q/\Phi)$ *vs* $\log(\beta t)$. If the theory is correct these curves should superpose, and the difference in the values of the axes of the two plots should be $\log(\beta)$ and $\log(q/\Phi\nu kTN^{\frac{1}{3}})$. This test has been carried out and the theoretical curve superposes as shown by the broken curve of Fig. 4. It is clear that the theory predicts the central portion of the curve quite well. However, difficulties arise at both long and short times.

The discrepancy at long times is actually a confirmation of the theory. It will be remembered that, although no correction in F is to be made for cross-section changes resulting from elastic extension of the sample, viscous flow results in an apparent increase in F. When proper account is taken of this effect using the value previously given for the viscosity at 92°C, the experimental points no longer deviate from the theoretical curve. From this it is apparent that the theory is valid in the long-time portion of the curve as well as in the central region. (The correction was made by plotting the points at values of FA_0/A rather than at F where A_0 is the original cross-section area and A is the area after viscous flow has taken place.)

The deviation of the experimental data from the universal breaking curve observed at short times is a result of the neglect of the initial instantaneous deformation term in Eq. (2) (that is, the term in F/Y). When this term is carried, the curve is no longer universal in nature and one must make some assumption about Young's modulus in order to plot the curve. In order to do this, we notice from Eqs. (2) and (3) that for t near zero one has

$$Y = F_m(q/\Phi')^{\frac{3}{2}\frac{1}{3}}, \tag{4}$$

where F_m is the ultimate tensile strength of the material and $\Phi' = (\Phi^2 - \ln N)^{\frac{1}{2}} \cong \Phi$.

From the experimental data one observes that the ultimate strength of the sample appears to be about 1.5×10^8 dynes/cm² (i.e., 2200 lb/in.²). We therefore

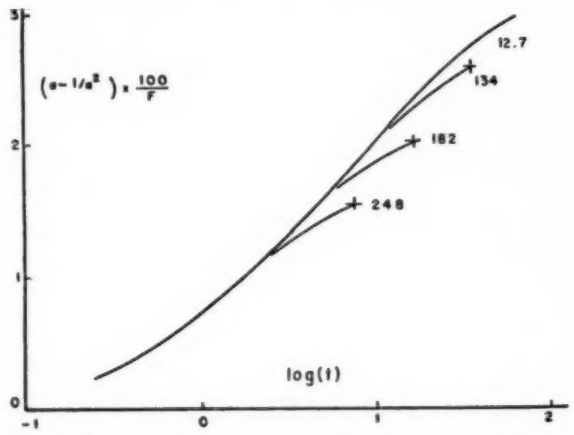

FIG. 3. Response of poly butyl methacrylate under large loads. The load in g/mm² is indicated on each curve. F is in g/mm² and t is in minutes.

[7] J. D. Ferry, J. Am. Chem. Soc. **72**, 3746 (1950).

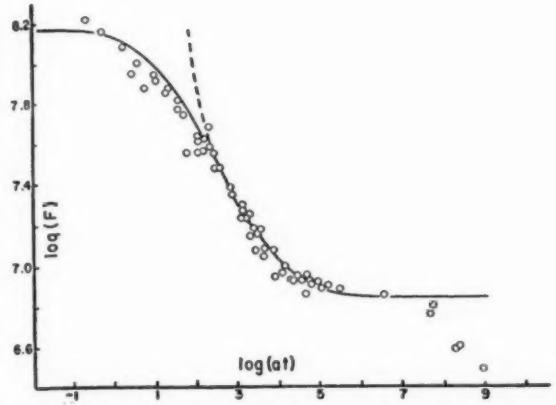

FIG. 4. Experimental (points) and theoretical (solid line) tensile strength curve for poly butyl methacrylate. F is in dynes/cm², t is in minutes, and a is 1 min^{-1} at 30°C.

find Young's modulus to be given by

$$Y=(1.83\times10^8)(q/\Phi'). \tag{5}$$

Also at $t\rightarrow\infty$ one has from Eqs. (2) and (3) that $F_0/\nu kTN^{\frac{1}{2}}=2.48(\Phi'/q)$, where F_0 is the limiting tensile strength at long times, 6.7×10^6 dynes/cm². The quantity $1/3\nu kT$ is merely the elastic compliance of the material at the plateau of Fig. 2 (see reference 4) and this is about 1×10^{-8} cm²/dyne. This leads to the result

$$(q/\Phi')=1.24N^{\frac{1}{2}}. \tag{6}$$

We therefore have

$$Y=2.27\times10^8N^{\frac{1}{2}}\text{ dynes/cm}^2. \tag{7}$$

This enables one to evaluate the quantity $(q/\Phi)\times(F/\nu kTN^{\frac{1}{2}})$ without dropping the last term from Eq. (2). When this is done, the solid curve of Fig. 4 is obtained.

Although the agreement between theory and experiment is quite reasonable, it is easily recognized that the value of F_m chosen above is somewhat uncertain. Unfortunately, experimental difficulties prevented us from extending our measurements to still shorter times so a more accurate value could not be obtained. However, work is now in progress on poly ethyl methacrylate which will enable us to extend our measurements into the glassy state. Until this is done, we cannot be sure that the substantial agreement found between theory and experiment will persist into the region of still shorter times. In any event, the theory appears to fit experiment rather adequately over at least eight decades of time.

Evaluation of N

The quantity N, the number of segments between network junction points, can be found by a comparison of the data of Figs. 2 and 4. It has been shown[4] that the tensile creep data may be used to evaluate τ_1, the characteristic response time of the polymer. By comparing the experimental strength curve with the theoretical curve one can evaluate β as outlined in the experimental section of this paper. However, from the definition of β we have $\beta=N^2/\tau_1$ and so it is possible to find N. We find at 30°C that $\beta^{-1}=1.7\times10^4$ sec, $\tau_1=1.5\times10^6$ sec and therefore $N=9$. This means there are approximately 9 ± 1 segments in each network chain. But the molecular weight of the network chains may be found[4] from the data of Fig. 2 and we shall take it to be about 8000. This means that there are about 12 chain atoms or 6 monomer units in a segment for this particular substance. As far as we are aware, this is the first time that it has been possible to calculate this quantity with any accuracy and so we have no basis for comparison. However, the value obtained seems quite reasonable.

Evaluation of Young's Modulus

Since we have found N to be equal to about 9, it is possible to evaluate Y from Eq. (7). When this is done, we find $Y=7\times10^8$ dynes/cm². This value is about twenty to forty times smaller than one would expect. The reason for this discrepancy will be pointed out in the next paragraph. It is shown there that the fault lies, not with an improper use of Young's modulus, but with a rather too naive evaluation of the tensile force causing fracture of the sample.

This unreasonable value for Y is a result of a well-known difficulty encountered in all tensile strength measurements. It is commonly accepted that the ultimate strength of glasses and plastics in the glassy state is never attained experimentally, the experimental value being from 10 to 100 times too small. The reason for this is generally agreed to be the fact that all these test specimens contain minute flaws which give rise to uneven distribution of stress in the sample.[1] As a result, the regions of high stress fail before the average sample would ordinarily do so thus leading to a much lower value of F_m than one would predict. It is therefore not surprising that our computed

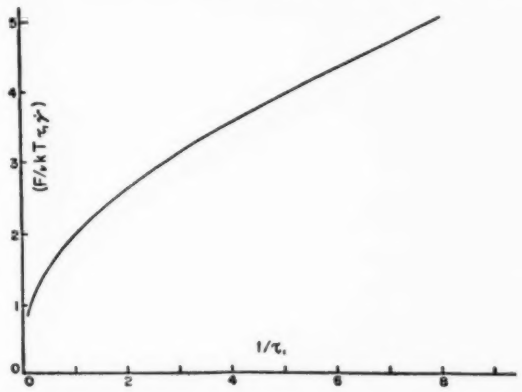

FIG. 5. Theoretical relationship showing the force needed to maintain a constant rate of elongation in a tensile test of a plastic. (On the abscissa, the numbers 2, 4, 6, and 8 should read 0.2, 0.4, 0.6, and 0.8.)

value for Young's modulus is not correct. On the other hand, it is interesting to notice that the present method for calculating the strength of the glassy polymer leads to the same concept of flaws which is indicated by the much different previous methods of calculation.[1]

In conclusion, it appears that the picture presented here for the dynamic tensile strength of plastics above the glass temperature T_g is basically correct. Although our data on poly butyl methacrylate indicate that the variation of strength with time is correctly predicted by the theory, no test has yet been made of the predicted variation of strength with N and ν. We now have at hand a few data on poly ethyl methacrylate which indicate that this feature of the theory is also correct. However, a real test requires work on several other systems as well. It might be mentioned that Flory's data on the strength of rubber as a function of ν follows the behavior predicted here. However, there is considerable reason to believe that crystallization effects are important for that system and so the agreement may be fortuitous. At the present time we are extending our measurements to the glassy state and to other polymers. It is hoped that these measurements will eventually result in a more extensive test of the theory.

TESTS UNDER CONSTANT RATE OF ELONGATION

The previous discussion has been concerned with the behavior of the plastic under a fixed load. In practice, the common testing method is to measure the force needed to maintain a constant rate of elongation $\dot{\gamma}$, and the tensile strength is also obtained in the same type test. It is a simple matter to extend our calculations to this interesting case and we have done this in Appendix II. The results are given in the following.

It is of value to know how the force needed to maintain a fixed tensile shear rate varies during the time of elongation of the sample. This is illustrated in Fig. 5 and Table II where we show $(F/\nu kT\tau_1\dot{\gamma})$ as a function of (t/τ_1). It will be remembered that $\tau_1=f_0N^2l^2/3\pi^2kT$, ν is the number of active network chains per unit volume and $\dot{\gamma}$ is the constant shear rate. At longer times than shown in Fig. 5 the curve is a straight line with unit slope. The curve is not seriously changed by variations in N when plotted in this way. In addition, it is apparent that the horizontal axis could equally well be plotted as strain since the time and strain are related through the relation $(\Delta L/L)=\dot{\gamma}t$.

The form of the curve of Fig. 5 is in qualitative agreement with the existing data in the literature. Unfortunately there is very little data available to provide a quantitative test of the relation. This is particularly true since the relation is only expected to be applicable in the region of small strains. However, the fact that the theoretical curve for creep has been verified experimentally would lead us to think that the present relation should also be substantially correct.

TABLE II. Force needed to maintain a constant rate of elongation.

t/τ_1	0.02	0.05	0.10	0.20	0.40	1.00
$F/\nu kT\dot{\gamma}\tau_1$	1.05	1.46	1.95	2.63	3.58	5.74

The tensile strength under constant rate of elongation has also been computed and is illustrated in Fig. 6 and Table III where we show the variation of $(q/\Phi)\times(F/\nu kTN^{\frac{1}{2}})$ with $\dot{\gamma}_0/\dot{\gamma}$. The function plotted vertically in Fig. 6 is identical to that plotted in Fig. 1 for tensile strength under creep. We represent the constant tensile shear rate by $\dot{\gamma}$, and $\dot{\gamma}_0$ is a characteristic shear rate equal to $(\Phi/q)(1/\tau_1N^{\frac{1}{2}})$.

It will be observed that the general shapes of the curves of Figs. 1 and 6 are nearly the same. Further, the latter curve is found to have the same universal character and insensitivity to N which was found for the curve of Fig. 1. In addition, since the two test methods must give the same result under very slow test conditions, it is gratifying to notice that both curves approach the same limit under this condition.

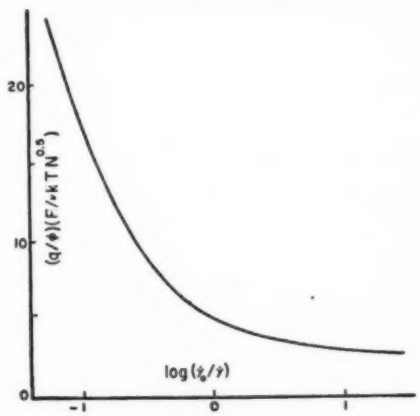

FIG. 6. Theoretical relationship showing the tensile strength of a plastic obtained at various constant rates of elongation.

From the result shown in Fig. 6 we, therefore, conclude that the previous remarks made concerning tensile strength in a creep test will apply here also. There is one slight difference. Since the variables plotted on the horizontal axis are not identical, the variation at fixed time and shear rate is not quite the same. In any event, the general strength behavior can be predicted from the relationship given here.

Although there appears to be no really suitable data available for making a quantitative test of the above relation, it appears that qualitative agreement is found with the data at hand. Inasmuch as the tensile strength predicted under creep conditions seems reasonably correct, we would expect the curve of Fig. 6 to be equally valid. However, it will suffer three limitations. First, it cannot be expected to apply at short times unless the correction involving Young's modulus is applied as already shown. Second, the relation will certainly not be valid if the shear rate is large enough to heat

TABLE III. Tensile strength under various constant rates of elongation.

$\dot{\gamma}_0/\dot{\gamma}$	0.06	0.10	0.30	1.00	3.00	10.0	∞
$(F/\nu kTN^{\frac{1}{2}})(q/\Phi)$	24.5	17.8	9.40	5.00	3.73	2.93	2.45

the test sample to any great extent; and third, since the theory assumes no viscous flow, it will not apply in its present form to cases where viscous flow is important.

We have attempted here to give a first approximation theory for the tensile strength of rubbery plastics. It is clear that much experimental work is needed before the results can be adequately tested. In addition, no provision has been made for such complicating factors as crystallization, the presence of fillers, and other complexities often encountered in practice. Recognizing these obvious limitations, it appears, however, that the concepts presented here are substantially correct and will form a good basis for future more detailed investigations.

ACKNOWLEDGMENTS

I am indebted to Professor J. D. Ferry, Dr. T. G. Fox, and Dr. S. Gratch for their valuable comments on an early draft of this paper. This work was made possible by a Cottrell grant in aid from the Research Corporation and it is a pleasure to express my appreciation for it.

APPENDIX I

In the text it was assumed that the applied force acted only at the ends of the network chains. Such is not the case at short times. It is easily shown that the intermediate segments experience an external force

$$\mathfrak{F}_i=[(i-N/2)/N]Rf[d(\Delta L)/dt], \quad i\neq 0, N$$

$$\mathfrak{F}_N=-\mathfrak{F}_0=-\alpha(x_1-x_0)+\tfrac{1}{2}Rf[d(\Delta L)/dt], \tag{8}$$

where

$$\Delta L=(x_N-x_3)/R.$$

We know that each cross section must support a force F and so

$$F/K=(1/N)^2[2\sum_{i=0}^{N/2} f\dot{x}_N(2-N)-2\alpha N(x_1-x_0)]$$

or

$$F/K=\tfrac{1}{2}f\dot{x}_N-(2\alpha/N)(x_1-x_0), \tag{9}$$

where K is dependent upon the number of chains traversing the cross section. The quantity K can be found by referring to the known result at $t\rightarrow\infty$. It turns out to be $(16\nu R/N^{\frac{1}{2}})$ for a chain of ten segments. We may now substitute Eq. (9) into (8) so as to eliminate x_1-x_0. One then calculates F_n as in reference 3 which leads to the following equation for q_n:

$$\dot{q}_n-(1+8/n^2\pi^2)\sum_{p\,\text{odd}}^{N}\dot{q}_p\cos(p\pi)+(m\omega_n^2/f)q_n=-2mNF/Kf(2mN)^{\frac{1}{2}}. \tag{10}$$

We try solutions of the form

$$q_n=A_n\exp(\lambda t)-2NF/K\omega_n^2(2mN)^{\frac{1}{2}}.$$

This gives rise to a secular equation for λ of order $\frac{1}{2}N$. The secular equation may be simplified to give

$$y(1+y)\sum_{n\,\text{odd}}^{N}(y+\omega_n^2/\omega_1^2)^{-1}+2.80y+1.00=0,$$

where $y=(f\lambda/m\omega_1^2)$ and so λ has $\frac{1}{2}N$ independent roots.

One may determine the constants A_n by substitution in the original equations and by applying the boundary conditions that at $t=0$, $q_n=0$. Although the computation is tedious, it involves no difficulties and has been carried out for $N=10$. Typical results are those for $i=0$ and 1.

$$x_0=\frac{NF}{25\nu Rm\omega_1^2}\{1.1814e^{-0.34\beta t}+0.0340e^{-5.91\beta t}+0.0059e^{-15.9\beta t}+0.0008e^{-27.6\beta t}+0.0002e^{-37.3\beta t}-1.2223\}. \tag{11}$$

The equation for x_1 is identical except that the coefficients are now 1.0520, -0.0344, -0.0099, -0.0095, -0.0064, and -0.9918.

These new expressions for the x_i are not far different from our previous ones. However, the quantity $x_{i+1}-x_i$ is smaller at $\beta t\rightarrow 0$ than was previously obtained by about a factor $1/N$. Since the two results are identical at $t\rightarrow\infty$ we see that the more accurate result given here does nothing but cause the breaking force to increase somewhat more rapidly with decreasing βt. But since the curve is already rising so swiftly, the accurate calculation given here will not change its shape to any great extent. In view of this fact, we shall continue to use the more convenient approximate form given in the text.

APPENDIX II

We will calculate here the response of a plastic under constant rate of elongation. At this time we will consider the network type of response only, the network being the result of true cross links or of entanglements.

Consider what happens when a small tensile load $\psi(t')$ is applied to the end of a sample. As shown previously,[4] the unit cube sample will elongate according to the relation

$$(8/3\pi^2\nu kT)\psi(t')\sum_{n\,\text{odd}}^{N}(1/n^2)\times\{1-\exp[-(t-t')n^2/\tau_1]\} \tag{12}$$

for $t'<t$.

In order to maintain a constant rate of elongation we must keep adding weights continuously. Superposing all of these responses leads to the following rela-

tion for the elongation of the sample:

$$(\Delta L/L)=(8/3\pi^2\nu kT)\sum(1/n^2)\int_0^t \psi(t') \times\{1-\exp[-(t-t')n^2/\tau_1]\}dt'. \quad (13)$$

Since the sample is elongating at constant rate we may also write $(\Delta L/L)=\dot{\gamma}t$, where $\dot{\gamma}$ is the tensile shear rate.

Equation (13) is a rather complex integral equation for $\psi(t')$ which cannot be solved easily by analytic methods. However, $\psi(t')$ may be evaluated quite simply by numerical methods and we have done this. Actually we are interested in the total force on the sample at any time t. This is merely the integral of $\psi(t')$ from $0\leqslant t'\leqslant t$. After carrying through the necessary numerical computations one is finally able to plot a curve relating the applied force needed to maintain a constant rate of elongation to the length of time for which the sample has been stretched. The result is plotted in Fig. 5 and given in Table II.

For the tensile strength calculation we really need $x_{i+1}-x_i$. We find this by use of the approximate relations $\Delta L/L)=(x_N-x_0)/R$ and $(x_{i+1}-x_i)=(x_N-x_0)/N$. One then obtains the result given in the text.

JOURNAL OF APPLIED PHYSICS VOLUME 26, NUMBER 9 SEPTEMBER, 1955

Dislocations in Germanium*

S. G. Ellis
RCA Laboratories, Princeton, New Jersey
(Received February 3, 1955)

A light microscope study of etched germanium crystals has shown the dislocation distribution in them. The dislocations form a network in the crystal.
The formation of small angle grain boundaries is discussed.
Screw dislocations with large Burgers vectors have been found in some germanium crystals.

INTRODUCTION

THE dislocations in germanium are of interest from two points of view: the mechanical and the electronic. The high purity and geometrical perfection of germanium single crystals permits the metallurgist to study the mechanics of slip under conditions not yet attained in metal single crystals. To the solid-state physicist, germanium, the best understood semiconductor, is the natural material in which to study the influence of dislocations on carrier trapping and other electronic properties.

In all such studies it is necessary to observe the distribution and type of the dislocations present. In special cases x-ray diffraction measurements will yield an average dislocation density.[1] For example, if there are D dislocation lines of Burgers vector b randomly distributed in a crystal, the half-width of a Bragg reflection $\Delta\theta$ will be given by:

$$D\doteq\left(\frac{\Delta\theta}{3b}\right)^2. \quad (1)$$

The calculation of D from $\Delta\theta$ will be in error if the dislocations are not distributed at random, or if they have different strengths.

Dislocations in germanium can cause local variations in the rate of etching, and, therefore, the terminations of the dislocations at the surface of the crystal can be detected, provided that they are far enough apart.[2] In germanium of quality satisfactory for transistor manufacture the dislocations are in general far enough apart that the pits they nucleate can be resolved in the light microscope. This paper describes light microscope techniques for examining dislocations in germanium and reports some of the conclusions reached in studying crystals grown under different conditions.

TECHNIQUES AND OBSERVATIONS

The shape of etch pits in germanium depends both on the crystallographic surface under attack and the composition of the etch which is being used. One conclusion reached from the work described in this section is that if the etching conditions are properly chosen each dislocation meeting the surface of the crystal nucleates a separate etch pit. The dislocation line must not be too oblique to the surface if this is to happen. The fine structure in the etch pits yields additional information on the type of dislocation causing the pits and, in some cases, indicates the shape of the dislocation line.

The techniques used here differed from the standard metallographic techniques in that little emphasis was placed on obtaining a flat specimen. The major emphasis

* Parts of this paper have been presented at the American Institute of Metallurgical Engineers' annual meeting in New York, February 15–18, 1954, and at the Conference on Mechanical Effects of Dislocations in Crystals, Birmingham University, England, July 19 and 20, 1954.

[1] Gay, Hirsch, and Kelley, Acta. Metallurgica **1**, 315 (1953).

[2] Vogel, Pfann, Corey, and Thomas, Phys. Rev. **90**, 489 (1953).

was on obtaining the maximum amount of structure in the pits.

The crystals to be examined were cut within a few degrees of one of the lower index planes: (100), (110), or (111). After fine grinding they were given a preliminary acid etch until the disappearance of the smooth-bottomed pits showed the worked layer had been removed. Further etching, in most cases with a slower etch, then produced pits characterized by a central depression.† When the pits had reached a terminal form the crystals were examined and sometimes photographed under vertical, nearly parallel, illumination. The etches, called number 2, dilute number 2, number 7, and CP–4 are described in the Appendix.

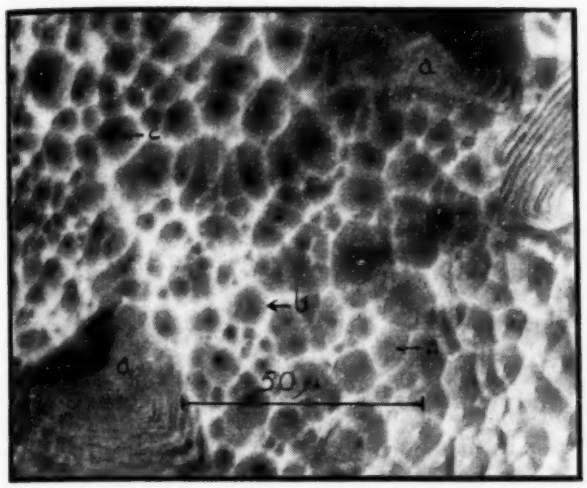

(a)

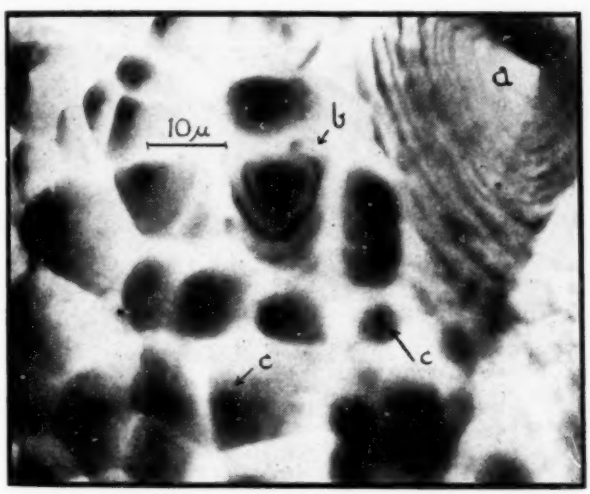

(b)

FIG. 1. (a) Germanium (111) surface treated with number 7 etch. The pits are identified in the text. (b) A spiral, type (b) pit at higher magnification.

† This is true of the slower etching faces. On the fastest etching faces the regions of the dislocations, in some cases, etched less rapidly than the surrounding crystal.

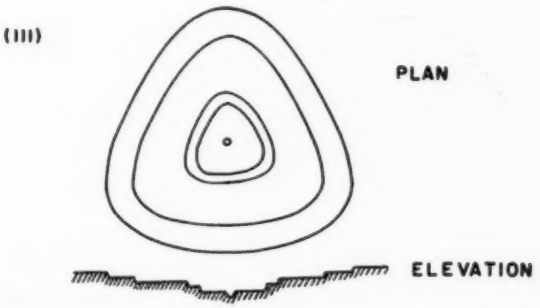

FIG. 2. Pit on (111) surface formed by number 2 etch. The edges of the terraces appear dark under vertical illumination.

When the slow, alkaline, number 7 etch was used on the (111) surfaces of germanium crystals, three types of pits were observed:

(a) large pits with a density (i.e., number per cm^2) of the order 10^3 to 10^4 cm^{-2},
(b) pits with spiral terraces,
(c) small pits with closed terraces.

The combined density of the type (b) and (c) pits was of the order 10^6 to 10^7 cm^{-2}. Because of the limits of contrast and resolution in reflection light microscopy, it is not always possible to assign a small pit to the class (b) or (c).

In some dendritic crystals the spiral, type (b) pits are very clear. It is believed that they are due to a dislocation with a large screw component, the Burgers vector being equal to the pitch of the terrace. This may approach 1000 A. Figure 1 shows such a dendritic crystal. The pits are labeled in the foregoing notation.

When such a crystal is etched with CP–4, pits are found only at the sites of the large type (a) pits described in the foregoing. It is concluded therefore that the type (a) pits produced by an alkaline etch are nucleated by the edge dislocations described by Vogel and his co-workers.[2]

There are three reasons for believing that the small type (c) pits indicate dislocations. They correspond to a structure which persists in depth. They have been found in linear arrays suggestive of small angle grain boundaries. Their density corresponds to the density of dislocations deduced from the half-width of Bragg reflections from such crystals.‡

The number 2 etch, like CP–4, shows only the edge dislocations described by Vogel *et al.*[2] Unlike CP–4, the number 2 etch develops considerable structure within the pits on (111) surfaces. Typical pits are sketched in Fig. 2. The characteristic features are a central depression surrounded by a number of irregularly spaced terraces. The same arrangement of terraces is sometimes seen in adjacent pits. Generally, however, the arrangement of terraces differs between pits. Occasionally the form shown in Fig. 3 is observed.

‡ The x-ray studies were made for us by Dr. Sigmund Weissmann and his co-workers at Rutgers University.

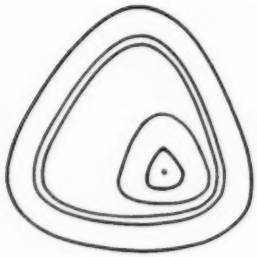

FIG. 3. Pit form when the center of attack shifts during etching.

There the inner, and lower terraces are concentric with the central depression while the outer ones are not. It is suggested that the terraces indicate kinks or jogs in the dislocation, and the rate of attack of the etch, normal to the surface, is reduced when the kink or jog is reached.

If the number 2 etch is diluted with 50 parts of water it develops a pit density as high as the number 7 etch though it does not usually show as much detail in the small pits. Figure 4 shows a pit with a spiral terrace developed by dilute number 2 etch.

Using these etching techniques, crystals grown in a variety of ways have been examined.

CRYSTALS GROWN FROM THE MELT

Chalmers has recently reviewed the subject of crystal growth from the melt.[3] He shows that the temperature gradient in the melt will have a decisive effect on the process of crystallization. The temperature, T_E, at which a given face of the crystal is in equilibrium with the melt will depend on the impurity concentration in the melt. If impurities are being rejected from the solid into the liquid they will be more concentrated near the liquid-solid interface and there will be a gradient, dT_E/dz, of equilibrium temperatures in this region. If T_M is the melt temperature at the point (xyz), the values of dT_E/dz, and dT_M/dz control the nature of the crystallization process. In the growth of germanium crystals three different conditions may be obtained:

(I) $dT_M/dz > dT_E/dz$. With a high gradient in the melt the solid-liquid interface, at least on a macroscopic scale follows the form of the isothermal surfaces in its vicinity.

(II) dT_M/dz and dT_E/dz small and nearly equal. The crystal grows until it is bounded by the faces for which T_E is lowest. For germanium these are the {111} planes.§ This can be demonstrated, Fig. 5, by suddenly withdrawing the crystal from the melt. This form of the crystal, which has also been observed by Robinson *et al.*[4] will be referred to as the equilibrium form.

A triangular depression is often found at the center of the octahedral faces. It can be seen in the illustrations of reference 4, but is not present on all crystals, as shown by Fig. 5. It does not have the orientation of the trigons[5] on diamonds and its origin is unknown. In the center of the depression there is a conical protuberance which probably originates when a drop of liquid germanium withdrawn from the melt, with the crystal, solidifies.

(III) $dT_M/dz < dT_E/dz$, and particularly dT_M/dz negative. In this case the growth is dendritic. Such growth can be demonstrated by plunging a germanium seed into a super-cooled melt, and then rapidly withdrawing it, Fig. 6. The dendrites are spear shaped, elongated in the ⟨211⟩ direction, and are bounded by {111} surfaces.

It is known that the conditions of growth can fluctuate, producing resistivity striations.[6] There is some evidence that the growth conditions can fluctuate between one in which the solid-liquid interface is smooth to one in which the growth is equilibrium or even dendritic.

Small angle grain boundaries revealed by rows of the large, type (a) pits have been found in crystals grown in the [100], [110], and [111] directions. They are common in [100] crystals and rare in [111] crystals. Where they occur they become more clearly defined as the growth proceeds. In [100] crystals grown under conditions tending towards equilibrium growth the solid-liquid interface may show several pyramids bounded by the octahedral faces, Fig. 7. The small angle grain boundaries form in the valleys between these pyramids. This is very clearly demonstrated in some silicon-germanium crystals. Cycles in the growth rate have produced corresponding variations in composition. These become visible on etching and show the successive

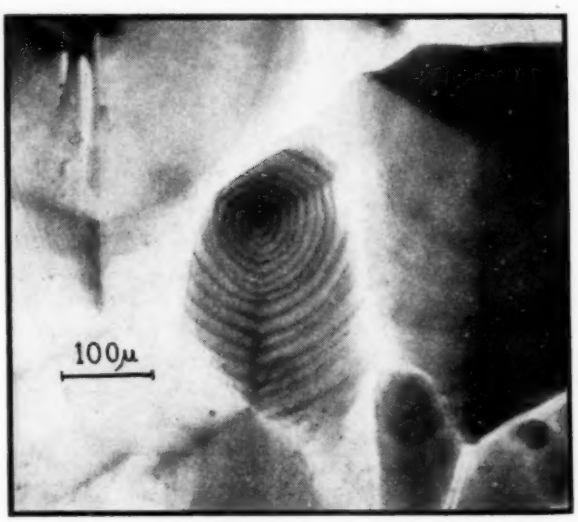

FIG. 4. A pit with a spiral terrace formed by a dilute number 2 etch. (111) surface.

[3] B. Chalmers, J. Metals **6**, 519 (1954), Sec. 1.

§ {111} is used here to describe (111) planes in general, including (1,1,−1), (−1,1,1) etc.; ⟨111⟩ will be used for the directions [111], [1,1,−1] etc., in general.

[4] Robinson, Ostapkovich, Schlegel, and Gazzara, Science **116**, 362 (1952).

[5] A. Halperin, Proc. Phys. Soc. (London) **B67**, 538 (1954).

[6] P. R. Camp, J. Appl. Phys. **25**, 459 (1954).

positions of the solid-liquid interface. Figure 8(a) is of a section which includes the growth direction. The growth was from left to right and has changed from the high-gradient to the equilibrium form. When a section perpendicular to the growth direction is etched with CP-4 the striations, which have an octahedral habit, appear as in Fig. 8(b). The dots show the position of edge dislocations. When a dilute etch is used rows of smaller pits are also found in the hollows between the equilibrium forms. The dislocations which cause these smaller pits terminate not only in the hollows but also within the areas marked by the faint rectangles.

The small-angle grain boundaries shown by the number 2 etch can be traced back through crystals by etching off successive layers in a direction opposite to the growth direction. It is seen that some of the dislocations diverge from the boundaries. The pits due to them eventually disappear. They do this singly, and not in pairs. This result will be discussed later in connection with the formation of edge dislocations.

Screw dislocations with large Burgers vectors (of the order 1000 A) have been found in neither high gradient nor equilibrium crystals. They are not uncommon in dendritic crystals. Screw dislocations with Burgers vectors at the limit of detection of the light microscope have been observed in a few crystals grown under supposedly high gradient conditions.

Slip bands have been observed on dendritic crystals. It is not known whether slip occured while the dentrites were in contact with the liquid or later soon after removal. If the slip occured while the dendrites were in the liquid, because of temperature gradients in the crystal, we have one mechanism for the production of dislocations during growth from the melt.

FIG. 5. The octahedral, or equilibrium form of germanium. The conical mounds seen on the bottom, and also the right-hand face, form when a drop of liquid withdrawn from the melt freezes.

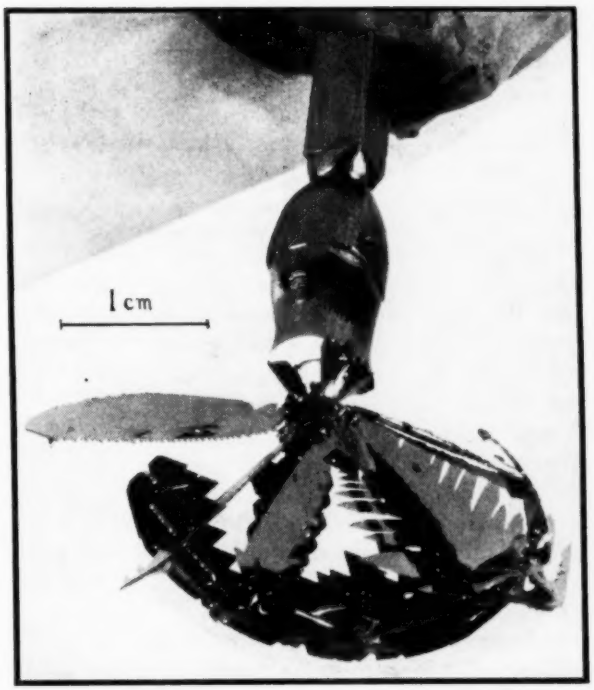

FIG. 6. A group of germanium dendrites. The dendrite running forward and to the right has well-developed secondary dendrites on it.

The small, type (c), pits are seen scattered at random on surfaces cut parallel to the liquid-solid interfaces. Very rarely they form what is believed to be a small-angle grain boundary in [111] grown crystals.

CRYSTALS GROWN FROM SOLUTION

In one method of making alloy junction transistors, a small piece of indium is melted on a germanium single crystal wafer and the temperature is raised until some of the germanium has been dissolved. The system is then cooled and germanium recrystallizes out, epitaxially on the substrate germanium. The recrystallization could take place without supersaturation even in the absence of dislocations since the substrate germanium is concave towards the solution and provides many nuclei at which the regrowth can start. This is not the case in the system studied by Pankove[7] where the substrate was convex towards the liquid and the usual arguments in favor of growth on screw dislocations would apply.

The fine structure seen on the un-etched surfaces of the recrystallized material suggests that growth takes place by the addition of {111} layers, nucleated at the higher parts of the crystal, and growing out most rapidly in the ⟨211⟩ directions. Edge dislocations in the

[7] J. I. Pankove, RCA Rev. XV, 75 (1954).

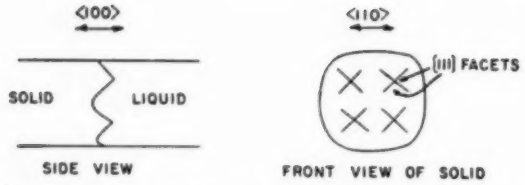

FIG. 7. A crystal growing in the ⟨100⟩ direction under equilibrium conditions has four pyramids forming on it.

substrate are reproduced in the regrowth crystals. Some dislocation lines have been found in the surface which separates the substrate from the regrown crystal. These may be due to a misfit between the relatively pure substrate and the impure regrown material.

Spiral terraces have been seen on the un-etched recrystallized material but they are not common, at least with step heights visible in the light microscope. The regrowth is often most rapid (measured in a direction perpendicular to the substrate) around an unwetted region of the substrate. It is suggested that the original regrowth fronts advance and are divided by the unwetted area and that when they rejoin after passing it they do so with a mistake in height forming a screw dislocation. Growth then proceeds rapidly on this dislocation, often to a greater height than that of the germanium surface outside the area contacted by the indium. The unwetted area is sometimes covered over by further growth on the inner concave walls of the vertically growing recrystallized germanium. The mistake in height causing the screw dislocation may, again, be due to variations in impurity content. A very similar mechanism has been described by Fisher, Fullman, and Sears.[8]

DISCUSSION

The presence of large screw dislocations in dendritic crystals can be explained in the following way. Suppose that a dendrite A, Fig. 9, gives rise to secondary dendrites B, B', and a tertiary dendrite C which joins B to B'. Temperature gradients, or a nonuniform impurity content may cause C to grow forward (with respect to the plane of the figure) as it grows downwards so that a mistake is made in closing the circuit $ABCB'A$. This appears as one or more screw dislocation lines as the void V solidifies. The experimentally produced dendrites were cooled rapidly after removal from the liquid so that there was little opportunity for the large dislocations to decompose into smaller ones.

This mechanism for producing dislocations is not open to crystals grown under high enough gradients to preclude constitutional supercooling. Teghtsoonian and Chalmers[9] have advanced an hypothesis to cover this case based on a mechanism suggested by Frank,[10] Seitz,[11] and Crussard.[12] In this hypothesis, vacancies aggregate to form a disk-shaped void which then collapses to form a dislocation at the perimeter of the void. If the void meets the solid-liquid interface a dislocation will be formed which begins and ends at the solid-liquid interface. Teghtsoonian and Chalmers then suppose that the dislocations move in the crystal eventually forming small angle grain boundaries, or in other words a macromosaic or lineage structure.

The macromosaic structures in germanium are generally much larger than those observed in metal

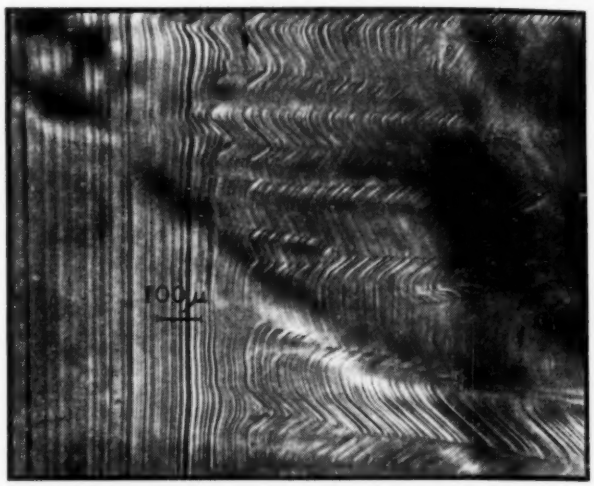

(a)

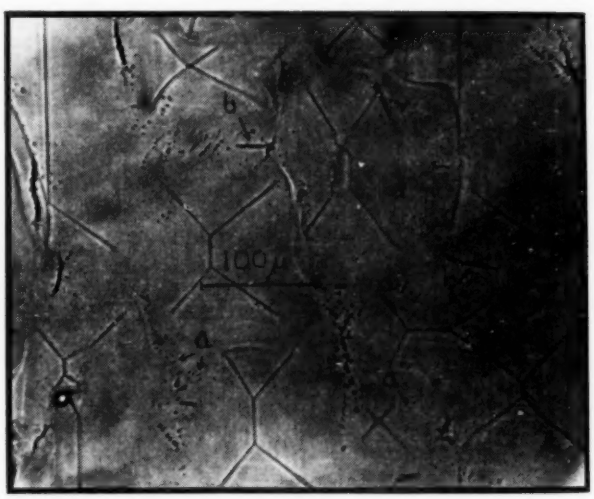

(b)

FIG. 8. (a) A germanium−15% silicon crystal has been grown in the ⟨100⟩ direction and cut to include the direction of growth. The striations show the form of the solid-liquid interface. Growth was from left to right and has become equilibrium. (b) A section perpendicular to the growth direction, has been etched with CP-4. The heavy straight lines show where the pyramidal, equilibrium projections occurred. The pits (a) indicate edge dislocations. In some places (b) these have congregated into small angle grain boundaries.

[8] Fisher, Fullman, and Sears, Acta Metallurgica **2**, 344 (1954).
[9] E. Teghtsoonian and B. Chalmers, Can. J. Phys. **29**, 370 (1951).
[10] F. C. Frank, Symposium on Plastic Deformation, Pittsburgh, Pennsylvania (1950).
[11] F. Seitz, Phys. Rev. **79**, 890 (1950).
[12] C. Crussard, Métaux & corrosion **25**, 203 (1950).

single crystals. This is probably the result of the higher purity in germanium melts which makes it less probable that equilibrium growth will be approached. When the equilibrium growth conditions are approached the distances between the troughs on the solid-liquid interface are larger with the high purity melt. This is supported by experience with germanium-silicon melts.

The fact that the small-angle grain boundaries occur in the troughs between the octahedral faces in the equilibrium growth suggests that the formation of these boundaries is not entirely due to crystallographic effects in the solid, as suggested by Teghtsoonian and Chalmers. It appears to be connected with the form of the solid-liquid interface and may be explained in the following way: Suppose that dislocations are generated at random and that the solid-liquid interface approximates the equilibrium form, Fig. 10. At any instant a dislocation can become shorter by moving from A to A'. Therefore, as the growth proceeds the dislocations tend to concentrate in the troughs on the solid-liquid interface. In this region the forces between the dislocations become large and lead to the formation of the small angle grain boundaries.

The problem of the original generation of the dislocations requires further consideration. Suppose a crystal to be growing in the [111] direction. If vacancy disks are formed they may be expected to have a minimum surface energy if they are bounded by {111} planes with single bonds pointing into the voids. The most probable Burgers vectors for the collapse of the $[1\bar{1}1]$ disks are:

$$\pm\tfrac{1}{2}a[101],\ \pm\tfrac{1}{2}a[1\bar{1}0],\ \pm\tfrac{1}{2}a[0\bar{1}1].$$

If the disks intersect the solid-liquid interface and if on further growth the dislocation lines bend to run in the [111] direction, the first vector gives a composite edge and screw dislocation and the second two give pure edge dislocations.

Since the large etch pits are due to edge dislocations, it is tempting to ascribe the small pits to the composite dislocations. The observed ratio of small to large pits is of the order 100 : 1. On the hypothesis given above it should be 2 : 1.

If some diffusive motion takes place, the dislocations postulated above could interact to reduce their total

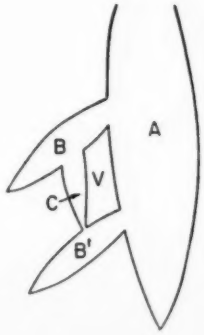

FIG. 9. The formation of screw dislocations during dendritic growth.

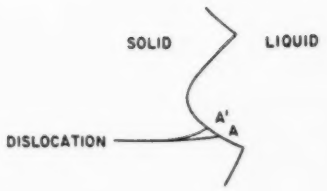

FIG. 10. Movement of dislocations during crystal growth to form small angle grain boundaries.

number. But without making further specialized assumptions it is difficult to see how the observed distribution would result. It is possible that the dislocation lines tend to run in directions other than the edge orientation.

The light microscope observations do not, therefore, give unqualified support to the vacancy-disk-collapse hypothesis for the generation of dislocations. The possibility that the dislocations are generated by slip should not be overlooked. The crystal, close to the solid-liquid interface is plastic. It is acted on by its weight and by the surface tension of the liquid, and it often has large and nonlinear temperature gradients in it. To distinguish between these possible causes will require the examination of crystals grown under a wider range of conditions than have been used up to the present.

Any two of the dislocations described above can combine if their Burgers vectors are 120° apart. The following reactions are therefore possible:

$$\text{edge}+\text{edge}\rightarrow\text{edge}, \tag{2}$$

$$\text{edge}+\text{composite}\rightarrow\text{composite}, \tag{3}$$

$$\text{composite}+\text{composite}\rightarrow\text{edge}. \tag{4}$$

Since the small pits are not developed by the number 2 etch, reaction (4) can explain why, on etching back into a crystal, the large pits may deviate from a small angle grain boundary and eventually disappear. Reaction (2) can also explain why under similar conditions a large pit may divide into two large pits. Another reason for the disappearance of large pits could be that the direction of the dislocation changes from the edge to the composite orientation. The observations strongly suggest that the dislocations are not isolated but form a connected network.

CONCLUSIONS

Under proper etching conditions most, if not all, of the dislocations in germanium cause etch pits which are characteristic of the dislocations. Two necessary conditions are that the etching shall be slow and that the etch shall attack some other face of the crystal faster than it attacks the one under study.

It is apparent that there is more than one type of dislocation in germanium and that, at least near small angle grain boundaries, these form an interconnected network. The results also show that large screw dislocations can exist in germanium.

Under equilibrium growth conditions the dislocations become concentrated in the valleys on the solid-liquid interface and there interact (in part by combination) to form the low-energy small-angle grain boundaries.

ACKNOWLEDGMENTS

I am indebted to Mr. Paul R. Camp for helpful discussions on etching germanium and to Dr. S. M. Christian for directing my attention to the striations in silicon-germanium crystals.

APPENDIX

The reagents used in preparing the etches are:

H_2O_2	Technical quality	Assay 30–35%
HNO_3	Reagent quality	Assay 69.2%
HF	Reagent quality	Minimum assay 48%
CH_3COOH	Reagent quality	Minimum assay 99.8%

The number 2 etch has the following composition:

10 ml HF
10 ml H_2O_2
40 ml H_2O.

Its reaction with germanium has been studied by P. R. Camp[13] who finds that the rate of attack at room temperature is of the order a few microns per minute. The order of attack on the different faces is (110) fastest, (110), (111) slowest.

[13] P. R. Camp, Electrochem. Soc. Enlarged abstracts of papers presented by the Electronics Division, spring meeting, Chicago, May, 1954, p. 115.

If one part of the above composition is added to 50 parts of water, this slower etch will develop small pits as described above.

The usual procedure in using this slow etch has been to remove the worked layers of the crystal with CP–4, then etch for two hours in dilute number 2 etch to observe the distribution of dislocations. On etching for 16 hours some pits become very large and obscure the smaller ones. Such long etches are required to show the spiral terraces.

Number 7 etch. The following method of making the etch was developed empirically. The composition is critical and the etch deteriorates both at room temperature and under refrigeration after a few days.

Chlorine is bubbled slowly into an ice-cold 0.8 N potassium hydroxide solution until the *p*H is in the range 8 to 9. As needed 15 ml of this solution is diluted with 60 ml of water to which 0.3 mg. (three small pellets) of potassium hydroxide has been added.

The attack of this etch is slow so that it is convenient to remove any worked layers with CP–4. The number 7 etch will then develop the small pits in three hours, or the sample (if small compared with the volume of etch) may be left in it over night. The order of attack is (100) fastest, (110), (111) slowest.

CP–4 etch has the following composition:

50 ml HNO_3
30 ml CH_3COOH
30 ml HF
0.6 ml Br.

JOURNAL OF APPLIED PHYSICS VOLUME 26, NUMBER 9 SEPTEMBER, 1955

Effect of Nitrides on the Coercive Force of Iron*

J. KERR AND C. WERT
University of Illinois, Urbana, Illinois

(Received April 21, 1955)

The effect of plates of nitrides on the coercive force of iron has been determined. A pronounced particle size effect was observed. The maximum effect on the coercive force was produced by particles whose largest dimension was of the order of the domain wall thickness, δ. For particles much larger than δ, an expression given by Néel for the effect of inclusions is found to be valid. The results of this study are in good agreement with earlier results reported for the effect of carbides on the coercive force of iron.

I. INTRODUCTION

THE coercive force of ferromagnetic materials is a highly structure sensitive property; it is strongly dependent both on the state of internal strain and on the state of aggregation of impurity atoms. Furthermore, the physical size of the strain centers and inclusions to which the coercive force is most sensitive is small—for some materials of the order of 1000 A to 10 000 A. Since it is often difficult to prepare specimens containing inhomogeneities of this size, meaningful experiments are difficult to carry out.

The effect of inhomogeneities on the coercive force is only partially understood, but a number of calculations have been attempted. Several general reviews of these have recently appeared,[1] so only a brief resumé of the theories will be presented here.

The first of these was a calculation by Kersten on the effect of inclusions of nonferromagnetic material.[2] He considered the problem of pushing a 180° domain wall through a regular network of spherical particles of size large compared to the domain wall thickness, δ. The energy of the material is lowered when the domain wall intersects a sphere by an amount that corresponds to the energy of the wall area which is, in effect, removed by the inclusion. For a given total volume of inclusions per unit volume of metal, he found the coercive force to vary as the reciprocal of the particle size. Numerical calculations made for specific materials give about the value of the coercive force actually observed.

Kersten's initial calculation has been improved upon in several respects. Néel has proposed that (for large particles at least) the chief factor contributing to the coercive force is not Kersten's "surface tension" and that the general agreement of these calculations with observed facts is only fortuitious.[3] Néel has presented a new theory in which magnetic poles around large inclusions were considered to be of prime importance. According to this theory, the domain wall will seek to assume those configurations for which the magnetostatic energy is lowest. He included, in addition, the effect of internal strain inhomogeneities, but the result which is of most interest here is his calculation for inclusions. He found that for iron the effect on the coercive force, H_c, of a volume fraction of inclusions, ν_i, is given by

$$H_c = 360\nu_i. \tag{1}$$

In a more recent paper, Dijkstra and Wert made a further calculation.[4] They attempted to evaluate the effect of both large and small particles on the coercive force. They included both the surface tension of Kersten and the magnetic poles of Néel. They were able to compute the effect for spherical particles both much larger and much smaller than δ. For large particles, the coercive force decreased with increasing particle size and for small particles it increased with increasing particle size. Clearly then, it must go through a maximum at some particle size; they found this critical size to be that for which the diameter of the spheres was of the order of δ.

The general correctness of the points of view outlined above has been demonstrated by the experimental work of Dijkstra and Wert.[4] They found that for a given volume fraction of inclusions of carbide in iron ($\nu_i \approx 0.003$), the maximum effect was observed for a particle diameter of about 1200 A. This is close to the value of about 1000 A calculated for δ from knowledge of the anisotropy energy of iron. Furthermore, the value of slightly less than 1 oersted which they observed for particles much larger than δ is close to the value of 1.1 oersted given by Eq. (1) above for $\nu_i \approx 0.003$.

The present paper reports coercive force measurements made on iron containing as inclusions platelike precipitates. Measurements of coercive force were made during the precipitation of nitrides out of solid solutions of N in iron. The fineness of dispersion of the inclusions was controlled using heat treatments described in the next section. While the above calculations for spheres may not be applicable to the flat disks of this experiment, the results demonstrate that a critical

* This work was supported in part by the Office of Ordnance Research, U. S. Army.

[1] K. Stewart, *Ferromagnetic Domains* (Cambridge University Press, New York, 1954); U. Martius, Chap. 5 entitled "Ferromagnetism," in *Progress in Metal Physics* (Interscience Publishers, Inc., New York, 1952), Vol. 3.

[2] M. Kersten, *Grundlage Einer Theorie der Ferromagetischen Hysterese und der Koerzitivkraft* (S. Hirzel, Leipzig); reprinted by Edwards Brothers, Inc., Ann Arbor, 1943.

[3] L. Néel, Ann. univ. Grénoble **22**, 299 (1946).

[4] L. Dijkstra and C. Wert, Phys. Rev. **79**, 979 (1950).

particle size does exist for these nitrides. Here also it is a size for which the large dimension of these plates is about the same as δ. Again, Néel's expression for the coercive force of large particles is about satisfied. The data which are presented are in excellent agreement with some observations recently reported by Köster and Bangert.[5]

II. EXPERIMENTAL DETAILS

The chief problems of these measurements were the preparation of proper samples and their subsequent heat treatment. Fortunately, the testing methods used are nondestructive so that a given sample could be followed completely through the precipitation process at a given temperature. Each sample was handled in the following way: After an appropriate solid solution of N in iron had been prepared, it was heated at a temperature to cause all or a part of the N to be converted to a nitride. At intervals during this heat treatment, measurements of internal friction and coercive force were made. The internal friction measurements were used to follow the course of the precipitation; the coercive force could then be determined as a function of the quantity of nitride present.

The internal friction method used was the standard torsional pendulum technique used many times in the past to follow aging in such interstitial solid solutions. The details and basic ideas of such measurements are described in numerous earlier papers and will not be repeated here.[6–8] The coercive force measurements were made by the conventional ballistic galvanometer method.

The choice of composition of the alloy is fixed within the general limits of about 0.01- and 0.05-wt %N by the metallurgical properties of solid solutions of N in iron near room temperature. Below 0.01 %N, the time of the experiment is long and the quantity of precipitate is small. The reaction goes so fast above this range even at room temperature that one would have a hard time establishing a stationary state during measurement. The level chosen was the middle of this range, 0.03-wt %N. This choice was fortunate in that it, too, was the choice of Köster and Bangert[5]; hence direct comparison of our observation with theirs is easy.

The early work of Köster on aging in these alloys had already established the fact that the effect on the coercive force was most pronounced between 50°C and 200°C.[9] The present experiments were designed to examine this region systematically. Twelve specimens were prepared; one of these was aged at a given temperature until the N in solid solution was converted to the nitride as far as this reaction would go at that temperature. Aging temperatures were chosen every 25°C from 25°C to 300°C.

A typical measurement was made in the following way: A specimen was prepared by first heating a 6-inch length of iron wire at 590°C in a mixture of NH_3 and H_2 and then quenching the wire into water at room temperature. A measurement of internal friction at 25°C (for a frequency of 1 cps) gave a measure of the N in solid solution. The coercive force was then measured, after which the specimen was heated in a furnace at some aging temperature for an appropriate period of time and quickly cooled to room temperature. Measurements of both internal friction and coercive force were again made. Repetition of this cycle several times showed how both the internal friction and coercive force changed during aging at that temperature.

A study of the low N portion of the constitution diagram for Fe—N alloys shows that for the conditions of this experiment two nitrides can be formed (see Fig. 1). These are the metastable $Fe_{16}N_2$ and the stable Fe_4N, which are in general formed in succession. Fortunately the work of Dijkstra[6] has shown how the internal friction behaves during aging of N at these temperatures; this may be described for the conditions of the present experiment as follows: The interval between 25°C and 300°C will be broken up into three distinct regions. The first of these is that between 250°C and 125°C, where only the precipitate $Fe_{16}N_2$ will form.† The second is that region between 125°C and 250°C, where the nitride $Fe_{16}N_2$ first forms, then quickly dissolves, with the N reforming (along with a part of that N which had remained in solid solution) as Fe_4N.

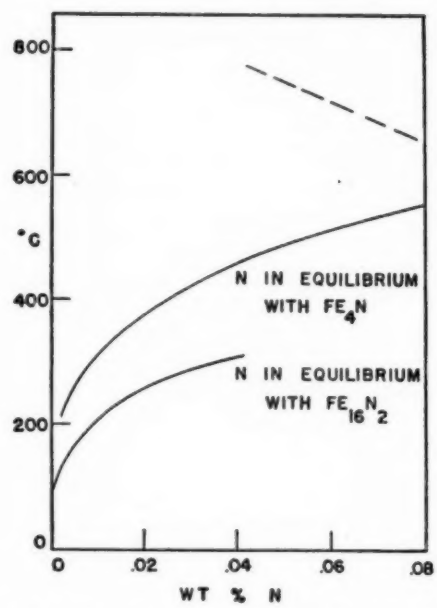

FIG. 1. The low N part of the constitution diagram of Fe and N. These curves are plotted from data obtained by Dijkstra.[6]

[5] W. Köster and L. Bangert, Arch. Eisenhüttenw. **25**, 231 (1954).
[6] L. Dijkstra, Trans. Am. Inst. Mining Engrs. **185**, 252 (1949).
[7] C. Wert, J. Appl. Phys. **20**, 943 (1949).
[8] T. Ke, Phys. Rev. **74**, 914 (1948).
[9] W. Köster, Arch. Eisenhüttenw. **3**, 553 (1930).

† The amount of N in equilibrium with $Fe_{16}N_2$ below 125°C is so small that the Fe_4N will form exceedingly slowly and, in fact, will not form in the time of these experiments.

The third region is that above 250°C, where the only nitride which forms in any quantity is Fe_4N. The distinct behavior of the precipitation phenomena in these three regions is reflected in the coercive force measurements as well.

For proper interpretation of the coercive force observation, it is important to know how the number of precipitate particles varies with the temperature of aging. Fortunately, such information is known qualitatively from previous observations by Dijkstra[6] and from some of our own preminiinary studies using an optical microscope. Three facts are pertinent here: (1) The $Fe_{16}N_2$ precipitate is more finely divided at low aging temperatures than at high; (2) at those temperatures where both form, the Fe_4N is much coarser than $Fe_{16}N_2$; and (3) during aging at a given temperature, the number of particles decreases continuously; at least during the later stages of aging, coalescence occurs.

III. RESULTS AND DISCUSSION

Four sets of data will serve to illustrate the behavior of the coercive force during aging of the alloys. These data are presented in Figs. 2 to 5 for the aging temperatures 54°C, 100°C, 150°C, and 300°C. Each figure shows: (1) the fraction, F, of the nitrogen which had precipitated at a given time and (2) the change in coercive force, ΔH_c, which had occurred at that time. ΔH_c is the difference between the coercive force at time t, H_t, and the initial value of coercive force H_0, i.e.,

$$\Delta H_c = H_t - H_0.$$

H_0 was about 1 oersted for all samples.

A description of the metallurgical phenomena which take place during aging at the various temperatures is given in the paragraphs which follow. Also included are our interpretations of the way in which the various precipitate structures affect ΔH_c. The internal consistency of the arguments is so good that, together

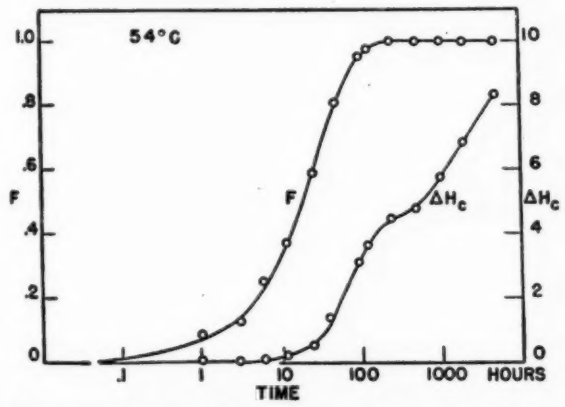

FIG. 2. The fraction of N precipitated, F, and the change in coercive force, ΔH_c, produced by aging at 54°C. A sample of iron containing 0.03-wt %N. ΔH_c is measured in oersteds.

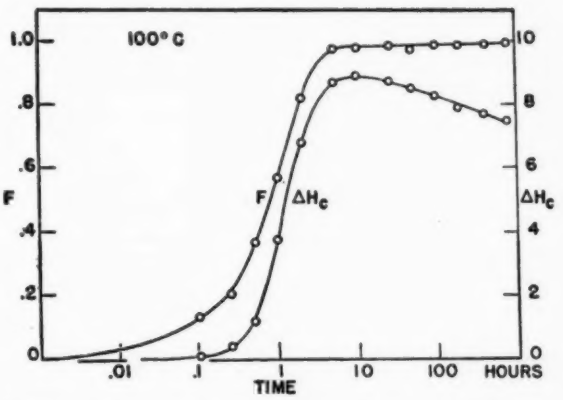

FIG. 3. The fraction of N precipitated, F, and the change in coercive force, ΔH_c, produced by aging, at 100°C, a sample of iron containing 0.03-wt %N.

with the work previously reported,[4,5] the over-all picture must be close to the correct one.

At 54°C the curve F in Fig. 2 shows that practically all the N has precipitated as $Fe_{16}N_2$ after 100 hours. The total volume of precipitate remains constant after this time, but the number of particles decreases as time goes on. The coercive force has increased by only 4 oersteds just at the close of precipitation, but it continues to increase with further aging. This is presumably so because at the end of precipitation the inclusions were too small to produce the optimum effect, but came closer to being of critical size as coalescence proceeded. A further increase in particle size which would accompany even further aging at this temperature would cause the coercive force to increase even more to a maximum at some optimum particle size. Further coalescence, with its attendant particles of even larger size, would cause the coercive force to fall. The curve shown in Fig. 2 is similar to that observed for coercive force changes accompanying precipitation of carbides in iron at low temperatures.[4]

As the aging temperature is increased from 54°C, the behavior of ΔH_c changes gradually until the inflection of the curve at the close of aging disappears. It first does so at 100°C; the behavior of F and ΔH_c at this temperature is shown in Fig. 3. Here ΔH_c goes through a maximum of about 9 oersteds just at the close of the precipitation. Further aging, resulting in coalescence, yields inclusions which are oversize for maximum effect, so the coercive force falls.

At 150°C (Fig. 4), the situation is qualitatively the same: The coercive force goes through a maximum just at the close of precipitation, then falls off again as coalescence proceeds. However, there are some small but significant differences between this behavior and that of Fig. 3. The most important of these is that the maximum of the coercive force is somewhat smaller than that at 100°C. There are two reasons for this: (a) At the close of precipitation the particles are oversize, hence their effect is reduced; (b) the total volume of

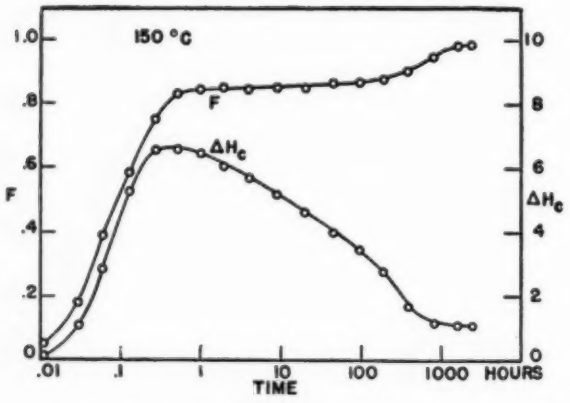

FIG. 4. The fraction of N precipitated, F, and the change in coercive force, ΔH_c, produced by aging, at 150°C, a sample of iron containing 0.03-wt %N.

precipitate at 150°C is smaller than that at 100°C, since the solubility of N in equilibrium with $Fe_{16}N_2$ at this temperature is appreciable. Approximately 15% of the N still remained in solid solution. This in itself would certainly cause the maximum to be lower since ΔH_c must be a function of both particles size and the total volume of precipitate. This point will be discussed later.

The stable precipitate Fe_4N began to form after about 500 hours at 150°C. It continued to form until after some 3000 hours, when all the N (both that in the $Fe_{16}N_2$ and that which had remained in solid solution) had been converted to this form. Since these plates of precipitate are much coarser than the $Fe_{16}N_2$, the formation of the Fe_4N is accompanied by a continuous decrease in ΔH_c to a low value of about 1 oersted when the process is complete.

As the aging temperature is increased above 150°C, the maximum in ΔH_c continues to decrease both because of the particle size effect and because the total volume of $Fe_{16}N_2$ continues to grow smaller. Finally, at 300°C, the situation is that shown in Fig. 5. The first rise in curve F at about 0.01 hour is very small, indicating that at this temperature almost all the 0.03-wt %N is in equilibrium in solid solution with the $Fe_{16}N_2$. This small amount of precipitate produces no change in the coercive force. When the Fe_4N precipitate begins to form in about 0.1 hour, ΔH_c increases somewhat, goes through a maximum of about 1.5 oersted at 1 hour when precipitation is just complete, then slowly decreases. Notice that at this temperature the solubility of N in equilibrium with Fe_4N is appreciable, so that when aging is complete, about 0.01 %N (about 30% of the N) is still left in solid solution. The slow rise in the curve F after more than 10 hours at 300°C is caused by the loss of N out of the sample to the atmosphere. This cannot be avoided.

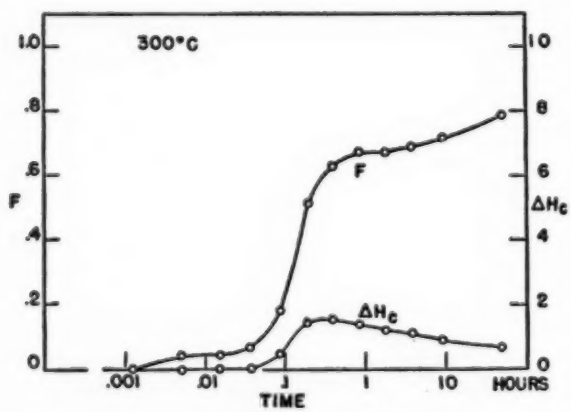

FIG. 5. The fraction of N precipitated, F, and the change in coercive force, ΔH_c, produced by aging, at 300°C, a sample of iron containing 0.03-wt %N.

The over-all picture of the behavior of the coercive force is the following: At low aging temperatures, where the size of particles formed during the primary precipitation is small, the effect on the coercive force is also small. Overaging, with its resulting larger particles, causes the coercive force to increase toward some maximum value. At somewhat higher temperatures, the coercive force goes through its maximum value just at the close of precipitation; overaging causes only a decrease in the coercive force. At still higher temperatures, the maximum is reached also at the close of precipitation, but it is a lower maximum than in the preceeding case. Finally, when the temperature is high enough so that Fe_4N is the major precipitate, the effect is relatively small because the particles are grossly oversize.

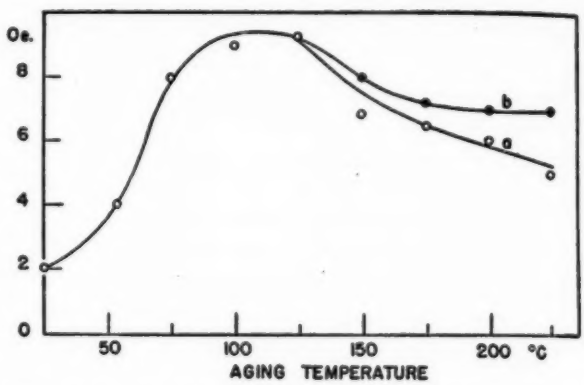

FIG. 6. The value of ΔH_c which occurred just at the close of precipitation of $Fe_{16}N_2$ at various temperatures. Curve (a) shows the original data; curve (b) shows the data corrected for the solubility of N.

It is possible to determine the critical particle size by actual examination of the precipitates. To see which specimen should be examined, we first look at the data in Fig. 6. Here is plotted, as a function of temperature, the value of ΔH_c observed when precipitation has just ceased (— o —). A maximum in the curve is observed at around 100°C. This direct plot is not quite a fair portrayal of a size effect, since at temperatures above 125°C considerable N may remain in solid solution.

A correction factor cannot be applied to the data with certainty since the relationship between the physical characteristics of the inclusions and the coercive force is not known exactly. However, one can guess that a reasonable correction would be supplied by using the expression

$$\Delta H_c = \nu_i f(d). \qquad (2)$$

where ν_i is again the fractional volume of precipitate and $f(d)$ is some unknown function of δ and the dimensions of an individual particle. This estimate of a linear dependence of ΔH_c on the volume of precipitate is that found by Dijkstra and Wert,[4] by Kersten,[2] and by Néel [Eq. (1)]. When the correction is made the curve is changed somewhat above 125°C (— ● —). However, the maximum around 100°C still persists.

To see directly the size of precipitates which were present in a sample aged at this temperature, 100°C, a series of electron microscope pictures were made. Some of these pictures are shown in Fig. 7. They show a sample aged for (a) 0 hours, (b) 5 hours, (c) 10 hours, and (d) 30 hours at 100°C. The magnification is 7500×; the series of pictures shows the precipitate during the precipitation proper and the coarsening of the precipitate upon overaging. The important picture is 7(c)—this is the precipitate just at the completion of aging; particles of this size have the maximum effect on the coercive force. The large dimension of the particles in 7(c) is about 1500 A; this is closely the same size as was found to give the maximum effect for sphere of carbides in iron,[4] and is close to the value of about 1000 A calculated for the domain wall thickness in iron.

Good confirmation of these observations is found in the work of Köster and Bangert.[5] They found upon aging of N in iron at 150°C, the maximum in coercive force to come for a particle size of about 1000 A (see Fig. 4 of their paper).

One more calculation can be made for comparison with the data presented in Figs. 4 and 5. The value of coercive force contributed by the large particles of Fe_4N ought to be, according to Eq. (1), about 2 oersteds, since $\nu_i \approx 0.006$. This is in reasonable agreement with the value of about 1 oersted read off the curves in Figs. 4 and 5 for the coercive force produced by large particles obtained after prolonged aging.

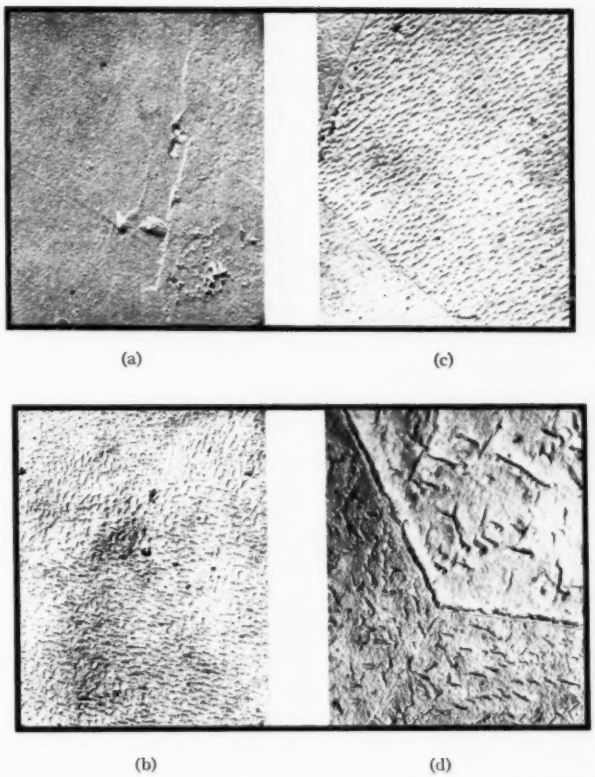

FIG. 7. Electron micrographs of a specimen aged at 100°C for: (a) 0 hours, (b) 5 hours, (c) 10 hours, and (d) 30 hours. ×7500.

ACKNOWLEDGMENTS

The writers are indebted to Mr. Albert Vatter and Mr. Thomas Noggle for assistance in the making of many of the electron micrographs. The micrographs of Fig. 7 were made by them, using a carbon replica technique.[10] The details of this work will be published by them at a later date.

[10] D. E. Bradley, Brit. J. Appl. Phys. **5**, 65 (1954); **5**, 96 (1954).

Application of the Wiedemann Effect to the Magnetostrictive Coupling of Crossed Coils

U. F. GIANOLA
Bell Telephone Laboratories, Inc., Murray Hill, New Jersey
(Received January 10, 1955)

A new construction for an electromechanical transducer makes use of the Wiedemann effect to produce a magnetostrictive coupling between an input and an output winding, which are orthogonally disposed so that there is no direct inductive coupling between them. A first-order theory of the operation of the transducer is given, and is used to derive an equivalent electrical circuit. The more important characteristics of the transducer are discussed in terms of the equivalent circuit, and are shown to be verified by experimental models. A method for deriving the equivalent circuit components by experiment is outlined, and the performance of a representative model is presented.

INTRODUCTION

MAGNETOSTRICTIVE materials have been frequently used in the construction of electromechanical resonators of various types.[1–4] Normally, these devices include only two accessible terminals, and are therefore in the nature of impedance elements. However, in some cases there are four accessible terminals, and the magnetostrictive element is used to provide a resonant coupling between an input and an output circuit.[1–3] Unfortunately, in these latter devices the magnetostrictive coupling is always supplemented by some undesired direct inductive coupling. The purpose of this paper is to show how a magnetostrictive coupling can be achieved between crossed coils by the application of the Wiedemann effect and its converse. By this means the direct inductive coupling is eliminated.

The construction considered is shown in Fig. 1. The magnetostrictive element is a ferromagnetic cylinder, which is clamped by supports at its midplane, but which is otherwise free to vibrate. A toroidal coil and a solenoidal coil are wound upon a surrounding form to provide input and output windings. For the ideal construction the fields that are produced by currents in each of the windings are everywhere orthogonal, so that there is no direct inductive coupling.

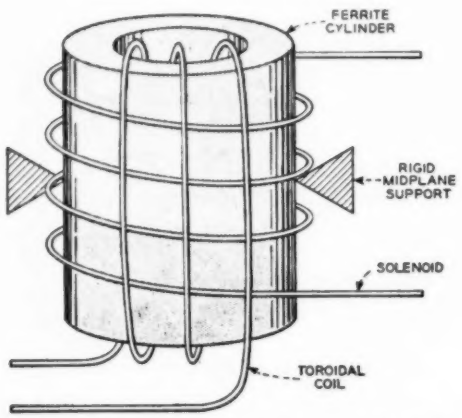

FIG. 1. A schematic diagram of the crossed-coil transducer. A ferrite cylinder is clamped rigidly by supports at its midplane, but is otherwise free to vibrate. Toroid and solenoid coils are wound round the cylinder, (in practice upon a polystyrene form) to provide input and output windings.

In a series of early experiments Wiedemann[5,6] showed that a magnetostrictive torque is produced in a ferromagnetic rod which is initially magnetized in the axial direction, and then subjected to a circular component of induction in a right plane of the rod. The converse also applies. Because of this effect, if a ferromagnetic cylinder is subject to an oscillatory driving induction in either the axial or the circular directions, in conjunction with a bias induction in the respective orthogonal direction, it will oscillate in torsion at the frequency determined by the driving field. If the driving frequency is an integral multiple of $2Lc$, c being the velocity of shear or torsion waves in the cylinder and L its axial length, the cylinder will oscillate in resonance. Furthermore, if the cylinder is made to vibrate in torsion while it is subject to a bias induction in either the axial or circular directions, then an oscillatory component of the induction will be induced in a direction that is orthogonal to the bias field.

It follows from a consideration of these effects that a magnetostrictive coupling between the input and output windings will be obtained if the cylinder is magnetically biased in *both* the axial and circular directions, since an oscillatory component in the axial induction combined with the circular bias will produce a torsional oscillation, which in turn will produce an oscillatory component of induction in the circular direction because of the presence of the axial bias. The resultant magnetic bias in this case has a helical configuration.

It is convenient to represent a two-pole electromechanical resonator by means of the equivalent circuit

[1] W. Van B. Roberts, RCA Rev. **14**, 3 (1953).
[2] H. H. Hall, Proc. Inst. Radio Engrs. **21**, 1328 (1933).
[3] G. W. Pierce, Proc. Am. Acad. Arts Sci. **63**, No. 1 (1928).
[4] P. Popper, *Soft Magnetic Materials for Telecommunications* edited by Richards and Lynch (Interscience Publishers, Inc., 1953), p. 35.
[5] J. A. Ewing, *Magnetic Induction* (D. Van Nostrand Company, Inc., New York, 1900), third edition.
[6] L. F. Bates, *Modern Magnetism* (Cambridge University Press, London, 1951), p. 415.

shown in Fig. 2.[1,4,7] This consists of a linear component Z_s, which represents the impedance of the winding in the absence of magnetostrictive oscillations, in series with a motional impedance Z_m, which represents the magnetostrictive contribution. Because of the similarity of operation of the crossed coil transducer, the two-pole equivalence may be adapted to give the four-pole equivalent circuit shown in Fig. 3. In this representation the arms of the T are the impedances of the input and output windings in the absence of magnetostrictive oscillation. The mutual impedance represents the mechanical vibration, and the electromechanical coupling through the windings is represented by impedance transformers. These components may be assumed to remain linear for small departures from the resonant frequency. This equivalent representation is confirmed by the first-order theory which is given in the next section.

SMALL SIGNAL THEORY

The following theory of the operation of the transducer is subject to a number of limiting approximations, but nevertheless presents a satisfactory explanation of the main features.

Let the magnetostrictive element be a thin cylinder of length L, radius r, and thickness d. Let it be subjected to a uniform magnetic bias having components in both the axial and circular directions, such that the resultant bias field is a helix, which makes an angle α with a right plane of the cylinder.

We shall assume that the Wiedemann effect is a special case of lineal magnetostriction, in other words, that the magnetostrictive shear stress in a right plane of the cylinder is a component of a lineal stress which is produced by the applied field in the direction of its resultant helix. The unit normal stress that is produced at constant strain in a magnetostrictive material by an increment ΔB in the magnetic induction is equal to $-\lambda\Delta B$, so that by our assumption the effective torque, produced at constant strain within the cylinder by an increment ΔB in the helical induction, is equal to

$$\Delta Q=-\frac{\lambda}{2}\frac{P}{r}\Delta B\sin 2\alpha \qquad (1)$$

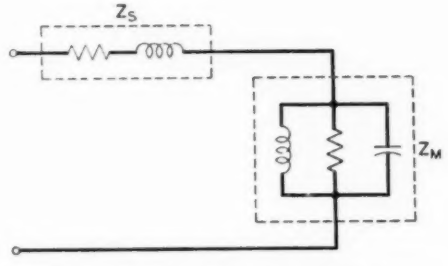

FIG. 2. The equivalent electrical circuit of a two-pole electromechanical resonator.

[7] N. W. McLachlan, *Theory of Vibrations* (Dover Publications, 1951), p. 34.

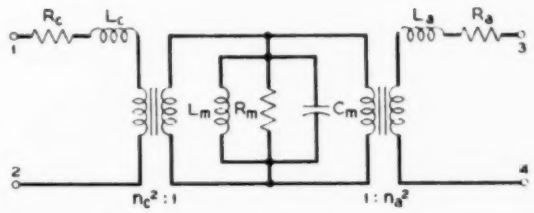

FIG. 3. The equivalent electrical circuit of the transducer. The electromechanical coupling is represented by impedance transformers n_c^2:1 and $1:n_a^2$, with $n_c=(\lambda P/2r)\mu F_1 N_c \sin 2\alpha\cos\alpha$ and $n_a=(\lambda P/2r)\mu F_2 N_a \sin 2\alpha \sin\alpha$. The mutual impedance is given in terms of the mechanical properties of the ferrite cylinder as follows: $L_m=1/K$, $L_mC_m=J/K=1/\omega_0^2$, $R_m=1/D$.

where $P\simeq 2\pi r^3 d$ is the polar moment of inertia of the cylinder.[8]

The volume effects associated with possible increments of stress and strain in the radial and axial directions will be neglected in the present discussion.

Upon the introduction of a sinusoidal component into the magnetic induction, an oscillatory torque will be produced within the cylinder. In order to simplify the discussion, this torque will be taken to be in phase with the induction, and will be considered to act upon a simple linear system, so that the steady-state equation of torsional oscillation of the cylinder may be expressed

$$(K+i\omega D-J\omega^2)\langle\Delta\theta\rangle=-\frac{\lambda}{2}\frac{P}{r}\sin 2\alpha\langle\Delta B\rangle \qquad (2)$$

$\langle\Delta\theta\rangle$ is the peak value of the total incremental twist, $\langle\Delta B\rangle$ the peak value of the incremental induction in the direction of the helix, ω the angular frequency of the driving field, J the equivalent moment of inertia of the cylinder, K its stiffness, and D the torsional damping constant. The natural frequency of torsional vibration of the cylinder will be equal to[9]

$$f_r=\frac{1}{2\pi}\left(\frac{K}{J}\right)^{\frac{1}{2}}=\frac{1}{4\pi L}\left(\frac{q}{\rho}\right)^{\frac{1}{2}} \qquad (3)$$

where ρ is the density of the cylinder and q its modulus of rigidity.

We have now to consider the change in the internal magnetic field H in the direction of the field helix, that is produced by twisting the cylinder, because of the inverse magnetostriction.

By analogy with the Joule magnetostriction equations,[10] the Wiedemann effect may be described by the following equations:

$$\Delta Q=\left(\frac{\partial Q}{\partial B}\right)_\theta\Delta B+\left(\frac{\partial Q}{\partial\theta}\right)_B\Delta\theta \qquad (4)$$

$$\Delta H=\left(\frac{\partial H}{\partial B}\right)_\theta\Delta B+\left(\frac{\partial H}{\partial\theta}\right)_B\Delta\theta. \qquad (5)$$

[8] den Hartog, *Strength of Materials* (McGraw-Hill Book Company, Inc., 1949), p. 19.

[9] Reference 7, p. 96.

[10] Sussmann and Ehrlich, J. Acoust. Soc. Am. **22**, 499 (1950).

Furthermore, $(\partial H/\partial B)_\theta=(\mu)_\theta^{-1}$ is the reversible permeability of a clamped sample at a given magnetic bias, and $(\partial Q/\partial\theta)_B=(qP/L)_B$.[11]

We have shown, Eq. (1), that $(\partial Q/\partial B)_\theta\simeq-\lambda P \sin 2\alpha/2r$, and by applying the principle of conservation of energy to the magnetostriction equations, it can be shown that

$$\left(\frac{\partial H}{\partial\theta}\right)_B=-\frac{4\pi}{V}\left(\frac{\partial Q}{\partial B}\right)_\theta \tag{6}$$

where $V\simeq 2\pi rLd$ is the volume of the cylinder.

In the following we shall assume that an increment ΔH, which is produced within the ferrite in the direction of the helical bias by inverse magnetostriction, produces component increments $\Delta H\cos\alpha$ and $\Delta H\sin\alpha$ in the circular and axial senses.

We are now in a position to determine the driving point impedance, and the transfer impedance, of the transducer.

Case 1. Axial Bias Constant

First consider the case when the solenoid is open circuited, and the toroidal coil carries a sinusoidal current having a peak value $\bar{I}_c$. This will produce a sinusoidal increment in the circular component of the induction having a peak value equal to

$$\langle\Delta B_c\rangle=\mu F_1 N_c\bar{I}_c \tag{7}$$

where F_1 is determined by the geometry of the coil with respect to the cylinder, and N_c is the total number of turns.

In this case, for steady-state oscillations, the peak increment of the magnetic induction in the direction of the bias helix is

$$\langle\Delta B\rangle\simeq\langle\Delta B_c\rangle\cos\alpha+\mu\langle\Delta H\rangle \tag{8}$$

where $\langle\Delta H\rangle$ is the peak value of the field increment produced by inverse magnetostriction.

By substituting this value for $\langle\Delta B\rangle$ into Eq. (2), and using Eq. (5) to express the relation between $\langle\Delta H\rangle$ and $\langle\Delta\theta\rangle$, we obtain

$$\langle\Delta H\rangle=-\langle\Delta B_c\rangle\cos\alpha/\mu x \tag{9}$$

where

$$x=1-(K+i\omega D-J\omega^2)/4\pi\mu y^2/V$$

and

$$y=\lambda P\sin 2\alpha/2r.$$

The peak induced back emf in the toroidal coil will be equal to $\bar{V}_c=i\omega N_c Ld(\langle\Delta B_c\rangle+\mu\langle\Delta H\rangle\cos\alpha)$, so that the driving point impedance of the toroidal coil is equal to

$$Z_c=\frac{\bar{V}_c}{\bar{I}_c}=i\omega L_c-i\omega\mu N_c^2F_1Ld\cos^2\alpha/x \tag{10}$$

where L_c is the inductance of the toroidal coil for zero magnetostriction.

For the same input conditions, the voltage appearing across the open solenoid winding will be equal to $\bar{V}_a=i\omega N_a 2\pi rd(\mu\langle\Delta H\rangle\sin\alpha)$. Therefore, the transfer impedance of the network is equal to

$$Z_m=\frac{\bar{V}_a}{\bar{I}_c}=-i\omega\mu N_aN_cF_1 2\pi rd\sin 2\alpha/2x. \tag{11}$$

Here, N_a is the total number of turns of the solenoid.

Case 2. Circular Bias Component Constant

Similar expressions can be obtained for the case when the toroidal coil is open circuited, and the solenoid carries a sinusoidal current. In this case the driving-point impedance of the solenoid is equal to

$$Z_a=i\omega L_a-i\omega\mu N_a^2F_2 2\pi rd\sin^2\alpha/x \tag{12}$$

and the transfer impedance is equal to

$$Z_m=-i\omega\mu N_aN_cF_2Ld\sin 2\alpha/2x. \tag{13}$$

This concludes the basic presentation. It is now possible to discuss the transducer in terms of its equivalent electrical structure.

Equivalent Electrical Circuit

If the network is to be reciprocal, it is necessary that the transfer impedances measured in the two directions must be equal. Inspection of Eqs. (11) and (13) shows that in the present approximation this requires that $2\pi rF_1=LF_2$. For the present discussion it is sufficient to assume equality. In this case the transducer can be represented by an equivalent T network, the arms of the T taking the values

$$Z_c-Z_m=\left[\frac{N_c}{N_a}\frac{L}{2\pi r}\cot\alpha-1\right]Z_m+i\omega L_c$$

$$Z_a-Z_m=\left[\frac{N_a}{N_c}\frac{2\pi r}{L}\tan\alpha-1\right]Z_m+i\omega L_a$$

with Z_m being the mutual impedance of the T, and L_c and L_a the inductances of the respective windings when magnetostrictive effects are absent.

This equivalent network can be reduced to the form shown in Fig. 3, in which the electromechanical coupling is represented by impedance transformers, and the mutual impedance is described simply in terms of the inertia of the cylinder, its elastance, and the torsional damping. Series input resistors R_a and R_c are introduced in order to include the resistance of the windings, which have been neglected to this point. In the derivation of this network it has been assumed that $F_1=2/r$.

An inspection of this equivalent circuit reveals that the transducer should have the following primary

[11] John Prescott, *Applied Elasticity* (Dover Publications, New York, 1946), p. 144.

properties. (a) The transducer is equivalent to a narrow-band frequency-selective filter. (b) The pass-band transmission is zero when either the circular component or the axial component of the bias field is zero, and is small when either component is dominant. This suggests the possibility of a gating application. (c) The voltage appearing across the output coil is reversed in phase when one component of the bias field is reversed. This suggests the application of the transducer as a memory device, since unit information may be reflected in the polarity of the bias field and referred to the phase of the output voltage. (d) The magnitude of the transfer impedance is dependent upon the incremental permeability of the material, and also upon the magnetomechanical parameters. (e) The amplitude of the transmission in the pass band can be continuously varied by varying one component of the bias field. This suggests the application of the transducer to amplitude modulation of a carrier signal in the pass band of the filter.

No account has been taken in this derivation of eddy current losses, hysteresis effects, and the temperature coefficient of the filter. The first will be small if a high-resistivity ferrite is used for the magnetostrictive element, and may in general be neglected. The second may be expected to add appreciably to the insertion loss, and to produce a lag in the phase of the transmission. The third should produce a fall in the resonant frequency with increase in temperature, of the order of 30 in 10^6/°C for ferrites.[1]

For a practical construction some residual coupling will always be produced because of stray inductive and capacitative interaction between the windings. An additional coupling, which is mentioned in an early paper,[12] is produced in a magnetized ferromagnetic by the rotation of the resultant induction vector between the two orthogonal planes. This last process sets a limit to the degree of decoupling that can be achieved at nonresonant frequencies.

EXPERIMENTAL CONFIRMATION

In order to confirm the existence of a magnetostrictive coupling between crossed coils by the application of the Wiedemann effect a number of experimental transducers have been constructed. A Ferroxcube IVE type ferrite has been used successfully to provide the intermediary resonant coupling for operating frequencies in the range 25 kc/sec to 150 kc/sec. Substantially their performance follows the predictions given in the preceding section, and the primary characteristics (a) to (e) have been verified. The sharpness of the resonant transmission, as determined from the frequency separation of the half-power points, corresponded to a Q as high as 2000 for some of the units. The transfer impedance is found to change considerably with the magnetic bias, as illustrated by Fig. 4, which

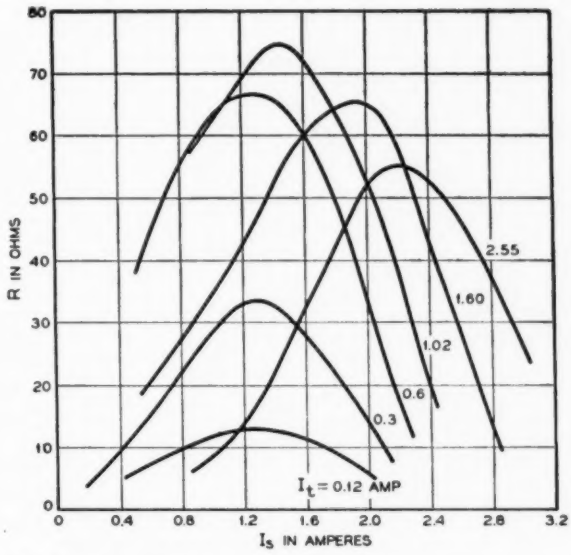

FIG. 4. The transfer impedance at resonance,

$$R = |V_{34}/I_{12}|_{I_{34}=0, I=I_r}$$

of the crossed-coil transducer is shown as a function of magnetic bias, which is expressed here is terms of dc energizing currents I_s and I_t in the solenoid and toroid coils, respectively.

gives the impedance at the resonant frequency as a function of the dc bias currents in the two windings. The trend of this characteristic is as anticipated, showing that small coupling is obtained when either component of the bias field is dominant, and showing a maximum coupling at an intermediate point, where the theory suggests that the two components of bias induction are equal. The magnitude of the individual peaks is seen to be dependent upon the absolute magnitude of the resultant bias field, suggesting that the coupling is related to the degree of magnetic saturation, and therefore to the incremental permeability, as proposed in point (d) in the previous section. No attempt has been made to establish a quantitative correlation because of the nonlinear nature of the magnetic and magnetomechanical parameters, and also because of the complication introduced by self-depolarization effects in the magnetic bias. The frequency of electromechanical resonance is also dependent upon the degree of magnetic saturation as previously noted by Roberts,[1] presumably because of the field dependence of the elastic parameters.[13] An increase in resonant frequency up to $\frac{1}{2}\%$ has been observed in going from weak to strong fields.

The magnetic bias in a practical unit may be provided by dc bias currents in the windings, but it is more conveniently provided by permanent magnetization of the ferrite. In the latter case, in order to counteract the effects of self-depolarization of the axial component of the bias field, it is advantageous to place a magnetized disk of a magnetically hard ferrite (e.g. Magnadur) at

[12] R. Goldschmidt, Elektrotech. Z. 9, 218 (1910).

[13] Reference 6, p. 424.

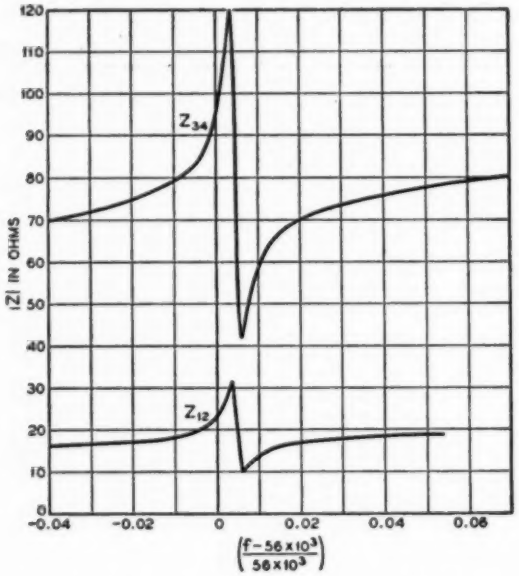

FIG. 5. The driving point impedances, $|V_{12}/I_{12}|_{I_{34}=0}$ and $|V_{34}/I_{34}|_{I_{12}=0}$, of a representative crossed-coil transducer.

each end of the transducer. As a representative illustration of the performance of these transducers the magnitudes of the driving point and transfer impedances of a typical self-biased transducer are given as a function of frequency in Figs. 5 and 6. The transfer impedance is resistive at the resonant frequency, inductive and capacitive at lower and higher frequencies, respectively. These characteristics are consistent with those predicted by the equivalent circuit in that the driving point impedances show both a series and parallel resonance, whereas the transfer impedance shows only an antiresonance. It is therefore judged that this equivalence is a satisfactory approximate representation.

The essential components of the equivalent circuit are conveniently obtained by means of the following sequence of measurements:

(i) $$L_c \simeq \frac{1}{2\pi f}\left|\frac{V_{12}}{I_{12}}\right|_{I_{34}=0,\, f \gg f_r} \qquad L_a \simeq \frac{1}{2\pi f}\left|\frac{V_{34}}{I_{34}}\right|_{I_{12}=0,\, f \gg f_r}$$

where f_r is the resonant frequency. The subscripts 12 and 34 refer to the voltages across and the currents into the terminals of the equivalent circuit of Fig. 3.

(ii) $$n_a n_c R_m = \left|\frac{V_{34}}{I_{12}}\right|_{I_{34}=0,\, f=f_r} = \left|\frac{V_{12}}{I_{34}}\right|_{I_{12}=0,\, f=f_r}.$$

(iii) $$L_m C_m = (2\pi f_r)^{-2}.$$

(iv) $$R_m/L_m = 2\pi f_r Q$$

where Q is determined from the frequency separation of the half-power points of the resonant transmission. (v) The total turns ratio is obtained by tuning out the series inductive components L_c and L_a at the resonant frequency by means of series capacitors, and then measuring the resulting driving point impedances

$$|Z_{12}^*|_{I_{34}=0,\, f=f_r} \quad \text{and} \quad |Z_{34}^*|_{I_{12}=0,\, f=f_r}$$

$$\frac{n_c}{n_a} = \left|\frac{Z_{12}^*}{Z_{34}^*}\right|^{\frac{1}{2}}.$$

(vi) The coupling coefficient, defined as the ratio of converted stored energy to input stored energy, takes the geometrical mean value

$$k^2 = \frac{n_a n_c L_m}{(L_a L_c)^{\frac{1}{2}}}.$$

(vii) A measure of the losses inherent to the intermediate coupling is obtained by series tuning L_c and L_a, as in (v), followed by a measure of the insertion loss between the resultant matching impedances at the resonant frequency, which are purely resistive in this case.

The following values of the essential circuit components of the transducer, which was used to obtain Figs. 5 and 6, are given as a representative example:

(i) $L_c = 50\mu h, \quad L_a = 210\mu h,$

(ii) $n_a n_c R_m = 44$ ohm,

(iii) $L_m C_m = 8.0 \times 10^{-12} (\text{sec})^2,$

(iv) $R_m/L_m = 160 \times 10^6 (\text{sec})^{-1},$

(v) $n_a/n_c = 2.1,$

(vi) $k = 0.045,$

(vii) insertion loss = 1.5 db.

The magnetostrictive intermediary in this example was a Ferroxcube IVE ferrite cylinder having dimensions $L = 1$ inch, $r = \frac{1}{8}$ inch, $d = \frac{1}{16}$ inch. The bias component B_c was provided by saturation to remanence, and B_a

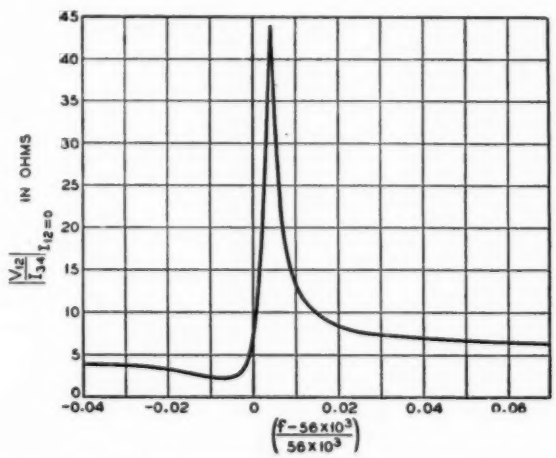

FIG. 6. The transfer impedance, $|V_{34}/I_{12}|_{I_{34}=0} = |V_{12}/I_{34}|_{I_{12}=0}$, of the crossed-coil transducer.

was produced by end disks of "Magnadur." The number of turns in the two windings were $N_c=27$, $N_a=130$. The fundamental resonant frequency was 56.04 Kc/s.

CONCLUSIONS

The existence of a strong magnetostrictive coupling between crossed coils, which surround a magnetostrictive cylinder which is magnetized in a helical manner, has been experimentally confirmed. The resulting transducer as a circuit component behaves primarily as a frequency selective filter. As such it has features similar to the electromechanical filters described in references 1, 2, and 3, but with the advantage of inductive decoupling of the coils at nonresonant frequencies. It furthermore has additional properties, for example the gating and phase reversal characteristics, which may find interesting application.

ACKNOWLEDGMENTS

I owe particular thanks to R. L. Wallace for discussions that led to the conception of this device, and to J. G. Kreer for his advice in the evaluation of the equivalent circuit.

JOURNAL OF APPLIED PHYSICS VOLUME 26, NUMBER 9 SEPTEMBER, 1955

Positive-Ion Drainage in Magnetically Focused Electron Beams

M. E. Hines, G. W. Hoffman,* and J. A. Saloom
Bell Telephone Laboratories, Inc., Murray Hill, New Jersey

(Received December 6, 1954; revised manuscript received May 25, 1955)

In electron tubes utilizing long electron beams ionization of residual gases can produce a positive space charge which can partially or wholly neutralize the negative space charge of the beam. Such neutralization has, under special conditions, been successfully utilized in focusing electron beams. In certain electron devices requiring long electron beams, this type of focusing is inadequate and an axial magnetic field is employed to focus the electron beam. However, when magnetic focusing is used, the assumption is usually made that the electronic space-charge fields of the beam are not neutralized by positive ions. Measurements have been made on a magnetically focused electron beam yielding information on (a) the longitudinal drainage of positive ions from the electron beam and (b) the degree of positive-ion neutralization of the electron beam. It is pointed out that localized ion traps may be present in the beam if the beam diameter varies periodically along its length because of the applied magnetic field.

I. INTRODUCTION

MANY modern microwave electron tubes require long narrow electron streams magnetically focused to flow along the axis of a conducting drift tube or traveling-wave interaction circuit. Such beams may be focused either by a uniform magnetic field[1] parallel to the axis of the beam, or by periodic or alternating magnetic fields.[2] In both cases, the theories of focusing involve the assumption that the space charge of the beam is not neutralized by positive ions.

An investigation has been made to determine the extent to which magnetically focused electron beams are neutralized by positive ions when an effort is made to remove the ions from the beam. It is pointed out that in the case of a magnetically focused beam, periodic undulations of the beam diameter may cause some ions to become trapped in the narrower portions of the beam, thereby decreasing the space-charge forces and encouraging further constricting of the beam.

Spangenberg, Field, and Helm[3] presented a theoretical treatment of the ion drainage problem and first proposed the mechanism by which positive ions could be trapped within or drained out of a cylindrical electron beam. Their theory for draining and trapping ions within a beam was tested by observing the effect of positive ions on the normal spreading of an electron beam in the absence of applied fields. The Spangenberg, Field, and Helm theory has recently been modified and extended by Ginzton and Wadia[4] to include the effects of the position and type of ion trap used. They showed that the entrance conditions are extremely critical for ion focusing of electron beams except in the case of thin electron beams of low perveance.

Linder and Hernqvist[5] have analyzed the role of positive ions in convergent electron flow and have demonstrated experimentally, by means of a special pulse technique, that positive ion trapping may be employed successfully in forming high current density electron beams. Other work on the role of positive

* Mr. Hoffman participated in this investigation as a summer employee at the Bell Telephone Laboratories while a graduate student at Harvard University. He is now associated with the Westinghouse Corporation, Pittsburgh, Pennsylvania.

[1] J. R. Pierce, *Theory and Design of Electron Beams* (D. Van Nostrand Company, Inc., New York, 1954).

[2] See reference 1, pp. 194–213.

[3] Spangenberg, Field, and Helm, Elec. Commun. **24**, 101–121 (1947).

[4] E. L. Ginzton and B. H. Wadia, Proc. Inst. Radio Engrs. **42**, 1548–1554 (1954).

[5] E. G. Linder and K. G. Hernqvist, J. Appl. Phys. **21**, 1088–1097 (1950).

ions in neutralizing electronic space-charge fields has been reported by Hernqvist[6] and Wagner.[7]

The aforementioned work had aims significantly different from those of the investigation reported herein. Generally speaking, the goal of previous investigations was to focus high-current density electron beams by canceling the radially outward space-charge fields by trapping positive ions within the electron beam. The work reported herein, however, assumes the presence of an axial magnetic focusing field and then attempts an analysis with this added assumption. An experimental check on the theory is then made by (a) measuring directly the drainage of positive ions from a long drift tube as a function of time from the application of a step function pulse and, (b) interpreting the difference between the number of ions collected and the number of ions formed in the beam as a quantitative measure of the average number of positive ions in the beam when dynamic equilibrium prevails.

II. ION DRAINAGE FROM CYLINDRICAL STREAMS

Spangenberg, Field and Helm[2] (hereafter abbreviated to SFH) showed that all of the ions formed in a cylindrical stream within a cylindrical drift tube can be drained out at one or both ends if a strong gradient of electric field is applied to remove all ions which appear at the ends, and if the ion production rate is not too great. Their theory is further limited by the following assumptions: (1) All ions have the same charge and mass. (2) Ion or plasma oscillations do not appear. (3) Electrons released in the ionization process escape quickly and do not appreciably add to the space charge. (4) Initial velocities of the ions upon generation are negligible. (5) The potential over a cross section of the stream is assumed constant at an average value which is directly proportional to the net linear charge density (electronic plus ionic). The latter portion of this assumption is a valid approximation for a slender drift tube if the net charge is a slowly varying function of longitudinal position and if the ions remain more or less evenly distributed across the electron stream. (6) As pointed out by Ginzton and Wadia, SFH also assume the beam to be parallel on entrance into an abruptly starting trapping field.

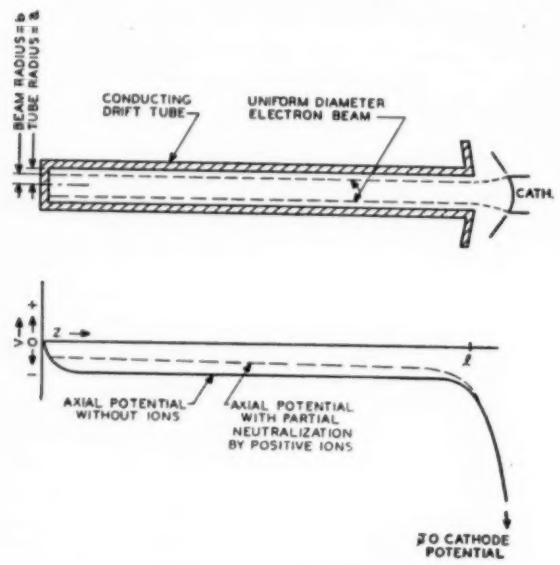

FIG. 1. Geometry for ion drainage for theory of Spangenberg, Field, and Helm.

Figure 1 shows the coordinates and the type of geometry considered. If the tube radius is a, the beam radius is b, and the net linear charge density in σ coulombs per meter, the potential depression V_0 at the axis is

$$V_0=\frac{\sigma}{4\pi\epsilon}\left(1+2\ln\frac{a}{b}\right) \tag{1}$$

and the potential V_b at the edge of the beam is

$$V_b=\frac{\sigma}{4\pi\epsilon}\left(2\ln\frac{a}{b}\right), \tag{2}$$

where ϵ is the dielectric constant of vacuum.

If the ionic charge density is of smaller magnitude than the electronic density, there is a negative potential trough along the axis and the slow moving ions formed there will not be able to escape radially but may move longitudinally along the z-axis. Referring to Fig. 1, no ions are formed to the left of $z=0$, and all ions formed at positive z are assumed to drain toward the right. If ions are being created at a constant rate of G_i amperes per meter, the steady-state ionic charge density at a point z will be given by an integral over the range from zero to z with the differential components of the ionic current from each element dz being divided by the velocity of that element. The velocity of such an element is proportional to the square root of the potential difference between the point of origin and the point of interest. Letting x represent the space variable in the integration, the expression for the total ionic charge density $\sigma_i(z)$ at a point z is

$$\sigma_i(z)=\int_0^z\frac{G_i dx}{\left\{2\frac{e}{m_i}[V(x)-V(z)]\right\}^{\frac{1}{2}}} \tag{3}$$

where e/m_i is the charge to mass ratio for the ions. Taking

$$V(z)=\lambda[\sigma_i(z)+\sigma_e] \tag{4}$$

where λ, the average value of V_0/σ and V_b/σ from (1) and (2), is

$$\lambda=\frac{1/2+2\ln\frac{a}{b}}{4\pi\epsilon},$$

[6] K. G. Hernqvist, Proc. Inst. Radio Engrs. **39**, 1541–1547 (1951).

[7] H. M. Wagner, Trans. Inst. Radio Engrs. **1**, 3–8 (1952).

(3) becomes

$$\sigma_i(z)=\frac{G_i}{\left(2\frac{e}{m_i}\lambda\right)^{\frac{1}{2}}}\int_0^z\frac{dx}{[\sigma_i(x)-\sigma_i(z)]^{\frac{1}{2}}}. \tag{5}$$

This is an integral equation whose solution as given by SFH is

$$\frac{3\pi G_i z}{2[\sigma_i(0)]^{\frac{3}{2}}\left(2\frac{e}{m_i}\lambda\right)^{\frac{1}{2}}}=\left(1+2\frac{\sigma_i(z)}{\sigma_i(0)}\right)\left(1-\frac{\sigma_i(z)}{\sigma_i(0)}\right)^{\frac{1}{2}}. \tag{6}$$

Figure 2 shows a plot of $\sigma_i(z)/\sigma_i(0)$ as a function of the left-hand side of (6). The solid portion of the curve in the region of positive z is that applicable to the geometry of Fig. 1. Both the left and right sides are applicable if ions drain from both ends. In that case $z=0$ would be in the central region of the tube. The charge density, and with it the potential, shows an infinite slope at $\sigma_i(z)/\sigma_i(0)=1/2$, at which point the left-hand side of (6) is equal to $\sqrt{2}$. It may be argued that the high gradient in this region must, in some manner, blend into the high gradient applied near the entrance of the tube. Assuming that this point occurs at the end of the tube where $z=l$, (6) gives a relationship between $\sigma_i(0)$, l, λ, and G_i, namely,

$$\frac{3\pi G_i l}{2\left\{2\frac{e}{m_i}\lambda[\sigma_i(0)]^{\frac{1}{2}}\right\}^{\frac{1}{2}}}=\sqrt{2} \tag{7}$$

where λ and l are geometrical factors and G_i may be calculated from published data[8] on ionization probabilities. For common gases in electron tubes, such as N_2, O_2, CO, etc., the probable number of ionizing collisions per electron per cm length at one mm Hg pressure is about 10 at 100 volts, 4 at 1000 volts, and 2.8 at 2000 volts. The probability at lower pressures is proportionately less. The ion current generation in amperes per meter is given by

$$G_i=100 i_e P_i p \text{ amperes per meter}, \tag{8}$$

where P_i is the ionization probability quoted in the aforementioned at one mm Hg pressure for 1 cm length, i_e is the electronic beam current, and p is the pressure in mm Hg.

It is of interest here to calculate the ratio of the maximum ionic charge density to the electronic charge density predicted by this theory for a typical traveling-wave tube. One such tube at the Bell Telephone Laboratories utilizes a beam of 37.5 ma at 2000 v, transmitted through a helix 0.080 inch in inside diameter. The ion production rate in this case is 11×10^{-6} ampere per meter at 10^{-6} mm Hg pressure, 11×10^{-7} ampere per meter at 10^{-7}, etc. Taking the beam diameter as one-half the helix diameter and the length l as 17 cm, we find that the ratio of the maximum positive ionic charge density $\sigma_i(0)$ to the negative electronic charge density σ_e is $\sigma_i(0)/\sigma_e=1.0$ at 3×10^{-6} mm Hg, 0.5 at 1×10^{-6} mm Hg, 0.1 at 1×10^{-7} mm Hg, 0.02 at 1×10^{-8} mm Hg, etc.

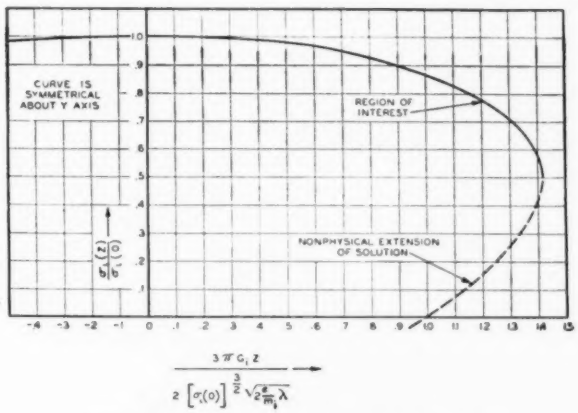

FIG. 2. Theoretical variation of ionic charge density with distance along the beam.

At pressures higher than 3×10^{-6} mm Hg, the magnitude of the ionic charge density predicted is greater than that of the electron stream, giving a net positive potential in the beam. In such cases, the excess ions will escape to the helix.

It is interesting to note that increasing the beam current in a given geometry at constant voltage and gas pressure will *reduce* the ratio σ_i/σ_e, and vice versa.

III. ION DENSITY WITH A BEAM OF NONUNIFORM DIAMETER

Practical traveling-wave tubes are ordinarily focused with the aid of a uniform parallel magnetic field of a few hundred gausses. Ideally, one attempts to establish the uniform-diameter "Brillouin-flow" condition. Theoretically, this condition requires the least magnitude of field assuming no ionic space-charge cancellations. Every known traveling-wave tube has required larger values of the field than the Brillouin value in order to obtain high-percentage beam transmission. In such cases the beam would not be of uniform diameter but might be scalloped to resemble a string of linked sausages. In this case the potential distribution would be quite nonuniform if no ions were present, with a series of isolated potential "wells" at the narrow places in the beam. In the tube previously used as an example these potential wells could be rather deep. If the beam undulated 2 to 1 in diameter, then the potential at the axis in the narrow parts of the beam would be about 20 volts more negative than at the axis in the wide places. Ions which form in such potential wells cannot leave except by recombining with electrons, by acquiring kinetic energies of the order of a few volts to

[8] Knoll, Ollendorff, and Rompe, *Gasentladungs Tabellen* (Verlag Julius Springer, Berlin, 1935), p. 66.

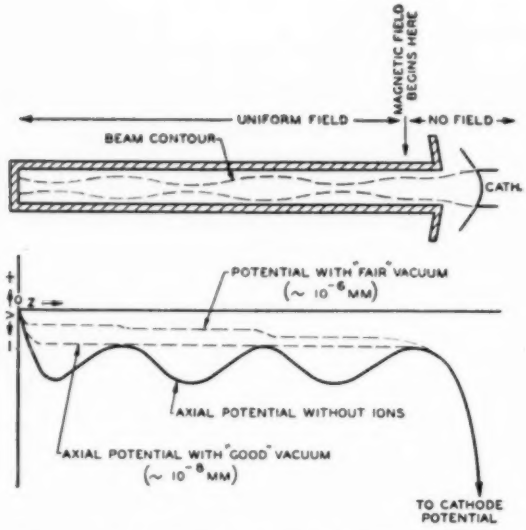

FIG. 3. Sketch illustrating types of potential patterns to be expected with a scalloped beam.

perhaps 20 volts or more depending upon the depth of the wells, or by accumulating in sufficient numbers to fill up the wells and overflow.

We might assume that the vacuum is "good" but not perfect and that the potential wells fill up with ions to the point where the potential profile along the axis is approximately uniform. When this condition occurs we might have a situation approximately as illustrated in Fig. 3. The excess ions, over and above that necessary to fill the wells, can drain longitudinally as predicted by SFH. The presence of ions in the narrow places in the beam must alter the paths of the electrons and one would logically expect that a final equilibrium state with ions present would involve undulations in beam diameter of greater magnitude than when ions were absent.

At some conceivable very high vacuum, these potential wells might not be able to fill. It is suspected that this would require a very high vacuum (perhaps 10^{-10} mm Hg) but there is no experimental evidence to support this contention.

IV. EXPERIMENTAL MEASUREMENTS OF SPACE-CHARGE FIELD NATURALIZATION

One way to check the ion drainage theory of SFH and to determine whether there is excessive trapping of positive ions in the electron beam at low pressures is to measure the degree of positive ion neutralization of an electron beam as a function of pressure. If the electron beam is cylindrical in form throughout the drift tube we may expect, at very low pressures, according to the ion drainage theory of SFH, that a relatively small number of positive ions will remain in the beam. On the other hand, if the electron beam is periodically broad and narrow along its length, positive ions may be trapped in the constricted sections of the beam and contribute to a higher degree of neutralization than predicted by the theory of SFH.

A. Description of Experiment

The degree of positive ion neutralization of a magnetically focused electron beam was measured in a modified version of a Bell Telephone Laboratories experimental traveling-wave tube. The modified tube, shown schematically in Fig. 4, contained an additional wire ion collector placed concentrically within the hollow electron collector. The dc potentials on the tube elements were adjusted so that positive ions created in the helix region of the tube could drain toward the ion collector [(anode voltage)> (helix voltage)> (electron collector voltage)].

The tube was operated from a pulsed power supply with a 60-cycle repetition rate and a pulse length of 700 μsec. The tube was normally conducting but was cut off during the 700 μsec pulse. As has been shown by Linder and Hernqvist this pulse length gives more than ample time for the ions in the beam to be swept out of the beam. When the tube began to conduct, the electron collector current increased to 99% of its maximum value within 3 μsec. However, several hundred μsec elapsed before the positive ion current to the ion collector reached its equilibrium value. The positive charge which did not immediately arrive at the ion collector, but which nevertheless began to form as soon as the electron current started flowing, represents ions remaining somewhere in the tube. Since the helix region represents a considerable part of the length of the electron beam, a reasonable assumption is that this positive charge remains to neutralize the electron beam in the helix drift region.

A time integration of the deficiency in ion current below the equilibrium value is, therefore, assumed to give the net ionic charge remaining in the beam. This integral, illustrated in Fig. 5, is

$$Q_i = \int_0^\tau [i_{i(\max)} - i_i(t)]dt \qquad (9)$$

where Q_i = the ionic charge in coulombs remaining in the beam, $i_{i(\max)}$ = the equilibrium value of the ion collector current in amperes, $i_i(t)$ = the instantaneous

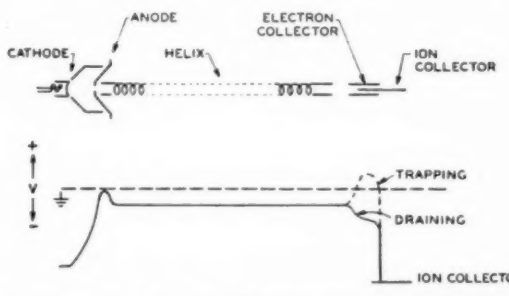

FIG. 4. Schematic of traveling-wave tube used in experiments and profile of the potentials applied to tube elements.

value of the ion collector current in amperes, and τ = the time in seconds required for the ion collector current to arrive at its equilibrium value. The total space charge of the electron stream in the helix region of the tube is given by

$$Q_e = \frac{i_e l}{(2\eta V)^{\frac{1}{2}}} \tag{10}$$

where Q_e = the electronic charge in the beam in coulombs, i_e = the electron current in amperes, V = the helix potential in volts above cathode potential, $\eta = e/m$ = charge to mass ratio of the electron, and l = length of the helix in meters.

The average degree of positive ion neutralization of the electron beam in the helix region of the tube is then given by the ratio of Q_i/Q_e.

In the experiment the beam was accelerated to 1000 v. The helix was maintained at 50 v below the anode potential and the electron collector at 100 volts below the anode potential. These potentials produce electric gradients which permit positive ions created in the helix region to flow toward the ion collector, which resides at 50 to 100 v below cathode potential, but not toward the gun. The cathode was heated by a half-wave rectifier power supply. The phase of the pulse on the cathode was so adjusted that measurements were made during the off-cycle of the cathode heater current in order to avoid heater magnetic effects.

The several tubes used in the experiment were all continuously pumped. The pressure within the tube was varied by varying the impedance of the pumping line. Pressures just outside the tube were measured with a Bayard-Alpert ionization gauge.

B. Results of Experiment

Oscilloscope patterns of the type shown in Fig. 5 were obtained for various pressures, but at a constant value of magnetic field strength. These traces were obtained when the dc potential profile was adjusted to drain ions from the helix region toward the ion collector. Oscilloscope patterns of this type were integrated as described above to give the amount of positive charge remaining in the beam.

It is important to determine what portion of the equilibrium value of ion current is generated within the helix region alone. This value of ion current, once obtained, could give a more realistic measure of the

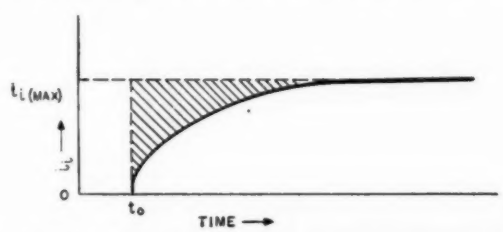

FIG. 5. Pulse shape of ion collector current illustrating how degree of neutralization of electron beam is obtained.

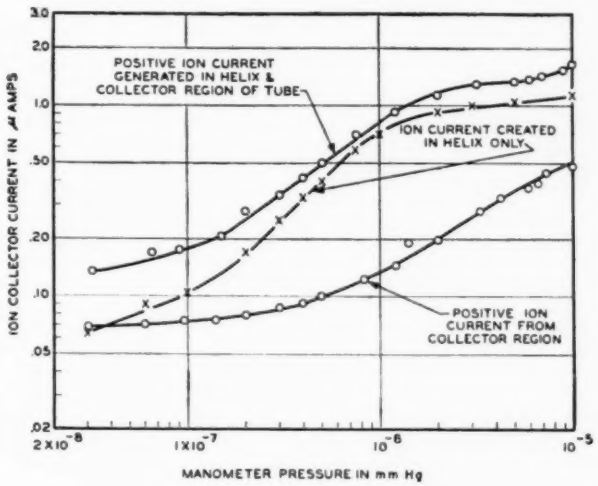

FIG. 6. Positive-ion current *vs* pressure.

pressure within the helix region of the tube than is indicated by the ionization gauge, which was somewhat removed from the helix. In Fig. 6, the upper curve represents positive ion current which originated in both the helix and electron collector region of the tube. The lower curve represents the case in which the positive ions created in the helix region of the tube were prevented from reaching the ion collector by raising the electron collector potential above the helix potential. The current received by the ion collector under this condition represents ion current created in the electron collector region of the tube as well as soft x-ray photoelectric emission of electrons from the ion collector itself. The center curve, obtained by subtracting the upper curve from the lower curve, represents ion current created in the helix alone. This difference curve shows three particular zones of interest. For the range of pressures from 1×10^{-6} mm Hg to 2×10^{-7} mm Hg, the ion current is nearly proportional to pressure and of a magnitude closely predicted by (8). At higher pressures, the ion current remains nearly constant, indicating that some of the ions are no longer reaching the ion collector. At lower pressures the current fell off more slowly probably because the pressure was not as low inside the tube as at the ionization gauge outside.

The break in the curve at 1×10^{-6} mm Hg pressure is interpreted as an indication that the beam becomes 100% neutralized at some point at that pressure. When this occurs, positive ions created in the helix move radially outward and are collected at the helix. Defining complete neutralization as occurring when

$$\sigma_i(0) = \sigma_e,$$

the pressure at which complete neutralization is to be expected may be deduced from (7). If we substitute into this equation the following experimental values, $i_e = 0.0145$ ampere beam current, $l = 0.17$ meters, $V = 950$ volts, and assume that the ions are singly

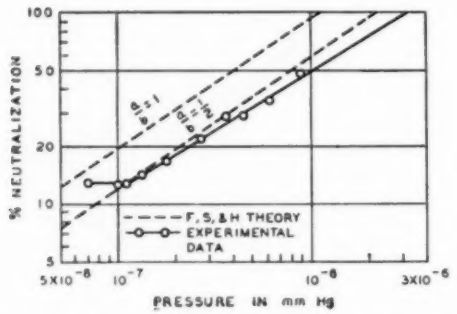

FIG. 7. Degree of positive-ion neutralization of the electron beam *vs* pressure in a traveling-wave tube operating at 1000 v, and 14.5 ma beam current. Beam transmission was 98% with a 750-gauss focusing field.

ionized molecules of mass 28 we obtain for $a/b=2$,

$$p=2.12\times10^{-6} \text{ mm Hg}$$

as the pressure at which complete neutralization should first occur. From Fig. 6 we can see that this calculated value of pressure is reasonably close to the value of pressure at the break point in the curve. It should be noted that we have no exact knowledge of types of gas present nor do we know the beam diameter exactly.

At pressures less than 1×10^{-6} mm Hg the equilibrium value of positive-ion current generated in the helix may be used to determine the average pressure within the helix since in this pressure range longitudinal drainage of ions occurs. Using (8) and the equilibrium value of positive ion current generated in the helix, the average pressure within the helix region was calculated. For the pressure range 1×10^{-6} mm Hg to 1×10^{-7} mm Hg the pressure obtained in this manner corresponded to within 10% of the value indicated by the ionization gauge. At pressures less than 1×10^{-7} mm Hg the equilibrium value of ion current from the helix appeared to level off, indicating that the pressure within the tube was higher than indicated by the ionization gauge.

Shown in Fig. 7 is the degree of positive ion neutralization plotted as a function of pressure as obtained from the ion current created in the helix region (Fig. 6). Plotted also in Fig. 7 are the values of maximum neutralization as predicted by the SFH ion-drainage theory. Agreement between the values of neutralization predicted by the SFH theory and the experimental values are seen to be reasonably close over an order of magnitude of pressure variation.

However, as the pressure is reduced below 1×10^{-7} mm Hg the degree of neutralization does not decrease as predicted by the SFH theory but levels off at a value of $Q_i/Q_e=0.13$ indicating that positive ions may be being trapped somewhere in the helix region of the tube. Originally we expected a higher limiting percentage neutralization at the best vacuum conditions. If the beam were to undulate such that the beam diameter varied as a series of half-sine waves just clearing the helix we might expect to trap roughly 40% as much ionic charge as electronic space charge in the beam under the limiting conditions of high vacuum as pictured in Fig. 3 and described in Sec. III. However, thermal velocity effects limit the minimum beam diameter obtainable, and the beam at its maximum diameter has a higher current density in the center than at the edge. These effects reduce the amplitude of possible undulation and thereby decrease the degree of ion trapping possible under high vacuum conditions. It is possible that plasma ion oscillations could cause the positive ions to leave the potential wells and hence limit the trapping action of an undulating beam. However, oscillations were only observed when the beam was almost completely neutralized.

V. SUMMARY AND CONCLUSIONS

The ion drainage theory of Spangenburg, Field, and Helm is applicable to magnetically focused electron beams for cases where the beam is essentially cylindrical in shape. There are theoretical reasons to believe that substantial numbers of positive ions may become trapped in the electron stream for focusing conditions which permit undulations of the beam diameter. In such cases, the trapped ions will modify the space-charge conditions in a manner which accentuates the beam diameter variations.

Measurements of neutralization effects in one type of traveling-wave tube show ion-drainage behavior at high pressures to correspond to the theory of Spangenberg, Field, and Helm. At lower pressures there is a somewhat inconclusive indication that ion trapping effects caused by beam scalloping are present.

A further point of interest is that ions can be prevented from draining longitudinally from one or both ends by a positive potential barrier. In these experiments, very large reductions in the ion current to the ion collector could be made by raising the collector voltage only 10 to 20 volts above the helix voltage. In unpublished work, Mr. D. O. Melroy of the Bell Telephone Laboratories obtained similar effects at an ion collector placed behind a small hole in the cathode of a traveling-wave tube electron gun. He found that the ion current was greatly reduced by operating the electron gun accelerating anode at a potential higher than that of the helix. It is believed that bombardment damage to the cathode can be greatly reduced in this way.

JOURNAL OF APPLIED PHYSICS VOLUME 26, NUMBER 9 SEPTEMBER, 1955

Oxide-Impregnated Nickel-Matrix Cathode

W. Balas, J. Dempsey, and E. F. Rexer
Honeywell Research Center, Hopkins, Minnesota
(Received February 28, 1955)

A new cathode is described consisting of an oxide-impregnated nickel matrix. A sintered nickel matrix of controllable porosity is prepared and impregnated with solutions which precipitate a mixed carbonate within the matrix. The resulting cathode is a dispenser type with a minimum of surface coating. The cathodes can be activated by schedules which approximate those of a normal oxide-coated cathode. Pulse-emission tests of these cathodes show properties intermediate between the oxide-coated cathode and the *L*-cathode, and of the same order as the molded cathode described by McNair, Lynch, and Hannay.

I. INTRODUCTION

DURING the last few years several reports have been made on modifications in the structure of cathodes which were considered to minimize some of the limitations of the common oxide coated cathode. One of the first cathodes of this kind was the mesh cathode in which a nickel mesh was employed as a matrix for holding sprayed (BaSr)O. More recently,[1,2] a dispenser type known as the *L*-cathode has been described which is reported to be capable of higher current densities, long life, and resistance to poisoning. Recently, brief reports[3,4] have been given on a molded cathode. The authors report that this cathode has a work function comparable with that of a (BaSr)O coated cathode and that it can be made in a variety of forms. In addition to work done in the United States, investigations made at the Siemens Company in Germany have been published[5] describing experiments on capillary cathodes whose performance is described as superior to the normal oxide-coated cathode.

The cathode which is described here employs a nickel matrix impregnated with (BaSr)O. Experiments performed so far indicate that it has a low work function and consequently can be operated at a low temperature. It is easy to fabricate and the processing schedules required are closely similar to that used in processing normal cathodes. In addition, it exhibits good arcing properties. Although no exhaustive experiments have been performed on it with respect to poisoning, evaporation and life, indications from preliminary tests are that this cathode will exhibit favorable properties along these lines.

II. DESCRIPTION AND FABRICATION

Nickel powder,[6] 37 to 44μ size is employed in fabricating the cathode matrix. The powder may be pressed and formed to the desired configuration in dies or it may be directly molded to shape in a cathode retainer cup (Fig. 1). Subsequently, the compacted matrix is sintered in a hydrogen atmosphere for approximately ten minutes at 1000°C. It should be noted that the cathode material is not within the matrix during the sintering operation and consequently the structure can be thoroughly cleaned without danger of contaminating or decomposing the carbonate material. The sintered matrices are mechanically strong and can withstand rough handling without any apparent damage.

Matrix porosity, defined as 1−density of matrix/density of nickel, can be controlled over a range varying from 30 to 50%; the results reported in this paper pertain to cathodes that had a porosity of approximately 50%.

After sintering, the matrix is impregnated with a water-soluble (BaSr) salt and then the (BaSr) carbonate is precipitated within the interstices by a second impregnation with a water-soluble carbonate. In order to effect an efficient impregnation technique and reduce the impregnation process to a minimum, it is necessary to use a (BaSr) salt solution of high concentration. (BaSr) acetate, which has a relatively high solubility, has been found to be adequate in this respect. $(NH_4)_2CO_3$ may be employed as the precipitating agent since it has the desirable advantage that its by-products in the precipitating reaction are water soluble and decompose at low temperatures. The reactions are as follows:

$$(NH_4)_2CO_3+BaSr(C_2H_3O_2)_2\rightarrow(BaSr)CO_3+2NH_4(C_2H_3O_2)$$

$$NH_4(C_2H_3O_2)\xrightarrow[100°C]{}NH_3\uparrow+CH_3COOH\uparrow \text{ or sublimation}$$

$$CH_3COOH(\text{liquid})\rightarrow CH_3COOH(\text{vapor})$$

(b.p. 118°C at atmospheric).

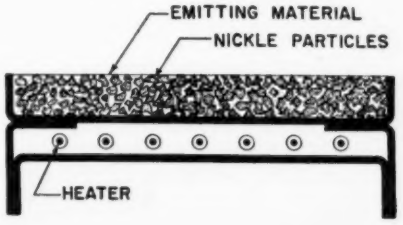

FIG. 1. Schematic drawing of impregnated matrix cathode.

[1] D. R. Hill, Electronics **24**, 104–106 (1951).
[2] R. Levi, J. Appl. Phys. **24**, 233 (1953).
[3] McNair, Lynch, and Hannay, J. Appl. Phys. **24**, 1335–1336 (1953).
[4] A. H. Beck *et al.*, Nature **174**, 1010–1011 (1954).
[5] H. Katz, J. Appl. Phys. **24**, 597–603 (1953).
[6] Impurity content of nickel employed: Fe, 0.05%; Cr, 0.005%; Mn, 0.001%; Cu, 0.03%; Co, 0.01%; Al, 0.01%; C, 0.014%; S, 0.011%; Si, 0.01%; Mg, 0.02%.

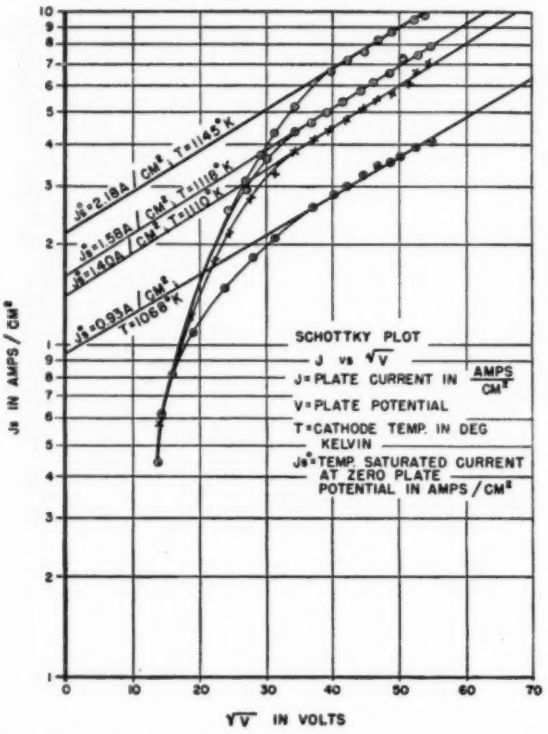
SCHOTTKY PLOT
J vs √V
J = PLATE CURRENT IN AMPS/CM²
V = PLATE POTENTIAL
T = CATHODE TEMP. IN DEG KELVIN
Js° = TEMP. SATURATED CURRENT AT ZERO PLATE POTENTIAL IN AMPS/CM²
Js° = 2.19A/CM², T = 1145°K
Js° = 1.58A/CM², T = 1118°K
Js° = 1.40A/CM², T = 1110°K
Js° = 0.93A/CM², T = 1068°K
J IN AMPS/CM²
√V IN VOLTS

FIG. 2. Typical Schottky plot for impregnated matrix cathode.

As a result of this technique, the matrix is adequately impregnated in a minimum number of steps and one is assured at the same time that the $(BaSr)CO_3$ become free of reaction products at temperatures well below the decomposition temperature of $(BaSr)CO_3$. Upon viewing the cathode under a microscope, $(BaSr)CO_3$ is found primarily in the interstices and there is a minimum of surface deposit. In addition, the carbonate is not only adhesively bonded to the matrix but also is held in the pores by mechanical means on the surface and within the matrix body. As a result, there is very little possibility of the cathode material flaking off, and the cathode surface is virtually metallic in appearance.

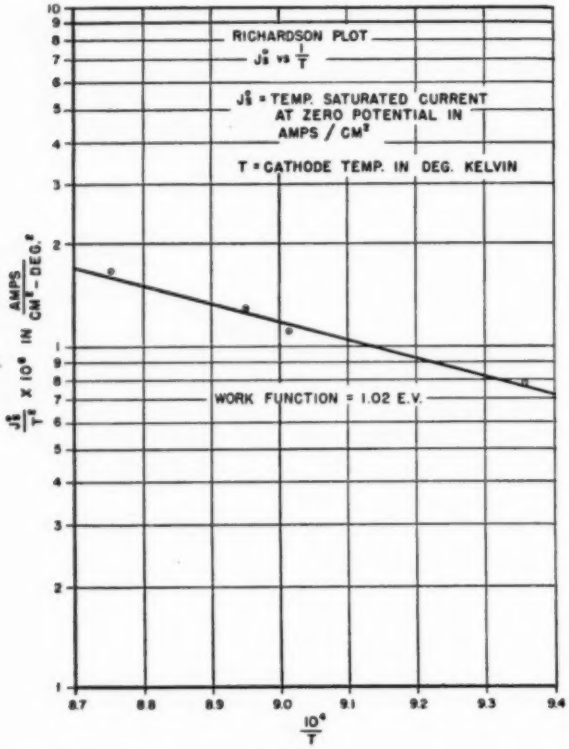
RICHARDSON PLOT
Js/T² vs 1/T
Js = TEMP. SATURATED CURRENT AT ZERO POTENTIAL IN AMPS/CM²
T = CATHODE TEMP. IN DEG. KELVIN
WORK FUNCTION = 1.02 E.V.
Js/T² X 10⁶ IN AMPS/CM²-DEG.²
10⁴/T

FIG. 3. Typical Richardson plot for impregnated matrix cathode.

III. EMISSION

Such cathodes have been mounted in a simple planar diode structure and evacuated to a pressure of 10^{-7} mm of Hg on a vacuum station employing an oil diffusion pump. The cathodes were decomposed in approximately 10 minutes; the maximum temperature never exceeded 1050°C and pressures were kept below 10^{-4} mm. Following this, the tubes were activated off the pump, employing a schedule similar to that of sprayed oxide cathodes and rapid activation resulted in most cases.

Pulse techniques were employed to determine the saturation current at zero field and from this data the work function was obtained. The pulser was built according to a design developed at the National Bureau of Standards.[7]

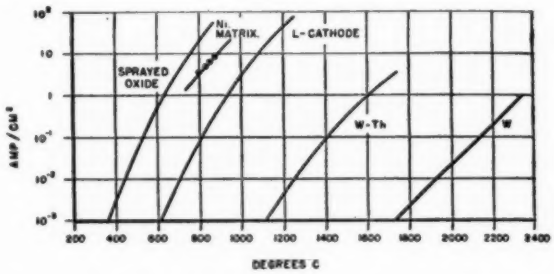

FIG. 4. Thermionic efficiency plot for impregnated cathode relative to conventional-type cathodes.

Figure 2 shows a typical Schottky plot for the matrix cathode. The ordinate is current density, assuming that the cathode area is the geometrical area, 0.322 cm². No arcing was observed at maximum current densities of 10 amp/cm² which were drawn. Limitations of the pulser prevented going to higher fields. It may be added that several conventional oxide-coated cathodes were pulsed under identical conditions and measurements were limited because of cathode arcing.

Figure 3 is a Richardson plot based on the data shown in the previous graph. The resulting work function computed from this graph yields a value of 1.02 ev. On the average, values of work function varying from 1 to 1.25 ev have been measured, the variation is probably due to modifications in activation techniques employed.

Figure 4 illustrates the thermionic properties of the nickel matrix cathode relative to (BaSr)O, the *L*-cath-

[7] L. A. Marzetta, Electronics **27**, 178–180 (1954).

ode, and the tungsten cathode. It will be noted that the Ni matrix is intermediate between (BaSr)O and the *L*-cathode. For purposes of clarity, values for the molded cathode have been omitted; and the results so far obtained for the nickel matrix are slightly below those reported for the molded cathode.[3]

A group of matrix cathodes have been life tested for several thousand hours at low current densities, but the results are limited and cannot be termed significant; the diodes tested had not been fabricated with any standardized procedure so that rather wide variations have resulted.

JOURNAL OF APPLIED PHYSICS VOLUME 26, NUMBER 9 SEPTEMBER, 1955

Internal Friction Peak Associated with Precipitation in an Al−Ag Alloy

A. C. DAMASK* AND A. S. NOWICK†
Pitman-Dunn Laboratories, Frankford Arsenal, Philadelphia, Pennsylvania
(Received April 1, 1955)

Internal friction and elastic aftereffect measurements have been made on wire specimens of an Al−20% Ag alloy at various stages in the precipitation process. A specimen quenched from the solid solution region and aged at 155°C shows an internal friction peak at 140°C for a vibration frequency of 0.25 cps. The relaxation strength associated with the peak is about 0.02. The peak is not greatly affected by further anneals although these anneals completely change the character of the precipitate from the initial spherical clusters of solute atoms to the plate-like transition (γ') precipitate. In the temperature range in which clusters redissolve (reversion), however, the internal friction shows a temperature hysteresis. The activation energy associated with the internal friction peak falls in the range 25–27 kcal/mole, depending on the state of precipitation. A mechanism is suggested whereby the peak originates in a stress-induced change in the local extent of precipitation. This behavior results from the interaction of the applied stress with the internal stresses about precipitate particles. In terms of this mechanism one can account qualitatively for the principal experimental observations.

INTRODUCTION

ANELASTIC effects have proved very useful in the study of atomic mobility in solid solutions.[1,2] A condition for the occurrence of anelasticity is that upon application of stress to the alloy, atomic redistribution occurs in such a way as to relieve the applied stress. If atomic redistribution is a simple relaxation process (involving a single time of relaxation), the internal friction (logarithmic decremen tof decay of vibration amplitude) can be described by the equation

$$\frac{\delta}{\pi}=\Delta\frac{\omega\tau}{1+\omega^2\tau^2} \tag{1}$$

where δ is the logarithmic decrement, ω is 2π times the frequency of vibration, τ is the relaxation time for atomic redistribution, and the constant Δ is called the "relaxation strength." Since the rate of atomic movement controls τ, this quantity may be expected to depend on temperature through an Arrhenius equation, i.e.,

$$\tau=\tau_0 e^{H/RT} \tag{2}$$

where H is the appropriate activation energy for atomic jumps, R the gas constant, T the absolute temperature, and τ_0 is a constant which depends on the relaxation mechanism and on the material.

If the internal friction, given by combining Eqs. (1) and (2), is plotted against temperature at constant frequency, a peak occurs at a temperature T_m. The relaxation time at T_m, is given by the relation

$$\tau(T_m)=\omega^{-1} \tag{3}$$

and Δ is $2/\pi$ times the maximum logarithmic decrement. From Eqs. (1) and (2), the half-width of this internal friction peak is

$$1/T_1-1/T_m=1.31R/H \tag{4}$$

where $T_1(<T_m)$ is the temperature at which the damping is equal to half maximum.

The occurrence of an internal friction peak in a substitutional solid solution was first observed by Zener[3] for the case of alpha brass and later studied in some detail for a series of Ag−Zn solid solutions.[4] This effect occurring in substitutional solid solutions will be referred to in this paper as the "Zener relaxation." The occurrence of this effect in a homogeneous solid solution apparently requires a substantial difference in the size of the solvent and solute atoms,[5] and

* Now Guest Scientist, Brookhaven National Laboratory, Upton, Long Island, New York.
† Permanent address: Hammond Laboratory, Yale University, New Haven, Connecticut.
[1] C. Zener, *Elasticity and Anelasticity of Metals* (University of Chicago Press, Chicago, 1948).
[2] A. S. Nowick, *Progress in Metal Physics, IV* (Interscience Publishers, Inc., New York, 1953).
[3] C. Zener, Trans. Am. Inst. Mining Engrs. **152**, 122 (1943).
[4] A. S. Nowick, Phys. Rev. **88**, 925 (1952).
[5] C. Zener, Phys. Rev. **71**, 34 (1947).

a large concentration of solute (or the order of ten atomic percent). The Zener relaxation may be attributed to local ordering in the solid solution induced by the applied stress.[4]

Another internal friction peak which occurs in polycrystalline metals and alloys is the grain-boundary peak. It occurs at a higher temperature than the Zener peak and is much broader. This peak was studied extensively in aluminum by Kê,[6] and may be related to stress induced atomic redistribution at the grain-boundary interfaces. In the case of precipitating systems one may anticipate additional anelastic relaxation effects associated with the various stages of precipitation. Such effects, if observed, could present a valuable method for the study of atomic mobility and possibly of structural changes during precipitation.

There have been few studies of anelasticity in precipitating systems. In the Al—Cu system Kê[7] performed measurements of a preliminary sort on a 4% Cu and also on a 0.5% Cu alloy, but no systematic investigation was carried out. An anomalous effect was observed[8] which showed a strong dependence on amplitude and previous history of vibration and which proved difficult to reproduce.[9] Investigation of precipitation in Al—Zn[9] showed large internal friction effects, which were related to the presence of a network of interfaces as a consequence of the occurrence of discontinuous precipitation. (*Continuous precipitation* is characterized by a more or less uniform precipitation throughout the grains and is such that the matrix is depleted at much the same rate at every point. *Discontinuous precipitation* is characterized by a preferential precipitation at the grain boundary which spreads inward, so that decomposition occurs at an advancing interface.)

The Al—Ag system has been a subject of extensive investigation in recent years. The phase diagram on the Al rich side, as recently determined by Rotherham and Larke[10] and by Raynor and Wakeman,[11] shows that up to 48 weight percent (18 atomic percent) silver can be dissolved in aluminum in the vicinity of 550°C, but that the solubility is only 3% at 300°C and falls to negligible values at room temperature. The silver rich (γ) phase that precipitates out of the terminal solid solution has a close-packed hexagonal structure. The x-ray studies of precipitation in this alloy by Barrett, Geisler, and Mehl,[12] show an intermediate phase (γ'). This phase is also close-packed hexagonal, but with different lattice parameters than γ, since it is held in register by the matrix until it grows large enough to break away from the matrix to form the γ structure. The Al—Ag alloys exhibit continuous precipitation of the γ' structure with a well-defined Widmanstätten figure; the transition from γ' to γ takes place at relatively high temperatures. Recently there has been renewed interest in the study of precipitation in this system principally by groups directed by W. Köster and by A. Guinier. The work of these groups will be discussed later in this paper.

The present investigation was inaugurated to see if any changes in the anelastic properties are observable as a consequence of precipitation. The 20 weight percent (5.9 atomic percent) alloy was selected because most of the previous studies of precipitation in Al—Ag use this concentration.

SPECIMENS AND PROCEDURE

High-purity aluminum and vacuum remelted silver, both of purity better than 99.99%, were cast into a graphite mold. The ingot, 0.5 inch in diameter, was homogenized for two days at 520°C and reduced by hot rolling and cold swaging to 0.045 inch diameter with appropriate intermediate anneals. The wire was then cold drawn to a final diameter of 0.032 inch. Chemical analysis showed 20.1% by weight of silver. In the final anneal, wire specimens were held at about 520°C for several hours and then quenched into cold water. This treatment resulted in a coarse grained structure with an average of 3 grains across the wire.

Before each series of measurements the wire was reheated to 520°C for fifteen minutes and immediately pulled into cold water. A specimen thus treated will be referred to as "freshly quenched."

In the course of this investigation it was found desirable to include a specimen in which precipitation had proceeded as far as conveniently possible. One wire specimen was subjected to the following anneal. The wire was heated to 520°C then slowly cooled to 380°C and held at that temperature for 18 hours. It was then cooled in 10°C steps and aged 14 hours at each step down to 310°C. The wire was then cooled to room temperature over a period of 14 hours. This wire will be referred to as the "long annealed" or LA specimen.

The internal friction, measured in a torsion pendulum in which a 6 inch length of wire specimen forms the suspension, is reported as δ, the logarithmic decrement. During these measurements the shear strain on the specimen does not exceed 8×10^{-5}; in this range of amplitude internal friction is found to be amplitude independent at all stages of precipitation. The frequency at which measurements are made is 0.25 cycles per second throughout, except where otherwise stated.

Elastic aftereffect measurements are made by maintaining a twist of the specimen wire through about 10°. In the course of twisting, the stress is partly relaxed at a rate determined by the relaxation time τ for that temperature. Therefore when the wire is released it does not return to the original zero point instantaneously; there is a residual anelastic strain which approaches zero in an exponential manner. To

[6] T. S. Kê, Phys. Rev. **71**, 533 (1947).
[7] T. S. Kê, J. Appl. Phys. **21**, 414 (1950).
[8] T. S. Kê, Phys. Rev. **78**, 420 (1950).
[9] A. S. Nowick, J. Appl. Phys. **22**, 925 (1951).
[10] L. Rotherham and L. W. Larke, J. Inst. Metals **81**, 67 (1952).
[11] G. V. Raynor and D. W. Wakeman, Phil. Mag. **40**, 404 (1949).
[12] Barrett, Geisler, and Mehl, Trans. Am. Inst. Mining Engrs. **143**, 134 (1941).

evaluate τ the anelastic strain is plotted against the logarithm of the time, t; an inflection point in the curve occurs where $t=\tau$. If the time of twist of the wire is long compared to τ, the ratio of the anelastic strain to the total torsional strain is equal to the relaxation strength Δ of Eq. (1). Thus, the parameters Δ and τ, which appear in the internal friction equation, may also be obtained by means of elastic aftereffect measurements. The latter measurements are most valuable in the low-temperature range where τ is too large to be measured by internal friction methods.

RESULTS

Internal Friction

A freshly quenched specimen was suspended in the torsion pendulum and the internal friction measured as a function of temperature up to 155°C. It was observed that the damping went through a peak, as shown in Curve *A*, Fig. 1. During the tracing of this curve, internal friction was not constant in time, but tended to decrease at each temperature. The sample was then held at 155°C for twenty minutes, after which the internal friction was measured during cooling. The peak thus obtained, which is illustrated by Curve *B*, Fig. 1, is stable and essentially reversible with respect to cooling and heating. Further anneals were carried out in steps of about 5°C for twenty minutes each. After each anneal the internal friction was measured at regular intervals starting from the annealing temperature and working down to room temperature. It was then remeasured in the course of heating the specimen to the next annealing temperature. For annealing temperatures between 155°C and 171°C the curves obtained were substantially no different from Curve *B*, Fig. 1. Longer anneals at 171°C, and anneals at higher temperatures produced changes in the internal friction curves. Figure 2 shows curves obtained during cooling after some of these anneals. (For the sake of clarity only curves from selected anneals are illustrated.) Curve 1, Fig. 2 is essentially the same as Curve *B*, Fig. 1. Except for the last two curves, the highest temperature shown on each curve is the temperature of the anneal. Curves 2 through 8 are for anneals of over one hour at each of the indicated temperatures, and Curve 9 is for the LA specimen (see the previous section). It should be noted that the peak first migrates toward higher temperature while increasing in height, then returns toward lower temperatures with a decrease in height.

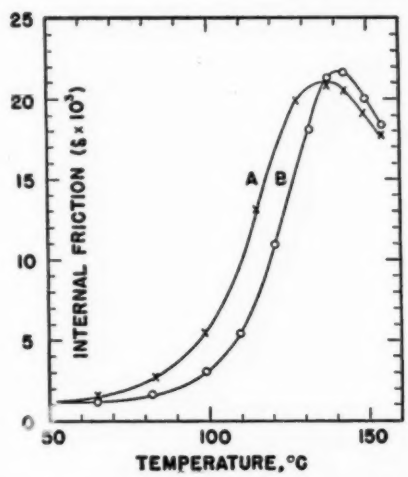

FIG. 1. Variation of internal friction of an Al-Ag wire with temperature at a frequency of 0.25 cps. Curve *A*: Freshly quenched specimen. Curve *B*: Same specimen after a 20-min anneal at 155°C.

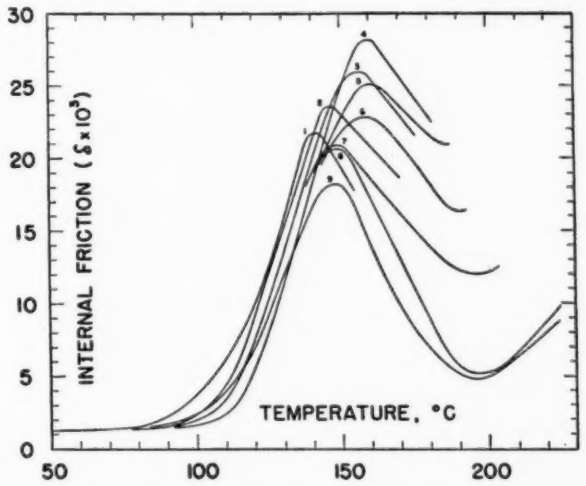

FIG. 2. Internal friction curves after a series of successive heat treatments. All curves were measured during cooling from the anneal temperature. The numbering on the curves corresponds to the following anneals: (1) 20 min at 155°C, (2) 120 min at 171°C, (3) 90 min at 177°C, (4) 75 min at 182°C, (5) 135 min at 188°C, (6) 90 min at 193°C, (7) 120 min at 204°C, (8) 130 min at 232°C, and (9) LA specimen.

For any given internal friction curve in the migration range (Curves 2 through 7, Fig. 2), the internal friction is not stable in time at temperatures below the annealing temperature. This results in a temperature hysteresis between the curves obtained on cooling and on subsequent reheating, as illustrated in Fig. 3 for the state of anneal corresponding to Curve 4 of Fig. 2. The closed hysteresis loop obtained is retraceable if not too long a time is spent near the annealing temperature. The temperature hysteresis first appears after the 171°C anneal, increases in magnitude with higher annealing temperatures, and attains a maximum after the 182°C anneal. It then decreases for subsequent anneals, and becomes negligible after anneals above 200°C. In view of this hysteresis, the temperature at which the peak occurs in the curve obtained on heating is several degrees lower than the temperature of the corresponding peak on cooling. In the region of the peak, for a given state of anneal, measurement of the change in internal friction with time at constant temperature indicates that there is an equilibrium value of damping which falls inside the hysteresis loop.

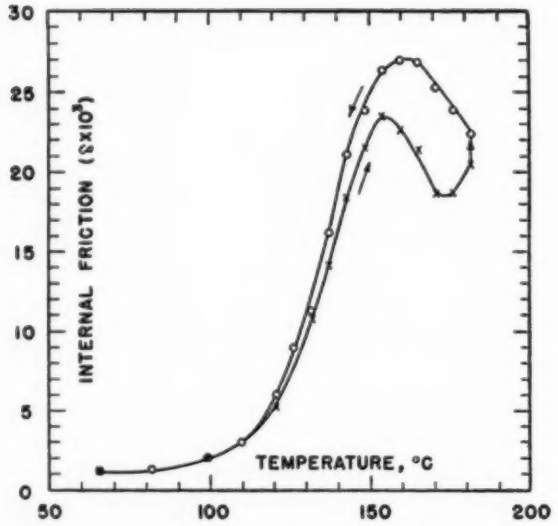

FIG. 3. Temperature hysteresis in internal friction after an anneal for 75 min at 182°C. Circles obtained on cooling after the anneal. Crosses obtained on subsequent reheating.

The temperature hysteresis, typified by Fig. 3, results from the fact that both the height and position of the internal friction peak, are themselves changing as the peak is being traced out. Specifically, the results obtained show that as the temperature is decreased, the peak is moving to the left and decreasing in height.

For annealing temperatures greater than 200°C, the internal friction peak remains at 150°C, within experimental error, while the height decreases gradually approaching Curve 9, Fig. 2 for the LA specimen. For this latter specimen measurements were made up to 315°C (not shown in Fig. 2). It was found that the curve rose continually from the minimum at 200°C and attained a value $\delta=0.1$ at 315°C. It was not possible to go to higher temperatures without substantial resolution of the precipitate. This second rise in damping may possibly be the grain boundary relaxation, but very likely includes a strongly temperature dependent "background" of uncertain origin.

Reproducibility of the behavior shown in Figs. 1 through 3 was demonstrated by performing a similar set of runs on the same specimen requenched from 520°C. The results obtained on the second set of runs agreed in all details with the results already quoted.

Elastic Aftereffect

In order to evaluate precisely the parameters τ_0 and H of Eq. (2), τ must be obtained over as wide a range of temperature as possible. Measurements of the internal friction peak at different frequencies, and of elastic aftereffect are therefore required. The magnitude of Δ obtained from elastic aftereffect measurements agreed well with the corresponding value from the peak height, showing that the same phenomenon was involved in both types of measurement.[13] The most extensive elastic aftereffect measurements were made on the LA specimen, for which the peak is stable with respect to further anneals and shows no hysteresis phenomenon. Data for τ plotted against T^{-1} are shown by the solid circles of Fig. 4. The high-temperature points (above 140°C) are from internal friction peaks measured at two different frequencies, 0.25 and 0.76 cycles per second, while the solid circles at lower temperatures (60° to 100°C) are from elastic aftereffect measurements. The best straight line through these points gives $H=25.0\pm0.5$ kcal/mole, and $\log\tau_0=-13.15\pm0.3$, (τ_0 in seconds).

When the value of the heat of activation is known, the theoretical half-width of the internal friction peak may be obtained from Eq. (4). The observed internal friction peaks for the LA specimen are about 40% wider than this theoretical value. This peak width is not quite as sharp as that obtained for the Zener relaxation in Ag–Zn alloys which is reported[9] to be 15 to 20% wider than the theoretical value.

Similar elastic aftereffect measurements were taken for the condition of the 155°C anneal (Curve 1, Fig. 2). This was the only other internal friction peak that had a precise location and exhibited no hysteresis. The 155°C anneal condition gave a slightly steeper slope

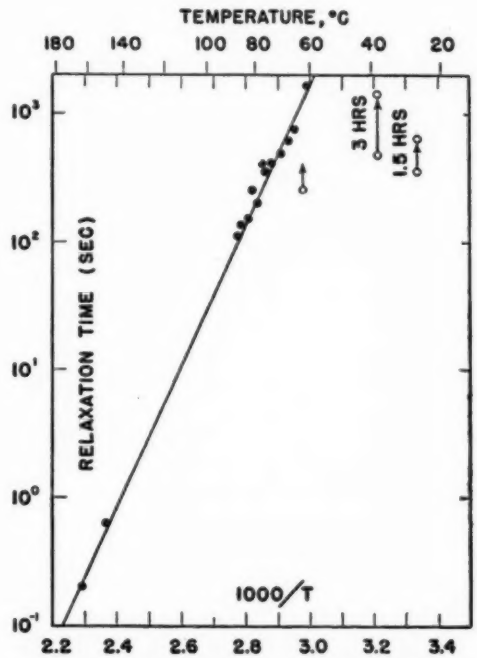

FIG. 4. Variation of relaxation time with temperature. Solid circles: Measurements on the LA specimen. (Some of the points represent the average of several measurements.) Open circles: Measurements on freshly quenched specimens.

[13] Actually the elastic aftereffect measurements showed a second relaxation effect which increased continuously in magnitude with time of twist and had a much longer relaxation time (i.e., required higher temperatures to anneal out) than the principal effect. This second effect is undoubtedly related to the increase in internal friction above 200°C.

than the LA specimen, with $H=27\pm1$ kcal/mole, and $\log\tau_0=-14.2$. Because this peak corresponds to a metastable condition, the quantities obtained do not have the same precision as those obtained from the LA specimen.

Behavior Directly After Quenching

It has already been noted that internal friction values, obtained during the first run on a freshly quenched specimen (Curve *A*, Fig. 1) are not stable in time. Not until the 155°C anneal is a stable and reversible internal friction peak developed. It is not convenient to study these early changes in anelastic properties by internal friction methods because the act of raising the temperature to locate the peak in itself changes the condition of the material.

Elastic aftereffect measurements were employed to study the condition of the alloy (in early stages) after quenching. The open circles in Fig. 4 show relaxation measurements on freshly quenched specimens. The points shown were obtained as follows. In the case of measurements at room temperature (26°C), the sample was quenched, and relaxation measurements begun immediately. The first measurement of τ is given by the lower open circle. The specimen was reheated to solution temperature and quenched, but now allowed to stand at room temperature for 1.5 hours before the relaxation time was measured. This resulted in the upper circle. Similar data were taken at other temperatures as indicated by the various open circles. The relaxation strength obtained from these elastic aftereffect measurements agreed in magnitude with that obtained from the height of the internal friction peak observed at higher temperatures.

From these results it appears that the relaxation peak, which is found near 150°C after anneals at temperatures of 155°C and higher, is also present for the as quenched specimen with about the same magnitude. However, in the freshly quenched specimen the peak is located at a much lower temperature. This interpretation explains why the internal friction was always falling in time, at a constant temperature, during the measurement of Curve *A*, Fig. 1, *viz.*, the peak was actually moving rapidly to higher temperatures while it was being measured. To explain why τ values should be so abnormally low (as shown by the open circles of Fig. 4) in the freshly quenched specimen, it seems reasonable to compare the present behavior with that of an Ag−Zn solid solution quenched from high temperatures.[14] In this latter case, abnormally rapid τ values for the Zener relaxation are observed, presumably due to the presence of excess vacancies trapped in the lattice by quenching. It therefore seems consistent to explain in the same way the abnormally low values after quenching in the present alloy. This interpretation assumes that the relaxation process in the Al−Ag alloy is also controlled by the rate of movement of atoms in the solid solution.

DISCUSSION

Stages in the Precipitation

Before an attempt is made to understand the origin of the observed internal friction peak in the Al−Ag alloy, it seems desirable to review what is known about the structural changes which take place at various stages of the precipitation process. The principal experimental information about the early stages in the precipitation process comes from mechanical property measurements, specific heat measurements, and low-angle scattering of x-rays.

The most extensive measurements of mechanical property changes which accompany precipitation in Al−Ag alloys are those of Köster and Braumann.[15] These authors have demonstrated, particularly by means of hardness measurements, that there are two distinct stages in the precipitation process. In stage I (which they call "cold hardening") there is first an increase in hardness and then a decrease with increasing annealing temperature. The drop in hardness is interpreted as a reversion phenomenon, i.e., it is believed that the drop is due to the re-solution of the metastable precipitate responsible for the cold hardening stage. In stage I, Köster and Braumann demonstrate that there is an equilibrium hardness at each temperature which is not dependent on previous history so long as anneals are not carried to the point where stage II begins. These authors interpret this result as due to a temperature dependent (metastable) equilibrium between silver rich and silver poor regions in the solid solution. In stage II (which they call "warm hardening") a second and much greater hardness increase occurs. The corresponding hardness maximum occurs at a temperature that is related to the time of anneal through an Arrhenius equation. For the 20% alloy they obtain an activation energy of 29 kcal/mole from the times and temperatures to attain this hardness maximum.

Isothermal plots of hardness against time show a major difference in the kinetics of stages I and II, *viz.*, whereas the curves have a finite initial slope for stage I, the initial slope is zero for the warm hardening stage. This result implies that nuclei of the metastable precipitate of stage I are present in the as quenched condition, whereas nuclei for stage II must form during an initial incubation period. The first line of Fig. 5 shows the stages and corresponding temperature ranges observed by Köster and Braumann for approximately two-hour anneals of a 20% Al−Ag alloy. The position of the principal hardness maximum is also shown.

The results of the specific heat measurements of Köster and Schell[16] support the conclusions concerning

[14] A. S. Nowick and R. J. Sladek, Acta Metallurgica **1**, 131 (1953); A. E. Roswell and A. S. Nowick, J. Metals **5**, 1259 (1953).

[15] W. Köster and F. Braumann, Z. Metallkunde **43**, 193 (1952).

[16] W. Köster and H. A. Schell, Z. Metallkunde **43**, 454 (1952).

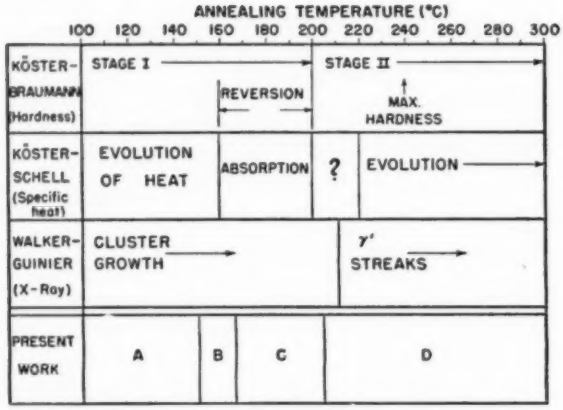

FIG. 5. Stages of precipitation in Al−20% Ag, as observed by different techniques. Anneals are approximately for two-hour periods. Rate of heating in the specific heat measurements: 0.8°C/min.

stages of precipitation drawn from the hardness measurements. Data obtained on various Al−Ag alloys, heated (after quenching) at a rate of 0.8°C/min, show the following successive stages: (1) a small evolution of heat at low temperatures; (2) an absorption of heat; (3) a large evolution of heat; (4) above 300°C, absorption of heat as a consequence of the increased solubility of Ag in Al at these elevated temperatures. The first three of these stages is shown in Fig. 5 for the 20% alloy. Although the continuous heating required to obtain the specific heat data is not exactly equivalent to the isothermal anneals used in the hardness measurements, the two methods of annealing should nevertheless give results which are closely comparable. Figure 5 shows that the first evolution of heat may be attributed to the formation of the metastable stage I precipitate. The heat absorption which follows provides almost incontravertible evidence that the reversion stage, observed by means of hardness measurements, represents resolution of the first metastable precipitate. Similar specific heat data have been obtained by Hirano,[17] whose results agree with those of Köster and Schell except in the region marked questionable in Fig. 5. In this region Köster reports a small secondary absorption peak, while Hirano shows essentially no deviation from the base line (the "normal" specific heat curve) which he claims was selected incorrectly by Köster. Except for this minor point, there seems no doubt of the agreement between stages observed by means of hardness and specific heat measurements.

A variety of x-ray techniques[18] show early stages of precipitation in the form of streaks which result from the presence of thin platelets of the γ' precipitate. Glocker *et al.*[19] have shown that the appearance of such streaks accompanies the onset of stage II of the precipitation. By the use of low angle scattering techniques, Guinier and co-workers[20,21] have been able to demonstrate the nature of stage I. They show rings of diffuse scattering at low angles which can be interpreted as due to the presence of spherical clusters of silver atoms surrounded by regions depleted of silver. In fact they show that spherical clusters, whose mean size is about 100 Ag atoms, exist in the as quenched alloy (though not in the solid solution at the quenching temperature[22]). In the early stages of precipitation they observe steady cluster growth (the arrow in line 3 of Fig. 5 shows the range of temperature of most rapid cluster growth) with no evidence for reversion in the appropriate temperature range.[21] Hardy and Heal[23] argue, however, that this result is not in conflict with other evidences of reversion, since the method is concerned with the average size of those clusters that are present, not with the quantity of precipitated material. Near 212°C (for about a two hour anneal) streaks appear abruptly in the low angle photogram due to the formation of thin γ' platelets (Guinier-Preston zones). From the temperature at which γ' begins to appear, it is apparent that this precipitate corresponds to Köster's stage II.

In summary, the experimental evidence quoted shows that precipitation takes place in two stages. The first corresponds to the growth of spherical silver-rich clusters which are already present in the as quenched condition. In the reversion range (160° to 200°C) these clusters (or at least, the smaller of them) redissolve, accompanied by a drop in hardness and an absorption of heat. The second stage begins with the formation of thin platelets (the Guinier-Preston zones) of the second metastable precipitate, γ'. These platelets account for the streaks in x-ray patterns, the second and major increase in hardness, and a large evolution of heat.

Origin of the Damping Peak

The measurements reported in this paper show the presence of an internal friction peak which is essentially unchanged in magnitude over an extremely wide range of conditions. In fact, except for the abnormally low relaxation times in specimens examined directly after quenching (which are attributed to the presence of quenched in vacancies), the peak is not very different over the entire range from the as quenched to the "long annealed" condition.

There are two possible sources of the peak: it may originate in the presence of precipitate particles or in the residual solid solution itself.[24] The sharpness of the

[17] K. Hirano, J. Phys. Soc. Japan **8**, 603 (1953).
[18] Reviewed by H. K. Hardy and T. J. Heal, *Progress in Metal Physics V* (Interscience Publishers, Inc., New York, 1954), p. 143.
[19] Glocker, Köster, Scherb, and Ziegler, Z. Metallkunde **43**, 208 (1952).
[20] A. Guinier, J. phys. radium **8**, 124 (1942).; Z. Metallkunde **43**, 217 (1952).
[21] C. B. Walker and A. Guinier, Acta Metallurgica **1**, 568 (1953).
[22] Walker, Blin, and Guinier, Compt. rend. **235**, 254 (1952).
[23] Reference 18, p. 206.
[24] The peak is too sharp and is located at too low a temperature to be a grain boundary peak, especially considering that the specimens were coarse grained.

peak and its occurrence over such a wide range of conditions tends to suggest that it is due to a Zener relaxation originating in the solid solution. From the value of the activation energy associated with the relaxation effect,[25] and the fact that quenched in vacancies appear to lower the τ value, it may be concluded that atomic mobility in the solid solution is the rate controlling factor. Also, the peak seems to increase in height with increasing temperature in the reversion range, where the concentration of solute in solution is increasing. These results are all in accord with the suggestion that a Zener relaxation is responsible for the peak. On the other hand, there are several reasons why this suggestion does not seem reasonable. In view of the solubility-temperature curve for Ag in Al and of the method of preparation of the LA specimen, there could not be more than one atomic percent (4 weight percent) of Ag remaining in solution in this specimen. Thus the magnitude of the peak would have to be substantial ($\Delta \sim 0.01$) for as little as one atomic percent solute. Such a magnitude is usually observed in solid solutions containing at least 10 atomic percent solute. Since the relaxation strength of the Zener relaxation goes essentially as the square of the solute concentration, its magnitude in the present alloy would have to be far greater than in any other alloy system studied to date. Furthermore, the atomic radii of aluminum and silver are essentially the same. If a substantial size difference between solute and solvent is taken as the criterion for a large Zener relaxation,[5] one would expect this relaxation to be unusually small in Al—Ag. Finally, the value of τ_0, Eq. (2), for the present relaxation effect is somewhat larger than that usually obtained for the Zener relaxation; this result implies that the number of atomic movements required for this relaxation process is larger (by 10 to 100 times) than that required for the Zener relaxation.

In view of the lack of a complete understanding of the Zener relaxation at the present time, these arguments cannot be regarded as conclusive. Therefore, experiments were conducted[26] to settle the matter definitely by means of observations made in the solid solution range using "high-frequency" apparatus. The results described in the Appendix, seem to establish that the peak in Al—Ag does not originate in the solid solution and therefore that the source of the peak must be in the precipitate. It thus appears that the Al—Ag peak represents a new relaxation phenomenon, different in origin from those studied in previous work.

Consideration of various possible interpretations of the Al—Ag peak has led the authors to only one reasonable mechanism which is consistent with the observations. This mechanism is based on the existence of internal stress about coherent particles, such as the clusters or the γ' particles. The stress is predominently shear, and may vary both in magnitude and in sign from one locality to another. Obviously, so long as internal stresses are present we are not dealing with an equilibrium situation, i.e., with the minimum possible total free energy. However, in each locality equilibrium will be established over distances comparable with the mean diffusion distance for the particular time and temperature of anneal. In the establishment of local equilibrium, stress and strain play a role as conjugate thermodynamic variables. The existence of strain energy in the matrix opposes precipitation, while the chemical free energy term favors precipitation. The equilibrium situation represents a balance of these factors so as to produce minimum free energy in each locality.

An externally applied stress will upset the local equilibrium situation; the local solute concentration in solution must then shift in such a direction as to oppose the effect of the applied stress. Thus, in some localities more solute atoms will go into solution while in others further precipitation will take place, depending on the relative signs of the internal stress in the region and of the externally applied stress. This is a relaxation process, whose rate is determined by the rate of atomic diffusion in the solid solution adjacent to the precipitate particle in each locality.

In terms of the aforementioned theory it is possible to account for the fact that the internal friction peak in Al—Ag is present both in the cluster stage and in the presence of the γ' precipitate. According to Walker and Guinier[21] clusters are present even in the as quenched condition. Thus it is not surprising that the relaxation effect also exists for this condition, as shown by the measurements made directly after quenching. The theory also predicts that the relaxation process is controlled by lattice diffusion in the solid solution adjacent to the precipitate particles. This prediction is in agreement with the facts that quenched in vacancies apparently hasten the relaxation process and that the activation energy for the relaxation process is comparable with that for lattice diffusion. (The fact that the activation energy for relaxation is actually lower[25] than that for diffusion is consistent with the presence of strains around precipitate particles.) The fact that τ_0 [Eq. (2)] for the present relaxation effect is larger than for the Zener relaxation is also explained; the atomic rearrangement required to produce relaxation in accordance with the above mechanism should require a relatively large number of atom movements.

Stages in Migration of the Peak

It now seems advantageous to attempt to correlate the various temperature ranges in the migration of the internal friction peak with the various structural changes in this alloy demonstrated in previous work (Fig. 5). The behavior of the present relaxation peak

[25] The values of the activation energy reported in this paper for the internal friction peak under discussion are slightly lower than the corresponding values reported for diffusion of solutes in aluminum [A. S. Nowick, J. Appl. Phys. **22**, 1182 (1951)] and lower than the value of 29 kcal/mole reported by Köster and Braumann[15] for attainment of maximum hardness.

[26] D. P. Seraphim (unpublished).

during annealing, as shown by internal friction as well as static measurements, may be divided into four stages, represented by A, B, C, and D in Fig. 5. In stage A the relaxation time increases rapidly as annealing takes place, presumably due to the presence of a non-equilibrium excess of vacancies. In stage B, the damping peak becomes temporarily stable; it remains at a constant temperature and may be traced while either ascending or descending in temperature. Stage C is the migration range in which the peak moves first to higher temperatures then back to lower temperatures as the annealing temperature is steadily increased. In this stage, internal friction also shows temperature hysteresis. Finally in stage D the peak location is again stable but the height very gradually decreases as annealing temperature increases.

Comparison of these stages with the ones observed by means of hardness, specific heat, and x-ray measurements may be made with the aid of Fig. 5. It is first to be noted that the transition from stage A to B does not correspond to an analogous transition observed by other workers. This lack of correspondence supports the contention that the cessation of the rapid peak migration in stage A is not due to structural changes but only to the elimination of excess vacancies retained by quenching. The migration range C agrees fairly well with the reversion range observed by means of hardness and specific heat measurements. Furthermore, the observed temperature hysteresis in this range, as typified by Fig. 3, agrees well with the reversible hysteresis in hardness measurements obtained by Köster and Braumann. However, the details of the migration of the internal friction peak in stage C are difficult to interpret at present.

Stage D correlates well with the γ' stage. It is of interest that the relaxation time (i.e., the position of the peak) is insensitive to the growth of γ' while the height of the peak decreases only very slowly as the annealing temperature increases and the precipitate becomes coarser. According to the present theory of the peak, when internal stresses are completely eliminated (perhaps through complete conversion of γ' to γ) the peak should also vanish. This condition is difficult to achieve with reasonable annealing times, as demonstrated by Barrett, Geisler, and Mehl[12] who show that the metastable γ' structure persists even after anneals at relatively high temperatures. In particular, for the annealing schedule used for the LA specimen, the x-ray measurements of these authors show the presence of both the γ' and γ structures, with at least 50% of the precipitate still in the γ' form. This persistence of the γ' structure in Al—Ag alloys seems to explain the persistence of the internal friction peak.

ACKNOWLEDGMENTS

In conclusion the authors wish to express their appreciation to Mrs. E. Zucker for assistance in the construction of the equipment and to Mr. D. P. Seraphim (Yale University) for information about his high-frequency experiments.

APPENDIX

The search for an internal friction peak in a solid solution of 5% Ag in Al (1.3 atomic percent Ag) was carried out by D. P. Seraphim as follows. The alloy was prepared in the form of a bar 0.25 inch in thickness and 5 inches long. This bar had a resonant frequency in flexual vibration of 1700 cps. For this frequency, it is predicted, by extrapolation of Fig. 4, that the peak should appear at 330°±10°C. However, from the phase diagram, the solubility of Ag in Al is 4% at 318°C and 5% at 348°C. Thus the damping peak will only appear if it originates in the solid solution, i.e., if it is a Zener peak. The results of Seraphim's measurements show a gradually rising internal friction above 300°C, passing through the values: $\delta=0.002$, 0.006, and 0.06, at 300°C, 350°C, and 400°C, respectively. There is no evidence for a peak in this range, regardless of whether measurements are taken with increasing or decreasing temperatures.

JOURNAL OF APPLIED PHYSICS VOLUME 26, NUMBER 9 SEPTEMBER, 1955

Shock Waves in Air Produced by Waves in a Plate*

WILLIAM A. ALLEN, JOE M. MAPES, AND EARLE B. MAYFIELD
Michelson Laboratory, U. S. Naval Ordnance Test Station, China Lake, California
(Received February 25, 1955)

A shadowgraphic technique has been used to measure surface motion of a series of steel plates while they deform under impact caused by ½-in. diameter steel cylinders fired into their back surfaces at about 2800 ft/sec. The strength of the air shock produced when an initial longitudinal wave in a plate strikes the free surface of the plate has been inferred from the measured shock wave velocity in the air. The shock strength has been related to particle velocity of the surface of the plate. The results are compared to previous work involving contact explosions of small charges on plates.

INTRODUCTION

THE phenomenon studied is produced when the back surface of a plate is loaded abruptly by means of an explosive charge or by impact of a high velocity projectile. In both cases, a curved shock-like compression pulse propagates into the plate. Interaction of this pulse with the free surface produces both transient and permanent deformation. Previous work,[1,2] using high explosives, has indicated that the free surface of the plate moves into the air in a complicated manner. Figure 1 is a graph that illustrates particle displacement of the free surface of a 2-in. thick 1025 steel plate while it deforms under explosive attack. This trace was obtained by means of the optical-lever technique discussed in the previous papers. Time is measured in μsec while the displacement axis is in arbitrary units. The free surface begins to move instantaneously at 0.0 μsec. The plate decelerates gradually until about 1.8μ sec when its velocity appears to increase rather abruptly. The surface has come to rest at about 2.5 μsec, and then begins to return to its equilibrium position. The surface stops again at about 4 μsec, and begins to move outward in large-scale plastic deformation. It is rather suggestive to resolve the complicated structure of the experimental curve into two pulses E and P. The initial pulse can be associated with elastic deformation; the secondary pulse can be attributed to plastic deformation. If this resolution of the experimental wave structure is valid, the phenomena can be interpreted as an elastic wave followed by a partially superposed plastic wave that travels about 5 mm/μsec. The maximum energy involved seems to be associated with the P wave, the E wave being simply a short-duration precursor pulse.

The experiment described using high explosives is open to objection because the steel plate often spalls near the free surface. It is difficult to prove that the shape of the experimental displacement curve is a result of wave interaction, and is not the mechanical effect of fracture. Spalling is induced, in general, by means of a sharply attenuated loading pulse. The experiment discussed was modified to attain more nearly step-function loading by use of a high velocity projectile instead of the explosive charge.

Consider the surface of the plate a piston moving into the air with constant velocity. It is well known that a shock wave will develop and precede the piston. If the piston subsequently accelerates or decelerates, additional shock and rarefaction waves will be created. Specifically, a shadowgram based on the piston motion illustrated in Fig. 1 should reveal two pronounced shock waves in air separated by about 4 μsec. The first shock wave will be associated with arrival of the initial wave in the metal, and the second shock wave will be associated with the minimum point on the curve. There may exist rarefaction waves between the two primary shocks, and possibly a third faint shock wave at about 1.8 μsec. Although associated with the plastic wave, the second shock wave will not necessarily measure arrival of the P wave because the two waves are superposed. If the plastic wave becomes sufficiently strong, or the specimen thickness sufficiently small, the minimum of the curve may disappear altogether, and the second air shock wave may not be formed. The single air shock wave, in this case, is closely associated with the plastic or shock wave in the metal. If the plastic wave does not appear at all, there still may be a weak shock wave associated with the tail of the elastic deformation pulse. The secondary shock wave produced by the piston motion should be approximately as strong as the primary shock wave, because the piston velocity associated with the two waves are about equal.

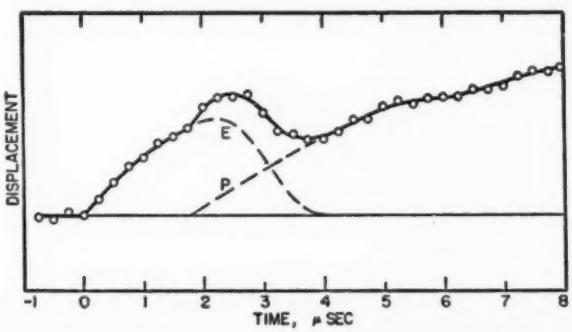

FIG. 1. Particle displacement of the free surface of a 2-in. thick 1025 steel plate while it deforms under explosive attack.

* Presented as a paper at the American Physical Society meeting at Berkeley, California, December 28–30, 1954. For abstract, see Phys. Rev. 98, 256 (1955).

[1] W. A. Allen and C. L. McCrary, Rev. Sci. Instr. 24, 165 (1953).

[2] W. A. Allen, J. Appl. Phys. 24, 1180 (1953).

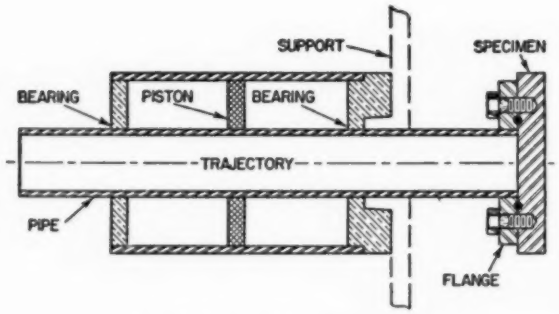

FIG. 2. Dashpot specimen holder.

Location of the shock waves are recorded by means of a shadowgraphic technique based on a 0.1 μsec duration spark gap[3] developed for this kind of experiment. Figure 2 illustrates the arrangement developed to hold the plate. The specimen is bolted to a flange threaded on the end of a 2-in. tube. A light-tight seal is maintained by means of an O-ring. The tube passes through the walls of the shadowgraph box, and is aligned by bearings at each end of a cylinder attached to the wall of the box. A piston attached to the tube divides the cylinder into two approximately equal chambers. When a projectile is fired down the trajectory through the tube into the back surface of the plate, the assembly of plate, flange, tube, and piston move forward as a unit until the force of the impact is cushioned by trapped air in the chambers acting as a dashpot. Figure 3 is a cross section of a 1-in. 1025 steel plate showing the crater produced by impact of a 25-g 0.50-cal 1020 steel projectile at about 2800 ft/sec. The objects in the foreground represent the projectile before and after impact. The cylinder on impact has a tendency to turn wrong side out. The plate has not fractured, although it has undergone extensive permanent deformation.

EXPERIMENTAL RESULTS

Results have been reported[4] of the different behavior of brass and copper when a 0.50-cal cylindrical steel projectile is fired into their back surfaces at 2800 ft/sec. Figure 4 illustrates the behavior of a 2-in. lead plate under the same impact conditions. A single shock wave is formed from the lead plate. Note the small metal jets produced by collapse of subsurface cavities in the plate.

Figure 5 is a compilation of results from several 5.5-in. diameter 1025 steel plates of thicknesses 2 in., $1\frac{1}{2}$ in., $\frac{3}{4}$ in., and $\frac{1}{2}$ in. Permanent deformation was produced on the surfaces of all plates but was more extensive for the thinner plates. The time scale for each shadowgram was obtained from the assumption that the initial air shock wave produced near the edge of the plate travels with sonic velocity. A Rayleigh surface wave generated at the edge of each plate travels with constant velocity toward the center. This wave is produced when the initial wave in the metal reaches the front rim of the plate. The second shock does not form on the axis of the $\frac{1}{2}$-in. plate, indicating that the plastic wave is the dominant feature for this specimen thickness.

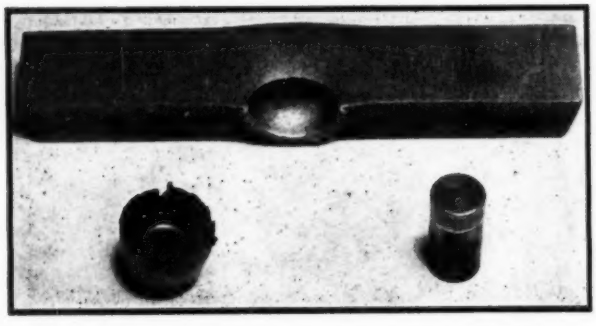

FIG. 3. Cross section of a 1-in. 1025 steel plate showing the crater produced by impact of a 25-g 1020 0.50 caliber steel projectile at about 2800 ft/sec. The projectile is shown before and after impact.

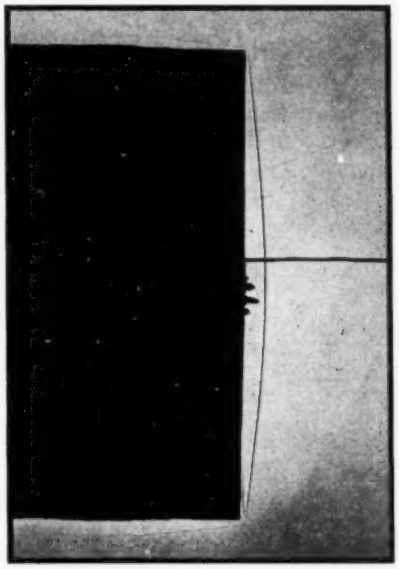

FIG. 4. Behavior of 2-in. lead plate when a $\frac{1}{2}$-in. diameter cylindrical steel projectile is fired into its back surface at 2800 ft/sec.

Figure 6 is a graph of initial air shock wave displacement on the axis of the plate as a function of time for each plate thickness. Each open point represents a separate experiment. The origin of time was chosen to coincide with impact on the back surface of the plate. The first point on each curve represents arrival time at the free surface based on the assumed sound velocity in steel of 6 mm/μsec. The second point on each curve is the displacement of the initial air shock wave at the time when the initial pulse in the metal reaches the front rim of the plate. This displacement was calculated from the extrapolated value of the Mach No. of the initial air shock wave back to the surface of the plate.

If the Mach No. is known of the shock wave produced by a piston moving into a gas, the piston velocity can be calculated by elementary fluid dynamics. The lower curve of Fig. 7 is a plot of piston velocities obtained

[3] Frank N. Miller, Phys. Rev. 93, 945(A) (1954).
[4] Allen, Mapes, and Mayfield, J. Appl. Phys. 26, 125 (1955).

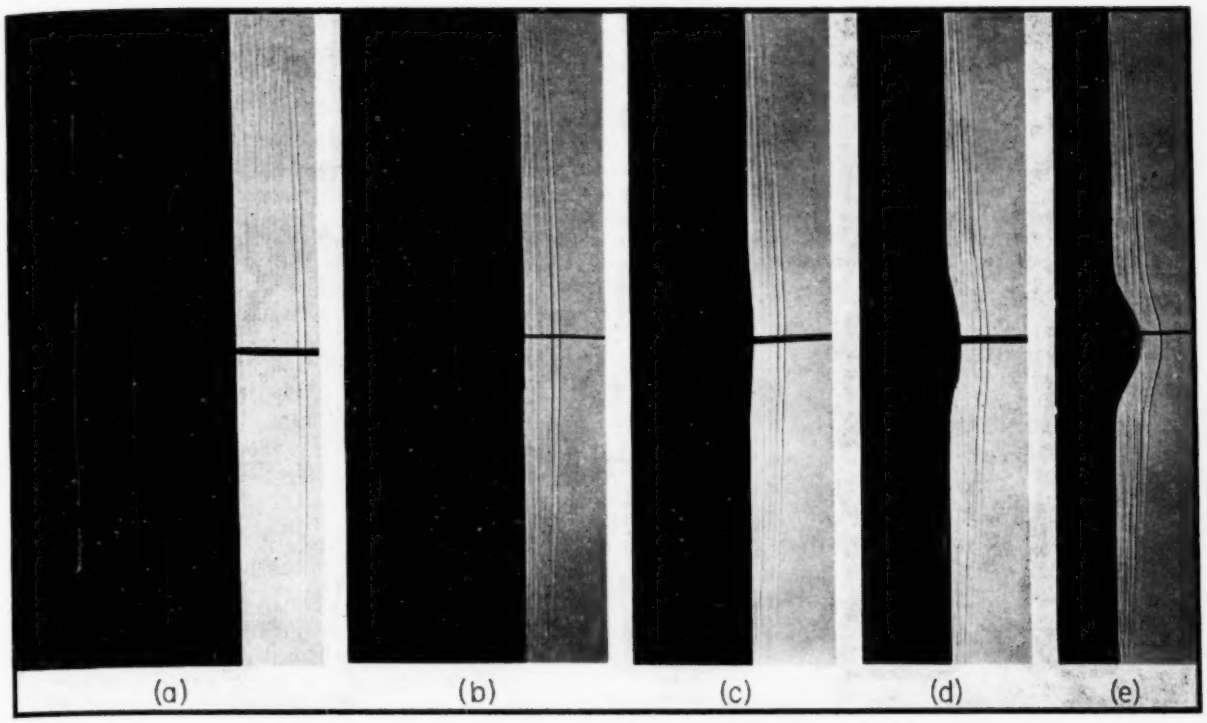

FIG. 5. Shock waves produced from steel plates of thicknesses 2 in., 1½ in., 1 in., ¾ in., and ½ in.

from such a calculation. The Mach No. of the shock wave was obtained from Fig. 6. The upper curve is a plot of particle velocities reported from the original work with high explosives. Since a 1-in. diameter charge was used in this previous work, the linear plate dimensions were scaled by a factor of one-half in order to be comparable with results from the ½-in. projectile. The extrapolation indicated in Fig. 7 beyond the experimental points is justified on the grounds that particle velocity is known at the interface; that is, for an infinitesimally thin plate. It is reasonable that high explosives should yield a higher curve than impact of a steel projectile at 2800 ft/sec, since equivalent pressures are obtained only at projectile velocities of about 4300 ft/sec. Permanent deformation of appreciable magnitude is not observed in this experiment for plate thicknesses greater than 2 in. The maximum stress produced in steel at this distance by impact of a projectile is about 2 or 3 times the yield point of the steel. These results are in general agreement with those of other investigators.[5]

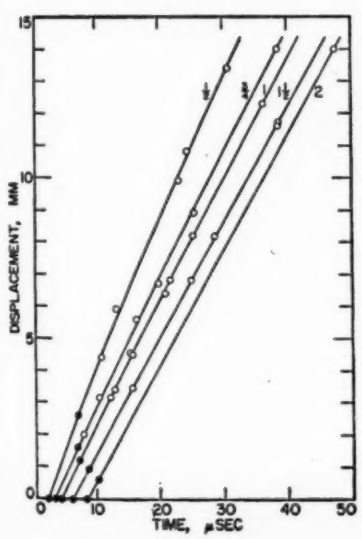

FIG. 6. Initial air shock wave displacement as a function of time for plates of various thicknesses.

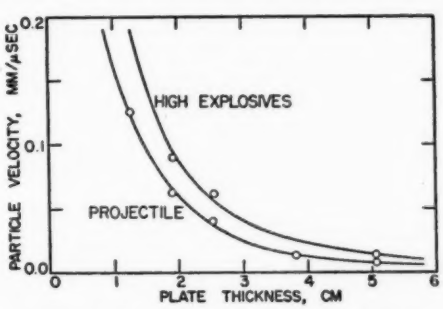

FIG. 7. Free surface velocities of plates.

ACKNOWLEDGMENTS

Credit is due C. P. Pentoney and Z. W. Hohanshelt for preparation of the steel specimens used in this investigation and J. W. Rogers for analysis of the data and for the illustrations.

[5] A. C. Whiffin, Proc. Roy. Soc. (London) **194**, 300 (1948).

Emission from Hollow Cathodes

K. M. POOLE
Bell Telephone Laboratories, Inc., Murray Hill, New Jersey
(Received April 2, 1955)

The results of a phenomenological study of hollow cathodes are presented. Evidence has been accumulated to show that an oxide-coated hollow cathode has two regions of emission with significantly different properties. These are believed to be the coated inner surface of the cavity and a deposit of crystalline material formed on the orifice edge by evaporation from the original coating. Measurements of the relative importance of the two sources have been made under various conditions.

INTRODUCTION

WORK by several experimenters on internally coated cathodes has revealed major divergencies between the behavior of this and more conventional cathode forms.[1,2] Current densities ranging from 2 to 3 amp per square centimeter of orifice, at cathode temperatures below 800°C, to 25 to 100 amp/cm², at temperatures above 900°C, are frequently obtained. The anode current of a diode using a hollow cathode is not a simple function of the anode voltage; in particular it has been found to rise rapidly with voltage at the lower anode voltages and to be strongly temperature dependent. Attempts to locate the origin of electron emission by the use of plugs fitting into the cathode orifice or of constraining magnetic fields have led to widely differing results.

ANODE VOLTAGE: CURRENT RELATIONSHIP

In all experiments on diodes using hollow cathodes, the relationship between current and anode voltage has shown marked deviations from the three-halves power-law characteristic of more conventional cathode geometries. Figure 1 shows the variation of anode current with voltage in a diode using an oxide-coated hollow cathode. The cathode had a cavity diameter of 0.250 in., an orifice diameter of 0.020 in., orifice length of 0.005 in., and anode-cathode spacing of 0.030 in. The form of the higher temperature curves suggest the presence of two components in the anode current, one which rises very rapidly with voltage and saturates at 5 to 10 volts and another which rises slowly with voltage in this range but thereafter continues to rise. The saturable component seems more strongly temperature dependent than the other. Other tubes, differing both in their dimensions and cavity shapes, have shown similar effects.

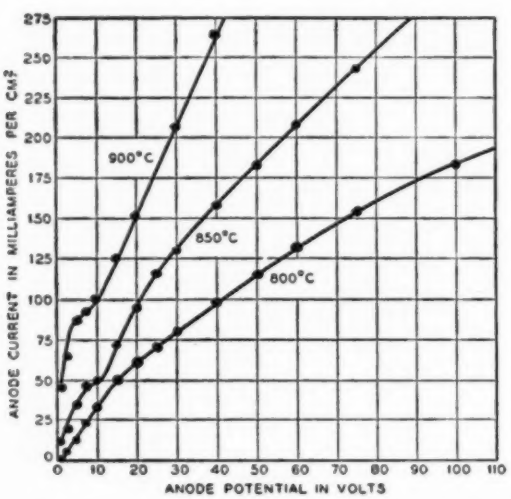

FIG. 1. Characteristic curves of an oxide-coated hollow cathode.

IMAGE TUBES

The possible presence of more than one component of emitted current emphasized the importance of locating the emitting regions. This was attempted in two tubes, each so designed that the plane containing the cathode orifice could be imaged by a simple electron optical system onto a fluorescent screen.

The first tube was built with a pure tantalum cathode, in which it could be assumed that the work function and emission constant were the same for all surfaces. Thus the effect of the cathode geometry could be studied. Figure 2(a) shows the form of the cathode and filament and Fig. 2(b) the electrode structure of this tube. The cathode is heated by electron bombardment from the tungsten filament and thermally insulated by a thin wall section as shown in Fig. 2(a). The electron optical system was designed to image the whole of the surface containing the orifice onto the fluorescent screen.

The image seen on this tube was a bright disk in a field of lesser illumination. From the relative sizes of the parts of the image, it was concluded that the bright disk was the image of the cathode orifice, being surrounded by a background formed by emission from the external surface of the cathode. The image of the orifice was brightest at the edges at low first-anode potentials and more uniform under high-accelerating fields.

A second image tube incorporated an oxide-coated hollow cathode; the electrode structure used is shown in Fig. 3 and was designed to give a rather higher

[1] Babcock, Holshouser, and VonFoerster, Phys. Rev. **91**, 755 (1953).
[2] Kumpfer and Brett, Institute of Radio Engineers Convention Record (1954).

magnification over a smaller field than that shown in Fig. 2(b). Figure 4 is a set of photographs of the image seen at constant cathode temperature and various first-anode voltages and Fig. 5 shows the image as seen at constant first anode voltage and various cathode temperatures. It can be seen that the outer ring in the image was present only at cathode temperatures above 750°C, the inner ring alone being observed at lower temperatures. The pattern of the outer ring did not vary; its brightness relative to that of the inner ring was greatest at high-cathode temperatures and low first-anode voltages. The inner ring was predominant under high accelerating fields. At very low first-anode voltages the inner ring in the image became a disk of illumination.

The invariance of the basic form of the pattern of the outer ring suggested that it was associated with some structural or chemical feature in the tube. The tube was opened and all electrodes examined. A rim of microcrystalline material, which was believed to be cathode coating, was found on the orifice edge. The thickness was irregular, having a variation around the orifice edge which would account for the form of the outer ring in Figs. 4 and 5 if it was assumed that the thickest part of the coating gave the greatest emission. The mean thickness was approximately 0.002 in. The technique used in coating the cathode left no material visible through the orifice from the outside of the cathode at the time the tube was assembled and, to minimize the conversion of the oxides in the cathode coating to the less-dense hydroxides on exposure to the atmosphere, the cathode was examined within a few minutes after opening the tube envelope. Examination of the other electrodes of the tube showed no features which could be related to the pattern of the outer ring of Figs. 4 and 5.

DEPOSIT ON ORIFICE EDGE

In spite of the precaution taken to minimize conversion of the cathode oxides to hydroxides, the possibility of some change in the disposition of the cathode material having occurred on opening the tube could not be denied. Therefore, a hollow-cathode diode was made having an aperture in its anode somewhat larger than the cathode orifice. This was mounted in a glass envelope incorporating a plane window, which permitted visual examination of the cathode orifice during the period of operation of the tube. No coating was visible before or after evacuating the tube or after activating the cathode. The tube was operated at a cathode temperature of 810°C and an anode potential of 90 volts (anode-cathode spacing was 0.050 in.). During the first 70 hours of operation the anode current rose from 170 to 250 milliamperes per square centimeter of cathode orifice, the window became appreciably darkened by deposition of material evaporated from the cathode through the anode aperture, and a white microcrystalline growth was formed on the orifice edge. Operation of the tube was continued under the same conditions to a total of 200 hours. The blackened window was cleared by heating and the cathode was photographed. Figure 6 shows the appearance of the cathode orifice at that time. No further increase in anode current occurred after the first 70 hours of operation though some increase in the deposit on the cathode lip was apparent.

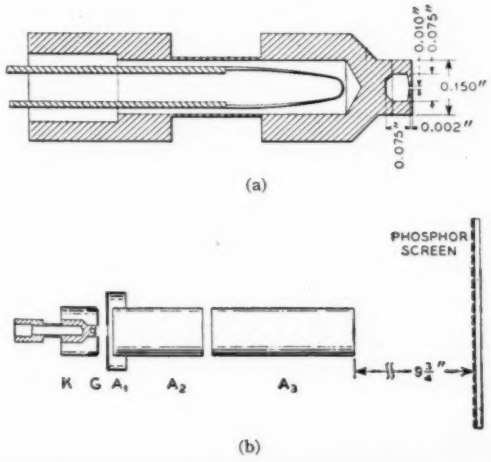

FIG. 2. Tantalum-cathode image tube. (a) Cathode and heater assembly. (b) Lens system.

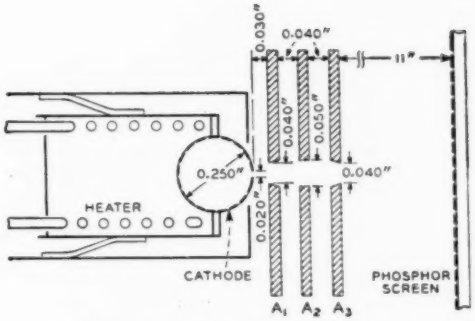

FIG. 3. Oxide-coated cathode image tube.

Presumably the microcrystalline deposit is a condensation of some material evaporated from the internal coating of the cavity, the temperature at the lip being lower than the other parts of the cathode. It seems certain that it is an active thermionic emitter and was responsible for the increase in current after initial activation. This experiment makes it evident that the formation of a thermionically active deposit on the orifice edge is to be expected in the operation of oxide-coated hollow cathodes. Hence, it is reasonable to conclude that the outer ring in Figs. 4 and 5 was indeed an image of the orifice deposit. Since the focusing was adjusted for maximum definition in this region of the image, the image was a representation of the current in the orifice plane and the inner ring observed was caused by current elements which were enclosed by the orifice edge at that plane. This ring was therefore due to emission from inside the cavity.

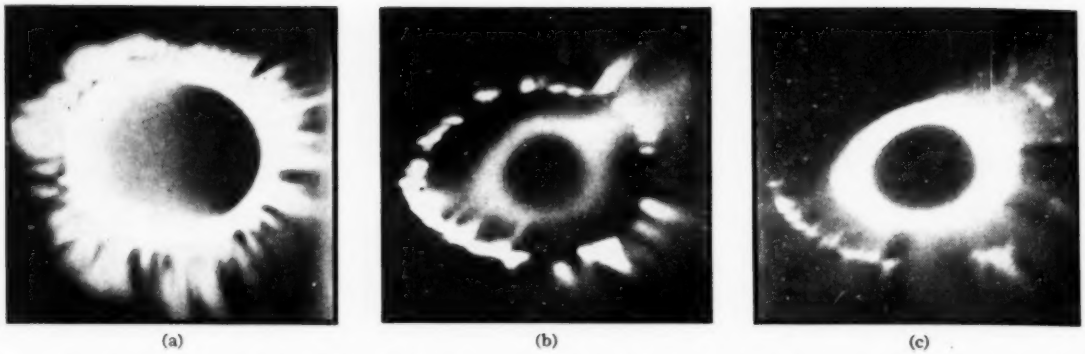

(a) (b) (c)

FIG. 4. Images from oxide-cathode image tube. Cathode temperature 800°C; second-anode potential 200 v (approximately); final-anode potential 950 v. (a) First-anode potential 23 v, (b) first-anode potential 170 v, (c) first-anode potential 450 v.

The evaporated rim forms a thin edge, giving local fields larger than would exist in a planar diode of comparable dimensions. Therefore, the current from this region should rise rapidly with anode voltage until saturation is reached. The variation of this saturation current with temperature will be determined by the balance between the rate of deposition of emitting material and deactivation phenomena. At higher anode voltages the current from inside the cavity should increase due to the increasing field penetration through the orifice. The configuration of a hollow cathode is such that extremely high anode voltages would be required to prevent the formation of a space charge minimum inside the cavity. Hence, for the range of voltages which have been used in the experiments, the current drawn from inside the cavity can be expected to increase continuously with anode voltage.

In conjunction with the results illustrated in Figs. 4 and 5, these conclusions suggest that the saturable component of anode current seen in Fig. 1 was the current from the orifice edge and that the nonsaturable component was from inside the cavity. A migrated layer was also visible around the orifice on the outer surface of the cathode of the oxide-cathode image tube, but no part of the image seen on its screen could be associated with this layer. This may be due to deactivation processes occurring at a rate greater than the rate of supply of material by migration.

EFFECT OF A MAGNETIC FIELD OR A PROBE

The curves plotted in Fig. 1 permit an estimate of the relative importance of the two sources of emitted current. The estimate requires the assumption that the current from the orifice edge saturates near the kink in those curves and remains constant at higher anode voltages.

To obtain a more quantitative idea of the ratio of the current from inside the cavity to that from the lip, two methods of discrimination were used. The application of an axial magnetic field to a diode incorporating a hollow cathode should reduce the current which can reach and pass through the orifice from within the cavity. To find the magnitude of the field required the tantalum hollow cathode image tube was mounted so that an axial magnetic field of several hundred gauss could be applied in the region of the cathode. The cathode could be focused onto the screen at any value of magnetic field. With this arrangement it was established that current from inside the cavity could be cut off by the application of a few hundred gauss. A field of 500 gauss was sufficient to reduce the brightness of the image of the orifice below the detectable limit. An oxide-coated hollow-cathode diode was then set up in a solenoid so that the anode current could be measured in the presence or absence of the magnetic field and over a range of anode voltages and cathode

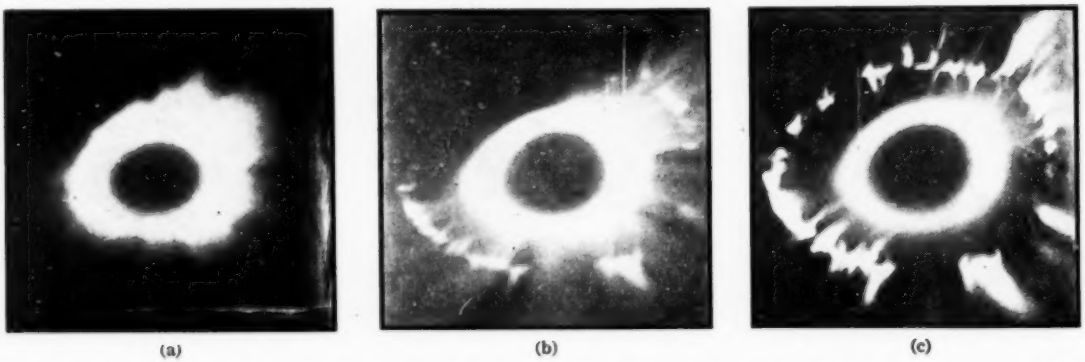

(a) (b) (c)

FIG. 5. Images from oxide-cathode image tube. First-anode potential 450 v, second-anode potential 200 v (approximately) final-anode potential 950 v. (a) Cathode temperature 725°C, (b) cathode temperature 800°C, (c) cathode temperature 875°C.

temperatures. The drop in anode current on applying an axial field, arbitrarily chosen to be 850 gauss, was taken to be the contribution of the cavity current to the total emission and the remaining current to be that from the orifice edge. In Fig. 7 the ratio of these currents is shown as a function of anode voltage and cathode temperature. The inset sketch shows the geometry of the tube.

Diodes were also built in which an insulated probe was mounted from the side of the cavity opposite the orifice, extending to the center of the cavity. The internal radius of the cavity was several times greater than the spacing between the anode and the cathode orifice. Hence, with the probe at cathode potential it collected only very small currents and both the cavity and edge currents were drawn to the anode. With a positive potential comparable to that of the anode, the probe collected the current emitted from the inside of the cavity, only the current from the orifice edge reaching the anode. This method of discriminating between cavity and lip currents gave results similar

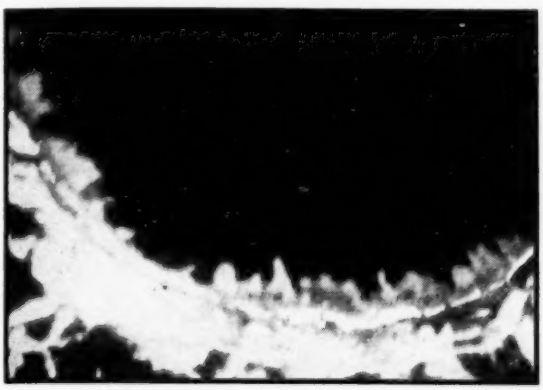

FIG. 6. Crystalline growth on rim of oxide-coated cathode.

to those obtained with a magnetic field. Measurements with partially poisoned hollow cathodes showed more complex variations of the cavity current to edge current ratio presumably connected with the different deactivation phenomena appertaining to the two regions.

CONCLUSIONS

We conclude that the major characteristics of operation of hollow cathodes follow from the presence of a component of emission from cathode material dispensed to the orifice lip and a second component drawn from

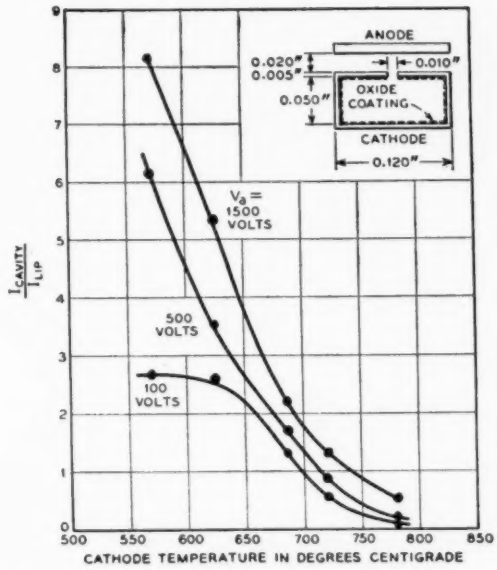

FIG. 7. Ratio of cavity current to lip current as function of anode potential and cathode temperature. Inset: Details of structure on which measurements were made.

the internal coating by penetration of an accelerating field into the cavity. At low-anode voltages the current from the orifice edge rises rapidly to its saturation level with increase of anode voltage, due to the concentration of field near the edge. Further increase in the anode voltage causes the inner surface of the cathode to become saturated over an increasing area around the orifice.

The electrons emitted from the orifice edge are likely to have a wide distribution of velocities transverse to the cathode axis and the necessary conditions for focusing the two components of current into a desired beam configuration will not, in general, coincide. It is possible to use an axial magnetic field to eliminate the cavity current.

ACKNOWLEDGMENTS

The author has discussed various topics covered in this paper with several members of the staff of the Electronics Department and the Chemical Electronics Research Department of Bell Telephone Laboratories and acknowledges the benefit thereby received. Particular acknowledgment is due D. MacNair, A. M. Clogston, C. C. Cutler, and J. R. Pierce. Experimental tubes were built by V. C. Wade and P. M. Ness; P. E. Butzien was responsible for many of the measurements.

Letters to the Editor

Sticking Potential of CRT Screens

K. H. JURGEN ROTTGARDT AND WOLFGANG BERTHOLD
Standard Laboratory, C. Lorenz AG, Stuttgart, Germany
(Received April 15, 1955)

P. H. DOWLING and J. R. Sewell[1] have described their investigations on a cause for the change of the sticking potential of luminescent screens by electron bombardment. Investigating continuously pumped tubes, the authors showed that a decrease of the sticking potential is effected by carbon layers on the surface of the phosphor. These carbon layers originate from organic vapors adsorbed on the screen which are decomposed by electrons. The effects of the organic vapor were more pronounced with steady state than with scanning excitation.

We have been able to show in a previous paper[2] that the decrease of the sticking potential is also caused by an impoverishment in releasable gas molecules of the luminescent screen, and that the sticking potential can be restored by adsorption of hydrogen on the screen.

The results described by Dowling and Sewell suggested the investigation of the influence of the pumps (mercury and oil diffusion pumps, respectively) used in the manufacture of tubes, upon the sticking potential of the screen in sealed-off television tubes. When conducting such experiments in which the screen was scanned through 625 lines, we found the sticking potential to be dependent on the electron-beam energy (see Fig. 1). The curve is plotted from measurement values obtained from several tubes evacuated by mercury diffusion pumps with cooling traps filled with a mixture of CO_2 foam and alcohol. The anode voltage and the beam current during the electron bombardment were different for different tubes (marked differently in Fig. 1). We found that the measured values obtained from a tube manufactured by means of an oil diffusion pump (type 120, make Geraetebauanstalt Balzers) are covered by the same curve. These values bear different marks in Fig. 1.

Further investigations revealed that the slope of the curve of the sticking potential, as a function of the beam energy was dependent on the initial value of the sticking potential. Whenever the initial value of the sticking potential was the same, the variation of its decrease was also the same, regardless of whether the tubes were made on mercury or on oil diffusion pumps.

Under certain conditions it is possible to prove the effect of organic vapors on the sticking potential of sealed-off television tubes. Using the same experimental setup as in earlier investigations,[2] we made a tube with a glass balloon attached to it. The balloon was vacuum heated at 400°C and subsequently filled with oil vapor and sealed off. The oil vapor came from the silicone oil contained in a small tube and heated. The balloon was isolated from the tube in the initial stage; otherwise the tube had been pumped by a mercury pump and baked and gettered in the usual way. When the bombardment by electrons with a current density of 0.7 $\mu a/cm^2$ (anode voltage 16 kv) had caused the sticking potential of the screen to decrease from 22 kv to 15 kv, the balloon was opened so the organic vapors could enter the tube. After flashing another getter, the pressure in the tube had risen—through the vapor taken in—to 17×10^{-6} mm of mercury. Figure 2 shows the result of the investigation. The solid curve represents the variation in the decrease of the sticking potential of a (ZnCd)S:Ag phosphor as obtained from screens under normal operating conditions with an initial sticking potential of 22 kv. The balloon containing the organic vapors had been opened after 65 hours of operation. It is seen that after the intake of organic vapors the sticking potential drops considerably when the screen is further bombarded by electrons.

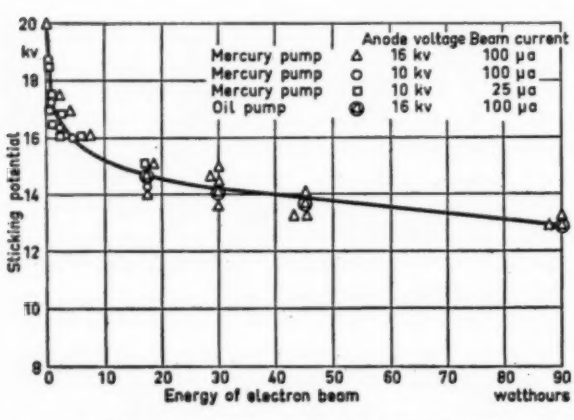

FIG. 1. Variation of the decrease of sticking potential under the effect of electron bombardment. Plotted measurements refer to tubes evacuated both by mercury and by oil diffusion pumps.

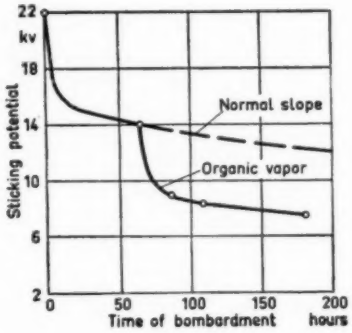

FIG. 2. Effect of organic vapors on the sticking potential of a (ZnCd)S:Ag screen.

In the normal manufacture of television tubes, then, the effect of organic vapor upon lowering the sticking potential is not noticeable, even when the tubes are pumped on oil pumps. Contrary to tubes operated on the pumps (particularly demountable tubes having opportunity to collect organic vapors over a long period of time), sealed-off tubes do not seem to get significant quantities of organic vapors during the pumping process. Another favorable factor in the case of television tubes is that the phosphor is excited by a scanning electron beam.

[1] P. H. Dowling and J. R. Sewell, J. Appl. Phys. **25**, 228–230 (1954).
[2] Rottgardt, Berthold, and Dietrich, Z. angew. Phys. **6**, 560–563 (1954).

Ferromagnetic Resonance in Magnesium-Manganese Aluminum Ferrite between 160 and 1900 Mc

H. SUHL, L. G. VAN UITERT, AND J. L. DAVIS
Bell Telephone Laboratories, Murray Hill, New Jersey
(Received June 2, 1955)

THE operation of microwave devices employing ferrites is closely related to the phenomenon of ferromagnetic resonance. Generally speaking, if a device is required to operate at a very low frequency, the ferrite it employs should be such that it can be made to resonate at a comparably low frequency. In polycrystalline materials of high saturation magnetization a low-frequency resonance is hard to realize, since the shape and/or crystalline anisotropy fields of the individual crystallites set a limit to the lowest attainable effective field for resonance.

This lower limit may be decreased by decreasing the magnetic saturation of the material or by employing oriented single crystals.[1] Previous work[2,3] had indicated that low saturation poly-

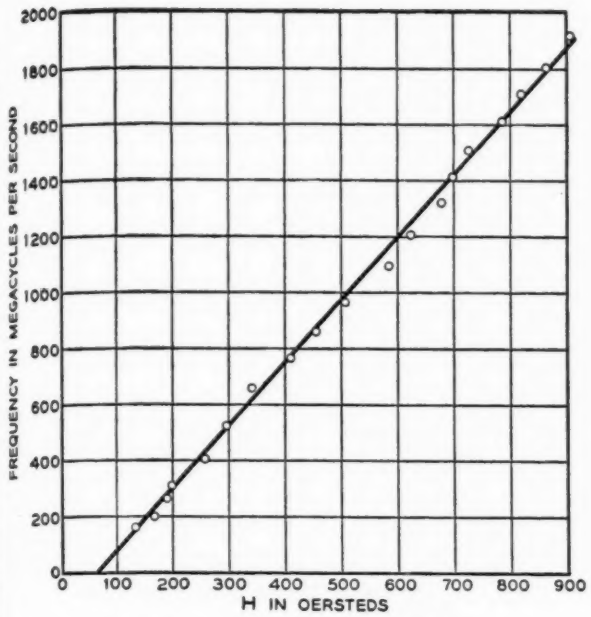

FIG. 1. Resonant frequency *versus* applied field.

crystalline ferrites suitable for microwave applications could be prepared in the magnesium manganese aluminum ferrite system. A series of compositions in this system was prepared. Of this, one sample containing the atomic ratios of metals Mg:Mn:Al:Fe =1.00:0.11:0.65:1.27 by analysis of the source powder previous to firing, was selected for study because it demonstrated the qualities requisite for obtaining a low ferromagnetic resonance frequency. These qualities are; low magnetic saturation, low coercive force, and nearly maximum density.

Preparation of the sample.—The source powder from which the ferrite sample was prepared was made by water mixing $MgCO_3$, $MnCO_3$, $Al(OH)_3$, and Fe_2O_3; calcining the mixture at 1000°C; water ball milling the resulting powder and repeating the calcination and ball milling steps. A binder was incorporated into the powder and a compact from which the final sample was to be formed and other test parts were pressed. These parts were fired at 1400°C for 48 hours in an oxygen atmosphere. Characteristic properties of the resulting sample at room temperature (76.2°F or 24.5°C) are as follows: Magnetic saturation $4\pi M=300$ gauss, coercive force=0.002 oersteds, density=4.14 grams/cm³, dc resistivity=10^{10} ohm-centimeter, low-frequency permeability=302 (measured at 0.1 Mc). The Curie temperature of the material is 30°C. Hence crystalline and magnetostrictive anisotropies are expected to be quite small in this sample at the measuring temperature. Evidence to support this is manifest in the extremely low coercive force found for this sample and the fact that a peak in μ_0 of over 660 is obtained by reducing the measuring temperature to 18°C.

Measurements and interpretation.—The sample was cut in the shape of a disk and magnetized normally to its plane. The reason for this choice of shape is the following: For a normally magnetized disk the field required to produce resonance at frequency ω is $H=(\omega/|\gamma|+4\pi M_0$, while for a sphere it is $H=\omega/|\gamma|$. Here M_0 is the saturation magnetization and γ the gyromagnetic ratio. It is desirable that the sample be fully saturated at resonance. Neglecting the polycrystalline character of the specimen, the normally magnetized disk should be saturated in a field $4\pi M_0$, while the sphere requires a field of $4\pi M_0/3$. Hence, no matter how small ω, the disk should always be saturated at resonance, while the sphere would be saturated only at frequencies above $(4\pi M_0/3)|\gamma|$, which in the present case is about 300 Mc/sec.

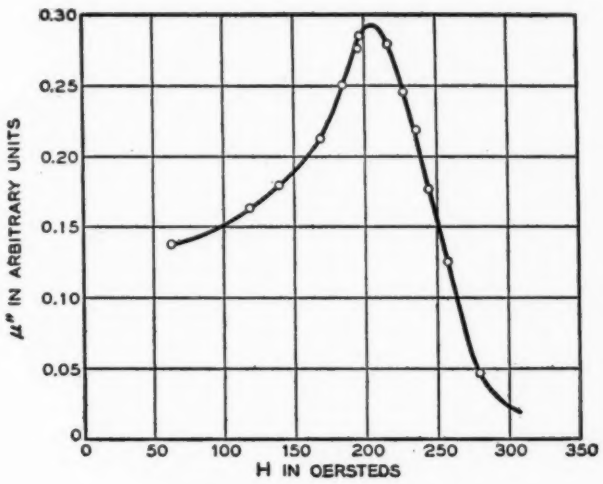

FIG. 2(a). Line profile at 843.64 Mc.

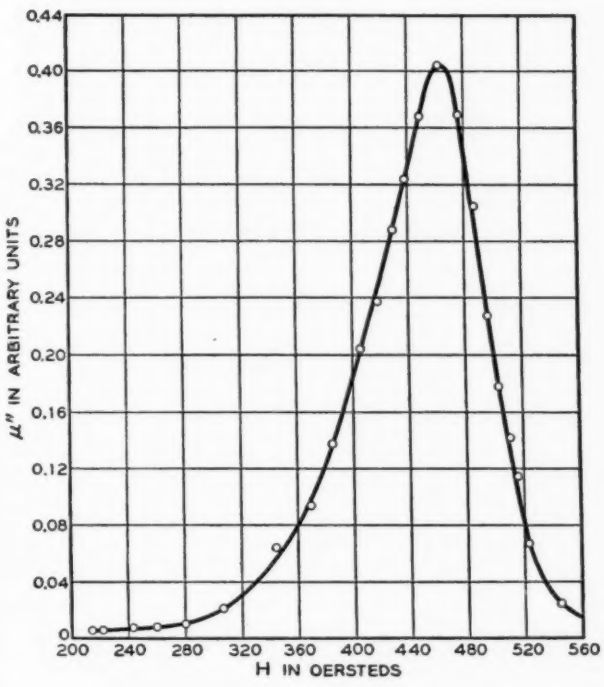

FIG. 2(b). Line profile at 310.00 Mc.

For a disk, this simple theory would predict a straight line for the frequency/field curve. This should intercept $\omega=0$ at $H=4\pi M_0$ =300 oe. The experimental curve shown in Fig. 1 however extrapolates to $\omega=0$ at a much lower value of H. The reason for this can be understood in terms of the incomplete saturation of the individual crystallites. Each of these has its own anisotropy axis, oriented at random to the direction of the applied field. The following drastically over-simplified picture shows qualitatively how this will cause the intercept to move from $4\pi M_0$ to zero: Let us define a mean magnetization $\bar{M}$ and a mean resonant frequency by the equation $|\gamma|(H-4\pi\bar{M})=\bar{\omega}$. When $H=0$, $\bar{M}=0$, so that $\bar{\omega}=0$. The resonance line is then very broad and the concept of a mean frequency not very significant. However, as H is increased some alignment of the crystallites takes place, and a sharper line begins to form. Suppose that each crystallite sees an effective field $H-4\pi\bar{M}$ and that it has uniaxial anisotropy, with axis inclined

at an angle φ to the direction of H. Suppose further that it is a single domain and let θ be the inclination of its M vector to H. Then its magnetic energy is

$$E=-(H-4\pi\bar{M})M_0\cos\theta-H_aM_0\cos^2(\theta-\varphi),$$

where H_a is some effective anisotropy field.

The direction θ is then determined from

$$\partial E/\partial\theta=0,$$

provided that $\partial^2E/\partial\theta^2>0$ at the same time.

Thus θ is the appropriate solution of the equation

$$(H-4\pi\bar{M})\sin\theta=H_a\sin2(\varphi-\theta).$$

When this equation is solved, the mean magnetization $\bar{M}$ can be found,

$$\bar{M}=\frac{M_0}{2}\int_0^\pi\cos\theta\sin\varphi d\varphi$$

$$=f(y,H_a),\text{ say,}$$

where $y=H-4\pi\bar{M}=H-4\pi f(y)$. The resonance condition can now be written in parametric form:

$$H=y+4\pi f(y,H_a),$$
$$\bar{\omega}=|\gamma|y.$$

The function f was determined by computation. The resulting $\bar{\omega}$ *vs* H curve begins at $\bar{\omega}=0$, $H=0$ and for large H approaches the asymptote $\omega=|\gamma|(H-4\pi M_0)$. For H up to a value of order a few times H_a the approach is rapid; the oversimplifications of the theory actually predict a discontinuous shift between certain values of H. Thereafter the approach is very gradual, the slope $d\omega/dH$ increasing slowly to its final value $|\gamma|$. These facts explain qualitatively why the g factor in Fig. 1 is only 1.58, while J. H. Rowen of these Laboratories found a g close to 2.1 at 10 kmc.

The line-profile was measured at two frequencies [Fig. 2(a) and (b)]. Particularly at the lower frequency, the line shows a marked asymmetry, being wider on the low-field side of resonance. This can be understood by noting that, at a sufficiently low frequency the individual crystallite can go through an additional resonance, and sometimes even through two additional resonances, as the field is increased from zero to the usual resonance value.[1] For a random distribution of crystallite axes, one will then find a general broadening of the resonance on the low-field side.

The large scatter in the data of Fig. 1 is partly caused by the proximity of the Curie point (the data were taken at about 24.5°C), and partly by the considerable line width.

[1] H. Suhl, Phys. Rev. 97, 555 (1955).
[2] F. F. Roberts, J. phys. radium 12, 301 (1951).
[3] Van Uitert, Schafer, and Hogan, J. Appl. Phys. 25, 925 (1954).

"Spiral Polygon" Tin Whiskers

PAUL W. LEVY AND OTTO F. KAMMERER*
Brookhaven National Laboratory, Upton, New York
(Received June 2, 1955)

RECENTLY Fisher, Darken, and Carroll[1] have shown that tin whiskers may be grown very rapidly from the edges of a stack of tin plate compressed in a clamp. We have used this technique to grow tin whiskers that are very similar to those obtained by these authors. Among these we find a number of whiskers that form "spiral polygons." Figure 1 shows a section of tin plate interface containing five of these spiral polygon whiskers in addition to the usual ones. The incidence of the polygons is low and it is unusual to find even two so close together. Altogether we have found 13 of these polygons lying close enough to the focal plane of the metallograph to permit sharp pictures to be taken and which contain at least four well-defined angles formed by the sides of the polygons. Only those angles were measured that are

FIG. 1. Tin whiskers growing from tin plate under compression. The wavy diagonal line from which the whiskers emerge is the plane of contact between two successive layers in a stack of plates. There are five spiral polygons in addition to more typical whiskers. Magnification approximately 80.

formed by straight sides that meet at a sharp corner. A considerable fraction of the observed angles are formed by sides that are curved and these have been excluded. Occasionally one finds that there are two distinct angles very close together. Thus, some of the angles near 60° may be two unresolved 30° bends. Figure 2 is a picture of the whisker containing the largest number of angles that we have found. From the 13 spirals containing at least four measurable angles the histogram in Fig. 3 has been constucted. It would appear that the significant concentrations of angles are in the region of 25°–35° (or twice these angles) and cluster at 27°, 29°, and 31°.

The growth of these whiskers and one spiral has been followed by time-lapse motion pictures. They clearly grow from the base and the bends appear to take place at the base. Also, bending takes place with the whisker projecting into space and not attached to other whiskers. Also, preliminary experiments indicate that there is no tin whisker growth at liquid nitrogen temperature.

An analysis of whiskers containing only one or two bends is yet to be made. However, one can speculate on the mechanisms responsible for the observed regularity in the spiral polygons. One immediately considers bending or kinking and both of these could result in a small range of angles. Assuming that the whiskers are crystalline twinning could be a conceivable mechanism. In tetragonal tin one expects twinning on the 101 and 301 planes, the latter being the observed twin plane for mechanical twinning.[2] Using these twin planes one can compute the angle defined in Fig. 3, and given in Table I, assuming that the whiskers grow along the

FIG. 2. The spiral polygon tin whisker containing the largest number of "bends" that we have observed. Magnification approximately 720.

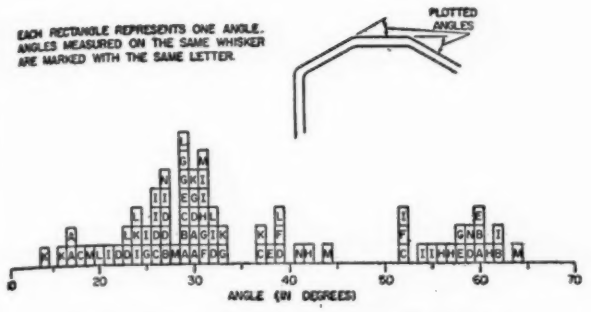

FIG. 3. Histogram indicating the frequency of observed angles in the spiral polygon tin whiskers.

indicated crystallographic directions. Considering that crystals usually grow in directions specified by low integer indices, and that the agreement between observed and calculated angles is good, it would appear that twinning could account for the angles in the region 25°–35°. The second, sixth, and last entries in Table I

TABLE I. Some twinning angles in tin.

Twin plane	Crystallographic direction of whisker axis on either side of twin plane	Calculated angle
(101)	[001], [100]	33°10′
	[102], [20$\bar{1}$]	28°40′
(301)	[100], [101]	34°52′
	[101], [104]	30°25′
	[103], [101]	33°20′
	[102], [201]	31°14′
	[001], [100]	26°43′

fit particularly well and the other possibilities may not occur. The other observed angle may arise from twinning on other than the indicated planes or twinning on the (101) and (301) planes but with different crystallographic directions along the whiskers. Also, the other angles may arise from additional mechanisms such as binding or kinking. X-ray determinations of the orientation on both sides of the "bend" would of course test this speculation. Similar spiral polygons have been found in indium whiskers grown by the same technique.

* Under the auspices of the U. S. Atomic Energy Commission.
[1] Fisher, Darken, and Carroll, Acta Metallurgica, 2, 368 (1954).
[2] E. O. Hall, *Twinning* (Butterworths Scientific Publications, London, 1954), p. 78.

Wattage Lost in a Fluorescent Lamp through Elastic Collisions

HOWARD L. STEELE, JR.
Research Department, Westinghouse Electric Corporation, Bloomfield, New Jersey
(Received May 23, 1955)

A FLUORESCENT lamp in normal operation contains mercury and argon at pressures of about 0.007 and 3.2 mm of mercury, respectively. The electron energy lost to argon atoms has been calculated[1,2] previously. One set of authors[1] used the measured[3] cross section for elastic collision, Q_R, rather than the cross section for momentum transfer, Q_d, for such a collision. The other set of authors[2] realized that Q_d should be used but obtained Q_d using an involved theoretical evaluation[4] of all existing Q_R data. Since the results[2] for helium using this method are in serious disagreement with latest microwave data[5] at low energies, their techniques must be questioned. Both sets of authors[1,2] were forced to use graphical integration to calculate the energy loss from graphs of the cross section. It will be demonstrated that for the case of argon atoms the Q_d data obtained graphically from Q_R

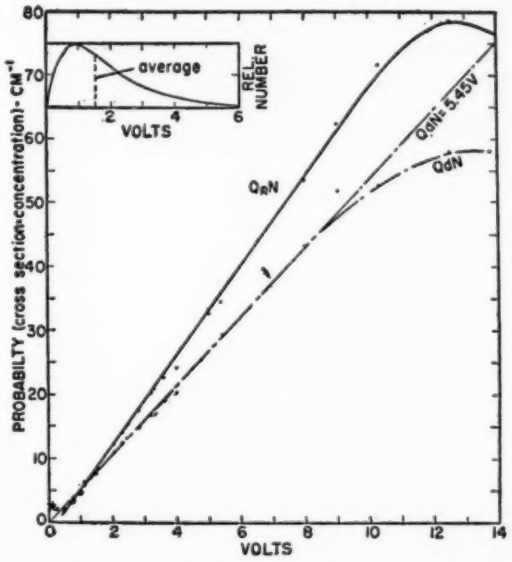

FIG. 1. Cross section for elastic collision of low-energy electron with argon atoms and cross section for momentum transfer in such a collision. Cross sections have been multiplied by density of argon atoms at 0°C and 1 mm mercury pressure. Points are taken directly from Barbiere's Table I (reference 6). Open circles are averages of Q_R data from Ramsauer and Kollath's first paper (reference 3). Star is microwave Q_d data of Phelps, Fundingsland, and Brown (reference 7). The electrons in a fluorescent lamp normally have a Maxwellian distribution of energy with an average energy of 1.5 volts. This distribution is plotted in the upper left-hand corner.

measurements is reasonably consistant with microwave data. Furthermore, the Q_d values so obtained increase linearly with electron energy for the range of energies found in a fluorescent lamp so that an explicit formula for the energy lost to argon atoms can be presented. The relationship has been very useful in energy balance considerations.

Figure 1 has Q_R multiplied by the atomic density, N, at 0°C and 1 mm pressure. These are values of Q_R averaged over all angles. The differential cross section, $qR(\theta,u)$, the value at a given angle, is known to vary as a function of the angle θ to which the electron is deflected and the electron energy u, as shown in Fig. 2. The function that correctly describes the momentum transfer over all angles is $(1-\cos\theta)$ so that

$$q_d(\theta,u)=q_R(\theta,u)(1-\cos\theta).$$

Using this relationship the Q_d must be calculated by integrating over all angles,

$$Q_d(u)=2\pi N\int_0^\pi q_R(\theta,u)\sin\theta(1-\cos\theta)d\theta. \quad (1)$$

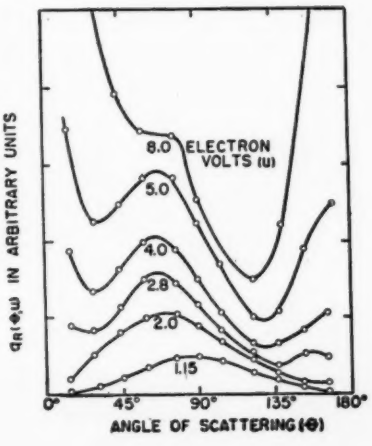

FIG. 2. Differential cross section $q_R(\theta,u)$ as a function of angle (θ) through which the electrons are deflected and the electron energy (u) in electron volts [C. Ramsauer and R. Kollath, Ann. Physik Leipzig 12, 529 (1932)].

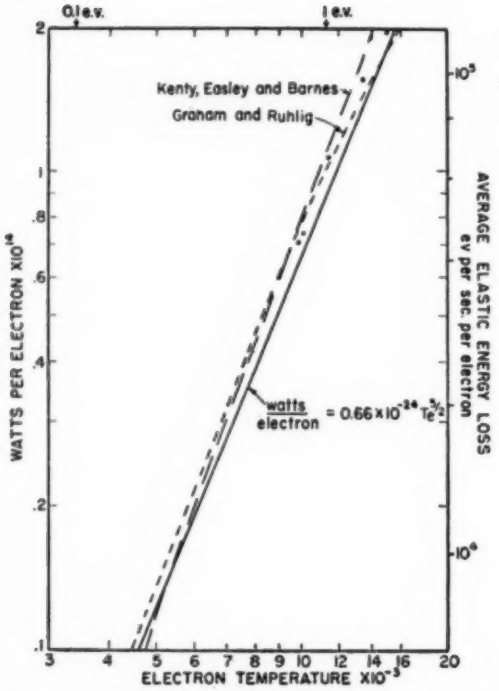
0.1 e.v.
1 e.v.
Kenty, Easley and Barnes
Graham and Ruhlig
watts/electron = 0.66 x 10^-24 Te^3/2
WATTS PER ELECTRON X10^24
AVERAGE ELASTIC ENERGY LOSS ev per sec per electron
ELECTRON TEMPERATURE X10^-3

FIG. 3. Comparison of explicit relation (3) with graphical results of references 1 and 2. Points are experimental measurements from reference 1. All data are for an argon pressure of 1 mm of mercury at 0°C.

Barbiere[6] evaluated this integral graphically. The results are also plotted in Fig. 1. The Q_d determined by recent microwave measurements[7] is indicated by a star.

Langmuir probe measurements[8] show that the electrons in a fluorescent lamp have, to a very good approximation, a Maxwellian distribution with an average energy of about 1.5 volts. This means a distribution about as noted in the upper left-hand corner of Fig. 1. The average energy lost by an electron per collision, $(2m/M)(1/2\ mv^2)$, is small but the collision rate, vNQ_d, is high. In both cases v is the electron velocity and m and M are the electronic and argon masses. The product of energy lost and collision rate must be averaged over all velocities of the Maxwellian distribution $f(v)$.

$$\text{Average energy lost/electron/sec} = \frac{m^2}{M}\int_0^\infty v^3 N Q_d(v) f(v)\,dv. \qquad (2)$$

Since NQ_d is a linear function of v, Eq. (2) can be easily integrated if written in terms of dv^2 or du.

$$\text{Average energy lost/electron/sec} = 0.66\times10^{-24} Te^{5/2}\text{watts/electron}, \qquad (3)$$

where Te is the electron temperature in degrees Kelvin. Under normal operation Te is about 11 000°K (average energy 1.5 volts). Because of the way density, N, was defined above, Eq. (3) should be multiplied by the ratio of the argon density at a pressure of 1 mm of mercury and 0°C to the argon density at the time the lamp was filled. Under the conditions specified in the first sentence this factor will be about 2.9.

If the fact that argon atoms are in motion is introduced, the average energy lost per collision is less[9] and another integral must be subtracted from (2). The result is that (3) must be multiplied by $(1\text{-}2/3\ Tg/Te)$. Tg is the gas temperature in degrees Kelvin. Te is about 30 times Tg in a fluorescent lamp. Thus the correction to (3) would be appreciable only in high pressure argon discharges where the argon atoms are more nearly in equilibrium with the electrons.

A comparison of Eq. (3) with the graphical results of other authors is given in Fig. 3. Five experimental points[1] are shown as dots. They were calculated from observations of the change in argon pressure when a lamp was turned on, such change in pressure being due mainly to this heating of the argon through inelastic collisions. The points are in surprisingly good agreement with all three curves.

Using electron densities measured by cylindrical Langmuir probes, and Q_R it was found[1] that in 40 w fluorescent lamps about 8.5 w are expended in heating argon. Recalculation of this loss using Eq. (3) and the same electron densities yields a value 18% less than this, or about 7 w.

[1] Kenty, Easley, and Barnes, J. Appl. Phys. **22**, 1006 (1951).
[2] J. Graham and A. J. Ruhlig, Phys. Rev. **94**, 25 (1954).
[3] C. Ramsauer and R. Kollath, Ann. Physik Leipzig **3**, 536 (1929); **12**, 529, 837 (1932).
[4] S. Westin, Kgl. Norske. Videnskab. Selskabs Forh. No. 2 (1946).
[5] L. Gould and S. C. Brown, Phys. Rev. **95**, 897 (1954).
[6] D. Barbiere, Phys. Rev. **84**, 653 (1951).
[7] Phelps, Fundlingsland, and Brown, Phys. Rev. **84**, 559 (1951).
[8] M. A. Easley, J. Appl. Phys. **22**, 590 (1951) and our own experience with planar probes.
[9] J. M. Benade and K. T. Compton, Phys. Rev. **22**, 333 (1923).

Theory of New Ferrite Modes in Rectangular Wave Guide*

BENJAMIN LAX AND KENNETH J. BUTTON
Lincoln Laboratory, Massachusetts Institute of Technology, Lexington, Massachusetts
(Received May 11, 1955)

THE problem of propagation in rectangular wave guide containing one or two transversely magnetized ferrite slabs against the side walls is of practical importance in a number of devices.[1] An exact theory and a method for obtaining numerical solutions has been developed.

The case of twin slabs against the guide walls is shown in Fig. 1. The analysis resembles that of the nonreciprocal phase shifter.[2] The rf electric field for the fundamental TE mode is given by

$$\begin{aligned} E_z &= (A\ \sinh K_m x)\ \exp(-j\beta y) && \text{Region 1,} \\ E_z &= [B\ \sinh K_m(L-x)]\ \exp(-j\beta y) && \text{Region 2,} \\ E_z &= [C\ \cos k_a x + D\ \sin k_a x]\ \exp(-j\beta y) && \text{Region 3,} \end{aligned} \qquad (1)$$

where $k_m = jK_m$ and other symbols are defined in reference 2. By matching E_z and h_y at appropriate boundaries, a transcendental equation in β is obtained. This is solved for the width of the guide,

$$L = 2\delta + \frac{1}{k_a}\tan^{-1}\left(\frac{p}{q}\right), \qquad (2)$$

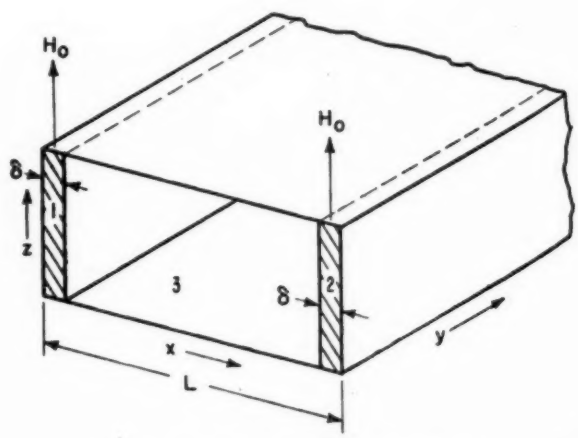

FIG. 1. Twin ferrite slabs at the side walls of a rectangular wave guide.

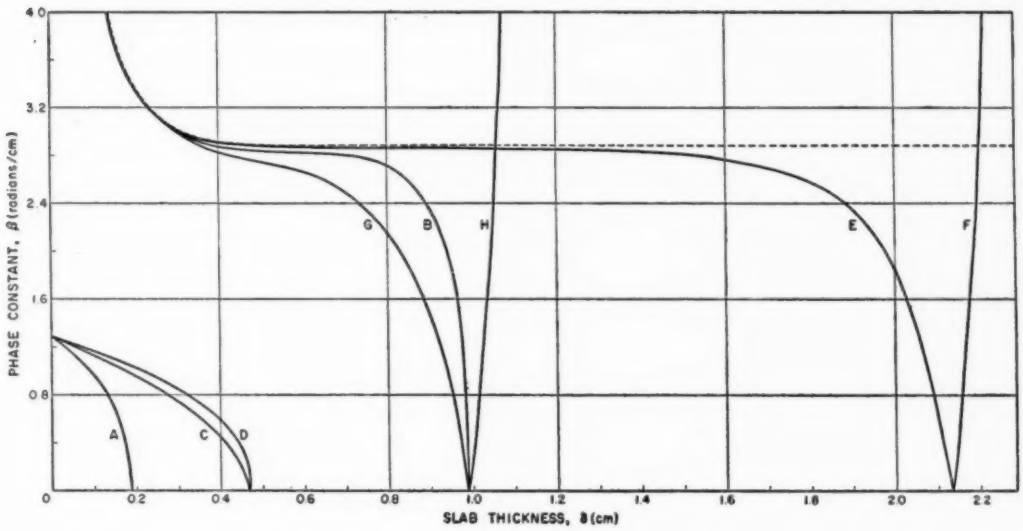

FIG. 2. Propagation constant of lossless ferrite modes in rectangular wave guide at 9000 Mcps as a function of ferrite slab thickness.

where

$$p=\frac{2K_m}{k_a}\cosh K_m\delta\,\sinh K_m\delta,$$

$$q=\left(1-\frac{B^2G^2}{k_a{}^2}\right)\sinh^2 K_m\delta-\frac{\rho^2k_m{}^2}{k_a{}^2}\cosh^2 K_m\delta,$$

and $G=\rho\chi_{xy}/1+\chi_{xx}$. Suitable values of β are chosen for a given δ until Eq. (2) yields a guide width L, corresponding to standard 9000 Mcps wave guide. A dielectric permittivity of $10\epsilon_0$ was used and the ferrite susceptibilities have been evaluated for an applied field of 1000 oersteds and a magnetization of 3000 gauss. The results are shown in Fig. 2. The phase constant for the fundamental mode as a function of δ is shown by curve A. This mode is cut off at $\delta=0.188$ cm. Another mode, not associated with a normal wave-guide mode, also propagates at a large value of β, as shown by curve B. Since Eq. (2) has no term linear in β, both of these modes are reciprocal.

The second and closely related problem is that of a single slab against a side wall. Using a similar analysis, the transcendental equation admits the solution

$$L=\delta+\frac{1}{k_a}\tan^{-1}\left(\frac{-k_a/\rho}{j\beta/\theta+k_m\cot k_m\delta}\right), \tag{3}$$

where $\theta=\rho/G$. All modes associated with this equation are nonreciprocal. Equation (3) is also applicable to twin slabs magnetized in opposite directions. Here L must be chosen as half the wave-guide width.[2] The propagation of the ferrite mode is shown by curve G for the forward direction and H for the reverse direction. The nonreciprocal fundamental mode associated with oppositely magnetized twin slabs has the same cut-off point as curve A but these two curves are not shown in Fig. 2.

For the single slab, Eq. (3) yields a nonreciprocal wave-guide mode.[2] Corresponding β's are shown by curves C and D with cutoff at $\delta=0.47$ cm. Again a ferrite mode propagates for larger β. The curves for forward and reverse propagation are given by E and F.

The ferrite modes for large β can be understood by considering a semi-infinite ferrite slab backed by a conductor as in Fig. 3. Solving for δ gives

$$\delta=\frac{1}{K_m}\tanh^{-1}\left(\frac{jK_m\rho}{\beta G-k_a}\right).$$

The forward direction yields a mode guided by the ferrite. The dashed line of Fig. 2 shows the propagation characteristic. Apparently these are "ferrite dielectric" modes analagous to dielectric propagation discussed by Schelkunoff.[3] However for the opposite direction of propagation, the mode is not guided for this choice of parameters.

Dimensional effects observed in wave guides and cavities can be studied by the analysis discussed here and some are probably associated with such ferrite dielectric modes. The presence of extra resonance peaks could perhaps be accounted for if the loss is included in the susceptibilities. The solution under such circumstances appears formidable.

We are indebted to Dr. G. S. Heller of Lincoln Laboratory for his criticism of this work and his helpful suggestions.

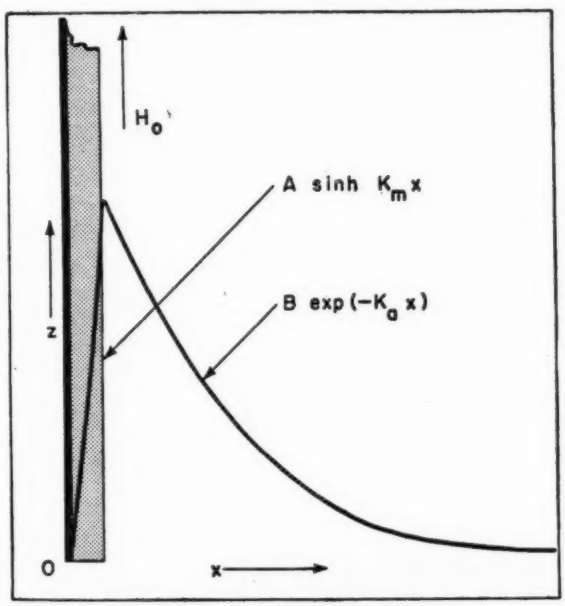

FIG. 3. Semi-infinite ferrite slab backed by a conducting plate. The electric field for the unidirectional guided mode is shown.

* The research reported in this document was supported jointly by the United States Army, Navy, and Air Force, under contract with Massachusetts Institute of Technology.

[1] Fox, Miller, and Weiss, Bur. Standards Tech. J. 34, 5 (1955).
[2] Lax, Button, and Roth, J. Appl. Phys. 25, 1413 (1954).
[3] S. A. Schelkunoff, *Electromagnetic Waves* (D. Van Nostrand Company, Inc., New York, 1943), p. 428.

New Ferrite Mode Configurations and Their Applications*

BENJAMIN LAX AND KENNETH J. BUTTON
Lincoln Laboratory, Massachusetts Institute of Technology, Lexington, Massachusetts
(Received May 11, 1955)

THE mathematical solution of propagation in rectangular wave guide containing one or two slabs against the walls has been discussed.[1] The rf electric and magnetic field configurations are also obtainable from this analysis and are helpful in interpreting the modes and in explaining related devices.[2] The method of deriving the expressions for the fields is similar to that developed for the nonreciprocal phase shifter.[3]

Figure 1 shows the mode configurations of the electric fields corresponding to each of the solutions in reference 1. The fundamental wave-guide mode is modified by twin slabs as shown by mode A. The ferrite dielectric mode B also propagates simultaneously. Mode B is reciprocal except that the direction of propagation determines which slab shall "guide" the wave as shown by the dotted line. The situation for the single slab case is similar in many respects except that the fundamental mode is nonreciprocal[3] as shown by C and D. The ferrite dielectric mode E is nonreciprocal and unidirectional. Reverse propagation is in mode F. For twin slabs magnetized oppositely, the electric field has a node at the center. The forward and reverse patterns are shown by G and H for appropriate slab thicknesses.

Figure 2 shows the magnetic field components of the ferrite mode B. The longitudinal component h_y is of particular importance for devices operating in the new modes.

For optimum operation, the twin slab resistance sheet isolator[2] requires propagation in mode B with mode A cut off. A resistance sheet placed against the left slab will cause attenuation because of the peaked electric intensity of mode B. The absorption in the reverse direction will be very small because the peak electric intensity of mode B will be near the right-hand slab and the electric field will be small at the resistance sheet.

The single-slab resistance sheet isolator[2] may propagate in modes C, D, and E. If the design is such that a substantial portion of the energy propagates in mode E, a resistance sheet placed against the slab will cause attenuation as in the previous case. Propagation in the reverse direction is in mode D resulting in less attenuation if the lossy material is near the electric node of mode D.

It is possible to choose the ferrite thickness from a wide range of values where modes C and D are cut off and propagation is exclusively in mode E which is unidirectional. These theoretical results indicate the possibility of one-way propagation without the use of a resistance sheet. However, on the assumption that this is a two-part device, thermodynamic arguments can be advanced which indicate that such a device cannot exist for a lossless idealized system. Further investigations will be made to resolve this apparent paradox.

The twin-slab three and four terminal circulator or slotted-wall isolator[2] requires propagation in mode B with mode A cut off. Figure 2 shows the longitudinal magnetic component for mode B. Placing the longitudinal slot near the left slab, appreciable coupling through the slot will occur for forward propagation since

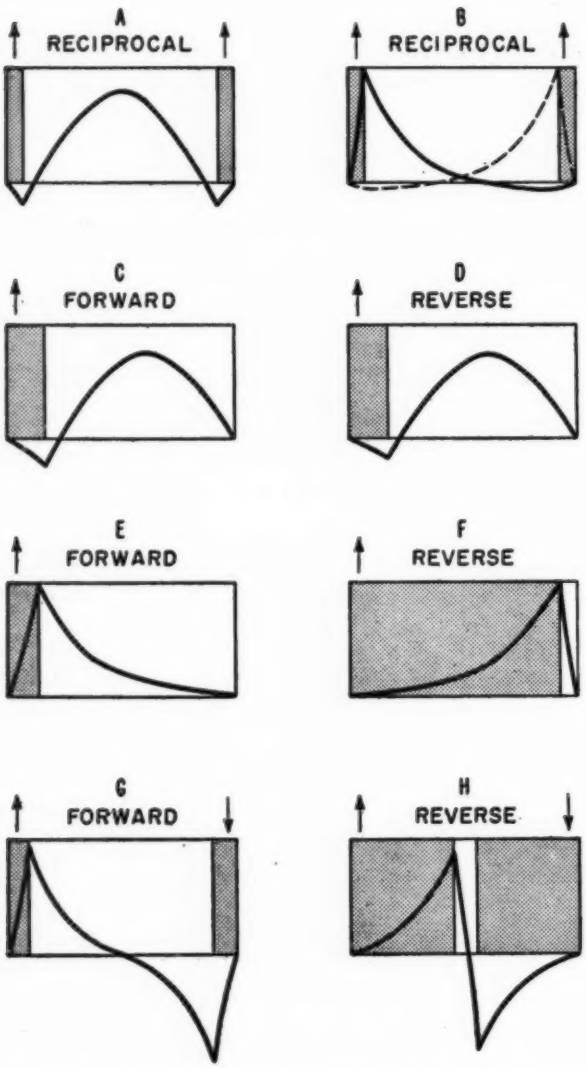

FIG. 1. The electric field patterns for ferrite modes in rectangular wave guide. Direction of magnetization is indicated by the arrows. Slab thicknesses shown correspond to real values of β.

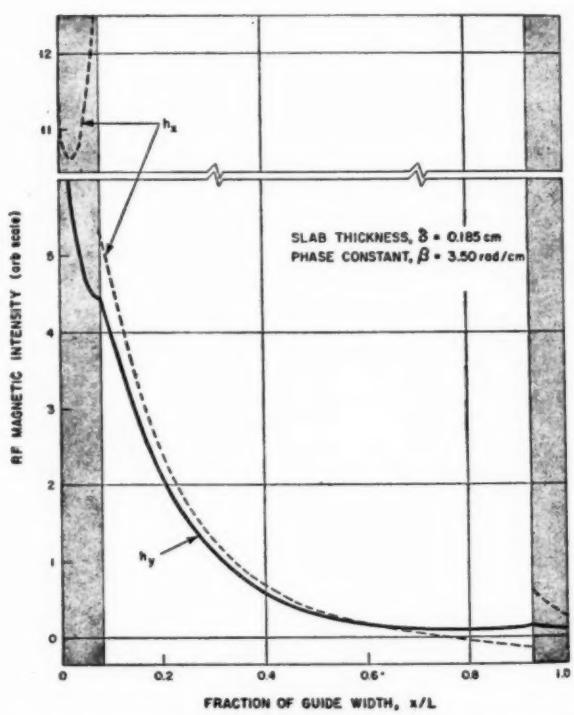

FIG. 2. rf magnetic field components of ferrite mode B for forward propagation. Peak intensities will appear on the right for reverse propagation.

h_y is large on the left. If only mode B propagates in the reverse direction, h_y is very small at the slot.

Frequency dependence within several bands is being investigated. Changes in applied field will include the region above ferromagnetic resonance for the design of low-frequency devices. The unidirectional modes and cut-off conditions suggest possibilities for circulators, filters, and radiation and switching devices. For such devices, two unlike slabs may be advantageous and, in principle, the analysis used here should apply.

* The research reported in this document was supported jointly by the Army, the Navy, and the Air Force, under contract with Massachusetts Institute of Technology.

[1] B. Lax and K. J. Button, J. Appl. Phys. **26**, 1184 (1955), preceding letter.
[2] Fox, Miller, and Weiss, Bell System Tech. J. **34**, 5 (1955).
[3] Lax, Button, and Roth, J. Appl. Phys. **25**, 1413 (1954).

Properties of Pore Conductors

RALPH FORMAN
National Bureau of Standards, Washington, D. C.
(Received May 25, 1955)

THE author has previously reported anomalous properties in oxide cathodes[1] (barium-strontium oxides), such as high values of electron mobility and large magnetoresistive effects. These phenomena have been interpreted by means of a pore conduction model.[2] These results prompted the belief that other materials having a similar anomalous behavior could be found and classified as porous conductors.

This has been tried for thoria having a porous structure at high temperatures, and the results are illustrated in Fig. 1. A thoria cylinder, approximately 70% of true density, was fabricated with platinum leads imbedded at both ends. A schematic diagram indicates the thoria tube used to make the measurements. Current which passed through leads 3 and 4 heated a tungsten filament adjacent to the thoria cylinder. The temperature of the thoria cylinder was then increased until its conductance was sufficiently high so that it could be heated directly by passing current through it. When this state was reached, the current through the tungsten heater was cut off, and the temperature of the thoria was maintained at a desired value by its own conduction current. At approximately 1500° to 1600°C, large transverse magnetoresistive effects, at comparatively low-field strengths, were found as is illustrated in Fig. 1. Another consequence of the magnetoresistive effect was a change in temperature of the specimen; this effect was avoided by adjusting the input power to the sample. No magnetoresistive effects could be detected below about 1400°C, but above this temperature the magnetoresistive curves, labeled T_1 and T_2, were obtained.

Figure 2 shows a tube which was originally constructed to study magnetoresistive effects on the oxide cathode. It was found that the resistance of the oxide cathode coating in this tube could be changed by an electrostatic field. This suggested a different type electronic amplifier the principle of which is illustrated in

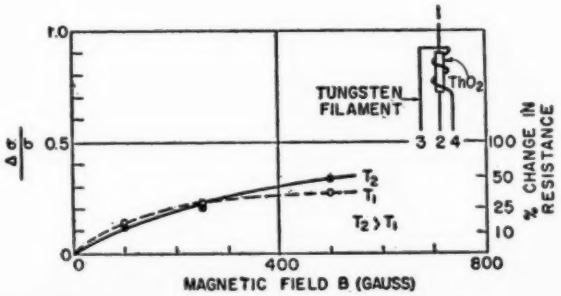

FIG. 1. Magnetoresistive properties of thoria at high temperatures.

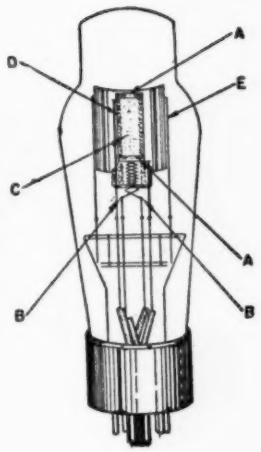

FIG. 2. Vacuum tube employing the oxide cathode as a pore conducting element. *D* denotes a slip cast MgO base having the form as shown. *B* describes a heater winding which fits inside the MgO base *D*. *A* denotes two metal ceramic brazes to the MgO, and metallic contact is made to the stem leads by platinum wires. The surrounding cylinder *E*, shown in cross section, is a heat shield and control element. If the MgO base is heated to approximately 1000°K, the oxide coating *C* can be used as a porous conducting resistor by applying a voltage across the metallic contacts *A*.

Fig. 3. The shaded element in the circuit diagram is the oxide cathode coating. If a variable retarding field voltage, E_c, is applied to an adjacent metallic element used as a control electrode (e.g., *E* in Fig. 2) the current, I_p, can be varied at a given fixed voltage, E_p. Since E_c is a retarding voltage, it draws no appreciable current and significant power gains can be obtained from the device. Some characteristic curves are plotted in Fig. 3 to show their similarity to the characteristic curves of conventional triodes.

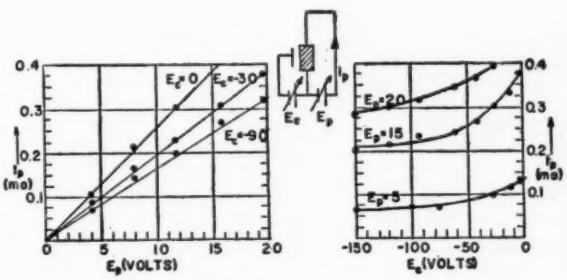

FIG. 3. Circuit and characteristic curves for electrostatic amplifier employing a porous conductor.

In principle, the output impedance of this amplifier could be varied by varying the dimensions of the pore conducting body (e.g., oxide cathode coating), and this might result in useful low impedance devices.

[1] R. Forman, Phys. Rev. **96**, 1479 (1954).
[2] R. Loosjes and H. J. Vink, Philips Research Repts. **4**, 449 (1949).

Errata: Experimental and Theoretical Aspects of Shock-Wave Attenuation

[J. Appl. Phys. **26**, 113–120 (1955)]
IRVINE I. GLASS AND WALTER A. MARTIN
Institute of Aerophysics, University of Toronto, Toronto, Canada

REFERENCE 10 should read: R. K. Lobb, "A study of supersonic flows in a shock tube," Institute of Aerophysics, University of Toronto, UTIA Report No. 8 (1950).

Reference 16 should read: R. J. Emrich and C. W. Curtis, J. Appl. Phys. 24, 360 (1953).

Page 119, third line, paragraph 2: References 9–13 should read 9, 11, 12, 13, and 16.

Page 120, end of Sec. 6: References 1, 15, and 16 should read 1, 14, and 15.

Neutron Irradiation Effects Upon Young's Modulus and Internal Friction of Copper

D. O. Thompson, D. K. Holmes, and T. H. Blewitt
Oak Ridge National Laboratory, Oak Ridge, Tennessee
(Received June 6, 1955)

THE adiabatic Young's modulus and the internal friction of a set of eight copper single crystals of 99.999% purity have been measured, both before and after a series of neutron irradiations. In several cases two or more crystals of the same orientation were grown simultaneously by the Bridgman method from the same melt. Measurements were made by means of a resonant bar technique. Within the range of flux values employed to date, the irradiation has produced, without exception, increases in the modulus and decreases in the internal friction. Data for the eight crystals are given in Table I.

In this Table the numeral in the crystal designation refers to the melt number, and the letter refers to a particular crystal in the subsequent growth. Thus crystals with the same number and different letter designations were of the same orientation, while crystals with different numbers had different orientations. f is the approximate resonant frequency of the crystal in kilocycles per second, E_0 and Δ_0 are the Young's modulus and logarithmic decrement, respectively, before irradiation, E_f and Δ_f are the final values after irradiation. The values of flux given are not necessarily the smallest values which would have produced the observed changes in the modulus and decrement; rather, they are the flux values after which the first irradiation data were obtained. The modulus and decrement showed no further changes, outside of experimental error, during repeated bombardments up to a total integrated flux of 15×10^{17} nvt (integrated flux) for crystal 1 and 10×10^{17} for crystals $2A$, $2C$, and $3A$. Considering remounting techniques and all associated handling, the experimental error in the modulus measurements is quite liberally placed at $\pm0.1\%$, while the repeatability of the decrement measurements upon removal of the crystal from the apparatus and remounting leads to a spread of not more than $\pm25\%$.

The simplest interpretation of the results to date seems to be in a dislocation model. Eshelby[1] has noted that the presence of dislocations would lower the apparent, or measured, elastic moduli because of a plastic contribution to the strain; the internal friction would be correspondingly larger. The present results indicate that the motion of the dislocation lines is impeded by the presence of interstitials and vacancies, which may act much as an "atmosphere" of impurity atoms in pinning down the lines. This analogy has in fact been noted before in other irradiation experiments at this laboratory but usually at much larger flux values. A similar interpretation has been given by Koehler[2] to experiments on the annealing of copper crystals in hydrogen atmospheres which show, qualitatively at least, effects similar to those observed under neutron bombardment.

The data to date indicate quite conclusively that the effects being observed are too large to be accounted for as a direct effect of the presence of displaced atoms, and hence the calculations of Dienes[3,4] do not apply. Instead, they are in at least qualitative agreement with a dislocation mechanism. One of the most striking features of the work is the relatively small total flux that is required to produce changes compared to the flux required in other physical properties. Greater bombardments than those so far carried out may reveal further changes in the modulus and decrement as damage to the lattice itself becomes more important.

[1] J. C. Eshelby, Proc. Roy. Soc. (London) **A197**, 396 (1949).
[2] J. S. Koehler, *Imperfections in Nearly Perfect Crystals* (edited by W. Shockley, John Wiley and Sons, Inc., New York, 1952), p. 197.
[3] G. J. Dienes, Phys. Rev. **86**, 228 (1952).
[4] G. J. Dienes, Phys. Rev. **87**, 666 (1952).

Rate-Grown Germanium Crystals for High-Frequency Transistors

H. E. Bridgers and E. D. Kolb
Bell Telephone Laboratories, Murray Hill, New Jersey
(Received June 6, 1955)

THIS report describes the production of germanium n–p–n crystals for the fabrication of experimental high-frequency tetrode transistors[1] which have oscillated at frequencies above 1000 Mc. The performance of earlier rate-grown tetrodes indicated that a reduction in base-layer resistivity without increasing its width (0.1–0.3 mil) was desirable. One way in which this could be accomplished was to employ the rate-growing technique[2] using boron as the acceptor impurity.

The advantages of boron as an impurity for rate-growing are easily recognizable from the Burton-Prim-Slichter[3] expression for the effective segregation coefficient of an impurity. Unlike that of all other acceptors and donors in germanium, the segregation coefficient of boron is greater than unity, and, therefore, decreases with increasing growth-rate. In addition, the fractional change of segregation coefficient with growth-rate is larger in absolute magnitude for segregation coefficients greater than unity, particularly at low growth-rates.

Difficulty is usually encountered in "doping" germanium with boron because of the formation of an oxide from traces of oxidizing agents present in the crystal growing machine. We have doped germanium with boron in a vacuum crystal-grower designed by F. G. Buhrendorf, and then regrown such crystals several times without loss of boron. The segregation coefficient of boron in germanium has been measured as a function of growth-rate,[4] and its behavior is as predicted by theory.

From a melt doped with boron and antimony, n–p–n structures were formed periodically by rate-growing. Following the growth of an n-type region, the direction of pull was reversed and the temperature increased. A steady meltback occurred, and this was abruptly interrupted by return to the original pull-rate and temperature. The doping was so adjusted that p-type material was grown at growth-rates near zero. Thus a thin p-layer was formed during the transient growth period from a steady meltback to steady growth. This growth cycle was repeated about 10 times in a given crystal.

As the melt is consumed by crystallization, it is rapidly depleted of boron and concentrated in antimony. The "doping" can be so adjusted, that during growth of the crystal, the melt becomes so

Table I. Young's modulus and logarithmic decrement before and after irradiation.

Crystal	f(kc/sec)	$E_f\left(\frac{\text{dynes}}{\text{cm}^2}\right)$	$E_f\left(\frac{\text{dynes}}{\text{cm}^2}\right)$	Δ_0	Δ_f	Integrated flux (nvt)	$\frac{E_f-E_0}{E_0}$(%)
1	17.5	1.227×10^{12}	1.344×10^{12}	24.8×10^{-3}	0.7×10^{-3}	5×10^{17}	+9.55
2A	14.7	1.008	1.023	2.2	0.4[5]	5×10^{17}	+1.49
2B	14.6	1.013	1.028	5.5	1.0	3.1×10^{15}	+1.48
2C	33.6	1.021	1.032[5]	2.5	1.2	5×10^{17}	+1.13
3A	15.9	1.460	1.472	3.6	0.4[5]	5×10^{17}	+0.82
3B	15.9	1.474	1.477	1.0	0.3[5]	8.5×10^{15}	+0.22
4A	19.0	1.107	1.149	5.4	0.8	2.4×10^{16}	+3.80
5A	10.2	0.725	0.736	4.7	0.4	1.4×10^{16}	+1.52

depleted of boron that it can no longer yield p-type crystal at slow growth-rates. This means that precision doping is not necessary to produce thin p-layers. By doping approximately and periodically forming p-layers by rate-growing, they become thinner and less heavily doped as the melt is consumed. The last two p-layers formed are quite suitable for tetrode fabrication. From probe measurements the widths of the last two p-layers are 0.1–0.3 mil and measurement of the base-to-base resistance in fabricated units shows that the p-layer resistivity is ten times lower than in previous rate-grown n–p–n's with comparable widths.

The advantages of boron described above are peculiar to rate-growing. An additional factor which reduces p-layer resistivity and which may be significant for thin p-layers, arises from the steady meltback. During meltback the liquid at the interface is richer in boron and poorer in antimony than it was during the preceding growth. As a result of this, the incorporation of boron is enhanced when growth begins abruptly, after a steady meltback. This effect is similar to that of remelt described by Pfann.[5]

Maximum oscillating frequencies of tetrodes prepared from this material are generally in excess of 500 Mc and several units oscillate at frequencies above 1000 Mc. The best material so far produced yields tetrode alphas as high as 0.95 at 30 Mc with a phase angle of 8°. The growing process which has been described should produce the sort of variation of resistivity in the p-layer which results in a "built-in" field which aids the transport of carriers across the base. This may account, in part, for the fact that alpha remains high at high frequencies.

The crystal-growing work reported here has been carried out in close cooperation with other areas of these Laboratories where the material has been used for the fabrication of experimental transistors. The authors are grateful to E. Dickten, W. F. Wolfertz, and C. E. Scheidler for the performance data quoted.

[1] Wallace, Jr., Schimpf, and Dickten, Proc. Inst. Radio Engrs. **40**, 1395 (1952).
[2] R. N. Hall, J. Phys. Chem. **57**, 836 (1953).
[3] Burton, Prim, and Slichter, J. Chem. Phys. **21**, 1987 (1953).
[4] H. E. Bridgers and E. D. Kolb (to be published).
[5] W. G. Pfann, J. Metals 294, (February, 1954).

Books Reviewed

Solar Energy Research. Edited by FARRINGTON DANIELS AND JOHN A. DUFFIE. Pp. 290+xv. University of Wisconsin Press, Madison, Wisconsin, 1955. Price $4.00.

A symposium on solar energy was held at the University of Wisconsin in 1953. The participants did not present formal papers but were invited to contribute papers to the present book. The individual articles discuss solar energy in all its aspects: need; available power; applications to heating, air conditioning, electrical power production, distillation, and evaporation; photosynthetic and photochemical utilization; and solar furnaces. An extensive bibliography is provided.

Quantum Theory of Solids. R. E. PEIERLS. Pp. 229+viii. Oxford University Press, New York and London, 1955. Price $4.80.

In his preface to *Quantum Theory of Solids*, Professor Peierls states that he has ". . . concentrated on the fundamental problems, on the known methods for solving them in suitably idealized situations, and on the important basic problems still awaiting solution." The nature of the approximations and simplifications made in handling these many-body problems is brought out and their usefulness demonstrated. Though designed for theoretical physicists, this book will be of value to experimentalists in search of the theoretical bases for the usual models of the effects they study. Certain topics have been intentionally omitted for lack of space: crystal structures, binding energies, plasticity of solids, and dielectric breakdown. The ones that are discussed are, by chapter: "Crystal Lattices," "Interaction of Light with Non-Conducting Crystals," "Electrons in a Perfect Lattice," "Cohesive Forces in Metals," "Transport Phenomena," "Magnetic Properties of Metals," "Ferromagnetism," "Interaction of Light with Electrons in Solids," "Semi-Conductors and Luminescence," and "Superconductivity." This material was originally presented as a course at Les Houches summer school in theoretical physics in 1953.

Dielectric Behavior and Structure. C. S. SMYTH. Pp. 441+x. McGraw-Hill Book Company, Inc., New York, 1955. Price $9.00.

In the twenty-five years since the publication of Professor Smyth's book entitled *Dielectric Constant and Molecular Structure*, the field has grown to the point where he felt that a completely new book was needed. The present volume, *Dielectric Behavior and Structure*, deals with the relations between dielectric constant and dipole moment measurements and the molecular structure of solids and liquids, including organic substances. The book begins with a discussion of static dielectric constant and dipole moment; then comes a chapter on dielectric relaxation in alternating fields followed by descriptions of experimental methods and data for actual substances, in particular glasses, ferro-electrics, high polymers, and electrets. The dipole-moment portion of the book starts with the calculation of molecular moments from experimental data and goes into chemical bonding, intramolecular energy, and resonance in certain classes of organic molecules. There is also a chapter on inorganic and organometallic molecules. The last chapter considers induced or deformation polarization—the polarization from displacement of electrons relative to atomic nuclei and from displacement of atomic nuclei relative to each other.

Modern Physics. JOHN C. SLATER. Pp. 322+xi. McGraw-Hill Book Company, Inc., New York, 1955. Price $5.50.

This book on the atomic and nuclear physics of the twentieth century emphasizes the logical, historical development of modern physics. It is intended as a textbook for advanced undergraduate students. It is primarily a history of the development of ideas rather than a detailed presentation of the experiments and theory of modern physics. The topics covered include kinetic theory, relativity, the nuclear atom, Bohr quantum theory, x-rays, atomic and molecular spectra, wave mechanics, the theory of atoms, molecules and solids, and nuclear physics.

Essentials of Biological and Medical Physics. R. W. STACEY, D. T. WILLIAMS, R. E. WORDEN, AND R. O. MCMORRIS. Pp. 586+xiv. McGraw-Hill Book Company, Inc., New York, 1955. Price $8.50.

The aim of this book is to provide in a single volume a unification of the diverse subjects comprising the field of "biophysics." The book is intended as an undergraduate textbook and includes the application of physics to the understanding of biological processes, the study of the effects of physical environment on biological systems, and the application of physical instrumentation to the study of biological systems. The physicist will find in this book a systematic application of mechanics, thermodynamics, acoustics, optics, fluid dynamics, electromagnetism, and nuclear physics to biological problems. The biologist will find the elementary physics underlying much of his work.

Vapor-Plating. C. F. POWELL, I. E. CAMPBELL, AND B. W. GONSER. John Wiley and Sons, Inc., New York, 1955. Price $5.50.

The term "vapor-plating" as used in this book refers to the chemical deposition of metals or compounds from the vapor phase onto hot surfaces. It does not refer to the evaporation or sputtering of metal vapors onto cold surfaces. A typical vapor-plating process is the coating of a solid with tantalum by heating the solid in a tantalum halide vapor. A typical application is the protection of a surface from corrosion at high temperatures. About one third of the book is devoted to metal coatings, coatings of carbides, nitrides, borides, silicides, oxides, boron, and silicon are considered in the remaining two thirds. This book is one of the Electrochemical Society series.

Machine Translation of Languages. Edited by W. N. LOCKE AND A. D. BOOTH. Pp. 243+xii. Technology Press and John Wiley and Sons, Inc., New York, 1955. Price $6.00.

Fourteen essays on the translation of languages by computing machines are presented in this volume, which also includes a foreword by Warren Weaver and a historical introduction by the editors. The substantial problems faced by the machine and its friends are apparent to the reader of this book, but ingenious schemes for solving or by-passing many difficulties are also apparent. The systems conceived and described vary all the way from a mechanized dictionary as an aid to a skilled translator to an automatic reading and translating machine.

Advanced Calculus. LOUIS BRAND. Pp. 574+xii. John Wiley and Sons, Inc., New York, 1955. Price $8.50.

Though dealing primarily with functions of a real variable, Professor Brand's *Advanced Calculus* introduces classical analysis with a chapter on the number system and includes another on complex variables. Questions of convergence of sequences and series are discussed in Chapter 2, and important theorems and ideas in the realm of real variables are developed in the third and fourth chapters. Chapter 5 is entirely devoted to vector analysis. Definite integrals, improper integrals, line integrals, and multiple integrals (a chapter for each) come next, followed by a chapter on the reversal of order in limiting processes, uniform convergence of sequences, series, and improper integrals. The chapter on functions of a complex variable contains a section on the evaluation of definite integrals using contour integration and another on conformal mapping. The book concludes with a chapter on Fourier Series and four appendices: "Cluster Points," "Difference Equations," "The Difference Calculus," and "Dimensional Checks."

The author, head of the Department of Mathematics at the University of Cincinnati, has completed each chapter with a problem set and has given the answers in the back of the book; a comprehensive test, with answers, is also included.

Books Received

Basic Processes of Gaseous Electronics. LEONARD B. LOEB. Pp. 1012+xvii, Figs., University of California Press, Berkeley, 1955. Price $13.50.

Patents Abstracts Journal. Published by Technical Information Company, Patents Department, Liverpool, England. Pp. 21+16.

Hydraulic Operation and Control of Machines. IAN MCNEIL. Pp. 324+xi, 16 Plates, Figs. 103, Ronald Press, New York, 1955. Price $7.50.